Enhancing Lithium Diffusion in Solid Polymer Electrolyte Batteries through Molecular Dynamic Simulations

Sergio Rodríguez Peña

2023

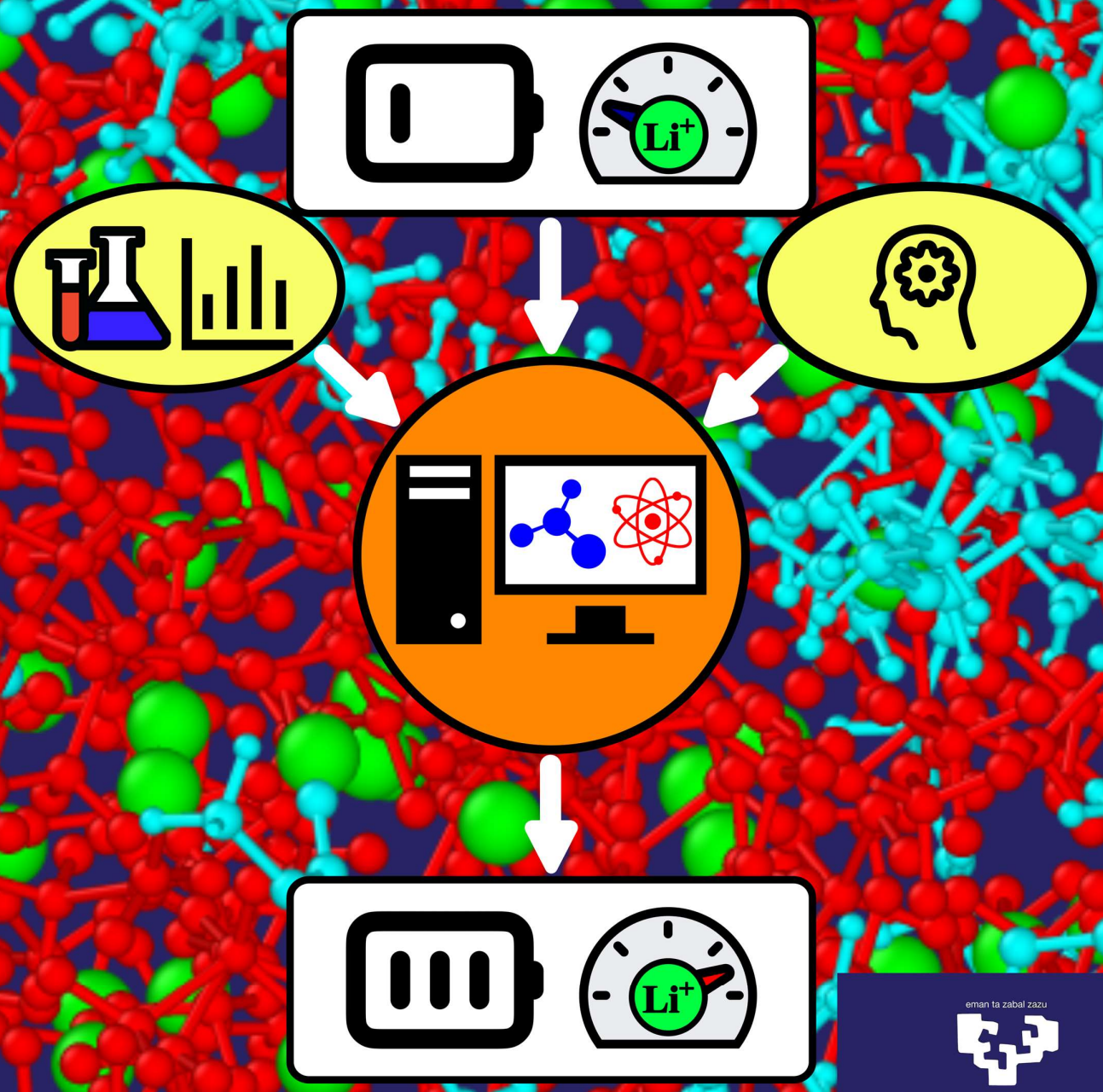

eman ta zabal zazu
Universidad del País Vasco
Euskal Herriko Unibertsitatea

Enhancing Lithium Diffusion in Solid Polymer Electrolyte Batteries through Molecular Dynamic Simulations

Autor:

Sergio Rodríguez Peña

2023

Co-Directors:

Javier Carrasco Rodríguez

Hegoi Manzano Moro

Enhancing Lithium Diffusion in Solid Polymer Electrolyte Batteries through Molecular Dynamic Simulations

Doctoral Thesis by:

Sergio Rodríguez Peña

2023

CIC energiGUNE Director:

Javier Carrasco Rodríguez

UPV/EHU Director:

Hegoi Manzano Moro

Index:

Abstract

The necessity for energy storage has been growing during the last few years due to the development of technology and to the energetic revolution necessary to fight against climate change with greener energies. Lithium-ion batteries (LIBs) have been widely used to power small portable devices and electric cars thanks to their lightness and high energy capacity. Most of the rechargeable batteries that we use in our daily life are LIBs. However, for the next generation of lithium-based batteries, the exponential advance of technology demands more efficient and powerful energy sources. The substitution of the anode (normally composed of graphite in LIBs) for pure Li metal is one of the best solutions since it increases substantially the theoretical capacity of the battery. The presence of a lithium metal electrode in these lithium-metal batteries (LMBs) comes with many problems when just this substitution is done, without varying the composition of the rest of the components of the battery. In LIBs, the electrolyte is commonly liquid, but when this same electrolyte is used in LMBs, the battery suffers from many safety problems. The use of polymers as electrolytes for LMBs has become increasingly attractive because their mechanical properties make them safer than liquids. Although solid polymer electrolytes (SPEs) solve many safety problems of liquid electrolytes, their main disadvantage is the low ionic conductivity that these systems show.

Much more investigation is needed in this field to develop new systems that overcome these problems. The good news is that the polymeric structures are very tunable and almost any desired structure can be obtained in the search for improved battery performance. The chemistry of the lithium salt dissolved in the polymer is also modifiable, which in combination with the tunability of the polymers, allows for a wide range of investigation paths to follow. Here is where the theoretical studies make their appearance as a great solution for investigating new polymeric systems, both before and after the experiments in the laboratories. Molecular dynamics (MD) simulations are a powerful tool that help to understand, at an atomistic level, what is happening inside the system, to identify the interactions between the molecules that can explain the behaviors observed at a macroscopic scale, and the results that are obtained in the labs. A wide variety of systems can be evaluated theoretically in the search for better performing systems before its synthesis attempt in the labs, which will take much longer times and economical efforts. The identification of these interactions can also guide the development of new combinations of chemistries that can further improve the performance of the future lithium batteries.

In this Thesis, we have investigated a wide variety of systems with potential application as electrolytes for LMBs. The research involved varying both the chemistry of the lithium salt and the structure of the polymeric matrix. The primary objective was to elucidate the specific interactions that govern the movement of Li^+ within these systems. Through a rigorous analysis performed via MD simulations and a thorough comparison of our results with experimental, we successfully identified and characterized these crucial interactions. Our theoretical results not only validated the hypotheses proposed experimentally but also provided essential insights into the design of novel molecular structures. These insights strongly suggest that optimizing these sought-after interactions can significantly improve the performance and safety of the

batteries. Overall, this Thesis has contributed substantially to our understanding of electrolyte design for LMBs, paving the way for further exploration and innovation in the future. New avenues for chemical modification can now be explored, informed by the knowledge acquired during the development of this Thesis.

Resumen

La tecnología actual de almacenamiento de energía se encuentra muy limitada a la hora de afrontar los retos que suponen la lucha contra los efectos del incesante cambio climático y la electrificación de la red de transportes global. La mayoría de las baterías que se usan en la actualidad, en aplicaciones donde se requieren baterías ligeras y recargables, se basan en la tecnología de litio-ion (*Lithium-Ion Batteries*, LIBs). Desde su primera comercialización en 1991 por la empresa Sony, su uso se ha extendido ampliamente y son la principal fuente de alimentación de los coches eléctricos desarrollados en la actualidad. El uso de litio como elemento principal les confiere una gran ligereza (debida a que el litio es el tercer elemento más ligero de la tabla periódica) y, por ende, una gran densidad de energía. Sin embargo, su capacidad teórica máxima está muy cerca de alcanzarse.

Esto se debe a que, en su concepción actual, las LIBs poseen un ánodo compuesto de grafito. El ánodo es uno de los tres componentes principales de una batería: ánodo, cátodo y electrolito. A pesar de que existen otros tipos de ánodos, como de $Li_4Ti_5O_{12}$ (LTO) o de nanotubos de carbonos (*Carbon Nanotubes*, CNTs), que permiten conseguir mayor seguridad en las baterías, su capacidad energética es menor, y su uso está mucho menos extendido que los ánodos de grafito. El cátodo sí que tiene una composición más variada. $LiCoO_2$ y $LiFePO_4$ (LFP) son comúnmente usados, variando la capacidad y seguridad de la batería, pero en general no existe una gran diferencia de rendimiento entre ellos y en función del uso que se le vaya a dar a la batería, se escoge uno u otro. En el caso del electrolito, las actuales LIBs poseen electrolitos líquidos (*Liquid Electrolytes*, LEs). Éstos se componen de una sal de litio (siendo la más común el $LiPF_6$) disuelta en un conjunto de compuestos carbonatados (EC, DMC, EMC, PC, etc.). La gran movilidad de estos electrolitos es lo que confiere a las LIBs su gran conductividad.

Dado esto, la única solución posible para dar un gran salto en el rendimiento de este tipo de baterías es cambiar la composición del ánodo. La sustitución del grafito por litio metal puro (Li^0) supondría un gran incremento en la capacidad teórica máxima, siendo hasta 10 veces mayor que con grafito (372 vs 3860 mAh/g respectivamente), dando lugar a la tecnología de baterías de litio-metal (*Lithium-Metal Batteries*, LMBs). Esta solución, sin embargo, conlleva la aparición de problemas severos de seguridad. La gran reactividad del Li^0, en contacto con los poco estables LEs, produce que los compuestos del electrolito se degraden con gran facilidad, siendo imposible el uso de este tipo de electrolitos en LMBs. Es por ello que electrolitos más robustos son necesarios, dando el paso a electrolitos sólidos (*Solid Electrolytes*, SEs). Desafortunadamente, su gran ventaja (su seguridad) viene dada por la gran robustez que les proporciona ser un sólido en lugar de un líquido, lo que conlleva una gran reducción de la conductividad iónica. Una solución intermedia se propone con el uso de electrolitos compuestos por polímeros. Éstos presentan una mayor estabilidad que los LEs, pero sin acarrear reducciones tan drásticas de la conductividad como los SEs.

Ya a finales de la década de los 70, el profesor Michel Armand propuso el uso del polímero *Polyethilene Oxide* (PEO) junto con una sal de litio fácilmente disociable como composición de los conocidos como electrolitos poliméricos sólidos (*Solid Polymer Electrolytes*, SPEs). Las

pruebas realizadas con la sal *Lithium-bis(trifluoromethanesulfonyl)imide* (LiTFSI) fueron fructíferas y demostraron su aplicabilidad como electrolito en presencia de un ánodo de Li^0. A pesar de esto, el sistema LiTFSI/PEO sufre de dos principales problemas. El primero es la baja movilidad del Li^+ en comparación con el $TFSI^-$ cuando la sal se encuentra completamente disociada por el PEO, lo que supone que la mayor parte de la conductividad iónica provenga del anión y no del catión, lo que se traduce en un número de transferencia del litio (*Lithium Transference Number*, Li TN) muy bajo. El segundo es la baja ciclabilidad de las celdas cuando se ponen a prueba, ya que debido al crecimiento de dendritas de Li^0 en la superficie del ánodo, se provocan fallos graves por cortocircuitos a los pocos ciclos de carga y descarga.

El trabajo de esta Tesis se centra concretamente en el estudio, mediante técnicas de simulación teórica, de nuevos sistemas que ayuden a superar esta barrera que impide la comercialización a gran escala de LMBs basadas en la tecnología de SPEs. En concreto, mediante el uso de simulaciones de dinámica molecular (*Molecular Dynamics*, MD) se estudian las interacciones atómicas y moleculares que definen el comportamiento de los sistemas, identificando aquellas que resultan más beneficiosas para el futuro diseño de nuevas combinaciones de químicas, y permitiendo el desarrollo de nuevos sistemas que mejoren las capacidades del LiTFSI/PEO.

Las simulaciones MD se basan en la resolución de las ecuaciones de Newton para cada uno de los átomos que componen el sistema bajo estudio. El conjunto de ecuaciones y parámetros que componen las interacciones atómicas se define como el campo de fuerzas (*forcefield*, FF). El FF se puede dividir en dos partes: las interacciones de enlace y las de no enlace. Las primeras corresponden a las interacciones que se producen entre átomos que se encuentran unidos entre sí, dentro de una misma molécula, y describen las variaciones de energía debido a cambios en la geometría de la molécula. Las segundas corresponden a interacciones a distancia debido a las cargas eléctricas (interacción de Coulomb y de van der Waals). Por simplicidad, los átomos se simulan como entidades únicas, sin diferenciación entre el núcleo y los electrones, y su carga eléctrica neta se trata como puntual e invariable.

Las aproximaciones usadas en este tipo de simulaciones (puramente clásicas) son relativamente sencillas, lo que tiene ventajas y desventajas. Al ser simples, permiten el estudio de sistemas compuestos por decenas de miles de átomos durante cientos de nanosegundos, en los que la descripción de las interacciones es suficientemente precisa para reproducir muchos resultados experimentales. Principalmente, los entornos de coordinación atómicos y moleculares, a través de los análisis de las funciones de distribución radiales (*Radial Distribution Functions*, RDFs), son comparables con los obtenidos mediante espectros de Raman e infrarrojos, pudiendo analizar concretamente cada tipo de interacción individualmente. El análisis de la difusividad de los iones a través de los sistemas poliméricos, con el cálculo de los desplazamientos cuadráticos medios (*Mean Squared Displacements*, MSDs), se puede correlacionar con las medidas de conductividad experimentales.

Por el lado contrario, la definición de las interacciones de enlace no permite ni la rotura ni la formación de enlaces, lo que impide estudiar la reactividad del sistema. Además, el tratamiento de las cargas eléctricas como puntuales y fijas, tampoco permite la formación de dipolos eléctricos ni la variación de carga por interacción entre ellas. En añadido a estos análisis de RDFs y MSDs (los más comunes en la interpretación de las simulaciones MD), se han realizado

una serie de análisis específicos para cada sistema y situación que se requería analizar. Dichos análisis se han escrito en lenguaje Python por el doctorando y se encuentran a disposición del público general.

A parte del uso de simulaciones MD, también se han utilizado en esta Tesis los cálculos *Ab Initio* mediante la teoría funcional de la densidad (*Density Functional Theory*, DFT). Estos métodos sí que hacen uso de cálculos mecano-cuánticos para definir las interacciones atómicas. Siendo mucho más complejos, permiten un estudio molecular mucho más preciso, pero su alto coste computacional imposibilita su uso para sistemas grandes y de larga duración. Su uso en los estudios incluidos en esta Tesis se restringe a la optimización de la estructura geométrica de algunas moléculas (principalmente los aniones de las sales de litio) y al cálculo de sus cargas atómicas parciales mediante el método del potencial electrostático (*Electrostatic Potential*, ESP). Dichas cargas son de crucial importancia ya que un cálculo incorrecto de su valor podría llevar a una incorrecta simulación de las interacciones intermoleculares, afectando severamente al comportamiento del sistema.

Utilizando estas técnicas de simulación teórica se han realizado 4 estudios diferentes en esta Tesis, cada uno de ellos centrado en un aspecto diferente. Los dos primeros se basan en la modificación estructural del $TFSI^-$, manteniendo como polímero el PEO. Mientras que en los dos últimos de mantiene la sal LiTFSI y se estudia una matriz polimérica distinta: *ε-caprolactone* (PCL).

En el primer trabajo incluido en esta Tesis se busca una reducción de la movilidad aniónica. Últimamente se han seguido diferentes caminos para inmovilizar a los aniones, generalmente fijándolos a una cadena polimérica o introduciendo aditivos que se coordinen con ellos y reduzcan su movilidad. Este tipo de estrategias logra incrementar el Li TN considerablemente, pero suelen tener como inconveniente una gran reducción de la movilidad general. En nuestro caso buscamos una estrategia completamente diferente. Manteniendo la mayor parte de la molécula de $TFSI^-$ intacta, para que la disociación de la sal de litio siga siendo completa cuando se disuelva en PEO, se estudian dos modificaciones diferentes. En una de ellas, se sustituye uno de los grupos $-CF_3$ por un anillo aromático de benceno (*benzenetrifluoromethanesulfonylimide*, $BTFSI^-$), mientras que en la otra se añaden grupos isopropilos a este anillo (*triisopropylbenzenetrifluoromethanesulfonylimide*, $TPBTFSI^-$). La idea es que estos anillos interaccionen a través del apilamiento $\pi - \pi$ ($\pi - \pi$ *stacking*) obstaculizando el movimiento de los aniones sin alterar la movilidad del Li^+, con el objetivo de incrementar el Li TN sin una gran reducción de la conductividad general.

Las simulaciones teóricas confirmaron las hipótesis iniciales. A pesar de que una pura interacción $\pi - \pi$ no es reproducible con las aproximaciones usadas en MD, debido a que ésta se debe a interacciones entre dipolos eléctricos, sí que pueden aparecer efectos estéricos (favoreciendo ciertas configuraciones espaciales) que hagan interaccionar a los nuevos aniones. Una gran reducción en la difusividad de los nuevos aniones se observa, sin una correspondiente gran disminución en la movilidad del Li^+. Esto se ve reflejado en un incremento del Li TN en los sistemas LiBTFSI/PEO y LiTPBTFSI/PEO. Además, estas modificaciones no alteran ni la estructura de solvatación del Li^+, lográndose una disociación casi completa de las sales, ni su mecanismo de difusión a través del sistema. Estudios más específicos de la interacción entre

aniones mostraron como ésta se producía efectivamente entre los anillos aromáticos introducidos, favoreciendo dos configuraciones espaciales en concreto. Esta interacción resulta más efectiva entre $BTFSIs^-$ debido a la simpleza de sus anillos. Estos estudios teóricos se corroboraron con medidas experimentales donde se constata la interacción entre anillos, además de medir valores de Li TN mucho mayores que los predichos teóricamente (y que ningún otro sistema de la familia de las amidas). Pruebas en celdas mostraron, además, un incremento en la estabilidad del electrolito con respecto al sistema LiTFSI/PEO, en especial del LiBTFSI/PEO.

En el segundo trabajo, se busca un incremento en la estabilidad electroquímica del electrolito. El $TFSI^-$ posee grupos $-CF_3$ que son bastante estables y no se degradan con facilidad en contacto con el ánodo de Li^0. Esto provoca que la interfase de electrolito sólido (*Solid Electrolyte Interface*, SEI) sea inestable y se formen dendritas de Li^0 que provocan problemas de seguridad. Además de su estabilidad, su alto contenido en flúor hace que no sean respetuosos con el medio ambiente. Por ello, en este estudio se sustituyen ambos grupos $-CF_3$ del $TFSI^-$ por grupos $-CF_2H$, formando *bis(difluoromethanesulfonyl)imide* ($DFSI^-$). La introducción de este hidrógeno en ambos grupos hace que sean menos estables y se degraden con mayor facilidad. Esto supone dos grandes mejores con respecto al $TFSI^-$. Al ser más degradables, el $DFSI^-$ es más respetuoso con el medio ambiente que el $TFSI^-$, además de reducir la cantidad de flúor. En segundo lugar, esto también permite la formación de nuevos compuestos provenientes de su descomposición al contacto con el ánodo de Li^0, favoreciendo la formación de una SEI en su superficie más estable debido a la presencia de compuestos como el LiH y mayor cantidad de LiF.

Los estudios teóricos se centraron en confirmar que la disociación de la sal LiDFSI en el PEO era completa. Los hidrógenos tienden a cargarse positivamente, a diferencia de los flúors que lo hacen negativamente, lo que conlleva una mayor polarización del anión. Esto hace que la concentración de carga negativa sobre los oxígenos sea mayor y, por ende, su fuerza de interacción con el Li^+. Esta mayor energía de disociación podría dificultar su disolución en la matriz de PEO. Sin embargo, los estudios del entorno de coordinación y mecanismo de difusión del Li^+ no muestran diferencias significativas. La adición de hidrógenos trae consigo otro efecto, que es la aparición de interacciones con el PEO mediante puentes de hidrógeno. Esto obstaculiza la movilidad del $DFSI^-$, pero como se realiza con el PEO y no entre aniones, también reduce la movilidad del Li^+, por lo que no se observa un incremento del Li TN. Esto se comprueba experimentalmente con una reducción, aunque no muy significativa, de la conductividad total. Desafortunadamente, con simulaciones MD clásicas no se puede estudiar la descomposición del $DFSI^-$, por lo que esta parte se debe dejar a los estudios en el laboratorio, donde sí que se probó que este electrolito daba una mejora sustancial en la vida de las celdas. Un estudio de la SEI muestra como su composición es diferente a la del sistema LiTFSI/PEO debido a la mayor degradabilidad del $DFSI^-$.

En el tercer trabajo se dilucida el mecanismo de difusión iónica de la sal LiTFSI en PCL. El PCL es otro polímero que se ha usado como sustituto del PEO en algunos casos. La presencia de grupos carbónicos (-C(=O)-O) hace que el comportamiento de este polímero sea diferente al PEO, donde sólo hay grupos éter (-O-). El PEO sufre de problemas de cristalización cuando

la temperatura disminuye por debajo de los 60 ºC, disminuyendo la conductividad. Es por ello que el uso de otro tipo de polímeros sea también una posible solución. El PCL, además, tiene similitudes químicas con los compuestos carbonatados usados en los LEs. Sin embargo, el mecanismo de difusión del Li^+ en él sea poco conocido. En el PEO, se conoce desde hace tiempo que la flexibilidad y pequeño tamaño de los monómeros permite que se enrolle alrededor del Li^+, coordinándose con 6 oxígenos diferentes, pero seguidos, de la cadena. El Li^+ se desplaza avanzando a lo largo de la cadena de PEO, de monómero en monómero. En este estudio, se caracteriza cómo varía el entorno de coordinación del Li^+ a medida que se aumenta la cantidad de PCL en el sistema de referencia LiTFSI/PEO ($PEO_{100}PCL_0$) hasta que su sustitución es total en el LiTFSI/PCL (PEO_0PCL_{100}), analizando también el efecto que esto tiene en la movilidad iónica.

Primeramente, se analizó esto último con las simulaciones, donde ambos sistemas puros, junto con la mezcla equitativa $PEO_{50}PCL_{50}$, se estudiaron. Se observa cómo se produce una reducción de la difusividad del Li^+ si pasamos del $PEO_{100}PCL_0$ al $PEO_{50}PCL_{50}$, pero ésta se mantiene al añadir más PCL y eliminar el PEO (PEO_0PCL_{100}). Al igual que el Li^+, el $TFSI^-$ también reduce su movilidad, pero lo hace de manera proporcional al incremento de PCL, llegando hasta una difusividad muy similar al Li^+. Esto se ve reflejado en un gran incremento del Li TN. Esto ya indica que el mecanismo de difusión del Li^+ debe ser diferente en el PCL que en el PEO. Análisis en profundidad de la coordinación del Li^+ muestran que cuando se encuentra interaccionando con el PCL, también lo hace con el $TFSI^-$ al mismo tiempo. Es por esto que la movilidad de ambos iones es muy similar en el sistema PEO_0PCL_{100}, porque se encuentran coordinados y se desplazan juntos. Además, el Li^+ no se mueve a lo largo de la cadena de PCL, como en el PEO, sino que salta de una posición a otra, de manera intramolecular o intermolecular indiferentemente. Los resultados del sistema $PEO_{50}PCL_{50}$ muestran que ambos polímeros no se mezclan especialmente bien y que el Li^+ tiene preferencia por la región del PEO. Gracias a esto, y a las medidas de la conductividad experimentales, se extrae que a medida que se añade PCL y se reduce el PEO, se reduce la disponibilidad de espacios para que el Li^+ se mueva, saturándose el PEO y reduciendo la movilidad del Li^+. Cuando la cantidad de PCL es lo suficientemente grande como para que el Li^+ tenga que estar coordinado a él, su movimiento es más lento que en el PEO, pero la gran disponibilidad de puntos de coordinación lo solventa, manteniendo constante su difusividad general. Sin embargo, cuanto más Li^+ se encuentre en la región de PCL, más $TFSI^-$ se coordina con él y reduce su movilidad.

Para finalizar, se realiza en el último trabajo de esta Tesis un estudio del efecto de la concentración de la sal LiTFSI en los sistemas LiTFSI/PEO y LiTFSI/PCL, sin mezclar los polímeros. La concentración de la sal es fundamental para la conductividad general, ya que es proporcional tanto a la velocidad de difusión de los iones como a su concentración. Si hay muchos iones que se mueven a una velocidad normal, la conductividad será mayor que si hay pocos iones, aunque éstos se muevan muy rápido. Por ello, se incrementa la concentración hasta alcanzar el régimen de polímero en sal. Este régimen se alcanza cuando el porcentaje de peso de la sal supera el 50 %. Hasta ahora, todos los estudios anteriores se han realizado a una proporción monómero-Li^+ de 20-1. Esta vez, comenzamos con una concentración de sal algo mayor, con una proporción de 6-1 (aún en el régimen de sal en polímero), y estudiamos tres

concentraciones diferentes en el régimen de polímero en sal: 1-2, 1-4 y 1-6 monómeros por Li^+.

En la comparativa de las difusividades, en el caso del PEO, la movilidad del Li^+ aumenta en el régimen de polímero en sal con la concentración, aunque en valores del orden de los de baja concentración. El $TFSI^-$, por el contrario, sufre una gran disminución de su movilidad una vez se entra en el régimen de polímero en sal y dentro de él se mantiene constante con la concentración. Esto conlleva un incremento en el Li TN hasta valores cercanos a 0.75 e indica un cambio en el mecanismo de difusión de los iones. En el caso del PCL, se ve un incremento gradual en la difusividad del Li^+ con la concentración, mientras que la del $TFSI^-$ se mantiene relativamente constante. Esto va incrementando el Li TN también hasta valores cercanos a 0.75. En ambos polímeros se observa un cambio en el mecanismo de difusión del Li^+ en los sistemas de polímero en sal, llegando incluso a converger los valores de difusividad a alta concentración. Los análisis de los entornos de coordinación también indican una convergencia entre ambos polímeros a altas concentraciones. Análisis en profundidad muestran que los polímeros se encuentran completamente saturados, quedando aún gran parte de la sal disponible y coordinándose únicamente entre sí. Es por esto que las características de los sistemas son tan similares, independientemente del polímero, ya que gran parte de los iones se encuentran en un entorno libre de polímero. En esta región iónica, los iones se mueven con bastante libertad, no se forman pequeñas agrupaciones aisladas una de otra, sino que todos los iones forman una especie de superagrupación que engloba todos los iones del sistema (incluso muchos que se encuentran coordinados al polímero, son parte también de esta superagrupación).

Los estudios desarrollados en esta Tesis han permitido el descubrimiento y la comprensión de varios sistemas con aplicabilidad como SPEs para su uso en LMBs. El uso de técnicas de simulación computacional, en especial las simulaciones MD, han logrado confirmar que las hipótesis con las que se diseñaban los nuevos sistemas eran correctas y se producían los efectos buscados. Con ello, diferentes puntos débiles del sistema LiTFSI/PEO se han conseguido corregir en pruebas realizadas con los sistemas reales en los laboratorios, pudiendo así guiar el futuro desarrollo de sistemas que sigan aumentando el rendimiento y la seguridad de las LMBs que usan SPEs como base.

List of Publications

Included in this Thesis:

- Qiao, L., Oteo, U., Zhang, Y., Peña, S. R., Martínez-Ibañez, M., Santiago, A., ... & Armand, M. (2020). Trifluoromethyl-free anion for highly stable lithium metal polymer batteries. *Energy Storage Materials*, *32*, 225-233. (https://doi.org/10.1016/j.ensm.2020.07.022)

- Meabe, L., Peña, S. R., Martinez-Ibañez, M., Zhang, Y., Lobato, E., Manzano, H., ... & Zhang, H. (2020). Insight into the ionic transport of solid polymer electrolytes in polyether and polyester blends. *The Journal of Physical Chemistry C*, *124*(33), 17981-17991. (https://doi.org/10.1021/acs.jpcc.0c04987)

- Qiao, L., Rodriguez Pena, S., Martínez-Ibañez, M., Santiago, A., Aldalur, I., Lobato, E., ... & Zhang, H. (2022). Anion π–π stacking for improved lithium transport in polymer electrolytes. *Journal of the American Chemical Society*, *144*(22), 9806-9816. (https://doi.org/10.1021/jacs.2c02260)

Non-Included in this Thesis:

- de Larramendi, I. R., Lozano, I., Enterría, M., Cid, R., Echeverría, M., Peña, S. R., ... & Ortiz-Vitoriano, N. (2022). Unveiling the Role of Tetrabutylammonium and Cesium Bulky Cations in Enhancing Na-O2 Battery Performance. *Advanced Energy Materials*, *12*(2), 2102834. (https://doi.org/10.1002/aenm.202102834)

- Fortuin, B. A., Meabe, L., Peña, S. R., Zhang, Y., Qiao, L., Etxabe, J., ... & Carrasco, J. (2023). Molecular-level insight into charge carrier transport and speciation in Solid Polymer Electrolytes by chemically tuning both polymer and Lithium salt. *The Journal of Physical Chemistry C*, *127*(4), 1955-1964. (https://doi.org/10.1021/acs.jpcc.2c07032)

- Fortuin, B. A., Otegi, J., Del Amo, J. M. L., Peña, S. R., Meabe, L., Manzano, H., ... & Carrasco, J. (2023). Synergistic theoretical and experimental study on the ion dynamics of bis (trifluoromethanesulfonyl) imide-based alkali metal salts for solid polymer electrolytes. *Physical Chemistry Chemical Physics*, *25*(36), 25038-25054. (https://doi.org/10.1039/D3CP02989A)

Conferences and Workshops:

- Workshop: *Modern Approaches to Coupling Scales in Materials Simulations*. Given by the Lehrstuhl für Theoretische Chemie TUM School of Natural Sciences. Online Assistance. June 29th – July 1st, 2020.

- Workshop: *Materials Design for Energy Storage and Conversion: Theory and Experiment*. Given by the Centre Européen de Calcul Atomique et Moléculaire (CECAM). Online Assistance. March 2nd – March 5th, 2021.

- Summer School: *Methods in Molecular Simulations Summer School 26th edition*. Given by Durham University and supported by The Computer Simulation of Condensed Phases (CCP5) and Centre Européen de Calcul Atomique et Moléculaire (CECAM). Online Assistance. July 12th – July 22nd, 2021. Participation with a poster: *New n-cyclic Li-salts for Solid Polymer Electrolytes (SPEs) Batteries. Screening and ESW analysis using MD Simulations.*

- Congress: GEP-SLAP2022 (XVI Reunión del Grupo Especializado de Polímeros – GEP 2022 y XVII Simposio Latinoamericano de Polímeros – SLAP 2022). May 8th – May 12th, 2022. Participation with an oral communication*: Insight into the Ionic Transport of Solid Polymer Electrolytes in Polyether and Polyester Blends*.

- Congress: ESPE23 (1st European Symposium on Polymer Electrolytes for Battery Applications). September 25th – September 27th, 2023. Participation with an oral communication: *Anion π-π Stacking for Improved Lithium Transport in Polymer Electrolytes*.

International Stay:

- Carried out an international stay in the William G. Lowrie Department of Chemical & Biomolecular Engineering of the Ohio State University, under the supervision of Prof. Lisa M. Hall. The stay was conducted from January 2nd to March 31st of 2023. The purpose of the stay was to train the doctorand in the implementation and use of coarse-grained models to perform molecular dynamics simulations of solid polymer electrolytes at time and length scales of interest for battery operation. Specifically, the research activity will aim at rationalizing ion transport dynamics in polycaprolactone-based electrolytes, with a focus on capturing the basic physics of polymer connectivity and long-range Coulomb interactions.

Acknowledgements

I want to start these acknowledgements by thanking CIC energiGUNE for giving me the opportunity to perform these investigations, for trust in me with zero experience outside the university. Thanks to all the people who have formed part of the Modelling group during these more than 4 years. Especially, to Javier Carrasco, who has guided me with a perfect mix between keeping an eye on my work and leaving me space to learn by myself. To the people who were there to help me give my first steps inside CIC (Oier, Oier, Heng, and Lian) and to all the people who have joined the group (Alfonso, Andrey, Alex, Brigette, Alexis, Anass, and Imelda). Also, outside our group, I want to thank all the people of CIC for transforming the job environment into a familiar place. We have gone through a global pandemic together, and that is something difficult to forget.

I also want to thank Hegoi Manzano for directing this Thesis from the university and helping me with all the bureaucracy that this implies. In addition, extend the acknowledgement to Lisa Hall, my supervisor during my stay in Columbus, for accepting me to form part of her group (Diego, Felipe, Mengdi, Jacob, Yuanhao and Spand) during those great three months.

Besides, I want to thank the Basque Government for their financial support through the PhD grants during the years 2020 and 2021 (Nº Ref.: PRE_2020_1_0353 MOD.:A and PRE_2021_2_0187 MOD.:A).

Para finalizar, y permitidme que cambie a mi propio idioma, quiero agradecer a toda la gente que me ha hecho llegar hasta aquí. A todos los profesores que me inculcaron el amor, ya latente en mí, por la ciencia a través de mi paso por el colegio e instituto. Siempre me han dicho que yo tendría que trabajar en un sitio donde me pagaran por estudiar y, más o menos, al final lo he conseguido. A la familia que hemos formado aquí en el CIC y cuya amistad quedará para siempre (Ainhoa, Carlos, Esti, Eku, Gelines, Ici, Jose Antonio, María, Miguel, Marian, Violeta y perdón, porque seguro me dejo nombres fuera de esta lista).

Por último y más importante, a mi familia. Papá, Mamá y Jorge, GRACIAS.

Chapter 1. Introduction

1.1. Need for (better) batteries

The world's energy consumption is nowadays strongly dependent on the combustion of non-renewable fossil fuels, and this trend is exacerbated by the modernization of society and increasing energy demands. This presents a significant challenge to the environment, as the International Energy Outlook predicts a 50% rise in global energy consumption by 2050, posing serious threats such as climate change, pollution, and the depletion of non-renewable energy resources *[1]*. Urgent action is needed to transit towards more sustainable and renewable energy sources, in order to mitigate these risks and safeguard the planet for future generations.

Electrochemical energy storage can play a pivotal role in the quest for an environmentally sustainable energy supply. Currently, rechargeable Li-ion batteries (LIBs) are at the forefront of the field. However, this technology is already reaching its theoretical energy density limit *[2]*, and besides, there is a safety concern ascribed to the use of volatile and flammable organic solvents as liquid electrolyte *[3]*. Therefore, there is a need for exploring new chemistries and systems that can enable technologies beyond LIBs, while addressing the growing demand forecasted for batteries in Europe by 2030, driven mainly by the transport electrification *[4]*.

To go beyond LIB technology, solid-state Lithium-metal batteries (LMBs) have attracted much interest in recent years from both industry and scientific community. In particular, LMBs based on the use of solid polymer electrolytes (SPEs) have emerged as the most promising candidate due to the favorable mechanical properties, cost, and processability of SPEs (see, e.g., *[5]*). Lithium bis(trifluoromethanesulfonyl)imide (LiTFSI) in particular, has garnered significant interest due to its good thermal and chemical stability, anion flexibility, and ability to plasticize the polymer matrix. Actually, SPEs comprising LiTFSI as conducting lithium salt and polyethylene oxide (PEO) as solvating polymer matrix have been successfully integrated into an electric vehicle by Bolloré *[6]*, demonstrating their potential application as power source. Nevertheless, the ethylene oxide (EO) units contained in PEO polymer lack enough anodic stability (3.9 V vs. Li/Li^+), limiting its use to low-voltage cathode materials and, therefore, preventing reaching high energy densities *[7]*. Additionally, the electrochemical performance of LMBs is heavily influenced by the nature of the salt anions present in the polymer electrolyte. LiTFSI, for example, presents three main drawbacks that must be addressed. Firstly, its low Li^+ transference number (Li TN) leads to low Li^+ conductivity and cell polarization *[8]*. Secondly, it exhibits poor electrochemical stability when in contact with the aluminum current collector *[9]*. Finally, it forms an unstable solid electrolyte interface (SEI) when used with a lithium metal anode *[10]*, *[11]*. In order to overcome these limitations, this Thesis is focused on developing new polymer electrolytes and new lithium salts that can mitigate these issues.

In the remainder of this introductory chapter, we aim to provide a comprehensive understanding of the working principles of rechargeable batteries, with a focus on LIBs and

LMBs. To achieve this goal, we begin in *Section 1.2* with a brief overview of the main concepts underlying the functioning of rechargeable batteries in general. In *Section 1.3*, we delve into the details of how LIBs work, highlighting their key components and the electrochemical reactions involved. To finalize in *Section 1.4* with an introduction to LMBs, outlining their unique features and potential advantages over LIB technology.

1.2. How does a battery work?

A battery is a device whose purpose is to store energy. Through a series of chemical reactions, batteries are capable of storing a limited amount of energy and provide it whenever and wherever it is necessary, without the need for a direct connection to the electric grid. With their widespread use in a variety of applications, from small electronic devices to electric vehicles and renewable energy systems, batteries have become an essential part of modern life.

Batteries can be broadly classified into two categories based on their construction and operation:

- **Primary batteries**: Also known as disposable batteries, are designed for one-time use, and cannot be recharged. The chemical reactions used to store energy are not reversible. Examples of this type of batteries are the alkaline or the button batteries. These batteries are especially useful to power small devices that consume little energy because their functioning consists of being in a kind of standby state (e.g., smoke detectors), and also devices that are only used during short times and are switched off most of the time (e.g., remote controls).

- **Secondary batteries**: These are rechargeable batteries that can be used multiple times by recharging them. This is because the chemical reactions involved are reversible. Lead-acid and LIBs are examples of secondary batteries. They are especially useful for powering devices where lightness is crucial and small batteries are needed, or electronic systems that need to be turned on for a long time (e.g., laptops and cell phones).

Independently of its type, all batteries are composed by the same basic components: two electrodes (anode and cathode) and electrolyte (see *Figure 1-1*). The electrolyte is placed between the electrodes and serves as an ionic conductive medium.

The electrodes are connected externally to close the electric circuit and allow the electrons to move from one electrode to the other, while cations move through the electrolyte. To create a potential difference, the electrodes of a battery must be made of varied materials that undergo different redox reactions. In the anode, cations and electrons are generated and travel separately to the cathode. At the cathode, they recombine via another reaction, but the initial and final products differ in the anode and the cathode. Notice that the redox reactions that take place in batteries convert chemical energy into electrical energy, but these reactions only occur if the electrodes are connected externally, and the electric circuit is closed. Without this connection, the reactions cannot take place and the battery cannot produce electricity.

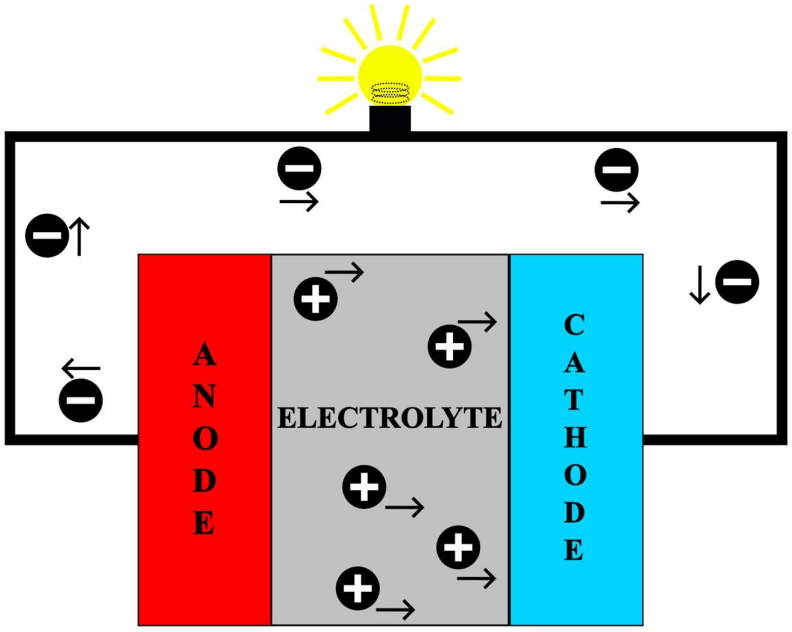

Figure 1-1: Basic scheme of a battery, with the anode in red, the cathode in blue and the electrolyte in gray. It is also shown the movement of the charged species during the discharge process.

In secondary batteries, the reactions are produced both during the charge and the discharge process, but they are inversed. During the discharge process, certain species oxidize in the anode, losing electrons, while in the cathode, they undergo reduction, gaining electrons. This process is energetically favorable, meaning that the reactions will occur if the electrodes are externally connected, and the circuit is closed. However, to charge a battery, an external source of energy is required, such as connecting it to the electric grid. This is because the reactions that occur during charge are opposite to those that occur during discharge and are therefore energetically non-favorable. In other words, charging a battery requires energy input to reverse the chemical reactions that took place during discharge.

Batteries are characterized by many properties. The capacity of a battery (Q), measured in ampere-hour (Ah), is the amount of electric energy (E) it can deliver at a certain voltage (V).

$$Q = \frac{E}{V} \qquad 1.1$$

Normally the energy is not given as an absolute number, but in density form. Energy density refers to the amount of energy stored in a certain volume of material and is typically measured in watt-hours per liter (Wh/L). However, when measuring the energy stored in a certain mass of the material, it is known as the specific energy and is measured in watt-hours per kilogram (Wh/kg). So, given a certain weight, a higher specific energy battery design will store more energy.

Another important characteristic of a battery is the battery potential ($E^0_{Battery}$), which is determined by the difference in electric potential between the reactions that occur at the cathode and at the anode.

$$E^o_{Battery} = E^o_{cathode} - E^o_{anode}$$

1.2

Specifically, it is the difference in the reduction potentials of the cathode and the oxidation potentials of the anode. This potential difference drives the flow of electrons through the external circuit and powers the device or system connected to the battery. In essence, the battery potential represents the amount of electric energy that the battery can provide.

However, to properly define these potentials we need a reference. Normally the reduction reaction of hydrogen, also called standard hydrogen electrode (SHE), is chosen as the reference of 0 V potential.

$$2H^+ + 2e^- \rightleftarrows H_2 \quad (E^o = 0\ V)$$

1.3

Although the SHE is commonly used as a reference for reduction potentials, in the field of LIBs, it is more frequent, and also convenient, to compare the different materials with the reduction potential of lithium ($E^o_{Li^+}$= -3.04 V *vs* SHE). So, when we refer to potentials versus lithium (*vs* Li^+/Li), we are taking the potential of the lithium as 0 V.

The C-rate is another key parameter used to evaluate the performance of a battery, as it indicates how quickly a battery can be charged or discharged relative to its capacity. Specifically, the C-rate is defined as the constant-current charge (or discharge) rate that the battery can sustain for 1 hour, typically measured in ampere hour rating of the battery multiplied by 1 h^{-1}. For example, if a battery has a nominal capacity of 200 mAh and is discharged at a rate of 1000 mA, it would have a C-rate of 5C (it will take 1 h / 5 = 12 min to be completely discharged); while if the discharge rate is 100 mA, it would correspond to a C-rate of 0.5C (2 hours to discharge it). It is worth noting that the C-rate can affect the battery's performance and lifespan. High C-rates can generate more heat and stress on the battery, which can reduce its capacity and overall lifespan over time.

In our modern world, secondary batteries play a crucial role due to the vast number of devices that rely on them for power *[12]*. Many of these devices are portable electronics or electric vehicles, and the ability to reuse the same battery multiple times is a key feature *[13]*, *[14]*. Amongst the most widely used and commercially successful batteries are LIBs *[15]*. If you own a device with a rechargeable battery, there is a good chance it is powered by a LIB.

1.3. Lithium-Ion Batteries

LIBs have been the leading technology in the field of energy storage for small portable devices since their introduction by Sony in 1991. The small size, lightness, and high energy density of these batteries made them an ideal choice for powering the rapidly growing market of small electronic devices such as cell phones, laptops, and wireless technology. Over the years, this technology has continued evolving and has now become a promising candidate for the revolutionary electric vehicle technology *[16]*, *[17]* and electric transport in general. As a result, the demand for LIBs has significantly increased in recent years, and their production is expected to grow exponentially in the future *[18]*.

Figure 1-2 illustrates a schematic diagram of the structure of a typical LIB. However, it is worth noting that the exact composition of these batteries can significantly vary depending on the specific application and manufacturer. The electrodes have a metal covering acting as an electron collector. These coverings are normally made of copper (for the anode) and aluminum (for the cathode), because of the great abundance of these elements in nature and their low prize *[19]*. Let us analyze the most common composition of the three main components of the LIBs.

- **Cathode**: Layered oxides, such as $LiCoO_2$, are typical cathode materials because of their ability to intercalate Li^+ between the layers *[20]*. However, $LiCoO_2$ suffers from low capacity (165 mAh/g) and operating voltage (4.35 V *vs* Li^+/Li). To address these issues, Co can be replaced with other metals such as Mn, Fe, and Ni to increase the operating voltage. Additionally, these metals can be combined in different ratios to achieve better performance combinations *[21]*, *[22]*, *[23]*, *[24]*, *[25]*. $LiFePO_4$ (LFP) has also gained popularity as a cathode material due to its safety and longer battery life, although it has a lower energy density than $LiCoO_2$.

- **Anode**: Currently, the anode materials show limited variability, with graphite being the most widely employed due to its high theoretical specific capacity (372 mAh/g) *[26]*, *[27]*. However, graphite has a low working potential (0.1 V *vs* Li^+/Li), which opens the possibility of Li metal plating caused by charging with high currents that poses safety issues and limits the charging speed. Therefore, alternative anode materials, capable of operating at higher potentials, are being explored. One such material is $Li_4Ti_5O_{12}$ (LTO) *[28]*, which is able to operate at potentials up to 1.5 V *vs* Li^+/Li. Yet, LTO has a reduced specific capacity of 175 mAh/g, as well as low electronic conductivity and Li^+ diffusion. Despite these drawbacks, LTO can compete with graphite for applications requiring extreme safety. There are some examples of electric vehicles *[29]*, *[30]* that are powered by Toshiba's SCiB battery *[31],* which uses this technology. Another alternative is the use of other carbon structures, such as carbon nanotubes (CNT) *[32]* to augment the capacity compared to the graphite anode. While CNT are more robust, they tend to trap more Li^+ within their structure than graphite, thus reducing the capacity of the battery over time. Overall, there is ongoing research into alternative anode materials that can

deliver higher performance and improved safety for LIBs. Several recent reviews provide valuable insights into the latest advancements in this field *[33]*, *[34]*, *[35]*.

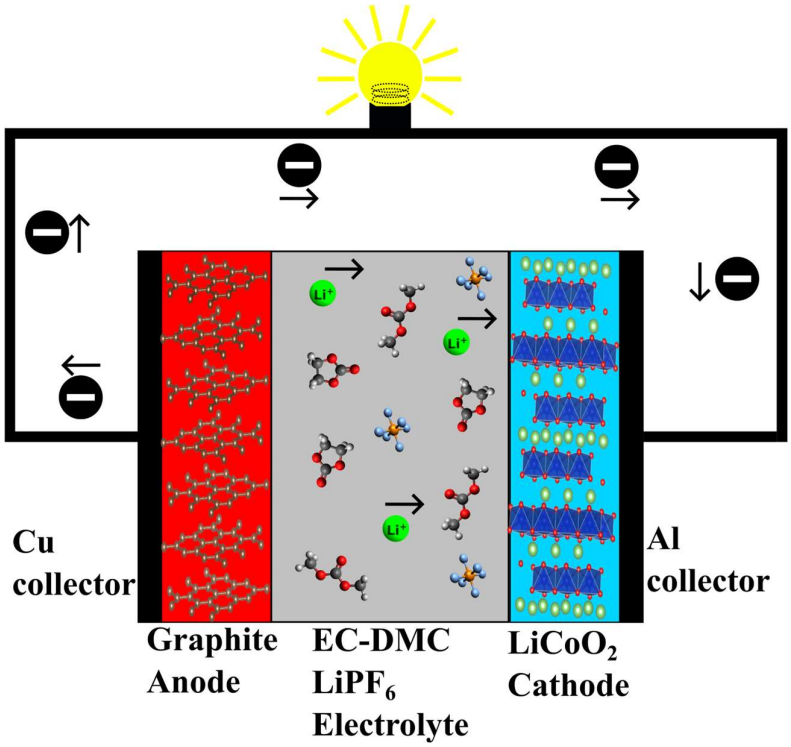

Figure 1-2: Basic scheme of a LIB. In this example, graphite is used as anode, $LiCoO_2$ as cathode, and $LiPF_6$ immersed in a mixture of EC and DMC as electrolyte.

- **Electrolyte**: The electrolyte in a LIB must be able to transport Li^+ from the anode to the cathode during discharge process and from the cathode to the anode during charge *[36]*. LIBs are normally based on liquid organic electrolytes constituted by lithium hexafluorophosphate ($LiPF_6$) dissolved in a mixture of various carbonate solvents such as ethylene carbonate (EC), propylene carbonate (PC), or ethyl-methyl carbonate (DMC). One of the advantages of these electrolytes is the low dissociation energy of $LiPF_6$ and the high stability of PF_6^-, which allows for the use of > 4 V electrodes. However, there are also some drawbacks. For example, $LiPF_6$ undergoes thermal decomposition at 105 ºC, and the carbonate solvents used in these electrolytes are highly flammable, which can pose safety risks *[37]*, *[38]*. To mitigate these issues, alternative lithium salts such as LiTFSI and lithium bis(fluorosulfonyl)imide (LiFSI), which belong to the family of imides, have been proposed. These salts offer improved stability compared to $LiPF_6$ and have demonstrated relatively high conductivities *[39]*, *[40]*, although not quite as high as $LiPF_6$. Another approach to enhance safety is to replace the carbonate solvents with ionic liquids *[41]*, *[42]*, *[43]*, *[44]*. While ionic liquids are generally considered safer than carbonate solvents, they typically exhibit lower ionic conductivities. Moreover, due to their higher price, ionic liquids have yet to be commercialized in LIBs and remain a

topic of intense research. As an alternative to liquid electrolytes, we also find polymer electrolytes *[45]*, *[46]*, *[47]*, *[48]*, which can be classified as either gel or solid depending on their structure *[49]*, *[50]*. While polymer electrolytes offer increased safety compared to liquid electrolytes, their conductivity tends to decrease, especially at room temperature. Moreover, as the electrolyte becomes more stable, the diffusion of ions through it tends to become more difficult, resulting in decreased conductivity and reduced battery power.

Let us now examine the reactions that enable the functioning of a LIB. Considering the scheme shown in *Figure 1-2*, which depicts a typical LIB with graphite serving as the anode and $LiCoO_2$ as the cathode, the battery's operation can be described as follows:

1) When the LIB is fully charged, Li^+ sits in the anode, where it intercalates into graphite to form Li_xC_6. In contrast, the cathode consists of Li_xCoO_2 and contains a depleted amount of lithium ($x < 1$); delithiating all the lithium from Li_xCO_2 ($x = 0$) applying voltages greater than 4.3 V *vs* Li^+/Li causes significant structural instability and severe capacity fade.

2) When the battery is connected (closing the circuit), the intercalated metallic lithium atoms in the anode oxidize and form Li^+.
$$Li_xC_6 \rightarrow C_6 + xLi^+ + e^-$$

3) Then, Li^+ moves through the electrolyte to the cathode, while the electrons move through the electric wire powering the electric device.

4) When Li^+ and electrons arrive at the cathode, the reduction occurs.
$$Li_{x<1}CoO_2 + xLi^+ + e^- \rightarrow Li_{x=1}CoO_2$$

Notice that the electrolyte itself does not participate in the electrochemical reactions that make the battery work. Rather, its sole function is to serve as a medium for the transport of Li^+ between the two electrodes. Despite this passive role, the composition of the electrolyte is crucial for the battery's overall performance. Specifically, the electrolyte establishes the rate of ion transfer between the electrodes, which in turn governs the amount of energy that the battery can deliver. In addition, the electrolyte must exhibit stability under the effect of the potential gradients that arise from the diffusion of charges. Therefore, choosing an appropriate electrolyte is a key consideration in designing a high-performing battery.

The composition of the electrolyte plays also another crucial role in the performance of a LIB, as it determines the characteristics of the so-called solid electrolyte interphase (SEI) that forms on the surface of the electrodes *[51]*, *[52]*, *[53]*, particularly the anode, upon decomposition of some of the electrolyte's components. A stable SEI is beneficial because it isolates the anode from the rest of the electrolyte, preventing further decomposition. It consists of various compounds, such as LiO_2, LiF, and Li_2CO_3, which form a crust-like layer on the electrode surface. However, this layer also contains some retained Li^+, which reduces the battery's capacity after the first charge-discharge cycle. Nonetheless, once the SEI has formed, it

provides stability and protection for subsequent cycles. In this regard, commercial electrolytes typically include additives such as vinyl carbonate (VC) or fluoroethylene carbonate (FEC), which decompose upon contact with the anode and help form a stable layer *[54]*.

1.4. Lithium-Metal Batteries

Conceptually, the general structure of a LMB is similar to a LIB, where the graphite anode is simply substituted by pure lithium metal (see *Figure 1-3*) *[55]*, *[56]*, *[57]*. This modification results in a theoretical specific capacity for the battery that is ten times greater than that of a conventional LIB. Specifically, the theoretical capacity of a LMB is 3860 mAh/g, compared to the 372 mAh/g capacity of a typical graphite-based LIB. Thus, LMBs are very promising candidates to substitute LIBs, especially in electric vehicles, where range and charge speed are crucial factors.

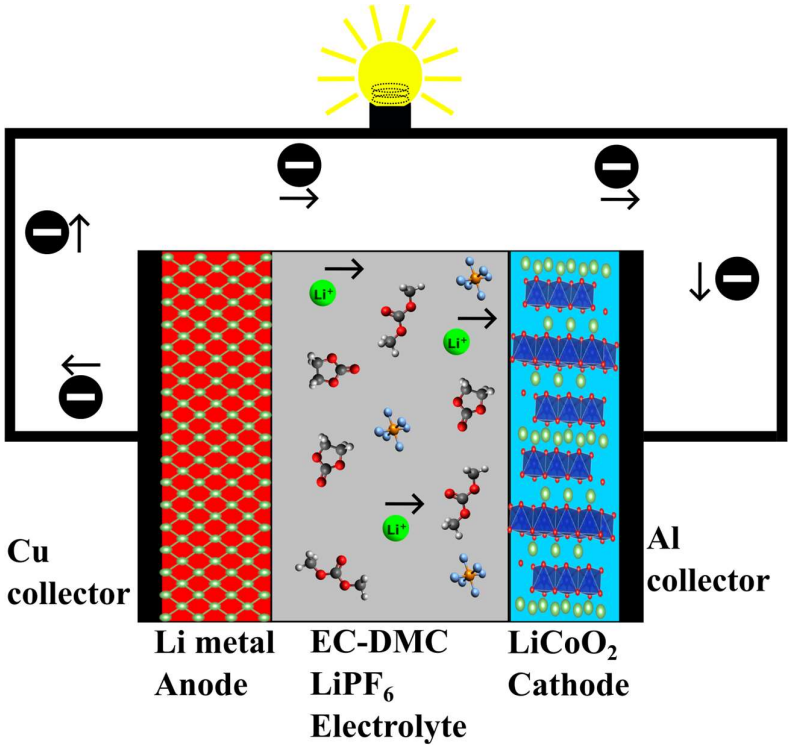

Figure 1-3: Basic scheme of a LMB, with pure lithium metal (Li^0) as anode, $LiCoO_2$ as cathode and $LiPF_6$ immersed in a mixture of EC and DMC as electrolyte.

Although the use of lithium metal as anode was first considered in the 1970s *[58]*, *[59]*, it has faced significant challenges in practical application due to the instability of the interphase between lithium metal and the liquid electrolyte. Compared to graphite, the lithium anode is much more reactive, which often leads to multiple problems *[60]*, *[61]*. For example, Li^+ are

prone to deposit on the anode surface forming lithium metal dendrites, which can reduce battery performance and pose serious safety risks *[62]*, *[63]*, *[64]*. These dendrites can also cause short circuits in the battery, and the inherent softness of the liquid electrolytes makes it difficult to prevent their formation. Moreover, the reactivity of lithium metal can induce a higher decomposition of the electrolyte, making the formation of a stable SEI quite challenging, hindering the proper functioning of the battery *[65]*.

One of the solutions for these safety problems is to use more stable electrolytes. Specifically, solid-state electrolytes have shown to effectively suppress dendrite growth, making them a promising option *[66]*, *[67]*, *[68]*. However, the ionic conductivity of solid-state electrolytes is significantly lower than that of liquid electrolytes. To strike a balance between safety and ionic conductivity, polymers can be used as the main component of the electrolyte. Solid polymer electrolytes, SPEs, offer an intermediate solution between liquid and solid electrolytes, providing improved safety without sacrificing ionic conductivity *[69]*, *[70]*. Moreover, SPEs can exhibit favorable electrochemical and mechanical properties, making them a promising alternative to liquid electrolytes.

PEO is a well-studied polymer among the many evaluated for its potential application as SPE in LMBs *[71]*, *[72]*, *[73]*. Michel Armand was the first to propose the use of PEO with LiTFSI, a lithium salt whose anion has a flexible structure and a weak coordination with Li^+ *[74]*, *[75]*. This SPE was expected to induce a near-complete dissociation of the lithium salt, allowing Li^+ to move freely through the polymer matrix from ether oxygen to ether oxygen. This hypothesis proved true, and LiTFSI has since become one of the most popular salts in LMBs *[76]*, *[77]*, *[78]*, *[79]*.

Despite its popularity, PEO-LiTFSI SPEs have one big problem, namely the lithium transference number, Li TN, is too low (≈ 0.2). Li TN is a measure of the portion of the total ionic conductivity that can be attributed to Li^+ (further details are provided in *Section 2.2.5*). Therefore, further investigations are necessary to improve this contribution and increase overall conductivity. In this regard, one of the greatest advantages of polymers is their high tunability, which provides countless opportunities for modification and optimization. With this in mind, researchers can focus on specific challenges of simultaneously optimizing key aspects of the polymer structure to enhance desirable properties and minimize undesired ones. For example, polymer design can be tailored to improve solvation of Li^+ and, at the same time, ensure stability when in contact with the lithium metal anode.

This Thesis tackles head-on this challenge by leveraging computational modeling and numerical simulations to gain deeper insights into the behavior of SPE components. By exploring the fundamental functioning mechanisms of SPEs, this research aims to identify potential pathways for improving their performance, durability, and safety. Through the use of cutting-edge computational tools, the study seeks to identify new materials with superior properties, as well as optimize the design and engineering of existing SPEs components. The results of this research will not only help advance the development of more efficient and reliable SPEs but also contribute to the broader field of electrochemical energy storage and conversion.

Chapter 2. Computational Methods

2.1. Introduction

Computational methods are used to theoretically predict the properties and behaviors of a model system. They can be used to study a diverse range of systems, from biological macromolecules like proteins to individual atoms with complete electron description. The level of precision of the calculations depends on the complexity of the system and the computational resources available. While simple models can be simulated quickly on a desktop computer, more complex systems may require the use of high-performance computing resources.

With the development of more powerful computers, the ability of computational methods to model increasingly complex systems has grown, enabling researchers to study phenomena that are difficult or impossible to observe experimentally. These theoretical calculations can provide detailed insights into the dynamics of atoms and molecules, including their motion, interactions, and thermodynamic and mechanical properties.

There exist different methods to perform these theoretical calculations (see *Figure 2-1*). The choice of method usually depends on the level of precision needed. For example, some methods use empirical force fields to approximate interatomic interactions, while others rely on quantum mechanical calculations for more accurate results. Higher accuracy often involves higher methodological sophistication and greater computational resources. As a result, selecting a particular approach involves making a trade-off between the length and time scale of the simulations, the level of predictability desired, and the available computational capabilities.

At smaller scales, density functional theory (DFT) is a powerful tool to accurately compute the electronic structure of atoms and molecules through quantum-mechanical calculations. DFT is especially useful to describe the behaviour of electrons, making it an essential tool in fields such as condensed matter physics. However, due to its high computational cost, DFT calculations are often limited in both time and size scales, with the ability to analyze only systems comprising up to a few hundred atoms during short periods, typically up to several picoseconds.

In contrast, mesoscale simulations take a completely different approach. They treat a collection of atoms that form a large structure as a single entity, using classical mechanics to make the calculations. This simplifies the calculations by losing individual atom information, thus expanding the scales of the studied system, reaching up to microscale systems. Although this approach implies the loss of individual-atom information, it allows the study of structures with sizes unattainable for other techniques. They can be found in fields such as material science, where mechanical behaviors and phase transitions are studied.

In between these two methods lies the classical molecular dynamics (MD) simulations, which maintain individual atom information but loses electronic structure. This enables the study of systems of much larger size than those with DFT, but still being able to identify the interactions

between specific atoms. Classical MD simulations can be found in biomolecular studies of proteins and lipids and, of course, polymers.

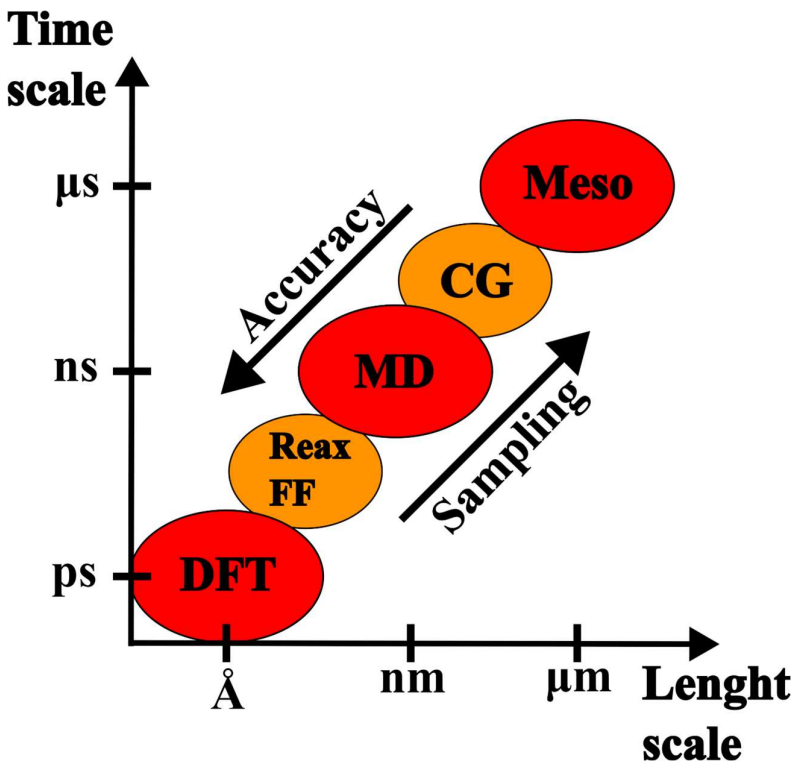

Figure 2-1: Representation of the scale of some of the most common computational methods of calculation.

In between these highly differentiated methods there are intermediate points. Calculation methods that are neither one thing nor another. For example, in between DFT calculations and MD simulations we have the use of much more complex definitions of the atomic interactions by the use of reactive force fields (Reax FF). Or in the middle of MD simulations and mesoscale simulations, we can find coarse-grained simulations, where the number of atoms that form a single entity is much lower than in mesoscale (see *Section 2.2.2* for more information).

In this Section we will give a clear explanation of the two computational methods used in this Thesis: MD simulations and *Ab Initio* DFT calculations. A detailed explanation of what there is behind the MD simulations (theory, approximation, methods of analysis, etc.) will be given in *Section 2.2*. While the historical development of DFT calculations, with all the steps and approximations proposed to front facing the successive problems is exposed in *Section 2.3*.

2.2. Molecular Dynamic Simulations

2.2.1. Introduction

MD simulations are a class of computational methods used to simulate the atomic-scale behavior and properties of matter. These simulations rely on the laws of classical mechanics and use numerical integration to solve Newtonian equations of motion for a system of atoms interacting through forces.

The starting point of any MD simulation is to define an initial atomic configuration. There are two ways of defining it. In the first option, the initial configuration is obtained from the result of a previous simulation that ended with a certain spatial distribution of the atoms moving at a specific velocity. This approach is commonly used when a simulation involves multiple steps, such as in the optimization process prior to the final simulation (as described in *Section 2.2.6*), where each step may have different temperature and/or pressure conditions.

The second option is to either provide the positions of the atoms or randomly generate them if the initial configuration is not critical for the simulation. This approach is usually used in the first step of a simulation where no specific spatial arrangement is needed. In either option, each atom must be assigned a certain velocity that follows the Maxwell-Boltzmann distribution corresponding to the desired temperature. However, this distribution must be adjusted to ensure that the velocity of the center of mass of the system is zero to prevent the system from drifting.

Let us now see the mathematical procedure behind an MD simulation. The equations of motion of the system are described by the classical Hamiltonian equations.

$$\dot{\vec{p}_i} = -\frac{\partial H(\vec{p_i}, \vec{r_i})}{\partial \vec{r_i}} \qquad \dot{\vec{r}_i} = \frac{\partial H(\vec{p_i}, \vec{r_i})}{\partial \vec{p_i}}$$

2.1

Where $\vec{p_i}$ and $\vec{r_i}$ are the momentum and coordinates of each atom of the system and $H(\vec{p_i}, \vec{r_i})$ is the Hamiltonian, defined by:

$$H(\vec{p_i}, \vec{r_i}) = \sum_{i=1}^{N} \frac{\vec{p_i}^2}{2m_i} + V(\vec{r_i})$$

2.2

$V(\vec{r_i})$ is the potential energy at position $\vec{r_i}$ and m_i is the mass of the i-atom. So, at each step of the simulation, the potential that affects each atom is calculated through the forces acting over it, and these forces give us the acceleration to calculate the position and velocity of the next step.

$$\vec{F_i} = -\nabla_i V = -\frac{dE}{d\vec{r_i}} = m_i \vec{a_i}$$

2.3

As *Eq. 2.3* can only be solved numerically, its derivatives must be approximated using Taylor expansions. Various algorithms exist for solving these equations, with different limits on the order to which the expansions are truncated. Including more terms in the calculation yields a more precise solution, but at the cost of increased computational resources. Therefore, a balance must be struck between precision and computational efficiency.

One of the most common algorithms is the Verlet algorithm *[80]*, as it often provides sufficient precision without requiring a high computational cost. This algorithm truncates the Taylor expansion of the position at fourth order. However, to compute the position of the next step, it considers the two previous steps, effectively eliminating odd-order terms.

$$\vec{r_i}(t+\delta t) = \vec{r_i}(t) + \vec{v_i}(t)\delta t + \frac{1}{2}\vec{a_i}(t)\delta t^2 + \frac{1}{6}\dot{\vec{a}_i}(t)\delta t^3 + O(\delta t^4)$$

2.4

$$\vec{r_i}(t-\delta t) = \vec{r_i}(t) - \vec{v_i}(t)\delta t + \frac{1}{2}\vec{a_i}(t)\delta t^2 - \frac{1}{6}\dot{\vec{a}_i}(t)\delta t^3 + O(\delta t^4)$$

2.5

$$\vec{r_i}(t+\delta t) + \vec{r_i}(t-\delta t) = 2\vec{r_i}(t) + \vec{a_i}(t)\delta t^2 + O(\delta t^4)$$
$$\vec{r_i}(t+\delta t) = 2\vec{r_i}(t) - \vec{r_i}(t-\delta t) + \vec{a_i}(t)\delta t^2 + O(\delta t^4)$$

2.6

However, this approximation has two main problems. Firstly, it is a two-step method, so we need the positions of the first two steps to start the simulation. And secondly, the velocity at each step is not explicitly present in the equations, although it can be calculated from the previous and subsequent steps.

$$\vec{v_i}(t) = \frac{1}{2}\frac{\vec{r_i}(t+\delta t) - \vec{r_i}(t-\delta t)}{\delta t}$$

2.7

Moreover, a challenge arises when computing the kinetic energy at a certain step, as it requires the position of the next step. The leapfrog algorithm *[81]* offers a solution to this problem. The leapfrog algorithm uses an intermediate step to first calculate the velocities, and then computes the positions at the next step using the velocities obtained at this intermediate step.

$$\vec{v_i}\left(t+\frac{1}{2}\delta t\right)=\vec{v_i}\left(t-\frac{1}{2}\delta t\right)+\vec{a_i}(t)\delta t$$

2.8

$$\vec{r_i}(t+\delta t)=\vec{r_i}(t)+\vec{v_i}\left(t+\frac{1}{2}\delta t\right)\delta t$$

2.9

The leapfrog algorithm explicitly calculates the velocities, but not at the same time as the position, although it can be approximated as the medium point of the velocities at the previous and next intermediate steps. A schematic representation of the Verlet and leapfrog algorithms is shown in *Figure 2-2*.

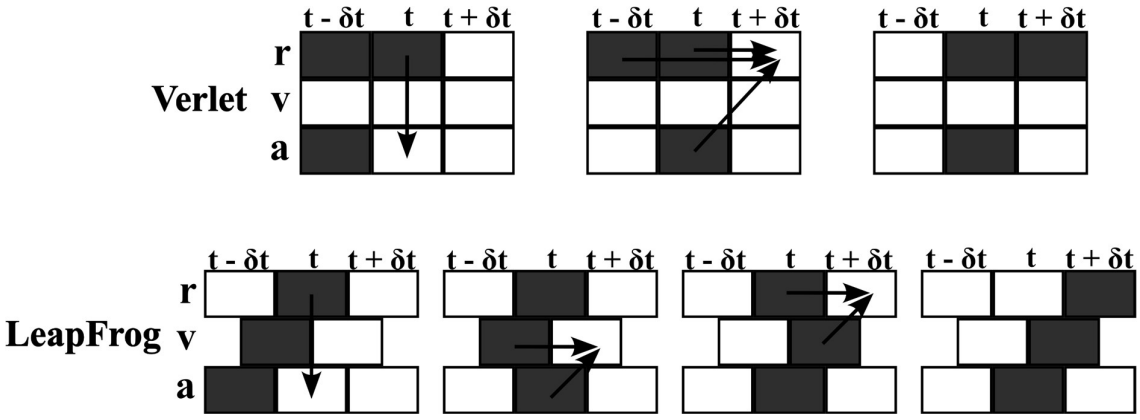

Figure 2-2: Schematic representation of how the Verlet algorithm (top) and the leapfrog algorithm (bottom) update the position, velocity, and acceleration at each time step.

After defining the equations of motion, it is necessary to describe the various interactions that define the potential energy affecting each atom. Interatomic interactions are determined by the force field, which is the cornerstone governing the behavior of the system.

2.2.2. Force Field

The force field (FF) is the combination of equations and parameters that describe the different interactions between the atoms of the system. The parametrization of a force field is a very complicated task and requires the combination of experimental data and quantum mechanical calculations. One can use data from X-ray diffraction, nuclear magnetic resonance (NMR) measures, Raman spectroscopy, and IR spectroscopy to measure the real distances between atoms and forces of interaction between them. But when complex systems are treated, or few experimental data are available, quantum mechanical calculations become indispensable to fit the FF parameters. And once this first fitting is done, a comparison between the results coming

from the simulations using these parameters and experimental results is crucial to make a fine adjustment.

A proper definition of the FF parameters to describe interactions between the atoms is the most critical aspect of conducting an MD simulation. Selecting incorrect parameters can lead to erroneous interpretations of atomic and molecular interactions, resulting in simulated behaviors that differ from reality.

The FF includes both bonded and nonbonded interactions.

$$E_{FF} = E_{bond} + E_{angle} + E_{torsion} + E_{improper} + E_{Coul} + E_{vdW} \quad 2.10$$

The former affect atoms within a molecule and are thus called intramolecular interactions. They describe the bond, angle, torsional and improper dihedral energies. The latter affect all atoms and are distance forces, corresponding to the Coulombic and the van der Waals (vdW) interactions.

We start with the description of the bonded interactions. They quantify how variations in the geometry of a molecule affect its energy. Various methods can be employed to describe each of these interactions, but we will focus on the most used approximations in FFs, as detailed in the following.

- *2 Atoms interaction*:

Bond energy describes the energy resulting from changes in the covalent bond length between two atoms (d_{ij}) from an equilibrium position (d_{ij}^0) (see *Figure 2-3*).

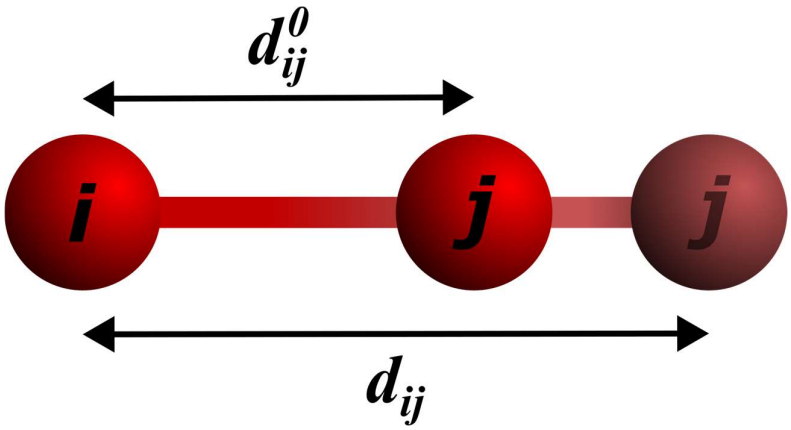

Figure 2-3: Representation of the variation of the bond length between two atoms with respect to the equilibrium length d_{ij}^0.

The harmonic approximation, a widely used and straightforward method, provides an accurate description of this interaction. Specifically, for each unique bond type present in the system, the interaction can be expressed as:

$$E_{bond}(d_{ij}) = \frac{1}{2} k_{ij}^{b} (d_{ij} - d_{ij}^{0})^{2}$$

2.11

Where k_{ij}^{b} is the bond force constant of the bond between atom types i and j.

- *3 Atoms interaction*:

Angle energy considers the energy variations due to the angle that form three interacting atoms (ϑ_{ijk}) with respect to the equilibrium angle (ϑ_{ijk}^{0}) (see *Figure 2-4*).

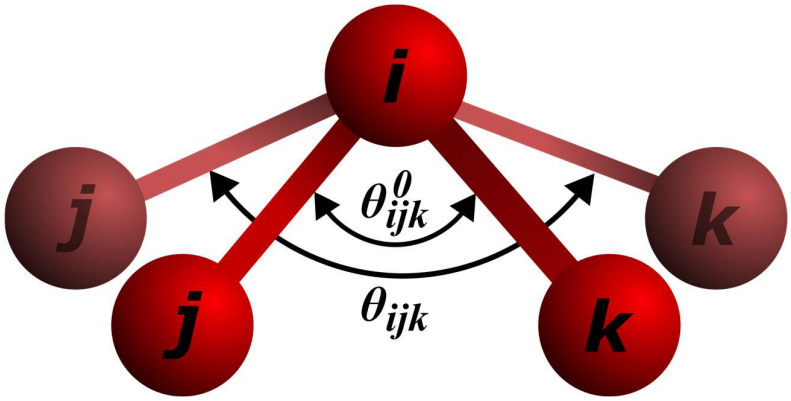

Figure 2-4: Representation of the variation of the angle formed by three atoms with respect to the equilibrium angle θ_{ijk}^{0}.

The harmonic approximation remains valid to describe the angle energy.

$$E_{angle}(\theta_{ijk}) = \frac{1}{2} k_{ijk}^{a} (\theta_{ijk} - \theta_{ijk}^{0})^{2}$$

2.12

Here, k_{ijk}^{a} is the angular force constant of the angle formed by atom types i, j, and k. As for the bond energy, we need to define it for each triplet of different atom types that form an angle in the system.

- *4 Atoms interaction*:

The last two bonded interactions involve four atoms and describe the dihedral angles of the molecule. The torsion energy is related with the proper dihedrals (four atoms in a row) and

considers the energy due to rotations of one part of the molecule with respect to another (φ_{ijkl}) (see *Figure 2-5*).

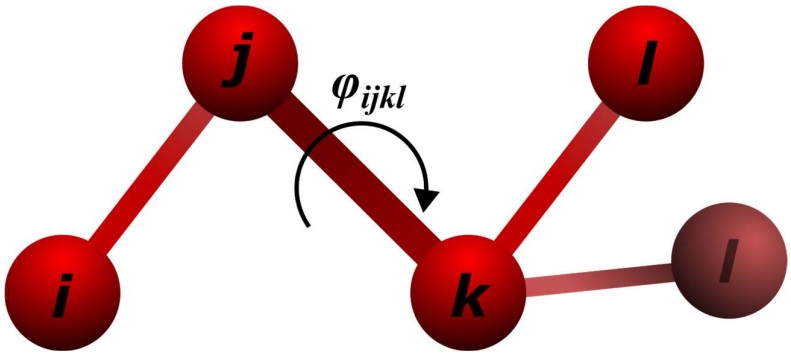

Figure 2-5: Representation of the variation of the proper dihedral angle φ_{ijkl} formed by four consecutive atoms.

For this interaction, two main approximations coexist in the literature to describe it. One is the Ryckaert-Bellemans function *[82]*:

$$E_{torsion}(\varphi_{ijkl}) = \sum_{n=0}^{5} (-1)^n C_n \left(cos(\varphi_{ijkl})\right)^n$$

2.13

Where the six coefficients from C_0 to C_5 must be defined for each four atom types i, j, k, and l bonded in a row. The other main way to describe the proper dihedrals are the Fourier dihedrals:

$$E_{torsion}(\varphi_{ijkl}) = \frac{1}{2}\sum_{n=1}^{4} F_n\left[1 + (-1)^{n+1}\, cos(n\, \varphi_{ijkl})\right]$$

2.14

In the Fourier definition, only four coefficients (F_n) are needed, and thanks to the properties of the cosine function, we can build the transformations between both coefficient sets.

$$C_0 = F_2 + \frac{1}{2}(F_1 + F_3) \quad ; \quad C_1 = \frac{1}{2}(-F_1 + 3F_3) \quad ; \quad C_2 = -F_2 + 4F_4$$

$$C_3 = -2F_3 \quad ; \quad C_4 = -4F_4 \quad ; \quad C_5 = 0$$

2.15

To finalize the bonded interactions, we have the improper dihedral energy. It is associated with the displacement of four atoms out of the plane (ξ_{ijkl}) with respect to the equilibrium angle (ξ^0_{ijkl}), as depicted in *Figure 2-6*.

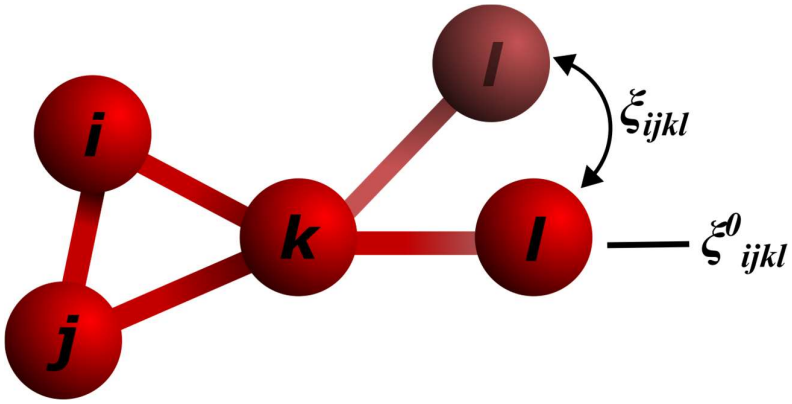

Figure 2-6: Representation of the variation of the improper angle formed by four no-consecutive atoms with respect to the equilibrium angle ξ^0_{ijkl}.

This interaction arises in molecules that have planar rings, and the harmonic approximation is typically employed to model this interaction.

$$E_{improper}(\xi_{ijkl}) = \frac{1}{2} k^{im}_{ijkl}(\xi_{ijkl} - \xi^0_{ijkl})^2$$

2.16

Where k^{im}_{ijkl} is the improper dihedral force constant of the dihedral angle form by atom types i, j, k, and l.

Now that we have gone through the bonded interactions, we now move on to the nonbonded interactions. These interactions are long-range. The nonbonded interactions that affect each atom are defined by the forces exercised by every other atom in the system. They are the Coulomb interaction and the vdW interaction between electric charges. For the calculation of the Coulomb interaction (the electrostatic interaction), we should use the electron densities of all the atoms, something feasible with quantum-mechanical calculations. However, due to the vast number of atoms that we normally use in MD simulations (1.000s to 10.000s of atoms) this is not computationally viable.

The approximation used in MD simulations is to assign to each atom a partial atomic charge and treat them as point particles. There are various methods available in the literature to calculate these charges using quantum mechanical techniques, such as electrostatic potential (ESP *[83]*, *[84]*), restrained electrostatic potential (RESP *[85]*), Hirshfeld *[86]*, and natural bond orbital analysis (NBO *[87]*), among others. However, since partial charges are not directly observable, direct comparison with experimental data is impossible. The choice of the method can significantly impact the simulation results. Even small variations in the partial charges can alter the interactions between atoms and change the coordination between the particles.

Furthermore, a scaling factor is necessary to be applied to the partial charges. This factor is used to account for the effects of polarization, which are not considered in conventional classical MD simulations since the charges are treated as unchangeable point charges. However, the scaling factor can also have a significant impact on the simulation results, and a proper choice of the scaling factor is necessary to accurately capture the polarization effects.

Once the values of the partial charges for each atom in the system are defined, one simply needs to use the Coulomb law between each pair of atoms i and j to compute the overall electrostatic energy.

$$E_{Coul}(d_{ij}) = \frac{1}{4\pi\epsilon_0\epsilon_r}\frac{q_i q_j}{d_{ij}}$$

2.17

Where ε_0 is the vacuum electric permittivity, ε_r the relative permittivity of the medium and q_i and q_j the partial charges of the atoms.

Van der Waals interactions are a mixture of a repulsive force, due to the overlapping of the electronic clouds, and an attractive force between induced dipoles. There are many forms to describe this interaction, but the most common is the 12-6 Lennard-Jones potential *[88]*, *[89]*, *[90]*.

$$E_{LJ}(d_{ij}) = 4\epsilon_{ij}\left[\left(\frac{\sigma_{ij}}{d_{ij}}\right)^{12} - \left(\frac{\sigma_{ij}}{d_{ij}}\right)^{6}\right]$$

2.18

This interaction is present between each pair of atoms and the parameters ϵ_{ij} and σ_{ij} control the intensity and interaction length (see *Figure 2-7*), respectively. These parameters depend on the individual values of each atom, and they can be calculated from them.

$$\sigma_{ij} = (\sigma_i\sigma_j)^{\frac{1}{2}} \quad ; \quad \epsilon_{ij} = (\epsilon_i\epsilon_j)^{\frac{1}{2}}$$

2.19

As we have seen, the number of interactions that need to be calculated at each step can be enormous, particularly for large systems. Bonded interactions are limited to the number of bonds, angles, and dihedrals in the molecules of the system. But there are cases where some of these interactions are not present such as with isolated atoms (e.g., free ions) or small molecules like H_2O, BF_4, and PF_6 that lack dihedral angles. To address this issue, nonbonded interactions become crucial.

Electrostatic and vdW interactions, in particular, are computationally expensive and decay with increasing distance (see *Figure 2-7*), making truncation of these interactions a useful practical solution to reduce computational cost. Various methods for truncation can be used, from simple

cutoff distances to more advanced approaches like smooth switching functions or FF corrections, each of them with their own benefits and limitations.

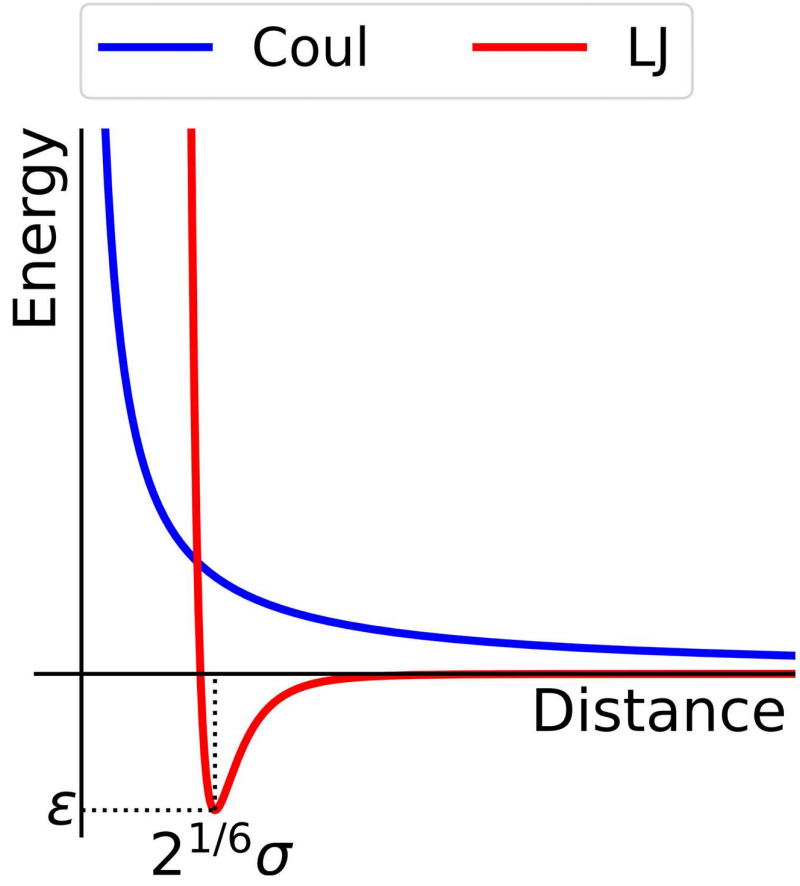

Figure 2-7: Example of the Coulombic (blue) and Lennard-Jones (red) interactions.

When calculating the potential energy that affects one atom, it is reasonable to assume that the influence of atoms located far away is negligible. To do so, we can define a cutoff distance (R_C) beyond which the interaction energies between atoms is zero by definition.

$$E_{Coul}(d_{ij}) = \begin{cases} \frac{1}{4\pi\epsilon_0\epsilon_r}\frac{q_i q_j}{d_{ij}}, & r_{ij} < R_C \\ 0, & r_{ij} \geq R_C \end{cases} \qquad 2.20$$

$$E_{LJ}(d_{ij}) = \begin{cases} 4\epsilon_{ij}\left[\left(\frac{\sigma_{ij}}{d_{ij}}\right)^{12} - \left(\frac{\sigma_{ij}}{d_{ij}}\right)^{6}\right], & r_{ij} < R_C \\ 0, & r_{ij} \geq R_C \end{cases} \qquad 2.21$$

R_C for the Coulombic and vdW interactions does not necessarily need to be the same, they may differ. Since the LJ potential decreases much faster than the Coulomb potential (*Figure 2-7*), a smaller R_C can be used for LJ interactions. However, truncating the potential at R_C creates a discontinuity in the potential energy, leading to problems with energy conservation.

Shifting the potential by its value at the cutoff radius is a simple solution that solves this problem, but it affects the potential at all points. If the cutoff radius is not properly chosen, this shift may severely affect the atomic interactions. Introducing a switching function within a small region around R_C provides a smoother transition to zero, without introducing a discontinuity in the overall potential. This approach, known as switching potential, does not affect the potential outside the switching region, making it a better option for avoiding discontinuities in potential energy calculations. *Figure 2-8* provides an example of how these different treatments of the vdW interactions work. Similar procedures can be used to treat Coulombic interaction.

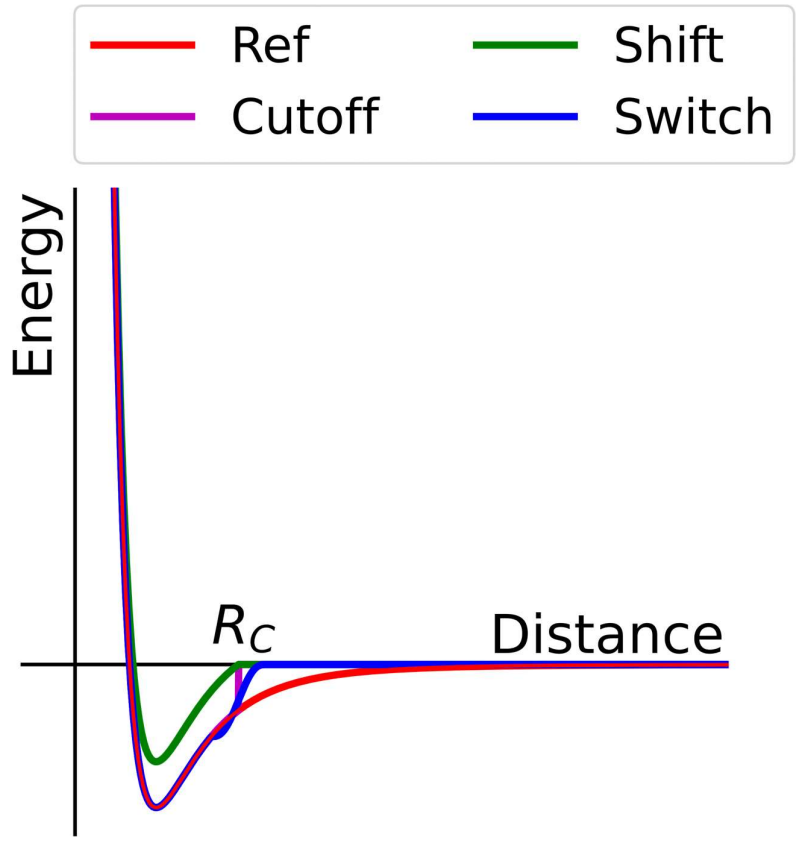

Figure 2-8: Different methods to treat the long-range interactions at a cutoff radius R_C, exacerbated for a better visualization.

To increase the speed of the calculations, there are also methods to avoid checking all the atoms of the system at every timestep to determine whether they lie within the cutoff region. One such method is building neighbors lists, which involves creating a list of nearby atoms for each

atom in the system. During the subsequent timesteps, only atoms in these lists are checked to see if they are closer than the cutoff radius.

However, because atoms are constantly in motion, the neighbor lists must be updated every few steps (typically 10-20 steps). One popular type of neighbor list is the Verlet neighbor list *[80]*, in which all atoms inside a sphere with a radius equal to the cutoff radius plus a small buffer are included in the neighbor lists. This buffer size enables the consideration of atoms that are outside the cutoff radius when the neighbor lists are created but may move within the cutoff region during subsequent steps. For example, see *Figure 2-9* for a 2-D representation. Other methods exist as well, such as dividing the simulation box into small cubes and creating neighbor lists based on the atoms of each cube and their surroundings. This approach can be useful for large systems with numerous atoms. Overall, neighbor list methods can significantly reduce the computational expense of MD simulations, enabling the study of more complex systems and longer simulation times.

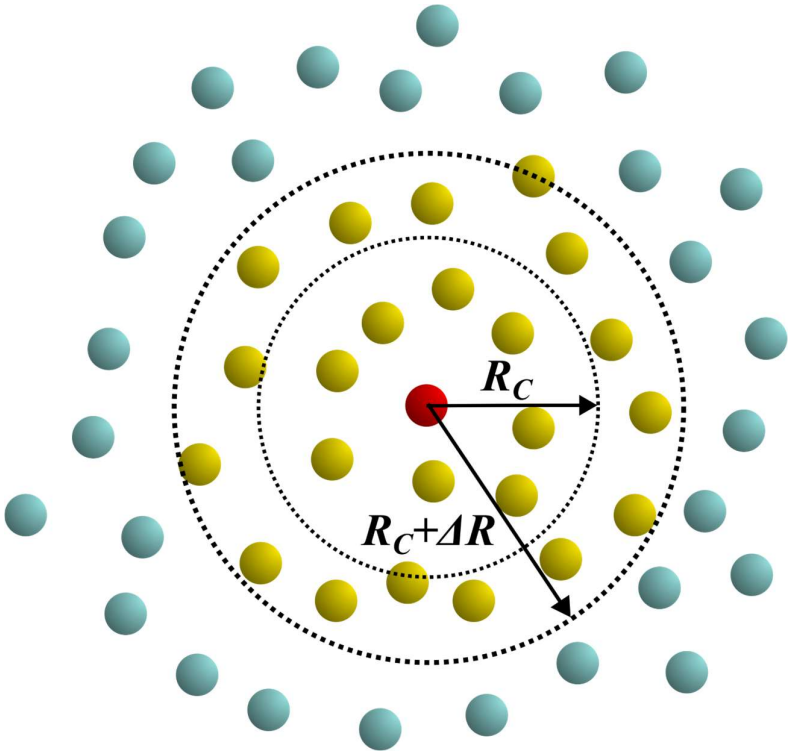

Figure 2-9:Schematic 2D-representation of how a Verlet neighbor list is build. From the reference atom (red) we save in the list all the atoms inside a sphere of radius $R_C + \Delta R$ (yellow). Only these atoms are considered in the next steps to compute the nonbonded interactions (but only those inside R_C contribute).

While classical FFs are widely used in literature, it is not without their limitations. Essentially, this approach remains a popular choice due to its simplicity, scalability, and ability to simulate large systems over extended timeframes. Despite its simplicity, it can still provide sufficient precision for studying the coordination environment of atoms and molecules, as long as the

method used to calculate the partial atomic charges is carefully considered. Additionally, classical FFs can be effective in studying diffusivity, although for systems with extremely low diffusion, simulation time may need to be increased (refer to *Section 2.2.5*). While there are more complex ways to describe FFs that can address some of these limitations, we will not delve into these details in this Thesis. However, it is worth noting that alternative approaches do exist in this field *[91]*, *[92]*.

As we have mentioned, partial atomic charges are crucial when describing electrostatic interactions, as they can influence the way atoms coordinate between them and affect the interaction between molecules. However, in reality, charges are not fixed points in space but rather exist as distributions that can change due to their interactions with neighboring atoms. To account this behavior, polarizable force fields (PolFFs) *[93]*, *[94]* are utilized. These types of FFs are capable of describing the effects of induced dipoles and adjusting the partial charges at each time step based on the surrounding environment. However, the use of PolFFs significantly increases the computational cost of simulations. Besides, to accurately capture the electronic configuration, the simulation timestep needs to be reduced, further increasing the computational expense. These two factors combine to limit the speed of simulations utilizing PolFFs.

Another problem of classical FFs is the absence of reactivity (i.e., molecules cannot be broken and form new ones). Independently of the geometry variations, the equations will always tend to return the molecule to the more stable geometry. So, we cannot study the chemical reactions that happen in real systems. PolFFs share this same limitation. To overcome this, reactive FFs such as ReaxFFs *[95]* have been developed. They consider the reactivity of the system and can break and form bonds. However, the implementation of ReaxFFs requires extensive calculations in each step to detect if any bond is broken or created due to the external forces. Additionally, ReaxFFs include polarization calculations, making the simulation more complex than plain PolFFs. Therefore, the time step for ReaxFFs must be reduced to 0.1 - 0.2 fs, compared to the 1 - 3 fs commonly used for classical FF. This can increase the computational cost by up to one hundred times when moving from a classical to a reactive FF.

We have seen that going down in the scales of *Figure 2-1* represents an increment in the level of knowledge and a better description of the system. But for other studies it is worth moving to upper scales. Coarse Grained (CG) *[96]*, *[97]*, *[98]*, *[99]* simulations enter in scene when the characteristics under study occur in longer scales (e.g., studies of diffusivity or great scale behaviors that affects the system). The strategy with these simulations is to group various atoms in one single grain or bead. With the proper definition of the interactions between the different beads, the behaviour of the simulated system is similar to the all-atom definition of the classical MD, but the number of elements and interactions decreases exponentially. Thus, allowing simulations of larger systems and during longer times with the same computational cost.

2.2.3. Boundary Conditions

Another potential limitation of MD simulations arises when we consider the size of the simulation box, since we are limited to a certain number of atoms within that box, typically from 1,000s to 10,000s atoms. More atoms can be used, but the computational cost increases with the number of atoms, and as much as we increase the number, we could never reach the number of atoms that are present in a real system (of the order of the Avogadro number, $N_A = 6.022x10^{23}$). To overcome this issue, we use periodic boundary conditions (PBC). PBC assume that the simulation box is periodically repeated in all directions, with the exact same positions and velocities of the atoms in each of the repeated units.

The use of PBC to describe perfect crystals, which already possess a periodic structure is a natural choice. However, when dealing with amorphous materials, such as the ones we study in this Thesis, PBC can introduce artificial symmetries that do not naturally exist in the system. Therefore, we need to be cautious about potential artifacts that may arise from this artificially imposed symmetry. To mitigate this issue, we can use simulation boxes that are large enough to capture the relevant physics while still computationally manageable.

When studying a system, we only consider the motion of the molecules of the main box, not the ones from the replicas, and we suppose that the molecules of the surrounding imaginary boxes move the same way. However, we must consider the effects that these imaginary particles have in the main box through long-range interactions (nonbonded part of the FF). As defined in *Section 2.2.2*, we make use of cutoffs to reduce the number of interactions, but atoms near the edge of the simulation box, would have imaginary neighbor atoms within their cutoff radius (see *Figure 2-10*).

Although it is very weird that a particle and one of its periodic images lie inside the cutoff radius of one particle at the same time, we must only consider the closest of them. This is known as the minimum image convention: a particle only interacts with the closest periodic image of the rest of the particles.

In systems with PBC, there exist methods to compute long-range interactions. The most common method is the Ewald summation method *[100]*. This is especially useful for Coulombic interaction since the intensity of the interaction is proportional to r^{-1} and it has very long range. For Lennard-Jones interactions is not so necessary due to its r^{-6} and r^{-12} dependence with distance. The total electrostatic energy inside the simulation box is:

$$E_C = \frac{1}{2}\sum_{\vec{n}}^{*}\sum_{i,j}^{N}\frac{q_i q_j}{4\pi\epsilon_0\epsilon_r\left|\vec{r_i}-\vec{r_j}\right|} \qquad 2.22$$

Where $\vec{n}$ is the coordinate vector of the imaginary box (n_x, n_y, n_z) and $*$ means that $\vec{n} = (0,0,0)$ and $i = j$ term is omitted.

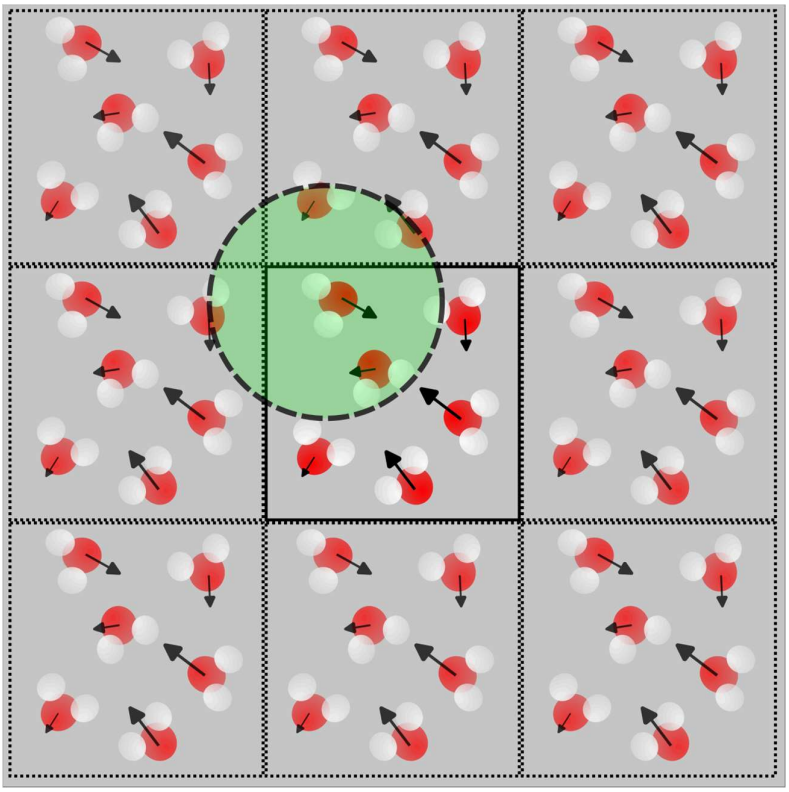

Figure 2-10: Schematic 2D-representation of the application of the PBC over a simulation box (the central square) where each molecule is represented with its respective velocity. The green circle represents the cutoff radius and the molecules inside it are considered to calculate the non-bonded interactions of the central molecule.

In the Ewald summation method, we work both in the position and in the momentum space (direct and reciprocal spaces respectively).

$$E = E_{dir} + E_{rec} + E_0$$

2.23

Where E_{dir} is the potential in the direct space, E_{rec} in the reciprocal space, and E_0 is a constant value.

$$E_{dir} = \frac{1}{2}\sum_{i,j}^{N}\sum_{\vec{n}} q_i q_j \frac{erfc\left(\beta\overrightarrow{r_{ij,\vec{n}}}\right)}{\overrightarrow{r_{ij,\vec{n}}}}$$

2.24

$$E_{rec} = \frac{1}{2\pi V}\sum_{i,j}^{N} q_i q_j \sum_{\vec{m}} \frac{1}{\overrightarrow{m^2}} e^{-\left(\frac{\pi\vec{m}}{\beta}\right)^2 + 2\pi i\vec{m}\cdot\left(\vec{r_i}-\vec{r_j}\right)}$$

2.25

$$E_0 = -\frac{\beta}{\sqrt{\pi}} \sum_{i}^{N} q_i^2$$

2.26

Where $erfc$ is the complementary error function:

$$erfc(x) = 1 - \frac{2}{\sqrt{\pi}} \int_0^x dt\, e^{-t^2}$$

2.27

$\overrightarrow{r_{ij,\vec{n}}}$ is the distance between the particle i and particle j in the $\vec{n}$ periodic box and $\vec{m}$ is similar to $\vec{n}$, but referring to the coordinates of the reciprocal periodic box. The energy in the direct space corresponds to a short-range interaction and the energy in the reciprocal space to a long-range interaction. β is the parameter that controls the relative rate of convergence of both interactions. Although this method is useful for MD simulations, it is computationally costly and thus only available for small systems.

When dealing with larger systems, the Ewald summation method can be enhanced through the use of the particle-mesh Ewald (PME) method *[101]*. In this method, the short-range part of the interaction is similar to the standard Ewald summation, but the long-range interaction is made in the Fourier space and considering the charges.

2.2.4. Thermodynamic Ensembles

A thermodynamic ensemble is the collection of all individual microscopic configurations or molecular states that have the same macroscopical properties, so we do not need to know the exact microscopic state to study the system as an entity. Macroscopic observables are calculated averaging over all possible microscopic states with identical properties. A macroscopic state is characterized by six thermodynamic variables: energy (E), pressure (P), temperature (T), volume (V), number of particles (N) and chemical potential (μ).

There are different ensembles in thermodynamics, and when we perform a MD simulation, we must choose which one is the most appropriate for our study. In each of the ensembles, some of the six thermodynamic variables are kept constant during the simulation. The three main ensembles that are most commonly used in MD simulations are NVE, NVT, and NPT (see *Figure 2-11*).

- *NVE ensemble*:

In the NVE ensemble (or micro-canonical ensemble), the variables that are kept constant are the number of particles, the volume of the system, and the energy (N, V, and E respectively). The NVE ensemble corresponds to an isolated system, without interactions with the outside.

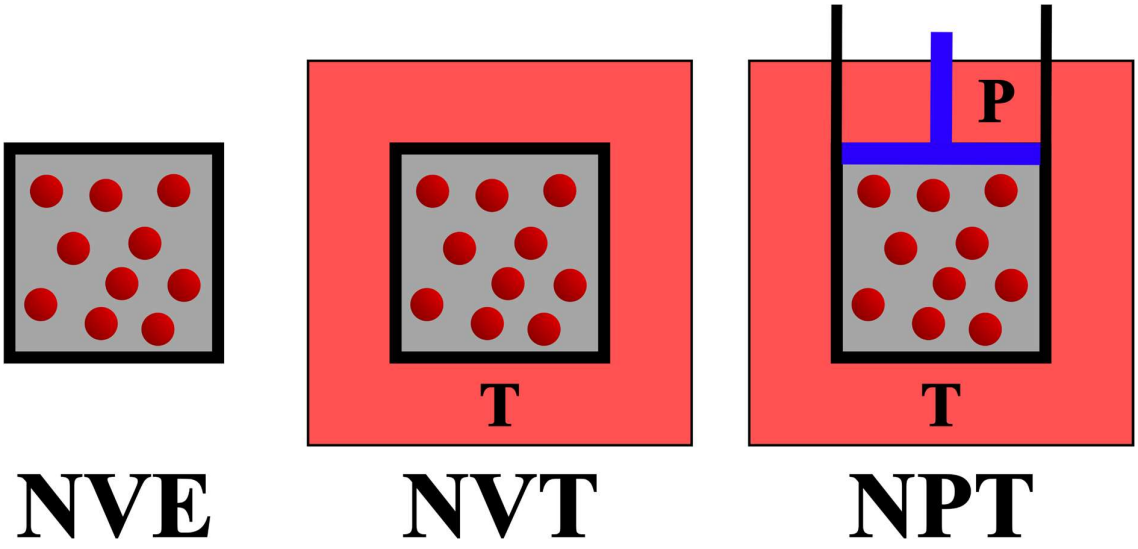

Figure 2-11: Schematic representation of the NVE, NVT, and NPT ensembles.

This ensemble is important because the total energy of the system is constant, and the system can only be in one of the microstates which possess that certain energy.

- *NVT ensemble*:

In the NVT ensemble (or canonical ensemble), we keep constant again the number of particles in the system and the volume (N and V), but this time we control the temperature (T) instead of the energy. The NVT ensemble corresponds to a system in contact with a heat bath that controls the constant temperature. Controlling the temperature is crucial in the simulations, because when comparisons are made with experimental results, the temperature is one of the easiest macroscopical properties to control in the laboratories. Besides, there are processes that occur as a function of the temperature (like the crystallization of the polymers) and if we want to be sure that a certain process is happening and avoid the possibility of other processes that may affect the results, we must control the temperature of the simulation.

To model this behavior in a simulation, a thermostat is included to rescale the velocities. Two of the most common thermostats are the Berendsen thermostat *[102]* and the velocity rescaling *[103]*. In the Berendsen thermostat there is a time constant (τ) to exponentially correct the temperature deviations from the equilibrium temperature (T_0).

$$\frac{dT}{dt} = \frac{T_0 - T}{\tau}$$

2.28

The fluctuations observed in the kinetic energy indicate that the simulation does not conform perfectly to a canonical ensemble. Nonetheless, the magnitude of this error diminishes with increasing system size, scaling as 1/N, and for sufficiently large systems, it becomes negligible.

Typically, one implements a velocity scaling procedure, which involves rescaling the velocities every n_{TC} steps by a factor λ.

$$\lambda = \sqrt{1 + \frac{n_{TC}\Delta t}{\tau_{TC}}\left(\frac{T_0}{T\left(t - \frac{1}{2}\Delta t\right)} - 1\right)}$$

2.29

Where the time constant τ_{TC} is not exactly equal to τ, but we always refer as time constant to τ_{TC}.

$$\tau = \frac{2C_V\tau_{TC}}{N_{df}k_B}$$

2.30

Where C_V is the heat capacity, k_B the Boltzmann's constant ($k_B = 1.3806x10^{-23}$ J/K), and N_{df} the degrees of freedom.

The velocity rescaling temperature coupling is similar to a Berendsen thermostat but adding a stochastic term to correct the distribution of the kinetic energy (K) around the equilibrium value (K_0).

$$dK = (K_0 - K)\frac{dt}{\tau_T} + 2\sqrt{\frac{KK_0}{N_{df}}}\frac{dW}{\sqrt{\tau_T}}$$

2.31

Here, dW is a Wiener process (like a Brownian movement).

Finally, there are other two common thermostats: the Nosé-Hoover *[104]*, *[105]* and the Andersen thermostat *[106]*. We will not enter into many details with these two since we have not used them in this Thesis. In the Nosé-Hoover thermostat, a friction term is the one making the work of the thermal bath and corrects the velocities when they deviate and vary the kinetic energy. Andersen thermostat is a randomization of the velocities every few time steps. Each randomization changes the velocities of the particles to those belonging to a Maxwell-Boltzmann distribution.

- *NPT ensemble*:

In the NPT ensemble (or isothermal-isobaric ensemble), the number of particles, the pressure, and the temperature (N, P, and T) are the constant variables of the simulation. The NPT ensemble corresponds to a system in contact with a thermal bath, but with a free mobile piston to vary the volume of the system to correct the variations of pressure and keep it constant. In this ensemble, we cannot keep the volume of the system constant. However, in an equilibrated system, keeping temperature and pressure constant will usually result in only minor changes in

volume. Nonetheless, volume is a variable that can be easily controlled in laboratory experiments, so simulations are often conducted at constant volume. While varying temperature can also adjust the system density, it is typically kept within a narrow range to avoid some processes. In contrast, pressure control is especially useful when we need to vary the system's density. In this Thesis, the simulations are performed with low initial densities due to the software employed, making it necessary to increase the density to levels comparable with experimental results. To achieve this, a simulation step at a high constant pressure is used to reduce the system's volume (more details in *Section 2.2.6*).

Like the NVT ensemble, to model an NPT ensemble we need to include a thermostat, but also a barostat. The two more common barostats are the Berendsen *[102]* and the Parrinello-Rahman *[107]*, *[108]*.

The Berendsen barostat is like its thermostat. The deviations of the pressure from its reference value ($\boldsymbol{P_0}$) are corrected according to a time constant (τ_P) exponentially each determined number of steps (n_{PC}) and with a scaling matrix μ.

$$\frac{d\boldsymbol{P}}{dt} = \frac{\boldsymbol{P_0} - \boldsymbol{P}}{\tau_P}$$

2.32

$$\mu_{ij} = \delta_{ij} - \frac{n_{PC}\Delta t}{3\tau_P}\beta_{ij}\left(P_{0i} - P_{ij}(t)\right)$$

2.33

Where β_{ij} is the isothermal compressibility of the system. To correct the pressure deviations, the simulation box size is variable, and the coordinates of the atoms are rescaled. Unless something more complex is needed, the pressure is isotropic. Thus, the pressure matrix $\boldsymbol{P}$ is a diagonal matrix.

The Parrinello-Rahman barostat is like the Nosé-Hoover thermostat but applied to pressure instead of temperature. A matrix to determine the coupling is introduced ($\boldsymbol{W}$).

$$(\boldsymbol{W}^{-1})_{ij} = \frac{4\pi^2\beta_{ij}}{3\tau_p^2 L}$$

2.34

Where L is the largest box size, and $\vec{b}$ the vector of the simulation box. Being V the volume of the box, $\vec{b}$ varies as:

$$\frac{d\overrightarrow{b^2}}{dt^2} = V\boldsymbol{W}^{-1}\overrightarrow{b'^{-1}}(\boldsymbol{P} - \boldsymbol{P_0})$$

2.35

2.2.5. Methods of Analysis

MD simulations generate vast amounts of data that require careful analysis to extract meaningful insights. One common objective is to compare simulation results with experimental observations. Two widely used techniques for achieving this goal are the mean squared displacement (MSD) and radial distribution function (RDF) analyses. The MSD measures the displacement of particles over time and provides information about their mobility, diffusion, and potential interactions. The RDF describes the distribution of particles around a central reference and provides information about their spatial arrangement and organization. Both MSD and RDF analyses are essential tools for characterizing the behavior of molecular systems and can help to validate the accuracy of MD simulations. The MSD results and the RDF analysis in this Thesis have been performed with the Trajectory Analyzer and Visualizer software (TRAVIS *[109]*, *[110]*).

Apart from the MSD and RDF analysis, some more specific and adapted to the required characteristic under study analyses have been developed by the doctorand in Python language. All these codes have been collected in a GitHub repository and an explanation of their functioning is provided in *Appendix A.1*.

- *Mean Squared Displacement (MSD)*:

The MSD is a measure of how much an atom, or group of atoms, moves during the simulation. Thus, it tells us how diffusive a particle is and how much it has moved from its starting position.

$$MSD(t) = \langle |\vec{r}(t) - \vec{r}(0)|^2 \rangle$$

2.36

However, to improve precision and the amount of available data to compute MSD, standard analysis of the diffusivity of a particle takes, as the starting point, all the points of the trajectory. So, the previous equation should be rewritten as:

$$MSD(\Delta t) = \langle |\vec{r}(\Delta t + t_0) - \vec{r}(t_0)|^2 \rangle$$

2.37

Where t_0 is the point at which we start to count time. This way, when we find in the literature or we refer to the MSD at a certain time (for example 10 ns), we are not referring to the displacement from 0 ns to 10 ns; but the average displacement in an interval of 10 ns. Using this method of counting time, the amount of data reduces as the time interval increases. Representing a simple example (see *Figure 2-12*), imagine we have a simulation in which we save data each Δt time, during a simulation of length 10Δt. We have eleven points of the simulation where we have the information of the coordinates of the atoms: the initial point (t_0), the final point (t_{10}) and nine intermediate points (t_1-t_9). When computing the MSD, the first point (MSD(Δt)) refers to the average displacement in the ten intervals Δt (t_1-t_2, t_2-t_3, etc.), so we have ten points to average and the statistics is good. The number of points is reduced (nine points for MSD(2Δt), eight for MSD(3Δt), and so on) until we reach the final point, at which

the interval equals the length of the simulation and we have only one point available, diminishing the precision of the statistic.

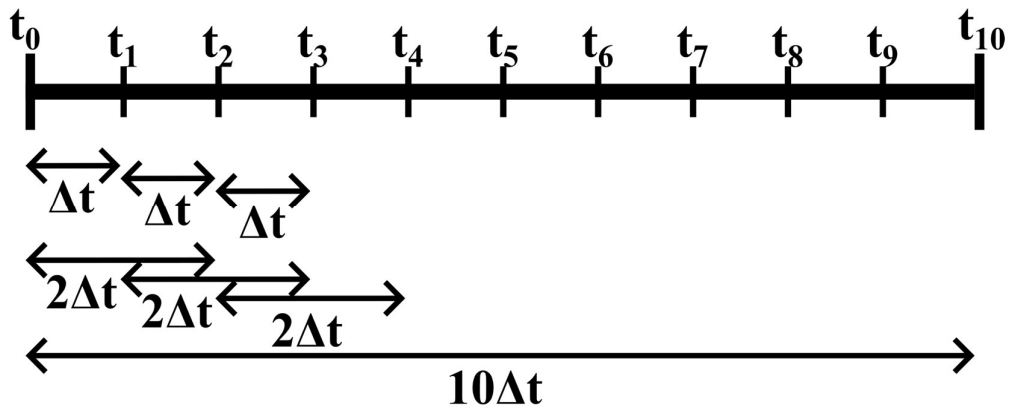

Figure 2-12: Representation of how the time step is used for the calculation of the MSD.

For this reason, the MSD analyses are usually truncated at a certain time interval, and when they are not truncated and the analysis is made until interval times similar to the length of the simulation, we observe weird behaviors of the MSD (as shown in the highlighted section of *Figure 2-13*). At these points, the MSD values may increase or decrease abruptly, which can be misleading and should be treated with caution. Such irregularities are because the time step used in the simulation is too large, leading to inaccurate results. Therefore, it is important to choose an appropriate time step size to ensure that the simulation accurately captures the underlying MD, and the MSD analysis yields reliable results excluding these erroneous points.

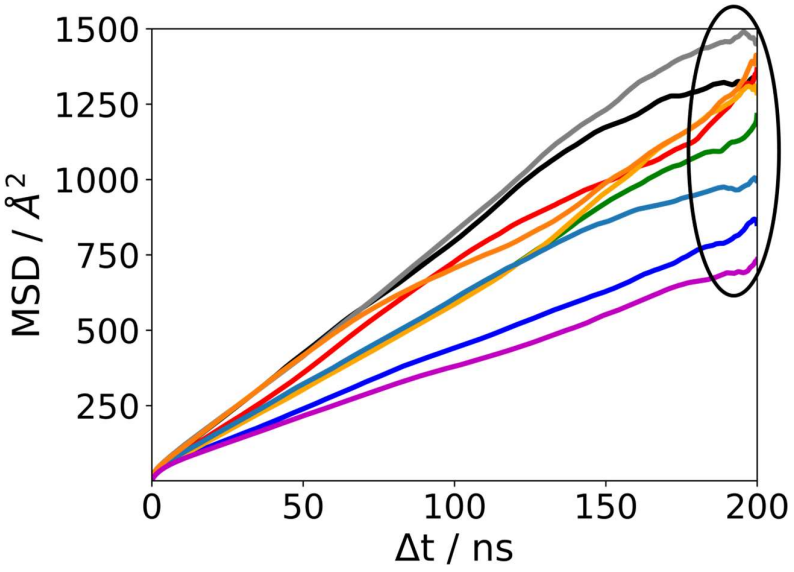

Figure 2-13: Example of various MSD curves, where the region with larger time steps is highlighted, showing erratic behavior.

MSD calculations are used to obtain the diffusion coefficient (D) through the Einstein relation.

$$2dD_A\Delta t = \lim_{\Delta t\to\infty} \langle|\vec{r}_i(t+\Delta t) - \vec{r}_i(t)|^2\rangle_{i\in A,t}$$

2.38

Where D_A is the diffusion coefficient of the specie A and d is the dimensionality (normally $d = 3$). Diffusion coefficients are also useful to obtain the lithium transference number ($Li\ TN$).

$$Li\ TN = \frac{D_{Li^+}}{D_{Li^+} + D_{Anion}}$$

2.39

Basically, $Li\ TN$ is the ratio of the diffusivity of Li^+ with respect to the entire ionic diffusion. Ideally, $Li\ TN$ should approximate to 1, meaning that all the ionic mobility in the system is due to Li^+.

However, to calculate the diffusion coefficients, we cannot use all the time intervals. MSD curves have two regions: the ballistic region and the diffusive region. The ballistic region corresponds to the low interval times and is due to the harmonic oscillations of the atoms due to vibrating movements. At these short times, the particles do not have time to interact or collide with other particles. In contrast, the diffusive region (also referred to as the Fickian region) appears at larger time intervals and, in this region, motion is driven by thermodynamic forces. At these long times, particles suffer from multiple collisions and interactions and their movement is an average of all these effects. This is the region from which we have to take the data to calculate diffusion coefficients, without using the data from large time intervals, which, as explained before (*Figure 2-13*), yield very poor statistics.

To effectively differentiate these two regions, logarithm scales can be used (see *Figure 2-14*). In this scale, the ballistic region of the MSD presents a straight line of slope equal to 2 and the diffuse region a straight line of slope equal to 1. Between these two regions, it appears a third regime (the subdiffusive regime) in which the slope is smaller than 1. At the time intervals corresponding to this region, the particles have enough time to interact with others, but not to capture an average effect.

It is worth mentioning that the ballistic region of the MSD is not of interest in our studies since we are more interested in simulating long times to reach the diffusive region. Besides, the interval times needed to properly capture the behavior corresponding to the ballistic region are very short. The time step between the different snapshots should be too short, which, joined to the long simulation times, would result in trajectory files difficult to manage.

This is why the time step between snapshot we use is too large to study the behaviour in the ballistic region. When results are analyzed in this Thesis (see e.g., *Figure 3-4*, *Figure 3-23*, or *Figure 4-12*), where MSD plots are shown in logarithmic scale, the straight section at low times does not correspond to the ballistic region. It is an artifact of including the (0,0) point in the analysis.

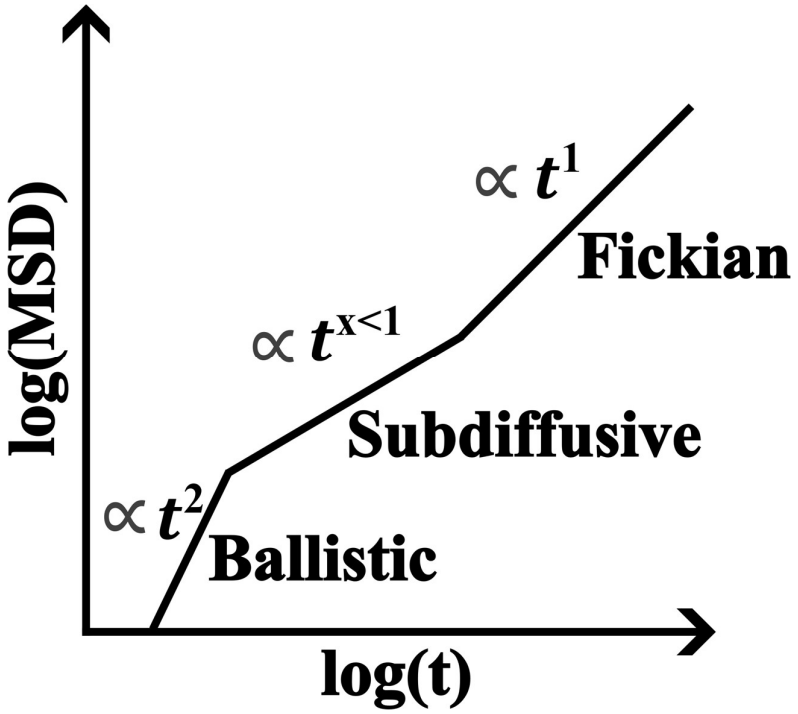

Figure 2-14: Schematic representation of the different regimes that appear in an MSD plot in logarithmic scale.

In this Thesis, we use the following specific procedure to identify the Fickian regime in the MSD plots, enabling the computation of the diffusion coefficient (refer to *Figure 2-15* for a visual representation of this procedure). Utilizing a logarithmic scale, we construct a reference straight line with a slope of 1 (representative of the Fickian regime) that intersect each point on the curve.

Then, we define upper and lower limit curves with a specified margin of error (typically 1 $Å^2$, but for enhanced visualization, 20 $Å^2$ was used in the example). We meticulously examine the tangent straight lines, determining the time interval during which each tangent line remains within the defined limit curves. Subsequently, we select the tangent line with the longest duration within these limits. This duration must be continuous to avoid the reentry of the tangent line at posterior times due to the weird behaviour of the MSD data at large times.

This approach allows us to accurately pinpoint the diffusive region. To calculate the diffusion coefficient, we isolate the data segment that most closely follows the reference line with a slope of 1, ensuring that the chosen region indeed represents the diffusive behavior, and fit this region according to *Eq. 2.38*. This procedure is written in a Python code (see *Appendix A.1* for a description of the code).

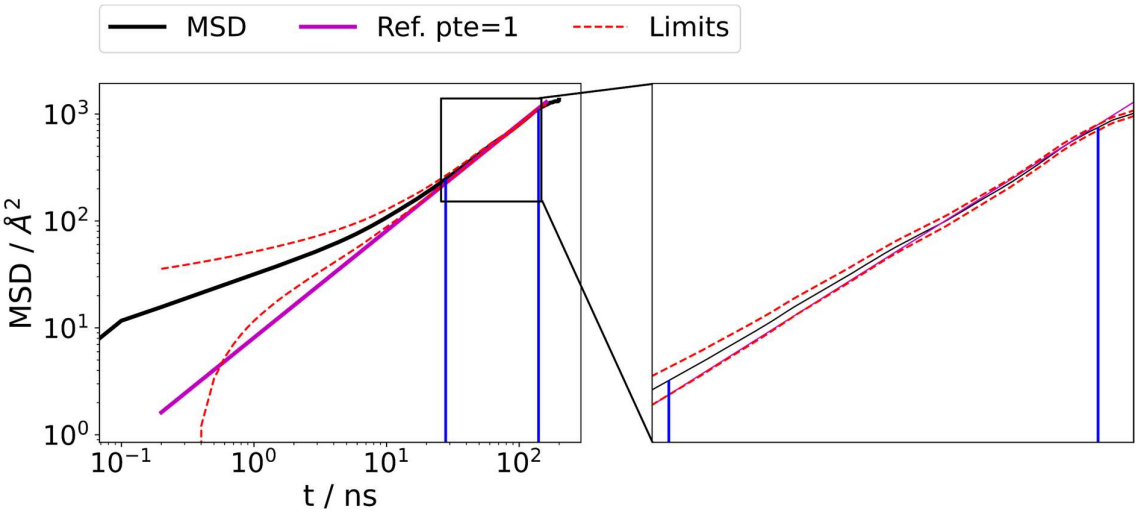

Figure 2-15: Example of the method of calculation of the diffusion coefficient, with the MSD curve in black, the defined limits in red, the reference curve of slope equal to 1 in violet and the selected region in which the reference line is inside the cutoff limits between the blue lines.

MSD analyses are a powerful tool for comparing the theoretical predictions of the conductivity (since a correlation between diffusion coefficients and conductivity can be made) and lithium transference number (*Eq. 2.39*) with the experimental measurements. However, it is crucial to take many simulation details into account, such as the length of the simulation, which must be sufficiently long to reach the diffusive regime. Another crucial factor is the accurate calculation of partial atomic charges. A wrong description of the charges can lead to underestimate or overestimate the electronic interactions, which can artificially increase or decrease the diffusivity of the species. Thus, it is essential to carefully consider these simulation details when using MSD analysis to compare theoretical predictions with experimental measurements.

- *Radial Distribution Function (RDF)*:

The RDF is an immensely powerful tool to analyze the coordination environment of the atoms and the system's structure. It is a measure of the probability of finding an observable particle B at a certain distance of a reference particle A.

$$RDF_{AB}(r) \equiv g_{AB}(r) = \frac{n_{AB}(r)}{\overline{n_B}} = \frac{V}{N_A N_B} \sum_{i \in A}^{N_A} \sum_{j \in B}^{N_B} \left\langle \delta \left(r_{ij}(t) - r(t) \right) \right\rangle_t \qquad 2.40$$

Where $n_{AB}(r)$ is the number density of particles B at a distance r of particles A, $\overline{n_B}$ is the average number density of particle B in the system, N_A and N_B are the number of A and B particles in the system respectively, and V the volume of the system.

However, the delta function in *Eq. 2.40* needs to be solved numerically. The easiest solution to carry this out is to create successive shells and count the number of atoms within each shell. In

the example shown in *Figure 2-16*, the red atom represents the reference atom, while the yellow atoms are situated within the shell at a distance of r from the reference atom.

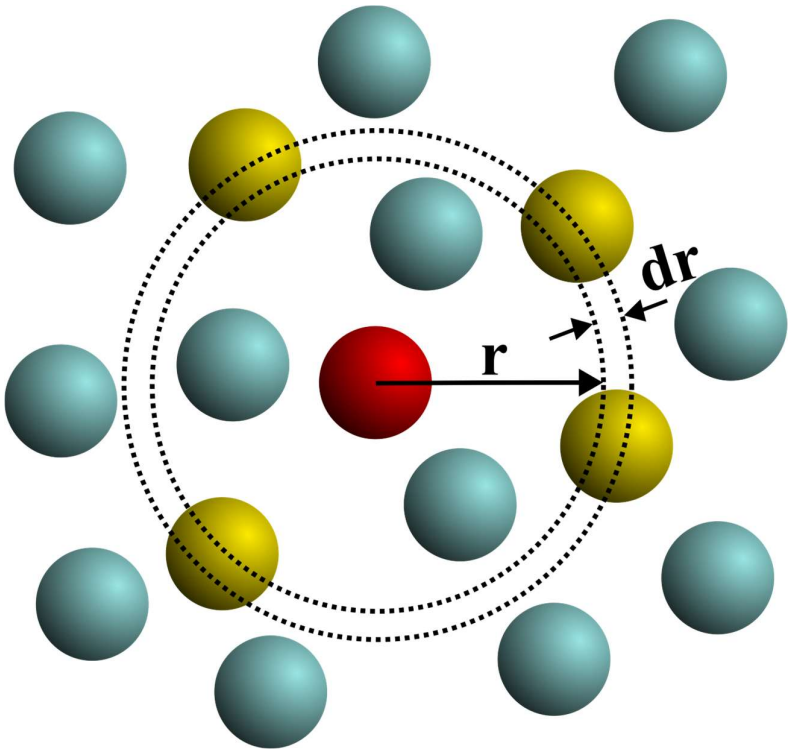

Figure 2-16: Schematic 2D-representation of how the RDF is calculated, with the red particle being the reference one.

The RDF is a normalized function, and it tends to value 1 at large distance. RDF values greater than 1 indicate that it is more probable to find a certain atom at that distance than compared to the average density of that atom, indicating that an interaction might exist between those atoms. Integrating the RDF allows for a clearer view of the environment of an atom. Specifically, the coordination number (CN) is a measure of the number of atoms that lie within a sphere of a certain radius around the reference atom.

$$CN_{AB}(r) = 4\pi\overline{n_B}\int_0^r dr\, r^2 g_{AB}(r) \qquad 2.41$$

In *Figure 2-17* we can see an example of a RDF analysis, together with the calculation of the CN. We see a high peak at around 2.1 Å, representing a high interaction between the particles analyzed. The minimum behind the peak indicates that no particles are located at these distances, allowing the CN to stabilize around a value of approximately 6. This means that, on average, the reference atoms are surrounded by 6 observable atoms. The RDF tends to value

equal to 1 at large distance and the CN increases since more atoms are counted as the distance increases.

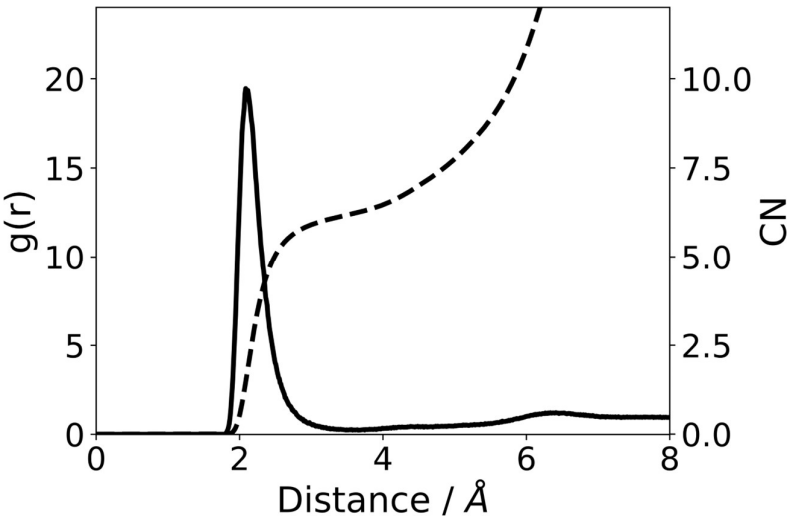

Figure 2-17: Example of an RDF analysis (solid line) with the calculation of the CN (dashed line).

It is worth noting that RDFs have not a clear correspondence with experimental data, as does MSD. In experiments, the coordination between the atoms and molecules is studied with different techniques, for example, analyzing the absorption spectra in different wavelengths and studying the variations in the vibrational frequencies with infrared and Raman spectroscopy. Yet, these frequencies vary depending on the coordination of the molecules and, therefore, allow for inferring changes in CN and local coordination geometries.

2.2.6. Typical MD Simulation Procedure

After having gained an understanding of how MD simulations work, it is important to have a clear overview of the various steps involved in the simulation process. *Figure 2-18* provides a schematic representation of the different components of a MD simulation. We will also explain the procedure used in the studies performed in this Thesis, giving information of each of the steps, although some differences may arise between them. Concrete information of these differences will be given in the *Theoretical Background* section of each of the studies.

Firstly, we start by defining the structure of the distinct types of molecules that will form part of the simulated system. This is done in two stages: generating the geometry of the molecules and defining the parameters of the FF. The geometry of the molecule includes just the positions of the atoms. In crystalline structures, the position of the atoms is crucial because it determines with which structure we are dealing. Similar atomic compositions can be arranged in different forms and result in distinct phases, which have different properties. However, in molecular liquid or amorphous solid systems, the exact position of the atoms is not so important as long

as they form the structure required, independently of rotations and translations. The description of the FF was explained in *Section 2.2.2*. For each molecule we must define the coefficients of the bonded interactions (bonds, angles, and dihedrals) and the parameters of the nonbonded interactions (electrostatic and vdW). The FF parameters of the different molecules were obtained using the OPLS-AA force field *[111]*, *[112]*, taking the values of ϵ and σ for the characterization of the Lennard Jones potential (*Eqs. 2.18*, *2.19*) for the description of the non-bonded interaction and the coefficients for the bonded interactions (bonds, angles, and dihedrals) (*Eqs. 2.11*, *2.12*, *2.13*, *2.16*). All the FF parameters can be found on *Appendix A.2*. The fast smooth particle mesh Ewald (PME) approach *[113]* was used to treat electrostatic interactions, with a cutoff of 10 Å for the van der Waals interactions and for the real space Ewald summation. While the partial atomic charges of the polymer matrix have been taken as the default ones taken from the OPLS-AA FF, all the anions of the studies have their structure optimized using DFT calculations with the electrostatic potential method (ESP) (more details in *Section 2.3.8*).

After the system is properly defined, we have to initialize the simulation system and optimize it. In this Thesis, we will perform the simulations using the GROMACS software *[114]*, *[115]*, *[116]*, *[117]* (see *Section 2.2.7*) and the usual way to introduce the molecules into the system is randomly. To this end, we typically create a cubic simulation box (although other alternatives exist, cubic boxes are the most common geometry) and randomly place the desired number of molecules inside to match the required concentrations and ratios between the different molecules. Due to the programming implementation of GROMACS, the initial simulation box needs to be quite big, thus resulting in low densities (see example of *Figure 2-19*). This is because GROMACS uses a criterion to assess whether a molecule can be inserted in the simulation box, as well as the changes in the geometry of the inserted molecule, which does not allow for high density systems.

After inserting the molecules into the simulation box, the first step is always to perform an energy minimization to ensure that the system's geometry is appropriate. During this process, the geometry of the molecules is adjusted to reach the minimum potential energy. Following the energy minimization, the system needs to be optimized to achieve the desired simulation conditions (including density, temperature, and pressure). The optimization process involves a series of steps to convert the initial system, which is randomly arranged and has low density, into a system that is suitable for simulation.

Due to the low-density initial systems, the first optimization step involves compressing the system through a short NPT simulation at high pressure. The simulation box shrinks until the system reaches a limiting density, at which point the repulsive interactions become stronger than the external pressure and the system stabilizes. This compression typically requires only moderate pressure (between 5 and 10 atm), although higher pressures (up to 100 atm) could be used to speed up the compression. We chose to apply a pressure of 10 bar in our simulations, using a Parrinello-Rahman barostat along with a temperature of 10 K using a Berendsen thermostat in this NPT compression step. Both the barostat and thermostat have a relaxation time of 1 ps. The importance of this first compression step can be observed in the example system of *Figure 2-19*, as the extremely low density of the initial system needs to be increased.

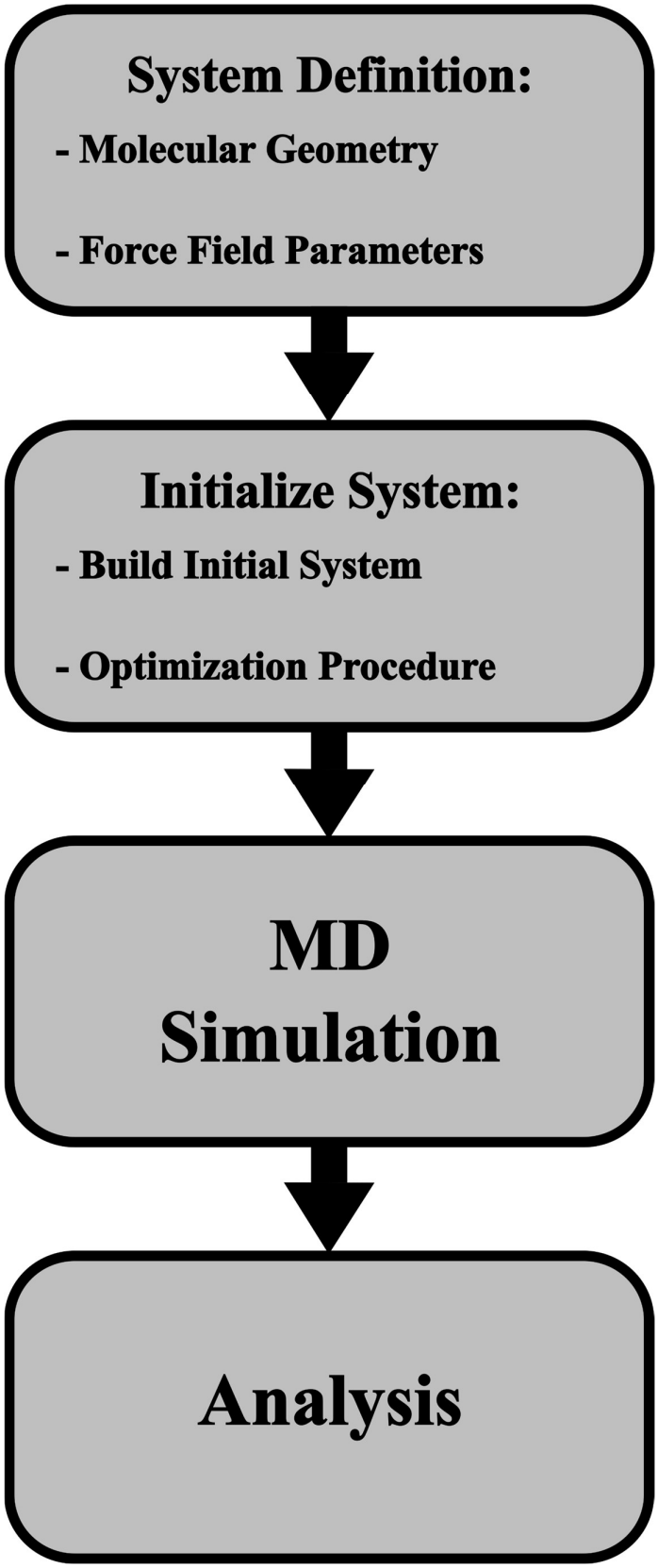

Figure 2-18: Schematic representation of a MD simulation procedure.

Once the system is compressed, there is no strict set of rules to complete the optimization process. In our case, we heated the system up to the simulation temperature, in an NPT ensemble, at a pressure of 1 bar, keeping the use of a Parrinello-Rahman barostat and a Berendsen thermostat with a relaxation time of 20 ps for both. The simulation temperature is commonly set at 343 K (70 ºC) in the studies. This allows the systems to adjust the density to values similar to the experiments (observe density change in *Figure 2-19*). Prior to this heating step, another energy minimization is done to relax possible high-potential-energy configurations formed by the high pressure applied on the previous step.

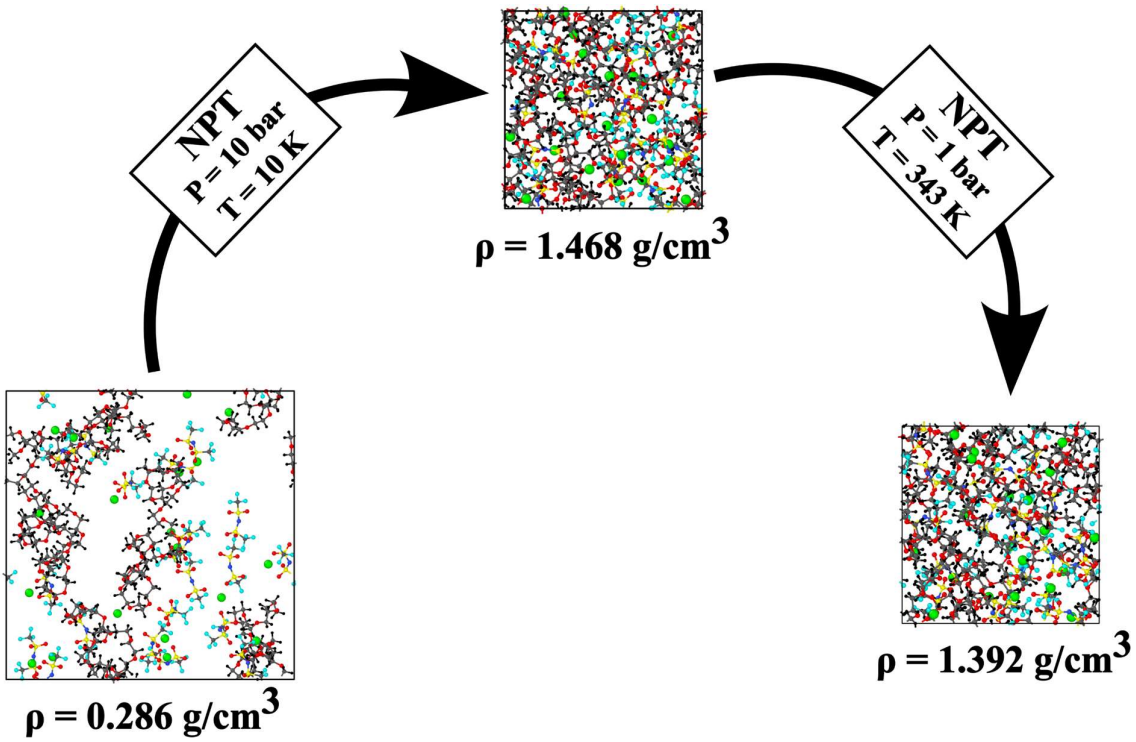

Figure 2-19: Example system of 5 PEO chains and 20 LiTFSI with the evolution of the system's density in the first steps of the optimization process.

Despite the optimization process followed, one common step is typically present in all optimization procedures. This is a longer final optimization step that is performed under the same simulation conditions as the actual simulation. This last step serves to erase any residual information from the previous optimization steps and ensure that the system is fully equilibrated. In some cases, this last step may be included in the simulation itself, with only the initial portion of the simulation being discarded for analysis. We make use of another energy minimization, followed by an optimization step in a NVT ensemble at the simulation temperature (343 K) during 1 ns with a relaxation time of 20 ps for the Berendsen thermostat used.

Once the system is optimized, the simulation phase starts. Compared to the optimization steps, the simulation is significantly longer, typically lasting anywhere from tens of nanoseconds to

even a few microseconds. While the details of the simulation procedure are covered in *Sections 2.2.1* and *2.2.3*. one key consideration is selecting the appropriate thermodynamic ensemble (*Section 2.2.4*) that aligns with the properties being studied. Additionally, it is important to choose an appropriate interval time for saving information, as a too short interval could result in unwieldy file sizes that are difficult to analyze. In general, an increment in the number of steps during the simulation does not necessarily translate to an increase in the precision of the analysis, as outlined in *Section 2.2.5*. In our simulations, we commonly employ a simulation time of 200 ns in a NVT ensemble, with similar conditions to the previous optimization step, and with a timestep of 1 fs.

Finally, the analysis is performed on the trajectory generated during the simulation (see *Section 2.2.5*). Despite the complexity of the system, the number of parameters to analyze is small. Specifically, we are only concerned with the position and velocity of the atoms, as well as generic data such as temperature, pressure, and energies. Thus, all the subsequent analyses are based on these variables.

2.2.7. Software description: GROMACS

We want to finish this section about MD simulations giving some information about the software used to perform these simulations.

The GROMACS software was developed in the University of Groningen, in the Biophysical Chemistry department, and released its first version back in 1995 *[114]*. However, since 2001, the Royal Institute of Technology and Uppsala University have continued their development.

GROMACS is a free community-driven software to perform molecular dynamics in the field of computational chemistry and biophysics, with a wide variety of packages to facilitate the resolution of the Newtonian equations of motion of all the atoms that compose the simulated system. Although firstly designed for biomolecular molecules (i.e., lipids, proteins, and nuclei acids) the great performance of GROMACS attracted the attention for simulating non-biological systems like polymers.

Enumerating some of the characteristics that make GROMACS stand out from the rest of the codes:

- It introduces some optimizations in the algorithms of the code to enhance the performance and extract the full potential of modern CPU and GPUs, adding the possibility of use both simultaneously.

- It is user-friendly, with no scripting needed, and force field files easily readable in text format, allowing for a clear understanding and localization of the parameters for each atom and interaction in case some modification is required.

- It supports various force fields to accommodate the parameters to the model that best fits the system under study.

- It can be run in parallel using the MPI protocol.

- It uses its own file format for storing and writing the trajectory information, with a high level of compression.

- It possesses a library of predefined tools for post-simulation analysis of the structural properties, thermodynamics of the system and other relevant properties.

There exist other software such as LAMMPS *[118]*, *[119]*, AMBER *[120]*, *[121]*, CHARMM *[122]*, *[123]* or NAMD *[124]* than are commonly used to perform the kind of simulations over polymeric systems present in this Thesis. But all the afore mentioned advantages of GROMACS made it the perfect software to use, because of its strength, high speed and great performance *[125]*.

2.3. *Ab Initio* Calculations

Ab Initio calculations are computational methods used to theoretically study atomistic and molecular systems, providing detailed information on the electronic structure and energetics of chemical systems, making them an indispensable tool in many areas of chemistry and materials science. In this Section we will introduce the development of the different approximations that, during the 20th century, were proposed to theoretically study atomic and molecular systems. We will follow the historic progression that led from the formulation of the Schrödinger equation in 1925 to the techniques that we use nowadays. A series of approximations, as we will see hereafter, were introduced to facilitate the resolution of the incredibly complex problem of studying atomic systems with their electronic structure. Finally, a brief description of the use of these techniques and the software used in this Thesis (FHI-aims *[126]*) will be made.

2.3.1. Schrödinger Equation

Ab Initio methods involve performing quantum mechanical calculations, which allow researchers to solve the time-independent Schrödinger equation.

$$\widehat{H}|\Psi\rangle = E|\Psi\rangle$$

2.42

Where Ψ is the wave function of the system and $\widehat{H}$ the Hamiltonian operator of the system. $\widehat{H}$ includes the contribution of all the nuclei and all the electrons of the system.

$$\widehat{H} = -\sum_{I} \frac{\hbar^2}{2M_I} \nabla_I^2 - \sum_{i} \frac{\hbar^2}{2m_e} \nabla_i^2 + \frac{1}{2} \sum_{I,J(I\neq J)} \frac{1}{4\pi\epsilon_0} \frac{Z_I Z_J e^2}{\left|\overrightarrow{R_I} - \overrightarrow{R_J}\right|} +$$

$$+ \frac{1}{2} \sum_{i,j(i\neq j)} \frac{1}{4\pi\epsilon_0} \frac{e^2}{\left|\vec{r_i} - \vec{r_j}\right|} - \sum_{I,i} \frac{1}{4\pi\epsilon_0} \frac{Z_I e^2}{\left|\overrightarrow{R_I} - \vec{r_i}\right|}$$

2.43

Where M_I and $\overrightarrow{R_I}$ are the mass and position of the nuclei; m_e, $\vec{r_i}$ and e the mass, position and charge of the electrons, and Z_I the atomic number of the I-nuclei. The first two terms correspond to the kinetic energy of the nuclei and electrons (expressed in terms of the Laplacian operator ∇^2), respectively. The last three terms are the electrostatic interactions between nuclei-nuclei, electron-electron, and nuclei-electron, respectively.

The solution of the Schrödinger equation allows us to know all the properties under study of the system. However, this is a many-body problem, and the solution of this equation is extremely complicated or even impossible without approximations.

2.3.2. Born-Oppenheimer Approximation

The Born-Oppenheimer approximation *[127]*, also known as the adiabatic approximation, is the most basic approximation when dealing with the resolution of the Schrödinger equation of a many-body system (*Eq. 2.42*). It is based on the mass difference between the nuclei and the electrons. An atomic nucleus, even the lightest of them (hydrogen), is various orders of magnitude heavier than an electron. The electrostatic interaction does not depend on the mass of the object, only on the electric charge, which is of the same order for nuclei and electrons. Thus, the movement of the nuclei is much slower than the electrons.

In the Born-Oppenheimer approximation we can split the movement of the nuclei and the electrons. The electrons are treated as if they are under the influence of the electrostatic potential created by the frozen nuclei. In this way we can decouple the Hamiltonian into an electronic part and a nuclear part. Focusing on the electronic Hamiltonian ($\widehat{H}_e$) of a N-electron system.

$$\widehat{H}_e = -\sum_{i}^{N} \frac{\hbar^2}{2m_e} \nabla_i^2 + \sum_{i>j}^{N} \frac{1}{4\pi\epsilon_0} \frac{e^2}{|\vec{r_i} - \vec{r_j}|} - \sum_{I,i} \frac{1}{4\pi\epsilon_0} \frac{Z_I e^2}{|\overrightarrow{R_I} - \vec{r_i}|}$$

2.44

Here, the nuclei positions ($\overrightarrow{R_I}$) are fixed parameters for the electronic Hamiltonian. When analyzing the electronic part, the nuclei can be treated as if they are static particles, because its movement is produced in time scales much larger than the electronic movement. Thus, the kinetic energy of the nuclei can be neglected when we want to solve the electronic part. Normally, the electrostatic interaction of the electron with the nuclei is also referred to as external potential ($V_{ext}(\vec{r})$) and it may also include some other external interactions, such as electric or magnetic fields.

This Hamiltonian affects only to the electron-wavefunction Ψ_e.

$$\widehat{H_e}\Psi_e = E_e\Psi_e$$

2.45

This electron-wavefunction possesses two essential characteristics: antisymmetry and normalization. Ψ_e is antisymmetric because the electrons are fermions (particles with half-integer spin). This means that an exchange between the positions of any pair of electrons leads to a sign change in the wave function (*Eq. 2.46*). As a result, it ensures that no two electrons can occupy the same quantum state, a principle known as the Pauli exclusion principle. Normalization is the property that ensures that the probability of finding the electrons in any position in space adds up to unity. Specifically, the square of the wavefunction gives the probability density of finding the electrons in a particular region of space. Thus, if we integrate the square of the wave function over all possible positions, the probability of finding the electrons is 1 (*Eq. 2.47*). Overall, the electron wavefunction is an essential concept in quantum

mechanics that underlies our understanding of the behavior of matter at the atomic and molecular level.

$$\Psi_e(\vec{r}_1, \vec{r}_2, \dots, \vec{r}_i, \vec{r}_j, \dots, \vec{r}_N) = -\Psi_e(\vec{r}_1, \vec{r}_2, \dots, \vec{r}_j, \vec{r}_i, \dots, \vec{r}_N)$$

2.46

$$\int d^3r_1 \int d^3r_2 \dots \int d^3r_N \ |\Psi_e(\vec{r}_1, \vec{r}_2, \dots, \vec{r}_N)|^2 = 1$$

2.47

The nuclear Hamiltonian ($\widehat{H}_n$) lacks the kinetic energy and only possesses the potential energy due to the interaction between the nuclei.

$$\widehat{H}_n = \frac{1}{2} \sum_{I,J(I \neq J)} \frac{1}{4\pi\epsilon_0} \frac{Z_I Z_J e^2}{|\overrightarrow{R_I} - \overrightarrow{R_J}|}$$

2.48

This is a consequence of the treat of the nuclei as frozen particles by the adiabatic approximation.

2.3.3. Hartree-Fock Approximation

The Born-Oppenheimer approximation facilitates the resolution of the Schrödinger equation (*Eq. 2.42*). However, the many-body problem continues. One of the ways to solve it is to express the complete wave function Ψ as a Slater determinant *[128]*.

$$\Psi_e \equiv \Psi_{HF} = \frac{1}{\sqrt{N!}} \begin{vmatrix} \psi_1(\overrightarrow{r_1}, s_1) & \psi_2(\vec{r}_1, s_1) & \cdots & \psi_N(\overrightarrow{r_1}, s_1) \\ \psi_1(\overrightarrow{r_2}, s_2) & \psi_2(\overrightarrow{r_2}, s_2) & \cdots & \psi_N(\overrightarrow{r_2}, s_2) \\ \vdots & \vdots & \ddots & \vdots \\ \psi_1(\overrightarrow{r_N}, s_N) & \psi_2(\overrightarrow{r_N}, s_N) & \cdots & \psi_N(\overrightarrow{r_N}, s_N) \end{vmatrix}$$

2.49

Where N is the number of electrons of the system. Ψ_e is now described as a product of individual electron wave functions ψ_i, each of them depending on the position ($\vec{r_i}$) and spin (s_i) of each electron.

Since it is defined as a Slater determinant, Ψ_{HF} is antisymmetric. The Hartree-Fock approximation *[129]*, *[130]*, *[131]* reduces the difficulty of solving the wavefunction of a N-electron system (*Eq. 2.45*) to solve a system of N equations each dependent on only a one-electron wavefunction.

$$\left[-\frac{\hbar^2}{2m_e}\nabla_i^2 + V(\vec{r_i})\right]\psi_i(\vec{r_i}, s_i) = \varepsilon_i\psi_i$$

2.50

Where $V(\vec{r_i})$ is the potential affecting the position $\vec{r_i}$ due to the rest of electron wave functions and ε_i the energy of the i-electron. In terms of computational cost, the second system is much easier to solve.

2.3.4. Density Functional Theory and Hohenberg-Kohn Theorems

Density functional theory (DFT) is an alternative method to the Hartree-Fock approximation to solve the Schrödinger equation. The HF approximation is computationally very costly when the system has some complexity, and thus another approach is needed. DFT works with electron densities ($n(\vec{r})$). In a N-electron system, the electron density is given by:

$$n(\vec{r}) = \langle \Psi_e | \sum_i^N \delta(\vec{r} - \vec{r_i}) | \Psi_e \rangle = N \int d^3 r_2 \dots \int d^3 r_N \, \Psi_e^*(\vec{r}, \vec{r_2}, \dots, \vec{r_N}) \Psi_e(\vec{r}, \vec{r_2}, \dots, \vec{r_N})$$

2.51

Where the electron-wavefunction Ψ_e is normalized and we can obtain the ground state wavefunction (Ψ_e^0) from the ground state density ($n_0(\vec{r})$).

$$\Psi_e^0 = \Psi[n_o]$$

2.52

From which the total number of electrons (N) can be obtained.

$$N = \int d^3 r \, n_0(\vec{r})$$

2.53

The usual way to find the electron density is to solve the Born-Oppenheimer Schrödinger equation (*Eq. 2.45*) given an electronic Hamiltonian (*Eq. 2.44*) to obtain the wave function, and from the wavefunction, obtain the electron density (*Eq. 2.51*). However, it can also be done the other way around, obtain the Hamiltonian from the electron density. This was formalized by Hohenberg and Kohn in two theorems *[132]*.

- **1st H-K theorem**: Two different Hamiltonians cannot have the same ground state energy density. Thus, it is possible to define the ground state energy as a functional of the electron density: $E = E[n(\vec{r})]$.

- **2nd H-K theorem**: The minimum energy of the system is given only by the true ground state density.

Given these two theorems, we can determine the ground state energy by minimizing $E[n]$, avoiding going through the wavefunction. The main problem is that the exact dependence of

the energy on the electronic density is unknown, and the H-K theorems do not provide any hint on how this relation might be. Yet, according to the 2nd H-K theorem, there exists a functional $F[n]$ which ensures that the energy functional gives the minimum energy for the ground state energy density.

$$E[n] = F[n] + \int d^3r \, V_{ext}(\vec{r})n(\vec{r})$$

2.54

Where $F[n]$ groups both the kinetic energy and the interaction between electrons. However, this functional is unknown.

2.3.5. Kohn-Sham Equations

Kohn and Sham came to solve the problem of the unknown functional $F[n]$ *[133]*. Their solution was on the way of the HF approximation. They proposed a system of non-interacting electrons for which they constructed a basis set for the one-electron orbitals (φ_i).

$$n(\vec{r}) = \sum_{i}^{N} |\varphi_i(\vec{r})|^2$$

2.55

In this set, Kohn and Sham defined an external potential which exactly reproduces the behavior of the electrons in an interacting system, thus given the same electron density and energy.

$$F[n(\vec{r})] = T_s[n(\vec{r})] + E_H[n(\vec{r})] + E_{xc}[n(\vec{r})]$$

2.56

Where T_s is the Kohn-Sham kinetic energy (the kinetic energy of a virtual system of N electrons with no interactions), E_H is the Hartree term of the Coulombic interaction and E_{xc} is the exchange-correlation energy. Both T_s and E_H are only a part of the exact kinetic energy and Coulomb interaction, respectively. However, they are a good approximation of the total energy because the other contributions are negligible.

T_s does not have an explicit expression, but we can solve the Schrödinger equations of the set of one-electron orbitals.

$$\left(-\frac{\hbar^2}{2m_e}\nabla^2 + V_{eff}(\vec{r})\right)\varphi_i(\vec{r}) = \varepsilon_i\varphi_i$$

2.57

This set of equations describes the movement of N non-interacting particles under the effect of an effective external potential V_{eff}.

$$V_{eff}(\vec{r}) = V_{ext}(\vec{r}) + V_{xc}(\vec{r}) + e^2 \int d^3r' \frac{n(\vec{r'})}{|\vec{r} - \vec{r}'|}$$

2.58

Where V_{xc} corresponds to the exchange-correlation potential.

$$V_{xc}(\vec{r}) = \frac{\delta E_{xc}[n(\vec{r})]}{\delta n(\vec{r})}$$

2.59

This way, we can obtain the ground state energy density of the system without minimizing the energy functional through the Kohn-Sham (K-S) equations *[133]*.

$$n(\vec{r}) = \sum_{i}^{N} |\varphi_i(\vec{r})|^2$$

2.60

$$\left(-\frac{\hbar^2}{2m_e}\nabla^2 + V_{ext}(\vec{r}) + V_{xc}(\vec{r}) + e^2 \int d^3r' \frac{n(\vec{r}')}{|\vec{r} - \vec{r}'|}\right)\varphi_i(\vec{r}) = \varepsilon_i \varphi_i(\vec{r})$$

2.61

Here, all the terms inside the left side parenthesis of *Eq. 2.61* are known as the Kohn-Sham Hamiltonian (H^{KS}). The way to solve the K-S equations is to do it recursively.

1) First, we make an initial guess of the electron density, and we calculate the effective external potential given by the electron density with it (*Eq. 2.58*).

2) Then we introduce this potential into the K-S equations to obtain the electron orbitals (*Eq. 2.61*)

3) After that, we calculate a new electron density based on the electron orbitals (*Eq. 2.60*).

4) With this new electron density, we start again the process: $n(\boldsymbol{r}) \rightarrow V_{eff}(\boldsymbol{r}) \rightarrow \varphi(\boldsymbol{r}) \rightarrow n(\boldsymbol{r})$. We do this until the electron density fulfills the convergence criteria. However, to follow this scheme, we need a way to define the exchange-correlation energy.

2.3.6. Exchange-Correlation Energy Functionals

The exchange-correlation energy represents all electronic interactions in a system, excluding pure electrostatic interactions. Unfortunately, the exact functional form of this energy is unknown, and thus we must rely on approximations. This exchange-correlation functional is

typically expressed as a mathematical formula that approximates the true exchange-correlation energy.

$$E_{xc}[n(\vec{r})] = \int d^3r\, n(\vec{r})\epsilon_{xc}\big(n(\vec{r})\big)$$

2.62

Where ϵ_{xc} is the exchange-correlation energy density. It can be divided into an exchange term and a correlation term.

$$\epsilon_{xc}\big(n(\vec{r})\big) = \epsilon_x\big(n(\vec{r})\big) + \epsilon_c\big(n(\vec{r})\big)$$

2.63

In DFT calculations, accurately defining the exchange-correlation energy density is essential, particularly when comparing the characteristics of different systems. These systems are often quite similar to one another, with only small variations in geometry or composition. Thus, their total energy values are likely to be of the same order, making it crucial to accurately calculate the energy difference between them. The contributions of the exchange-correlation energy are particularly important in this regard, as other energetic terms tend to be similar between the systems, and the contributions of the exchange-correlation energy could mark the difference.

In the following discussion, we will explore some of the most commonly used approximations for describing the exchange-correlation functional.

- *Local Density Approximation*:

The local density approximation (LDA) is the simplest definition of E_{xc}. In LDA, the interactions between electrons are approximated using those of a homogeneous electron gas, which assumes that the electrons are uniformly distributed throughout the system. The exchange energy density of this type of gas is one of the few that can be determined exactly *[134]*.

$$\epsilon_x^{LDA}\big(n(\vec{r})\big) = -\frac{3}{4}\left(\frac{3}{\pi}\right)^{\frac{1}{3}}\big(n(\vec{r})\big)^{\frac{1}{3}}$$

2.64

However, while LDA is a simple and computationally efficient method, it has limitations when applied to systems with strong electron correlations or inhomogeneous electron densities. To mitigate this, quantum Monte Carlo calculations can be used to describe with high precision the correlation energy density of a homogeneous electron gas *[135]*, *[136]*.

The LDA approximation is simple, but quite precise and is enough for many systems to perform DFT calculations. Moreover, LDA is an especially useful tool to describe the limit of high electron density. Yet, this approximation has some disadvantages when trying to represent electrons from external orbitals (i.e., *d* and *f* orbitals). It also badly describes the long-range

interactions (e.g., vdW or hydrogen bonds). Finally, LDA tends to overestimate bond energy and valence band energy.

- *Generalized Gradient Approximation*:

The LDA approximation assumes that the electrons are homogeneously distributed in space. Therefore, this approximation cannot account for the gradients between regions of high and low electron density. To overcome this limitation, the next step in improving the exchange-correlation functional is to incorporate a treatment of the electron density that accounts for its non-homogeneity. To this end, the generalized gradient approximation (GGA) is one such method that includes the gradients of density, allowing for a more accurate description of electron density variations. However, GGA functionals must be carefully constructed to avoid zones of divergence.

$$E_{xc}^{GGA}[n(\vec{r})] = \int d^3r \; e_{xc}^{GGA}\big(n(\vec{r}), \nabla n(\vec{r})\big)$$

2.65

Where e_{xc}^{GGA} is a function dependent on the both the electron density and its gradient. GGA functionals partially correct the LDA's tendency to overestimate bond energies and can accurately describe hydrogen bonding, which is important in many chemical systems. However, one important limitation of GGA functionals is that they cannot account for vdW interactions. Some of the most common GGAs functionals are: the BLYP (Becke, Lee, Yang, and Parr *[137]*, *[138]*), the PW91 (Perdew, Yang *[139]*), and the PBE (Perdew, Burke, Ernzerhof *[140]*).

There are another group of GGA which also include the Laplacian of the electron density ($\nabla^2 n(\vec{r})$) to improve precision. They are known as meta-GGAs. Although in reality, what these functionals do is to include the kinetic energy density, because it is more stable than the Laplacian.

$$\tau(\vec{r}) = \frac{1}{2}\sum_{i}^{N} |\nabla \varphi(\vec{r})|^2$$

2.66

- *Hybrid Functionals*:

Hybrid functionals are another approximation to describe the exchange-correlation energy, more complex than the GGA and meta-GGA functionals. In these functionals, there is a mix of the exact HF exchange energy with the exchange-correlation energy coming from DFT calculations.

$$E_{xc}^{hyb}[n(\vec{r})] = \alpha E_x^{HF}[n(\vec{r})] + (1-\alpha) E_{xc}^{DFT}[n(\vec{r})]$$

2.67

Where α is the parameter that controls how much part of the hybrid functional comes from each method.

Some of the most known hybrid functionals are B3LYP *[141]*, *[142]* and PBE0 *[143]* (modifications of the GGAs BLYP and PBE, respectively), and HSE *[144]* (Heyd, Scuseria, Ernzerhof). Each of them mixes the HF and DFT contribution in different ratios.

Overall, we have seen that there are many ways to approximate the exchange-correlation functional depending on the level of precision required to describe the electron density, but now we have to come back to the problem of solving the K-S equations.

2.3.7. Basis Set

The usual way to solve the K-S equations (*Eqs. 2.60-2.61*) is to expand the electron orbitals φ_i in a basis set of functions $\{\phi_\alpha\}$.

$$\varphi_i(\vec{r}) = \sum_\alpha c_{i,\alpha}\, \phi_\alpha(\vec{r})$$

2.68

Where $c_{i,\alpha}$ are the coefficients of the expansion that is inserted into the K-S equation (*Eq. 2.61*).

$$H^{KS}[n(\vec{r})] \sum_\alpha c_{i,\alpha}\, \phi_\alpha(\vec{r}) = \varepsilon_i \sum_\alpha c_{i,\alpha}\, \phi_\alpha(\vec{r})$$

2.69

Where all the left side of the K-S equation has been named as the K-S Hamiltonian (H^{KS}). Multiplying *Eq. 2.69* by another function of the basis set and integrating over space, we can write it in matrix form.

$$\sum_\alpha c_{i,\alpha} \int d^3r\, \phi^*_\beta(\vec{r})\, H^{KS}[n(\vec{r})]\phi_\alpha(\vec{r}) = \sum_\alpha c_{i,\alpha}\varepsilon_i \int d^3r\, \phi^*_\beta(\vec{r})\phi_\alpha(\vec{r})$$

2.70

$$\sum_\alpha c_{i,\alpha}\left(\boldsymbol{H^{KS}_{\alpha,\beta}} - \varepsilon_i \boldsymbol{S_{\alpha,\beta}}\right) = 0$$

2.71

Where $\boldsymbol{S_{\alpha,\beta}}$ is the overlap matrix. The set of functions $\{\phi_\alpha\}$ that can conform the electron orbitals is not unique, and the number of terms of the expansion is not set. From the computational viewpoint, the length of this set must be of course finite, and its choice is what will determine the precision and cost of the calculation.

2.3.8. Use of DFT in this Thesis

After having explained all the historical development of the DFT technique in *Ab Initio* calculations, we want to briefly explain the use we have made of this type of calculations in this Thesis.

Its importance has relapsed in the optimization of the molecular structure of the anionic species that form the different lithium salts studied. The Becke three parameter Lee-Yang-Parr (B3LYP *[137]*, *[138]*) hybrid functional was used, in conjunction with the *tight* "tier 2" default basis set of FHI-aims (more details in *Section 2.3.9*). Then the charges were computed using the electrostatic potential method (ESP) with a total charge of -1. However, to consider polarizability effects *[145]*, this value was uniformly scaled down to -0.7. Thus, to ensure the electroneutrally of the entire system, the charge of Li^+ was reduced from +1 to +0.7. The partial atomic charges obtained for all the lithium salts can be found on *Appendix A.2*.

As mentioned in the procedure used to perform the MD simulation (*Section 2.2.6*), the partial atomic charges of the polymer matrixes were taken as the default ones provided by the OPLS-AA force field (see *Appendix A.2*). This is done because, even the size of a polymer chain (at the sizes we commonly use in MD simulations) can be treated at DFT level, the ESP method fails to accurately predict the partial charges of such big molecules. Besides, it can be extremely dependent on the geometrical conformation of the chain. Single monomers could be used to perform these calculations, but then we would ignore the effect of adjacent monomers. Adding more monomers to the definition of the polymer makes their geometry becomes important to the final result. This is the reason to use the default partial charges provided by the force field to describe the atomic interactions.

2.3.9. Software description: FHI-aims

We want to dedicate this last Section to providing some information about the software used in this Thesis to perform the DFT calculations.

FHI-aims was developed by the Fritz Haber Institute and firstly released in 2009 *[126]*. It is a software dedicated to performing *Ab-Initio* first principle simulations using the electronic structure of the atoms and based on numeric atom-center orbitals.

FHI-aims possesses a preconstructed basis set for elements 1 (hydrogen) to 102 (nobelium). These default parameters for each element control the integration grids and the accuracy of the Hartree potential, to guarantee fast and precise convergence. There are four collections of parameters for all elements, depending on the required level of precision of the calculations: *light*, *intermediate*, *tight*, and *really_tight*. Increasing the precision improves the reliability of the results at the cost of longer calculation times.

For fast, pre-optimization calculations, *light* settings are enough, but better descriptions are needed for correct geometry optimizations (up to meV precision) and proper energy calculations (*tight* settings are sufficient for this). These different levels of precision increment

the atomic orbitals that are included in the calculation. *Light* settings include only the most relevant orbitals (denoted as "tier 1"), while *tight* settings include more orbitals ("tier 2") for the light elements, 1 to 10, and a modified version of the "tier 1" for some important heavy elements (Al, Si, P, S, Cl). This reflects the fact that "tier 1" is enough for describing heavy elements. *Tight* settings are enough for most DFT calculations, requiring an important computational cost, but reaching the precision of tens of meV/atom for most elements. The *really_tight* basis set is only needed for very specific calculations where something very concrete needs to be evaluated.

For the standard molecular optimization calculations performed in this Thesis, a first screening with the *light* default set is used and a more precise optimization is performed with the output geometry of the *light* setting as the input one of the *tight* configurations.

Enumerating some of the properties that make FHI-aims stand out from the rest of the codes:

- It includes relativistic effects to properly describe materials where these corrections are needed.
- It is well optimized to study periodic systems.
- It has support to perform molecular dynamics at *Ab Initio* level, allowing the study of molecular stability and chemical reactions.
- It employs algorithms to improve efficiency of the resolution of the Schrödinger equation.
- It is designed to be used in parallel programming.

Similarly to MD software, there exist other options to perform DTF calculations such as VASP *[146]*, *[147]*, *[148]*, GAUSSIAN *[149]*, or Quantum ESPRESSO *[150]*, *[151]*. FHI-aims was chosen to perform the molecular optimizations needed due to the scalability to large systems without precision loses, which ensures that the calculation for large molecules is reliable, and the different levels of precision and functional available.

Chapter 3. Modification of the Li-salt chemistry

3.1. Introduction

We have highlighted the key role played by LIBs in today's society and emphasized the need for better battery performance in the near future (*Section 1.1*). To address these challenges, LMBs have emerged as a potential solution, raising hopes for powering the next generation of electric vehicles with improved driving range and faster charging times. A fundamental requirement for LMBs is the substitution of the liquid electrolytes used in LIBs with the safer polymer electrolytes, primarily due to the high reactive nature of the lithium metal anode (*Section 1.4*). Among various systems, the LiTFSI salt dissolved in a PEO matrix stands out as the most extensively studied, offering a well-established understanding of its advantages and disadvantages *[74]*, *[75]*, *[76]*, *[77]*, *[78]*, *[79]*.

Standard polymer electrolytes typically consist of three components: Li^+, an anion, and a polymer matrix. In our research, we have focused on LMBs, thus the presence of Li^+ is essential and cannot be altered. Therefore, we are left with only two elements to play with. In this Chapter, our attention is directed towards exploring chemical modifications of $TFSI^-$ structure while keeping PEO as the polymer matrix used for dissolving the modified lithium salt. The main challenges lie in preserving the minimal interaction between $TFSI^-$ and Li^+, while reducing the mobility of $TFSI^-$. The chemical and mechanical properties of PEO offer significant advantages for enhancing Li^+ mobility since it has the capability to completely dissolve the LiTFSI salt *[78]*. Consequently, our strategy here involves strengthening the interactions between anions or between the anions and PEO to hinder the anionic mobility.

We can find in the literature various avenues for exploring the design of new anions, employing diverse strategies aimed at impeding anion mobility *[152]*, *[153]*, as illustrated in *Figure 3-1*. These strategies offer promising directions for research and development as briefly overviewed in the following.

1) **Covalent bonding**: the anion is grafted onto an organic polymer with high molecular weight *[154]*, *[155]*, *[156]*, *[157]* or with inorganic nanosized particles *[158]*. Adding a junction point between the anion and a big heavy molecule limits the mobility of the anion, since it is no longer a free molecule. These techniques are able to increase Li TN to values close to unity, thanks to the great reduction of movement of the anion, but they may suffer from a decrease in the total conductivity that does not compensate for the high Li TN. These systems, on the other side, often yield great cycling stability when evaluated in cells.

2) **Lewis acid-base interaction**: the anion behaves as an electron donor (Lewis base) and is trapped by an electron acceptor (Lewis acid), creating a pair acid-base *[159]*, *[160]*. This interaction creates larger molecules with lower mobility. Since the mechanism is

similar to the covalent bonding, but with weaker interactions, it suffers from the same problem: Li TN is increased, although it does not reach values so close to unity, but the total conductivity is often too low.

3) **Hydrogen bonding**: the anion is trapped due to the creation of hydrogen bonds with the inserted molecules *[161]*, *[162]*. Similar to the other mechanisms, the idea is to enhance the interaction between the free anions and the anion acceptors, but in this case, via hydrogen bonds. Again, the balance between increasing Li TN and decreasing the total conductivity is present in this strategy.

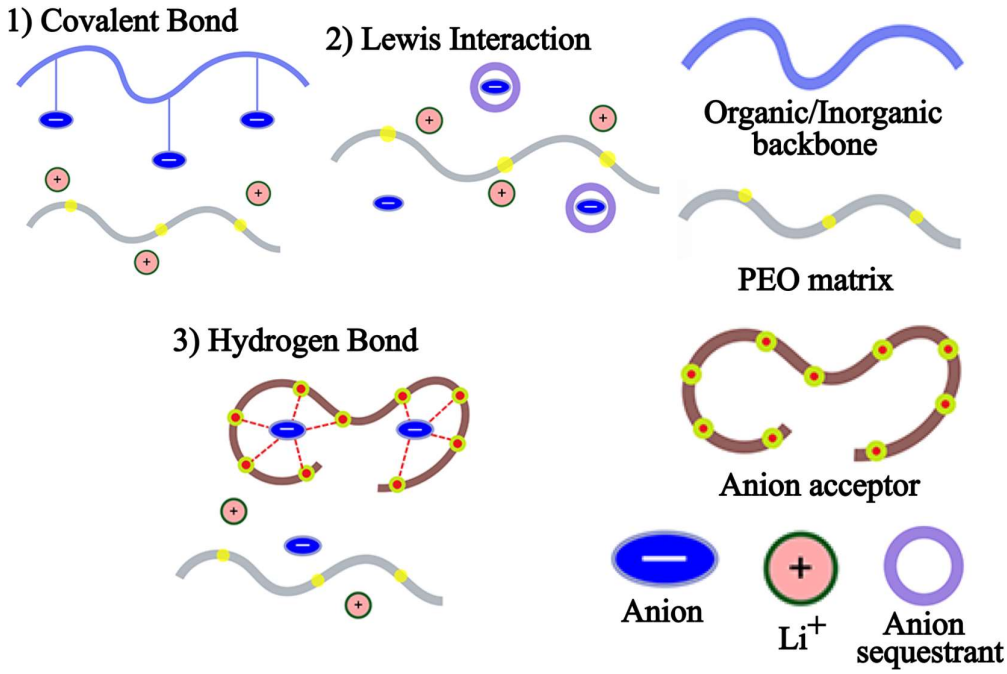

Figure 3-1: Schematic representation of different anion modification strategies to hinder anionic mobility in polymer electrolytes: 1) Covalent bonding, 2) Lewis acid-base interaction, 3) Hydrogen bonding. Adapted with permission from [174]. Copyright 2022 American Chemical Society.

All these strategies share one common aspect, they imply the addition of extra molecules inside the system. This may come with unwanted interactions that can difficult the mobility of Li^+. Besides, due to the diffusion mechanism of Li^+ when solvated by the PEO matrix *[78]*, any element that may hinder the mobility of the PEO, affects also to Li^+ transport.

To solve this challenge, modifying the chemical structure of the anion *[163]*, *[164]* came as a good solution. Taking as initial structure the paradigmatic $TFSI^-$, we have studied two different chemical modification approaches: benzenification and hydrogenation. In the benzenification (see *Section 3.2*), we replaced one of the $-CF_3$ groups of $TFSI^-$ by an aromatic ring. Specifically, we created two new molecules: benzenesulfonyl(trifluoromethanesulfonyl)imide, $BTSFI^-$, and (2, 4 ,6-triisopropylbenzenesulfonyl)(trifluoromethanesulfonyl)imide, $TPBTFSI^-$; with the idea

of creating a $\pi - \pi$ intermolecular interaction between the aromatic rings of two anions. In the hydrogenation (see *Section 3.3*), we replaced the -CF_3 groups of $TFSI^-$ by -CF_2H groups, obtaining bis(difluoromethanesulfonyl)imide, $DFSI^-$; with the idea of creating hydrogen bonds between the anions and PEO. The motivation of this substitution of fluorine by hydrogen also aimed at forming a more stable SEI as a result of the presence of H-containing compounds in the decomposition products that generate the SEI *[165]*.

3.2. Benzenification: from $TFSI^-$ to $BTFSI^-$ & $TPBTFSI^-$

3.2.1. Theoretical Background

The polymer matrix of PEO possesses a superior Li^+ solvation capacity that almost any other polymer, so the strategy of hindering the mobility of the anion forming the lithium salt dissolved in PEO becomes imperative to improve the low Li TN observed in the LiTFSI/PEO system *[8]*. Various strategies have been explored to achieve this goal, such as introducing different molecules into the system to interact with $TFSI^-$ and impede its diffusivity *[152]*, *[153]*. Alternatively, modifications to the chemistry of $TFSI^-$ have been considered to enhance interactions with the polymer *[164]*. However, these modifications may inadvertently create new interactions between the modified structure of $TFSI^-$ and PEO, consequently reducing the mobility of the PEO chains and even obstructing the paths of diffusion of Li^+ through the PEO chains.

The movement of Li^+ within the LiTFSI/PEO system is well-documented at low concentrations (with a ratio of [EO] monomer-Li^+ between 16-1 and 20-1), which are standard concentrations for studying this system *[76]*, *[78]*, *[79]*. In this regime, Li^+ becomes completely solvated by PEO and coordinates with 6 consecutive oxygen atoms (monomers) of the PEO, adopting a crown-like structure (see *Figure 3-2*).

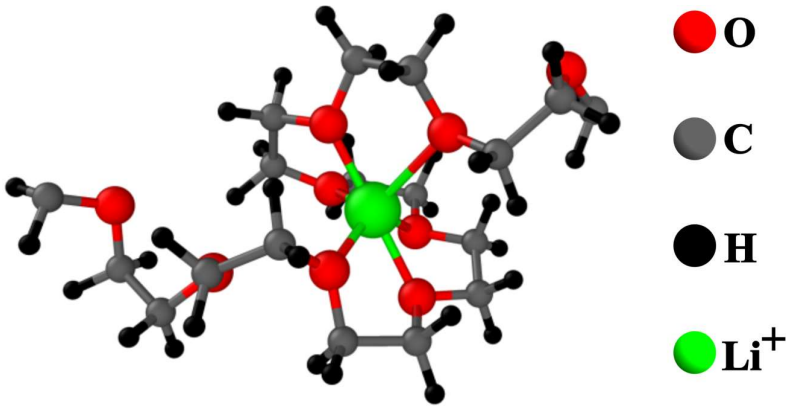

Figure 3-2: Representation of Li^+ coordination with 6 oxygen atoms from a PEO chain forming a crown-like structure.

During its movement, Li^+ jumps from one oxygen atom to another within the polymer chain and, occasionally, it also jumps between different chains *[166]*, *[167]*, *[168]*. This mechanism implies that, as Li^+ moves from one electrode to the other, it partially drags the PEO chains along with it. Thus, introducing additional interactions between PEO and the anion also hinders the mobility of Li^+, further affecting its transport properties within the system.

Our proposal for modifying the chemistry of $TFSI^-$ involves adding an aromatic ring to one end of the molecule, replacing the $-CF_3$ group. This substitution aims to introduce a different kind of interaction: $\pi - \pi$ stacking. This particular interaction is commonly found in various

materials used in fields like biochemistry and semiconductors *[169]*, *[170]*. Although it has been applied in batteries as electrode material *[171]*, *[172]* or binders *[173]*, its use in modifying anions has received limited attention.

Unlike hydrogen or covalent bonding, the $\pi - \pi$ interaction is relatively weak, making it suitable for our purpose. We are not seeking a strong connection between anions that might lead to cluster formation, as these clusters could hinder the movement of other elements within the system. Instead, the idea is to foster weak interactions between anions that can quickly form and break, merely slowing down their movement without impeding the overall system dynamics.

With these considerations in mind, we specifically designed two lithium salts: LiBTFSI and LiTPBTFSI (refer to *Figure 3-3* for the structures of these molecules). Our rationale behind this proposal was to preserve the low dissociation energy exhibited by the LiTFSI salt, which ensures complete salt dissociation when solvated in PEO, and create a new interaction between the added rings which hinders its movement.

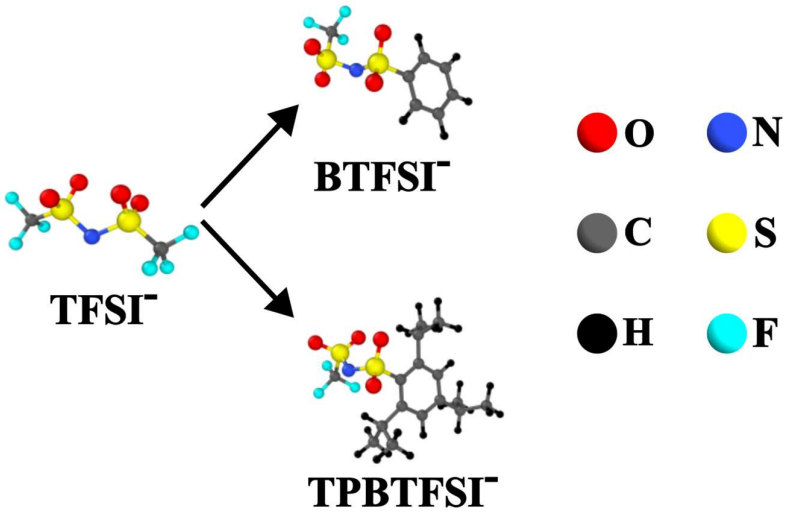

Figure 3-3: Structure of the newly proposed BTFSI⁻ and TPBTFSI⁻ compared with that of conventional TFSI⁻.

As a result, we maintained the sulfonamide structure of $TFSI^-$ in the new anions, which is the part of the molecule through which the coordination with Li^+ is produced. In the case of $BTFSI^-$, we introduced a simple benzene ring to investigate the pure $\pi - \pi$ interaction between aromatic rings. On the other hand, for $TPBTFSI^-$, we added isopropyl groups to the aromatic ring to observe their effect on the interaction dynamics. By examining these modifications, we aim to gain deeper insights into the impact of different structural elements on the $\pi - \pi$ stacking interactions within the LiTFSI/PEO system.

MD simulations were performed over the LiTFSI/PEO, LiBTFSI/PEO, and LiTPBTFSI/PEO systems following the procedure detailed on *Section 2.2.6*. In this study, the ratio [monomer]-Li^+ was 20-1 for the three systems (40 PEO chains of 20 monomers length and 40 Li-Anion

salts), the temperature selected to perform the simulations was 343 K (70 ºC) and the production simulation was 200 ns long. The structure of $TFSI^-$, $BTFSI^-$, and $TPBTFSI^-$ were optimized at DFT level and their partial atomic charges obtained with the ESP method (*Section 2.3.8*). These charges, as well as the FF parameters can be found on *Appendix A.2*.

It is important to highlight that the sought-after chemical effect of $\pi - \pi$ stacking, cannot be fully address by our computations due to the explained limitations of the FFs used in this study, as explained in *Section 2.2.2*. Specifically, $\pi - \pi$ stacking arises from the coupling between the π molecular orbitals of aromatic rings, resulting from induced polarization during their interaction. However, since the partial charges in the FFs are not variable, this effect cannot be effectively simulated. Nevertheless, we can examine another significant associated interaction at this level of theory: steric effects. Steric effects occur due to the spatial arrangement of the atoms, leading to energetically favorable geometric configurations. These effects have carefully been considered during the analysis of the theoretical results.

3.2.2. Theoretical Results

We started the analysis of the MD simulations by computing the MSDs of the ionic species (*Figure 3-4*). We can observe a decrease in the diffusivity of the benzene-based anions compared to that of $TFSI^-$, something expected due to the greater size of the anions, but that is also the desired effect. However, the most intriguing aspect emerges when we examine the trend followed by the anions. Surprisingly, $BTFSI^-$ shows lower mobility than $TPBTFSI^-$, despite $BTFSI^-$ being smaller and lighter. This intriguing finding suggests that the interanionic interactions between $BTFSIs^-$ might be stronger than those between $TPBTFSIs^-$.

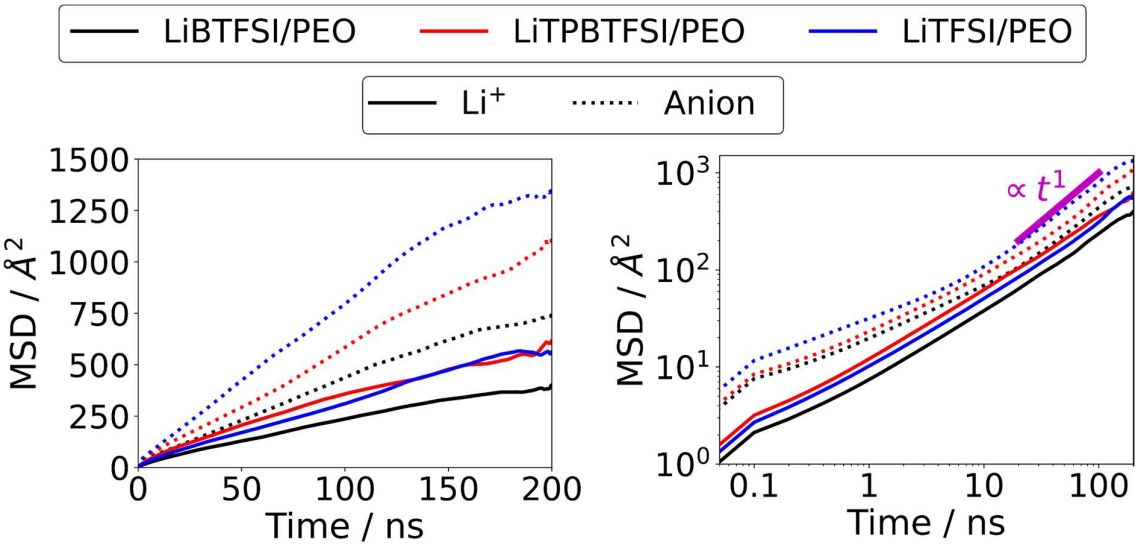

Figure 3-4: MSD of Li^+ (solid line) and anions (dotted lines) for LiBTFSI/PEO, LiTPBTFSI/PEO, and LiTFSI/PEO systems. The left panel displays the MSD in a linear scale, while the right panel shows the analysis in a logarithmic scale, with a reference line of slope equal to 1.

When looking at Li^+ mobility, we find that in the LiTPBTFSI/PEO system, it remains similar to the LiTFSI/PEO system, while a notable reduction is observed in the LiBTFSI/PEO system. Nevertheless, the reduction in Li^+ mobility is not so abrupt as the anion's, indicating a possible increment of Li TN in these new benzene-base systems compared to the LiTFSI/PEO.

Plotting the data in logarithmic scale allows the calculation of the diffusion coefficients and, from them, Li TN (*Eqs. 2.38*, *2.39*). Nevertheless, we observe that, compared with the reference line of slope equal to 1 (in the right panel of *Figure 3-4*), the MSD curves do not possess a clear slope equal to 1, especially in the case of Li^+. This means that these systems did not reach a proper diffusive regime, and thus the values of the diffusion coefficients and Li TN should be analyzed with care *(Table 3-1*). Nonetheless, we observe that Li TN is larger in both the LiBTFSI/PEO and LiTPBTFSI/PEO systems compared to the LiTFSI/PEO system.

D ($x10^{-7}$ cm^2/s)	LiBTFSI/PEO	LiTPBTFSI/PEO	LiTFSI/PEO
D_{Li^+}	0.401	0.558	0.523
D_{Anion}	0.720	0.992	1.405
Li TN	0.357	0.360	0.271

Table 3-1: Diffusion coefficients of the ionic species and Li TN for the investigated LiBTFSI/PEO, LiTPBTFSI/PEO, and LiTFSI/PEO polymer electrolyte systems.

We have observed that both $BTFSI^-$ and $TPBTFSI^-$ fulfill the objective of hindering the anionic mobility when compared to $TFSI^-$. Now, let us investigate whether this effect is primarily due to the introduction of aromatic rings or simply the result of their heavier molecular weight. The trends in the MSD analysis suggest that steric effects, if present, might be more pronounced in $BTFSI^-$ than in $TPBTFSI^-$. To assess whether structural changes in the anion influence the salt's solvability, we analyzed the RDF between Li^+ and the oxygen atoms of PEO and the anions (see *Figure 3-5*).

Our observations indicate that the coordination is quite similar in all three systems, with comparable coordination numbers. However, it is essential to note that the peak heights in the RDFs cannot be directly compared between different systems. For example, in the analysis of Li^+-O(PEO) interactions (left panel), we noticed a slightly higher peak in the LiTPBTFSI/PEO system than in the other two systems. While this might suggest stronger coordination, it can be attributed to an artifact due to how the RDFs are calculated. The RDFs are normalized by the average density of the observable molecule in the system (*Eq. 2.40*), and since $TPBTFSI^-$ is larger than the other anions, its simulation box is also larger than the other two systems. Considering that the coordination environment of Li^+ at short distances remains consistent, this normalization effect results in the seemingly higher peak in the LiTPBTFSI/PEO system, and

it does not necessarily imply a significant difference in coordination strength, as the similarity in the CN indicates.

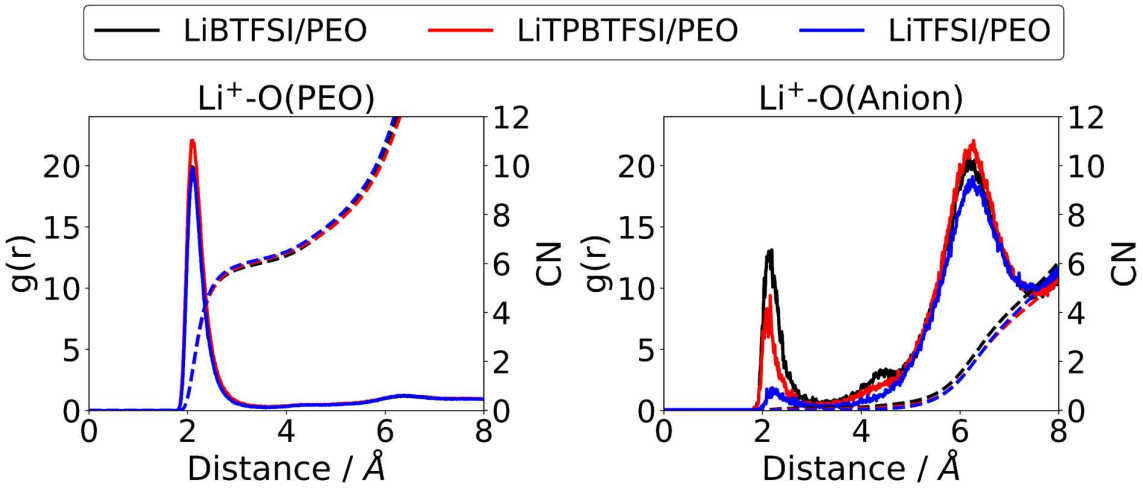

Figure 3-5: RDF (solid lines) and CN (dashed lines) analyses of the Li^+-O(PEO) (left panel) and Li^+-O(Anion) (right panel) interactions within the investigated LiBTFSI/PEO, LiTPBTFSI/PEO, and LiTFSI/PEO systems.

Analyzing now the Li^+-O(Anion) RDF (right panel), we observe that both $BTFSI^-$ and $TPBTFSI^-$ show a significant coordination peak at 2.2 Å, which is almost absent in the case of $TFSI^-$. However, these differences do not significantly affect the CN with Li^+, which remains nearly null even after this peak. Considering this observation, we may be dealing again with an effect more attributable to statistical variations rather than a fundamental difference in the behaviour of Li^+ coordination. While the presence of the coordination peak in $BTFSI^-$ and $TPBTFSI^-$ suggests some degree of interaction between Li^+ and the anions, the overall coordination environment around Li^+ remains consistent across the three systems.

It is important to notice that RDFs are focused only on individual interactions, so, from a dynamical viewpoint, we cannot know whether they occur at the same time or not. The results of *Figure 3-5* indicate that Li^+ mainly coordinates with PEO, but the coordination with the anions (especially in the case of $BTFSI^-$ and $TPBTFSI^-$) is not negligible. We might wonder: can these two interactions happen simultaneously? Or does the jump mechanism of Li^+ involve indeed some degree of coordination with the anion in addition to the surrounding oxygen atoms from PEO? Therefore, to delve deeper into the role of the Li^+-O(Anion) interactions, we analyzed the exact composition of the first coordination shell of Li^+ (*Figure 3-6*). To do so, we take all the snapshots of the simulation and check all Li^+ to identify to which molecules they coordinate with. To this end, we applied a cutoff of 3.25 Å, as this is the first minimum of the Li^+-O(PEO) and Li^+-O(Anion) RDFs. More information about this analysis can be found on *Appendix A.1*. We found that in over 95 % of cases, Li^+ primarily coordinates with PEO, while the coordination with the anions happens, in most of the cases, in the presence of PEO as well. However, some differences emerge when comparing the coordination behavior with different anions, shedding light on the variation in the height of the Li^+-O(Anion) peaks in *Figure 3-5*.

In the LiBTFSI/PEO system, we notice a slightly higher occurrence of Li^+-Anion-PEO and Li^+-Anion coordination, although in relative percental terms the differences remain quite low across all cases.

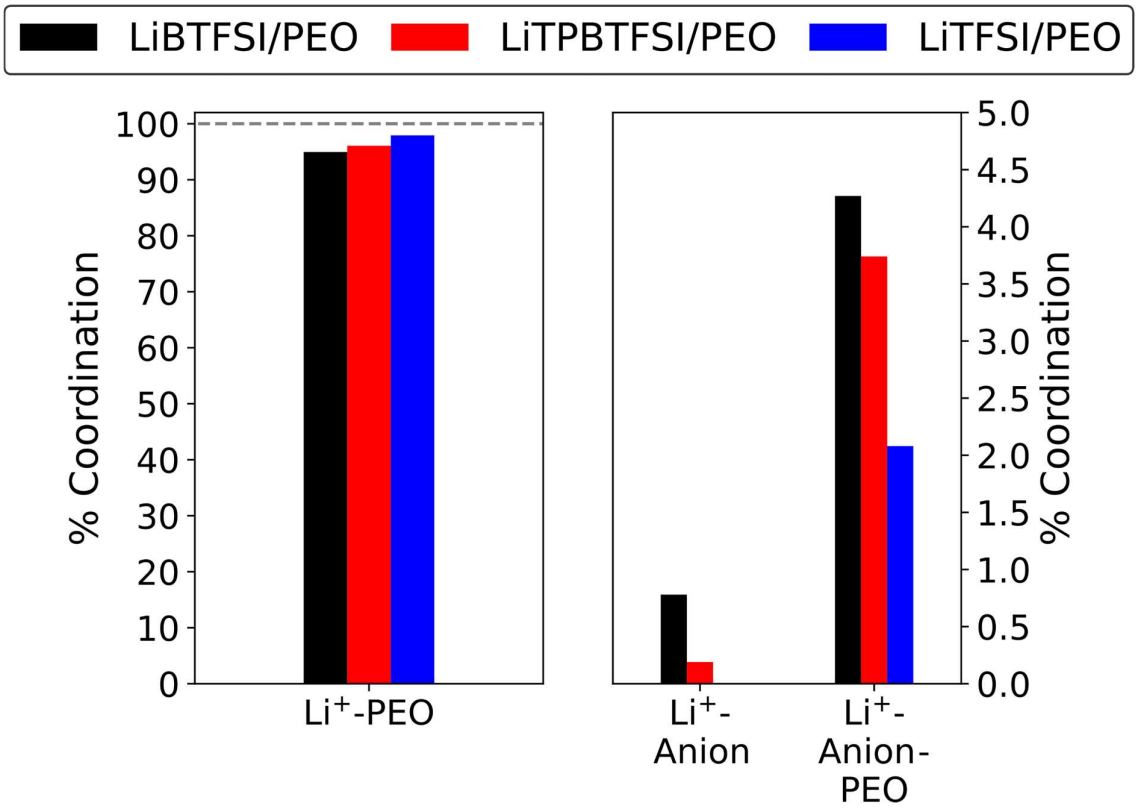

Figure 3-6: Percentage composition of the first solvation shell of Li^+ for the three investigated systems (LiBTFSI/PEO in black, LiTPBTFSI/PEO in red, and LiTFSI/PEO in blue).

Overall, we can conclude that while PEO plays a prominent role in facilitating Li^+ coordination with the anions, the specific characteristics of each anion lead to subtle variations in their interaction. Although the differences in coordination are present, they are limited in terms of the overall coordination environment. Our results indicate indeed that LiBTFSI and LiTPBTFSI salts exhibit less favorable dissolution compared to LiTFSI. However, a more in-depth analysis may provide insights to explain these differences.

To this end, in *Figure 3-7* we show representative examples of the variation in the coordination environment of some Li^+ instances, keeping a cutoff of 3.25 Å. Before delving into the analysis, let us explain how to interpret these types of analyses. The plots display the coordination points of a single Li^+ throughout the entire simulation time, categorized by molecule type. In the case of the anions (upper part shown with black points), the specific manner in which Li^+ coordinates with them are not of primary relevance. Whether the coordination involves one oxygen atom or all four simultaneously, we focus solely on whether Li^+ coordinates with the anion or not. The different anion indexes are used to indicate the number of different molecules

that enter Li^+'s coordination environment. They also help identify if the same molecule re-enters the coordination shell later in the simulation or if it is a new one. The horizontal dashed lines separate different anion molecules. In the lower part of the plot, a similar representation is provided for Li^+'s coordination with PEO. However, since understanding the precise coordination is crucial, we show the coordination with the individual oxygen atoms (monomers), and the dashed lines separate different PEO chains. This way, we can observe how Li^+ moves through the monomers of the PEO chain. Further explanations and the functioning of the Python code used for these analyses can be found on *Appendix A.1*.

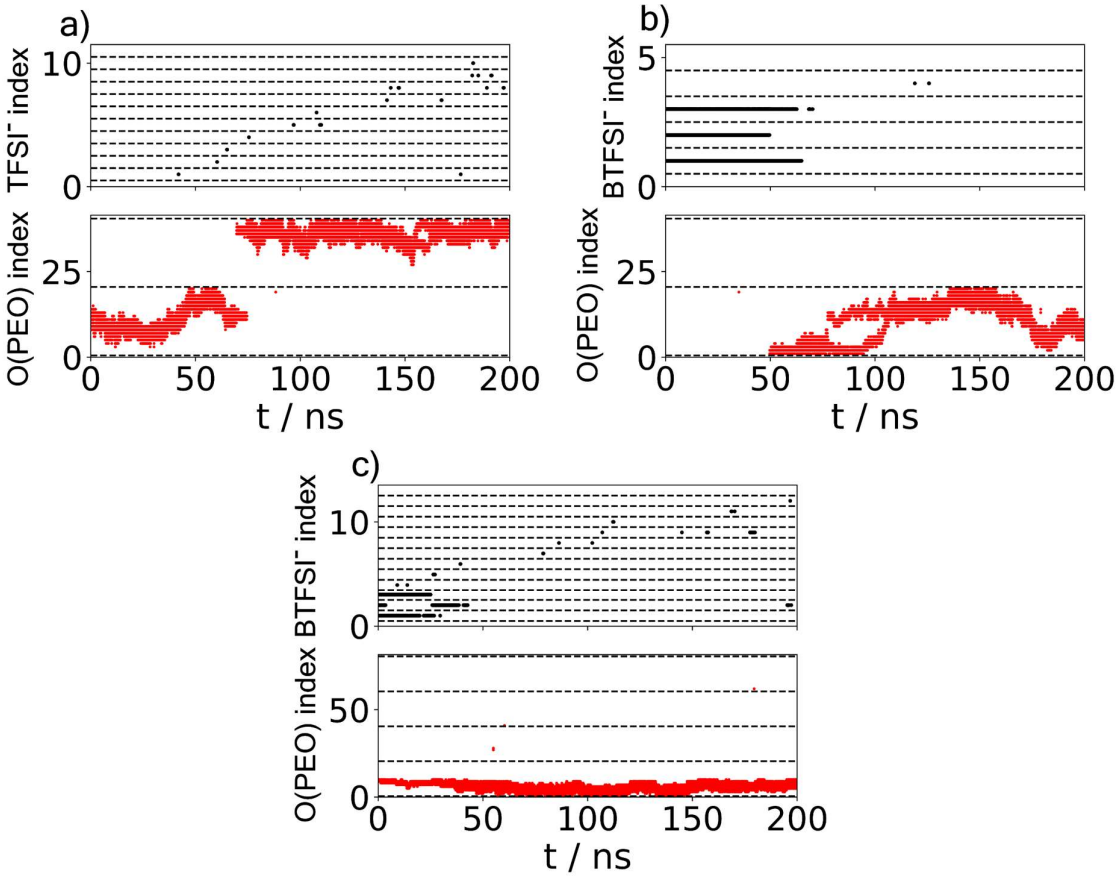

Figure 3-7: Three representative examples of Li^+ diffusion through LiTFSI/PEO and LiBTFSI/PEO systems, differentiating between the coordination with different anions (top panels) and with different oxygen atoms of different PEO chains (bottom panels).

In the LiTFSI/PEO system, shown in the a) panel, Li^+ moves nearly free along the PEO chain, where interchain jumps can eventually happen. During the whole simulation, some $TFSIs^-$ enter in the coordination shell, but their interactions are of very short duration. They just randomly find a space between the PEO monomers to interact with Li^+, but rapidly the PEO closes this space and expels $TFSI^-$.

Moving now to the LiBTFSI/PEO system, most of Li^+ presents a similar behaviour as the shown in the a) panel for LiTFSI/PEO. However, we found one case in which Li^+ coordinates

only with $BTFSI^-$ during the first part of the simulation, but later it presents the typical LiTFSI/PEO behaviour. This case is shown in the b) panel of *Figure 3-7*, and it alone explains the percentage of Li^+-$BTFSI^-$ interaction displayed in *Figure 3-6*[1]. This percentage is not due to a stronger interaction between Li^+ and $BTFSI^-$ compared to $TFSI^-$. Rather, it is a consequence of a single ion pair that remained undissolved during the optimization process and presents a coordination with three different $BTFSIs^-$ that lasts around 50 ns in the simulation. However, as soon as PEO enters the coordination, it takes precedence, and the influence of $BTFSI^-$ diminishes in Li^+'s diffusion mechanism.

A similar trend is shown in the c) panel of *Figure 3-7*, but this time illustrating the Li^+-$BTFSI^-$-PEO interaction for an alternative Li^+. Again, at the beginning of the simulation we observe a coordination behaviour that only lasts a few nanoseconds, followed by a dynamic that resembles that of the LiTFSI/PEO system. While this sole example does not explain the entire percentage of Li^+-$BTFSI^-$-PEO coordination, as it does the b) panel example, when combined with more similar cases, we can achieve the numbers presented in *Figure 3-6*. Additionally, there are isolated cases that also contribute to this type of interaction. The examples shown in the b) and c) panels in *Figure 3-7* illustrate cases corresponding to the LiBTFSI/PEO system, but something similar could be shown for the LiTPBTFSI/PEO system, explaining the results seen in *Figure 3-6*.

These examples show how the variation in coordination observed between the LiTFSI/PEO system and the LiBTFSI/PEO and LiTPBTFSI/PEO systems, as shown in the RDFs (*Figure 3-5*) and in the composition of the first coordination shell of Li^+ (*Figure 3-6*), can be attributed to incomplete salt dissociation during the optimization step in our simulation workflow. The suboptimal optimization failed to induce the complete dissociation of salts that PEO typically achieves in these systems. Therefore, these discrepancies should be viewed with caution when comparing these salts. Nevertheless, the reduction in anion mobility remains evident, indicating that the interactions with PEO do affect the anion dynamics. Consequently, we proceeded to further analyze the interactions between the anions.

To study the distribution of the anions over the simulation box, we studied the RDF between them, focusing on the distance between center of masses (CoM). These RDF do not show any significative difference between the three anions (left panel of *Figure 3-8*). The small difference between $TFSI^-$ and the other two anions can be attributed to the different geometry of the anions, so we can suppose that their spatial distribution in the simulation box is similar. However, when analyzing the RDF between center of rings (CoR) of the benzene anions (right panel), we observe the apparition of a coordination peak for them both. These two RDFs indicate that the interaction is not very strong, yet it induces an orientation of the anions to match the position of the aromatic ring. The peak is narrower and appears at a shorter distance in $BTFSI^-$ than in $TPBTFSI^-$. This can be easily understood by the presence of the isopropyl groups in $TPBTFSI^-$, which hinder the efficient interaction between the aromatic rings.

[1] 1 of the 40 Li^+ during approx. 50 of the 200 ns: $\left(\frac{1}{40}\right).\left(\frac{1}{4}\right) x\ 100 = 0.625\ \%$

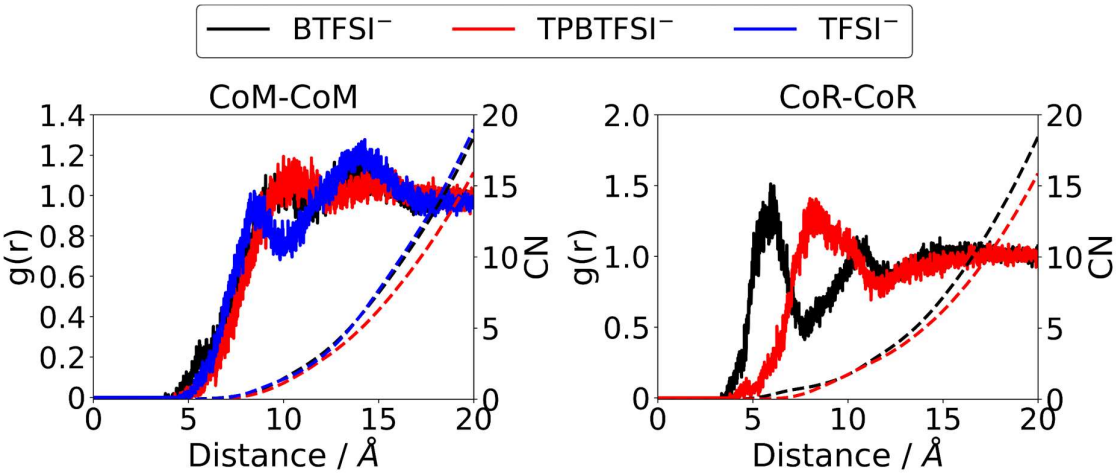

Figure 3-8: RDF (solid lines) and CN (dashed lines) analyses of the anionic interaction considering the distance between CoMs (left panel) and CoRs (right panel), as defined in the main text.

To gain further insights into the interaction of the benzene part of $BTFSI^-$ and $TPBTFSI^-$, we analyzed the orientation of the rings. To do so, we define two vectors (see *Figure 3-9*).

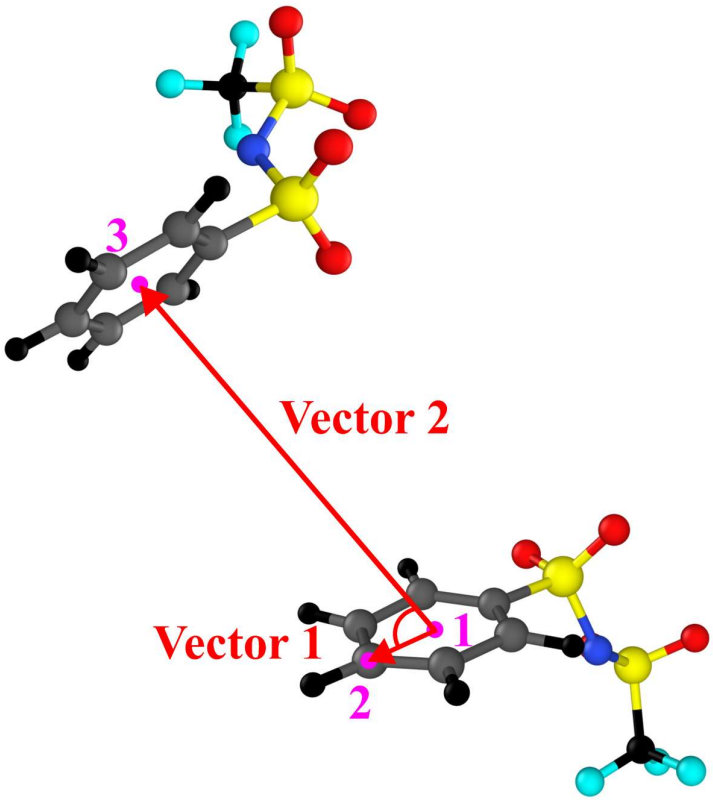

Figure 3-9: Scheme of vectors 1 and 2 between two $BTFSI^-$ molecules, as defined in the main text.

- **Vector 1**: This vector connects the CoR of the reference molecule (point 1) with the carbon atom opposite to the one bonded with the sulfur atom within the same reference molecule (point 2).

- **Vector 2**: This vector connects the CoR of the reference molecule (point 1) with the CoR of the observed molecule (point 3).

By measuring the angle formed between these two vectors, we can determine the relative orientation of the rings. This analysis provides valuable information on how the benzene rings of $BTFSIs^-$ and $TPBTFSIs^-$ interact between them, giving us a clearer picture of their spatial arrangement and potential bonding patterns.

This analysis, combined with the RDF between CoR, allows us to study the spatial configuration of the interaction between the rings. With the combined distribution function (CDF) tool implemented in TRAVIS, we can study the occurrence of these two analyses combined (*Figure 3-10*).

Interestingly we found that the peak observed in the RDF between CoR, for both $BTFSI^-$ and $TPBTFSI^-$, is actually composed of two different configurations in both systems. In the lower part of *Figure 3-10* it is shown the correlation function of the above plots. This analysis helps us to identify if the big occurrence regions are indeed correlated or if they are an artifact of the combinations of two different analyses which might not necessarily be correlated. They confirmed that the regions of high occurrence shown in the CDFs indicate a real effect. In $BTFSI^-$, these two configurations are located at 5 Å and 90º (point A) and 6 Å and 30º (point B). In $TPBTFSI^-$, the two configurations are located at 7.5 Å and 75º (point C) and 10.5 Å and 15º (point D).

The correlation functions also show how the two dominant regions are quite isolated and not joined by a bridge of high occurrence. This indicates that the systems do not move from one configuration to the other, or, at least, in case this happens, it is a quick movement relative to the times the systems stay in the dominant configurations.

The different width of the RDF peaks is also observable in the high occurrence regions, indicating that the interaction between $BTFSIs^-$ is much more concentrated than between $TPBTFSIs^-$. This difference is due to the isopropyl groups added to $TPBTFSI^-$, which difficult the interaction and spread it over more extent conformations.

Focusing on $BTFSI^-$, *Figure 3-11* depicts an example of the coordination between two molecules for points A and B. At point A, we observe an alignment of the aromatic rings, with one above the other, resembling the geometry expected in $\pi - \pi$ stacking. Although, as explained earlier, pure $\pi - \pi$ stacking interactions cannot be directly simulated within our computational framework, we do see how simply the Coulombic interactions give rise to such structures due to steric effects. The arrangement of the rings in this manner is a result of their spatial configurations and highlights the importance of steric effects in influencing the intermolecular interactions in our system.

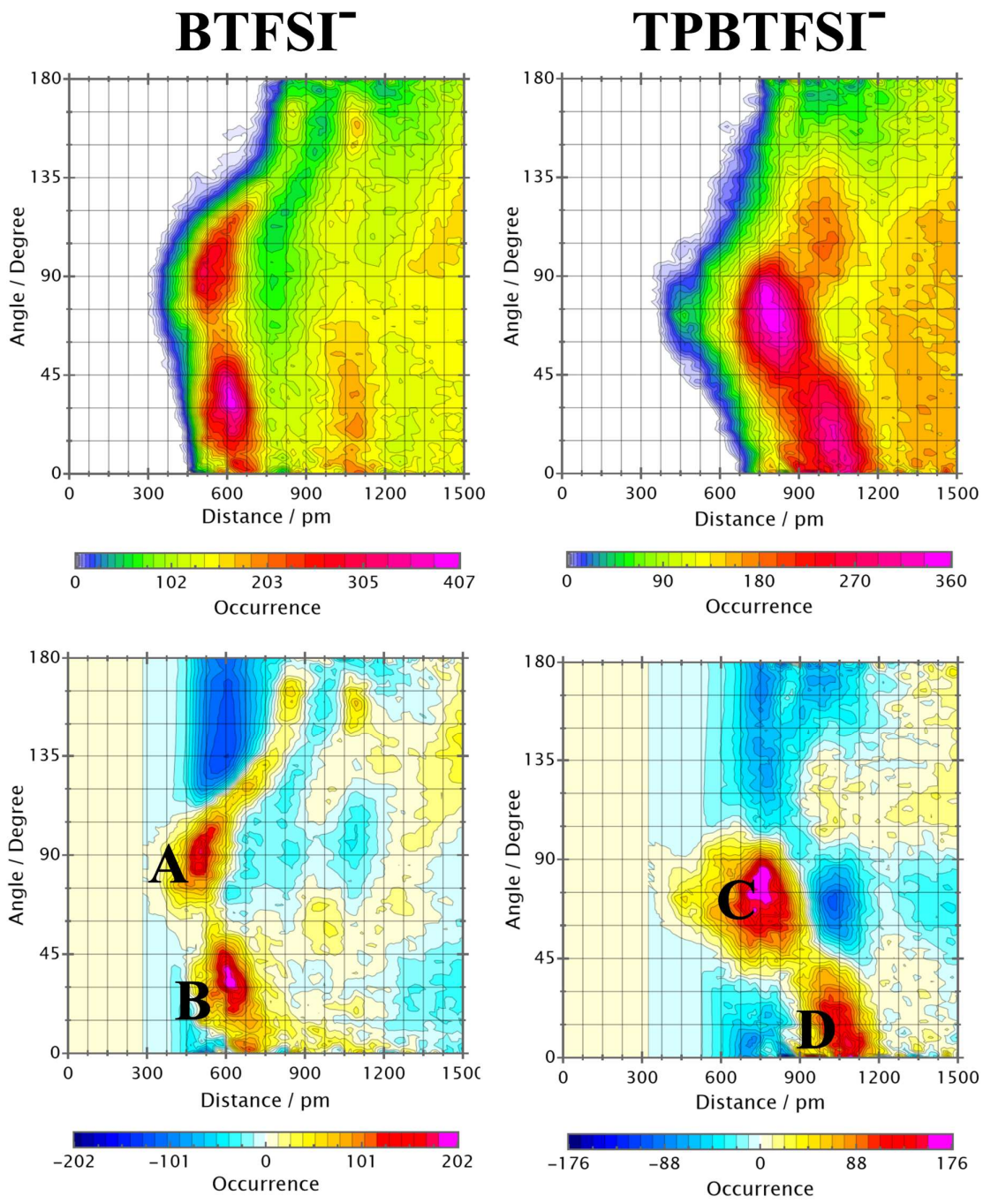

Figure 3-10: (Left panels) Combined distribution functions of BTFSI⁻ of the distance and angle between the CoRs, in the upper part, with the corresponding correlation function, in the lower part. (Right panels) Same analysis for TPBTFSI⁻.

Point B depicts the other preferential interaction, of slightly higher intensity than point A. However, the higher interaction distance and the angle formed can explain this higher occurrence. These analyses are symmetric with respect to the plane formed by the reference ring. So, configuration A can occur with the observable ring above the reference or below it

and transitioning from one configuration to the other is not possible. Point B configuration can more easily move from being above the plane of the reference ring to being below it. In fact, this region possesses higher occurrences in the correlation plot than between points A and B.

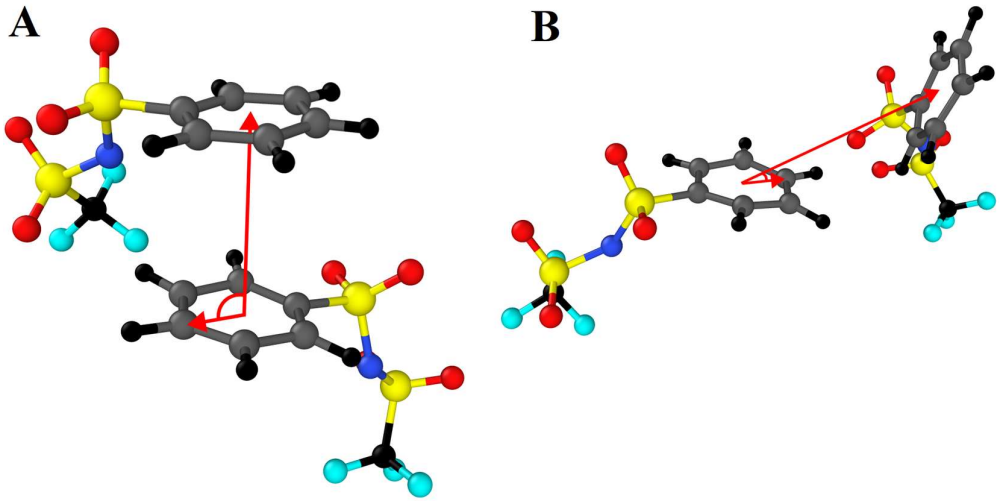

Figure 3-11: Representative examples of the BTFSI$^-$-BTFSI$^-$ interaction of the A and B geometries indicated in Figure 3-10.

In the case of points C and D for TPBTFSI$^-$, no examples are shown, but similar configurations to points A and B can be expected. But at longer distances and at the relative angles shown in *Figure 3-10*. In this case, point C possesses a higher occurrence than point D.

3.2.3. Experimental Validation

Thanks to valuable collaboration with experimental groups, we were able to corroborate the theoretical results obtained in this study with their analyses conducted on real systems. While these analyses were not performed by the doctorand, the results provided crucial insights to validate and enhance our theoretical findings. As a testament to the significance of these results, we have included them in this Thesis to demonstrate the practical applicability of our new polymer electrolyte systems, which have been thoroughly tested in the laboratory. In the following, we present an overview of the main results and findings, which have also been published in collaboration with our experimental colleagues in a joint research paper *[174]*. It is also important to remark that the theoretical analyses exposed in this Thesis go beyond what was covered in the joint publication. The publication had constrained related to space limitations, and certain analytical techniques were performed after the work was published. All the following images have been reprinted or adapted with permission from [174]. Copyright 2022 American Chemical Society.

Starting with the measure of the mobility properties (*Figure 3-12*), we obtained a reduction in the total ionic conductivity for the LiBTFSI/PEO and LiTPBTFSI/PEO systems, similar to the

theoretical MSD results (*Figure 3-4*), but here the conductivity in the LiTPBTFSI/PEO system is lower than in the LiBTFSI/PEO.

However, the computed Li TN in the LiBTFSI/PEO system resulted in a larger value compared to the LiTPBTFSI/PEO. Although a direct comparison between theoretical and experimental results is very complicated due to the approximations used in the simulations and the limitation both in time and size scales, both sets of results consistently demonstrate a reduction in ionic mobility compared to LiTFSI/PEO and an increase in Li TN. Notably, the experimental Li TN values are significantly larger than the theoretical values and exceed those observed in any other sulfonimide system. This observation suggests that the effect of $\pi - \pi$ stacking plays a crucial role in producing the expected results we sought.

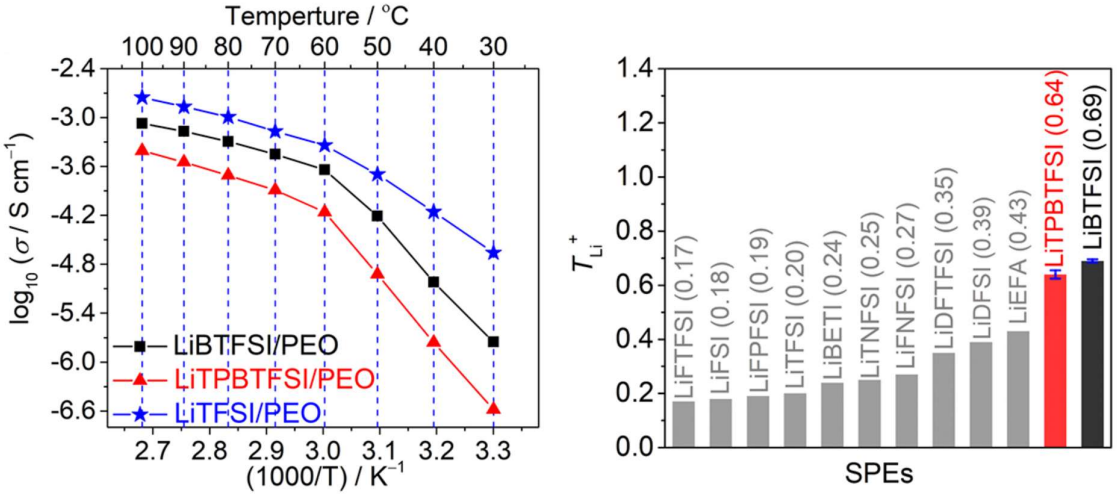

*Figure 3-12: (Left) Arrhenius plots of the total ionic conductivities at different temperatures for the three systems analyzed (LiBTFSI/PEO in black, LiTPBTFSI/PEO in red, and LiTFSI/PEO in blue). (Right) Li TN for different lithium sulfonimide salts in PEO, as compared with other relevant lithium salts reported in the literature [164], [175], [176], [177], [*163*].*

To confirm that the spatial configurations obtained in the simulations are a good representation of the experiments, X-ray diffraction (XRD), Raman spectroscopy, and ultraviolet-visible spectroscopy (UV-vis) analyses were performed (*Figure 3-13*). PEO possesses two characteristic diffraction peaks in XRD patterns: at 19.36º and 23.72º. The shifting of these peaks to lower angles when the salts are introduced (19.10º and 23.50º in LiBTFSI/PEO; 19.13º and 23.61º in LiTPBTFSI/PEO; and 19.09º and 23.41º in LiTFSI/PEO) indicates the coordination between Li^+ and oxygen atoms of PEO (a) panel). Besides, the absence of other peaks in the spectra suggests that the salts are completely dissociated. These results confirm the coordination environment of Li^+ observed in the MD simulations (*Figure 3-5*).

Additionally, in the Raman spectra (b) panel), we observed the characteristic peak at approx. 750 cm^{-1} of the S-N-S bending vibration. The shift in the position of the peak is lower in the LiBTFSI/PEO and LiTPBTFSI/PEO systems compared to LiTFSI/PEO, suggesting the presence of additional interactions between the anions. To gain more information about these

interactions, UV-vis spectroscopy was performed, at different concentrations, with the salts solvated in 1,2-dimethoxyethane (DME) (c)-e) panels). DME is a chemical analogue of PEO with similar solvating ability of Li^+. The red-shift observed in the absorption edge in the LiBTFSI/DME and LiTPBTFSI/DME systems, while increasing concentration, which does not appear in the LiTFSI/DME, is a clear evidence of $\pi - \pi$ stacking, in agreement with previous studies *[178]*, *[179]*, *[180]*, *[181]*. Again, all these experimental observations confirm the results of the MD simulations (*Figure 3-10*).

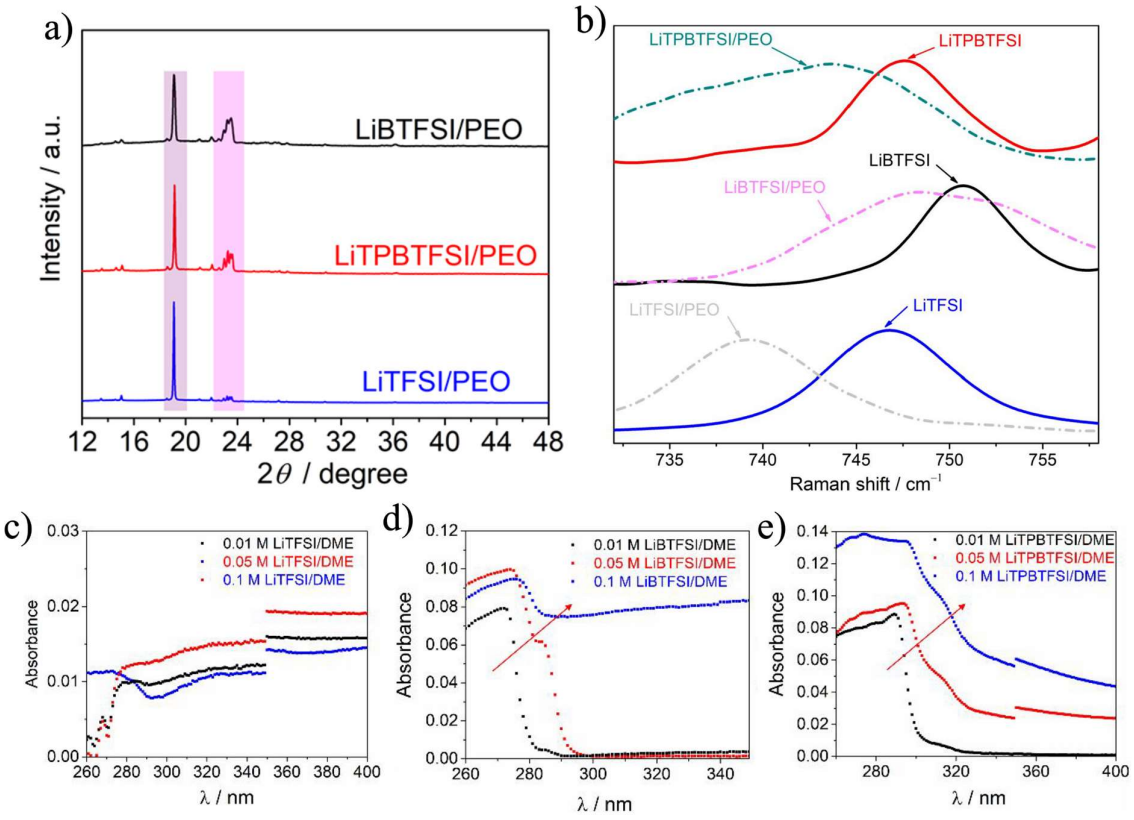

Figure 3-13: a) X-Ray patterns for LiBTFSI/PEO, LiTPBTFSI/PEO, and LiTFSI/PEO systems. b) Raman spectra of the neat salts (solid lines) and the corresponding solvent-free PEO-based electrolytes (dashed lines). (c-e) Ultraviolet-visible spectra of the liquid solutions in DME for c) LiTFSI/DME, d) LiBTFSI/DME, and e) LiTPBTFSI/DME.

After confirming that the mobility properties and coordination environment of Li^+ and anionic interactions in the systems align with MD simulations, we move now to the analysis of the electrochemical stability of the new benzene-based systems and its potential as effective polymer electrolytes in LMBs. First, we focused on the stability of the salts by performing Linear Sweep Voltammetry (LSV) analysis (*Figure 3-14*). The neat salts were dissolved in propylene carbonate (PC), and it was observed that the high stability of the LiTFSI/PC (5.9 V *vs* Li^+/Li) is preserved in LiBTFSI/PC (5.8 V *vs* Li^+/Li) (left panel). Despite a reduction in the LiTPBTFSI/PC system (5.0 V *vs* Li^+/Li), it remains significantly stable. Importantly, all three systems exceed the working voltages of typical LIBs (4 V *vs* Li^+/Li *[182]*), indicating that the

introduction of the aromatic rings has negligible impact on the electrochemical stability of the anions. The reduction observed in the LiTPBTFSI/PC system could be ascribed to the isopropyl groups and their strong electron-donating character. Furthermore, when these salts are dissolved in PEO (right panel), LSV was also used to confirm that all three systems remain stable and are thus suitable for < 4 V solid state LMBs.

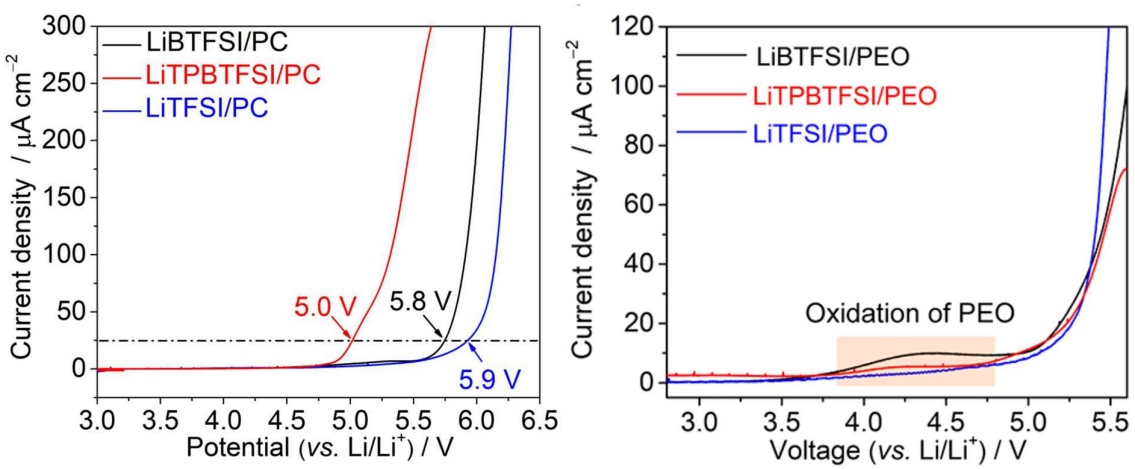

Figure 3-14: (Left) Linear sweep voltammetry profiles of the salts dissolved in PC. (Right) Linear sweep voltammetry profiles of the salts dissolved in PEO.

After having demonstrated the electrochemical stability of the polymer electrolyte systems, we assembled two different cells: a symmetric $Li^0||Li^0$ cell and a $Li^0||LiFePO_4$ (LFP) cell. This helped us to evaluate whether the stability shown in the previous analysis is maintained in real cells when the electrolyte is exposed to repeated cycles of charge and discharge.

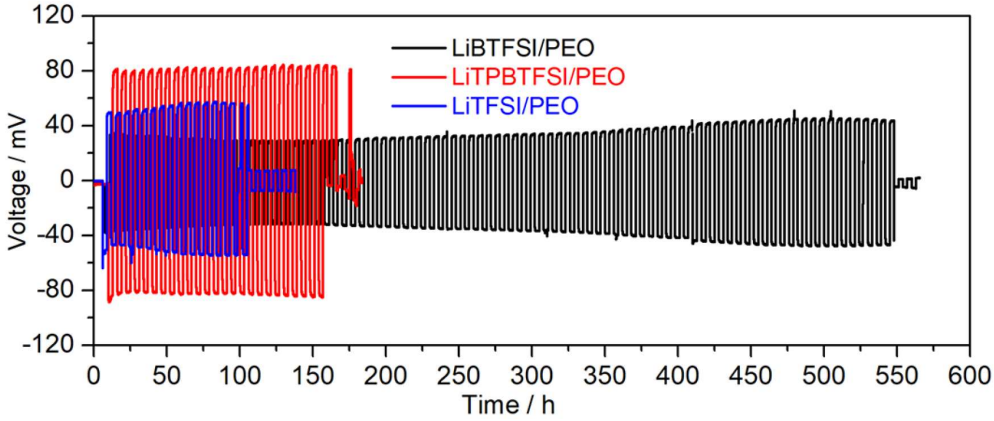

Figure 3-15: Galvanostatic cycling of symmetric $Li^0||Li^0$ cells for the three systems.

We found that the cyclability in the $Li^0||Li^0$ cell (*Figure 3-15*), at a current density of 0.1 mA/cm^{-2} with a duration of 3 h for a half-cycle, shows a superior cycle life for the

LiBTFSI/PEO system compared to the other two. LiTFSI/PEO encounters a short-circuit after ~100 hours, probably due to the growth of Li^0 dendrites that cause fatal failure *[62]*, *[63]*, *[64]*. LiTPBTFSI/PEO short-circuits after 160 h, but showing the highest overpotential of the three systems, due to its lower conductivity (*Figure 3-12*). Overall, LiBTFSI/PEO shows a great cyclability, suggesting the formation of a more stable SEI.

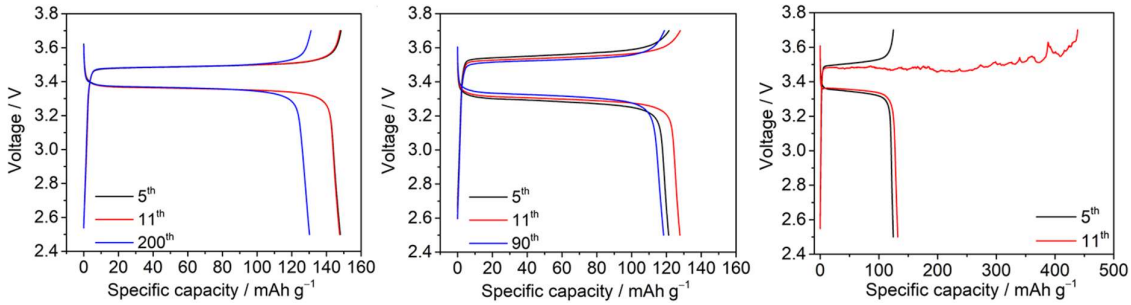

Figure 3-16: Discharge/charge profiles of the Li^0||$LiFePO_4$ (LFP) in the LiBTFSI/PEO (left), LiTPBTFSI/PEO (center), and LiTFSI/PEO (right) systems.

Similar observations were made in the Li^0||LFP cell (*Figure 3-16*). The cells underwent three formation cycles at a C-rate of C/5 and were subsequently charged and discharged with a constant C-rate of C/3 for continuous cycling in the voltage range of 2.5−3.7 V. Notably, the LiBTFSI/PEO system demonstrated superior performance, exhibiting a higher initial capacity (151.1 mAh g^{-1}) compared to 112.6 mAh g^{-1} and 113.7 mAh g^{-1} in LiTPBTFSI/PEO and LiTFSI/PEO, respectively. Furthermore, the LiBTFSI/PEO system also demonstrated excellent capacity retention throughout the cycling process.

3.2.4. Conclusion

Our comprehensive analyses have provided compelling evidence to support the initial design concept behind $BTFSI^-$ and $TPBTFSI^-$ molecules, where the substitution of one -CF_3 group of $TFSI^-$ with an aromatic ring was intended to induce specific geometric alignments that hinder the diffusion of the anions. The idea has been successfully validated. Both experimental and theoretical analyses concur in describing the coordination environment of the ionic species, showing that the complete salt dissociation of the LiTFSI in PEO is maintained upon the insertion of aromatic rings. Besides, both approaches show the appearance of an anion-anion interaction facilitated by the aromatic rings, attributable to the sought-after $\pi - \pi$ stacking interaction. It is worth noting that in the MD simulations, this interaction arises solely from steric effects, not genuine $\pi - \pi$ stacking.

The outcome of these interactions is a reduction in the mobility of the ionic species, resulting in a lower conductivity. However, this reduction is more pronounced in the anions compared to Li^+, producing an increase in the Li TN. Theoretical predictions indicate a modest 33 % increment in Li TN, but in experiments, it has been observed to reach up to 300%, multiplying

the value of Li TN by three, while only experiencing a minor reduction in the total ionic conductivity. As a result, the LiBTFSI/PEO and LiTPBTFSI/PEO systems stand out as great candidates within the sulfonamide family of molecules.

Furthermore, experimental investigation into the electrochemical stability of these systems demonstrated their potential application in LMBs, addressing certain challenges faced by the LiTFSI/PEO system. Specifically, the LiBTFSI/PEO system exhibits delayed occurrence of fatal failures that lead to short-circuits in the LiTFSI/PEO system, effectively extending the cycle life of the cells.

3.3. Hydrogenation: form $TFSI^-$ to $DFSI^-$

3.3.1. Theoretical Background

Previous studies have demonstrated that the substitution of only one of the $-CF_3$ groups of $TFSI^-$ by $-CF_2H$, forming (difluoromethanesulfonyl)(trifluoromethanesulfonyl) imide ($DFTFSI^-$) improves Li^+ conductivity due to hydrogen bonding with the PEO. Besides, an increment in the stability of the polymer electrolyte is observed in the contact with the Li^0 electrode due to the formation of a more stable SEI. This is due to the presence of compounds like LiH and LiF in the SEI *[165]*, *[176]*, *[183]*.

$-CF_3$ groups are difficult to degrade by chemical and biological methods *[184]*, *[185]*. Thus, the molecules that contain them cannot be considered environmentally friendly. Fortunately, the $-CF_2H$ groups exhibit significantly heightened degradability *[186]*, in addition to the reduction in the content of fluorine. This higher degradability reduces the time this group remains in nature before disappearing. Focusing on battery applications, its lower stability fosters the formation of stabilizing LiF and LiH compounds within the SEI. Based on this premise, we conceptualized a notion involving the hydrogenation of both $-CF_3$ groups, and by substituting one fluorine atom in each group with hydrogen, the novel bis(difluoromethanesulfonyl)amide, referred to as $DFSI^-$, can be envisaged (*Figure 3-17*).

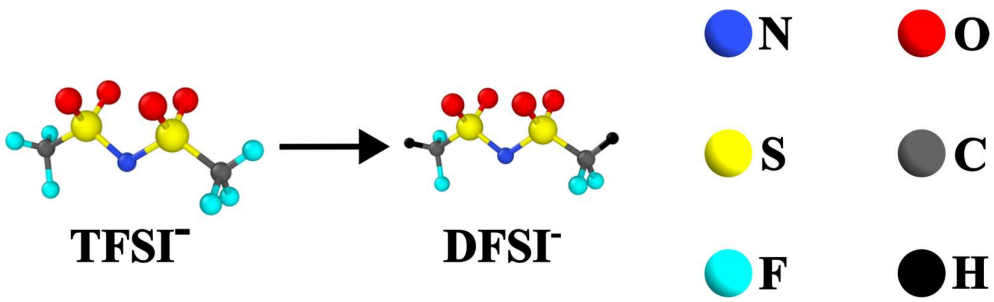

Figure 3-17: Structure of $TFSI^-$ and $DFSI^-$ molecules.

The central aim of this study is to juxtapose the performance of the LiDFSI/PEO system against the established LiTFSI/PEO counterpart. Should the behaviour observed in the LiDFTFSI/PEO system be replicated in the LiDFSI/PEO system, the outcome may yield an environmentally friendly compound, which could even possess amplified ionic conductivity and superior electrochemical stability, as depicted in *Figure 3-18*.

Like the investigation conducted on the LiBTFSI/PEO and LiTPBTFSI/PEO systems in previous section, we performed a comparative analysis by juxtaposing the outcomes derived from theoretical MD simulations with the experimental findings acquired through collaborative efforts with our laboratory partners.

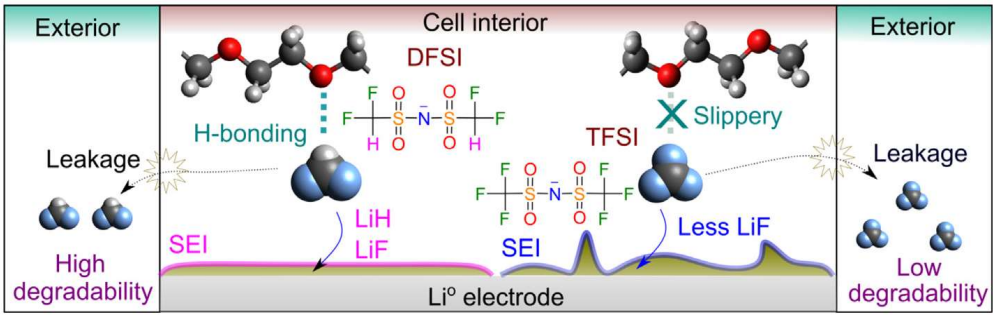

Figure 3-18: Summary of the expected behaviour of LiDFSI vs LiTFSI.

MD simulations were performed over the LiTFSI/PEO and LiDFSI/PEO systems according to the details explained on *Section 2.2.6*. The conditions chosen for this study are similar to the previous study, with a ratio [monomer]-Li^+ of 20-1 (with 40 PEO chains of 20 monomer length each and 40 Li-Anion salts), and a simulation temperature of 343 K (70 ºC) during 200 ns of duration. The structure of both $TFSI^-$ and $DFSI^-$ were optimized at DFT level and their partial atomic charges calculated with the ESP method (*Section 2.3.8*). These charges, as well as the FF parameters of all molecules can be found on *Appendix A.2*.

3.3.2. Theoretical Results

We started the theoretical analysis by examining whether the LiDFSI salt retains the crucial property observed in LiTFSI—complete dissociation upon dissolution in PEO. This distinctive trait underpins the relatively high ionic conductivities exhibited by the LiTFSI/PEO system, making its preservation in the LiDFSI/PEO counterpart highly desirable. However, the introduced hydrogenation in $DFSI^-$ leads to less efficient delocalization of the negative charge throughout the molecule, resulting in an increase in the dissociation energy of the salt *[176]*. Consequently, there emerges the potential for a less than ideal dissociation of the LiDFSI salt within the PEO matrix. Furthermore, the interaction of Li^+ with $DFSI^-$ could potentially engender undesired coordination environments, leading to a general reduction in ionic mobility.

To investigate this, we delved into the computation of RDFs between Li^+ and both the oxygen atoms of PEO and the anions (*Figure 3-19*). Notably, the analysis of the plotted RDFs undoubtedly demonstrated that the dissociation of the LiDFSI salt within PEO occurs analogously to that of LiTFSI. The RDFs show no discernible difference between the two systems, showcasing identical CN of 6 with PEO (yielding the expected crown structure shown *Figure 3-2*) and a CN of nullity with the anions. Thus, the behaviour of Li^+ is expected to be independent of the anion in these two systems.

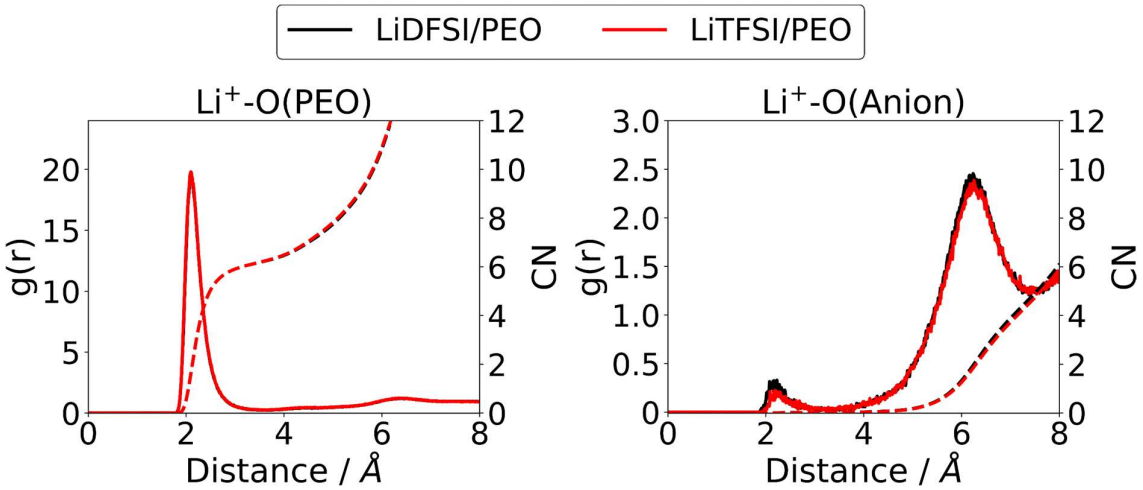

Figure 3-19: RDF (solid lines) and CN (dashed lines) analyses of the Li^+-O(PEO) (left panel) and Li^+-O(Anion) (right panel) interactions within the investigated LiDFSI/PEO, and LiTFSI/PEO systems.

To confirm that the minor peak observed in the Li^+-Anion RDF at around 2.2 Å corresponds to infrequent instances in the simulation wherein an anion temporarily positions itself amidst the EO monomers, engaging in a brief interaction with Li^+, we examined Li^+'s first coordination shell composition (depicted in *Figure 3-20*). In tandem, we present a specific instance illustrating Li^+ diffusion mechanism within the LiDFSI/PEO system in *Figure 3-21*. The Python codes used to perform these analyses are detailed on *Appendix A.1*.

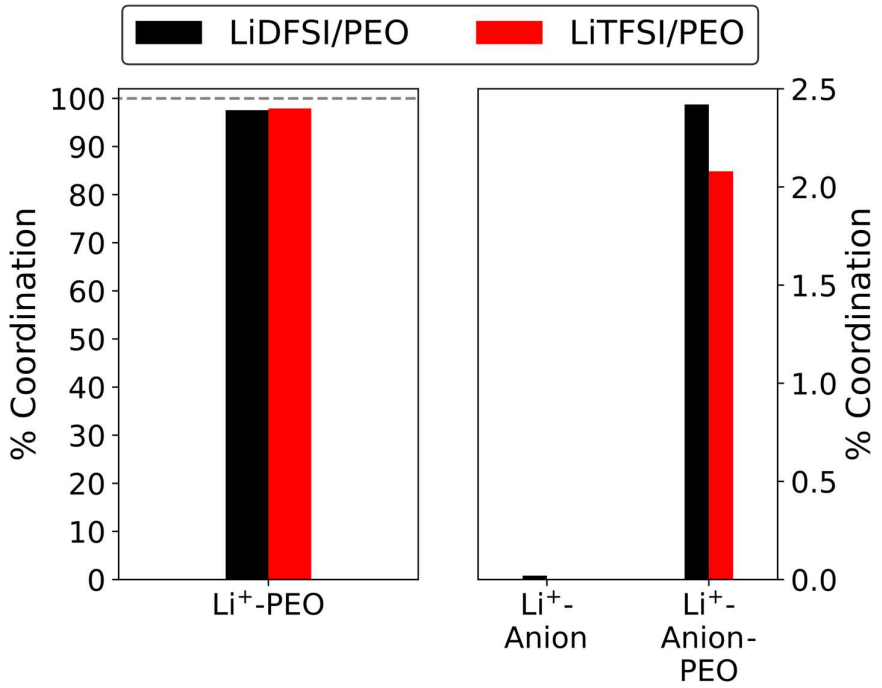

Figure 3-20: Percentage composition of the first Li^+'s solvation shell for LiDFSI/PEO (in black) and LiTFSI/PEO (in red) systems.

As expected, the discrepancies in Li^+'s coordination environment remain minimal between the LiTFSI/PEO and LiDFSI/PEO systems. Notably, there is a slightly heightened occurrence of the Li^+-$DFSI^-$-PEO coordination environment in the LiDFSI/PEO system when compared to Li^+-$TFSI^-$-PEO (2.42 % vs 2.08 %, respectively), however this difference should not correspond to any significance difference in Li^+ diffusion mechanism. Moreover, the example showcasing Li^+ diffusion mechanism mirrors a behaviour characteristic of the LiTFSI/PEO system (see *Figure 3-21*). The afore observed difference in the Li^+-Anion-PEO coordination case can be ascribed to a slightly higher appearance of $DFSI^-$ in the Li^+-PEO environment with respect to $TFSI^-$. However, these apparitions are in both cases of very short duration. It is worth noting that in *Figure 3-21*, akin to the a) panel of *Figure 3-7*, an interchain jump is observable. However, in this scenario, the jump transpires over an extended duration. This instance underscores a case wherein Li^+ coordinates with two PEO chains concurrently—each involving three oxygen atoms from distinct chains.

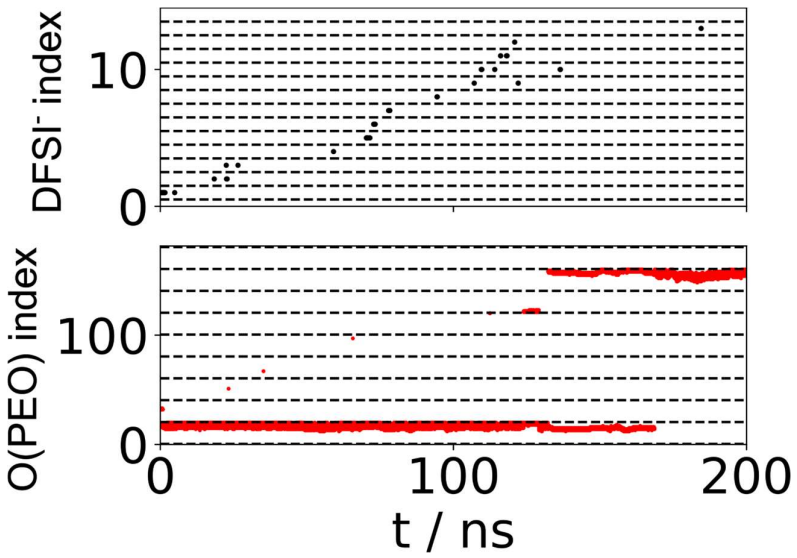

Figure 3-21: Representative example of Li^+ diffusion through the LiDFSI/PEO system, differentiating between the coordination with different $DFSIs^-$ (top panel) and with different oxygen atoms of different PEO chains (bottom panel).

To investigate whether the hydrogens introduced in $DFSI^-$ produce any extra interaction between $DFSIs^-$ or between $DFSI^-$ and PEO, we computed several RDFs comparing the interactions between $DFSIs^-$ and between $DFSI^-$ and PEO (*Figure 3-22*). These analyses were juxtaposed with the reference $TFSI^-$.

Firstly, we carried out an examination of center of mass (CoM) distances, shown in a) panel. Notably, the RDFs exhibited remarkable similarity, yet between $DFSIs^-$, the interaction onset occurred at a slightly shorter distance than between $TFSIs^-$. Given the inherent symmetry of both $DFSI^-$ and $TFSI^-$, minimal displacement of CoM was anticipated. Thus, the observation that $DFSI^-$ interact at closer distances suggests enhanced interactions.

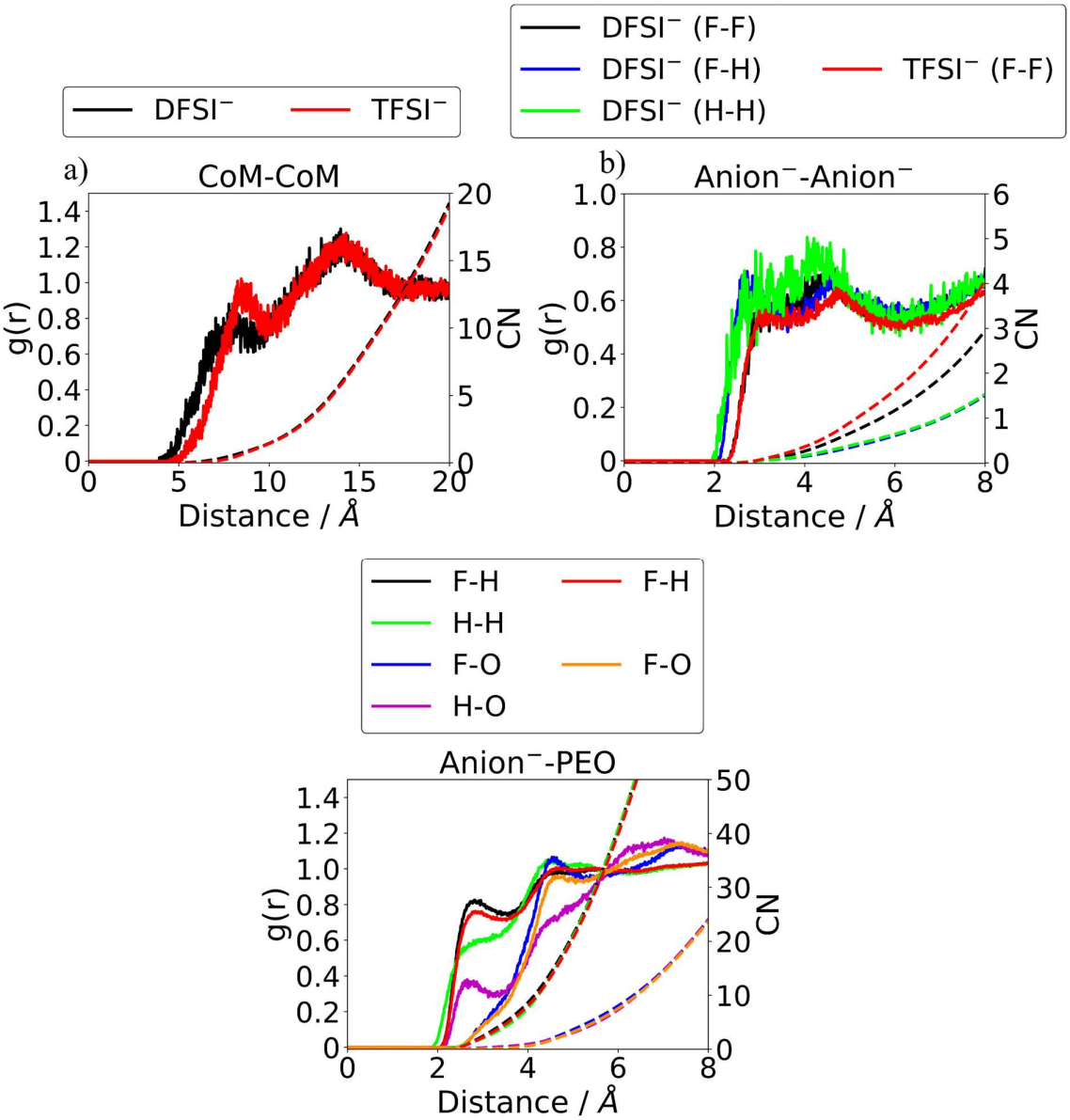

Figure 3-22: a) RDFs depicting the distances between anion's center of masses (solid lines) and their respective CN (dashed lines). b) Distinct RDFs detailing interactions between anion atoms (solid lines) and CN (dashed lines). c) Various RDFs illustrating interactions between anion and PEO atoms (solid lines) and CN (dashed lines).

Next, we delved into the interaction between the anions, focusing on the fluorine and hydrogen atoms (b) panel). The analysis of hydrogen atoms showed a similar trend: RDFs displayed an initial increase at closer distances, although definitive peaks were absent. This absence of pronounced peaks might stem from the smaller size of the hydrogen relative to fluorine. The F-F interaction emerged nearly indistinguishable between $DFSI^-$ and $TFSI^-$.

Our investigation extended to atomic RDFs encompassing anions and PEO (c) panel). By scrutinizing potential interactions between fluorine/hydrogen atoms of anions and oxygen/hydrogen atoms of PEO, certain nuances surfaced. Though conspicuous peaks akin to

Li^+ RDFs were absent, discernible trends were evident. Specifically, the F-O and F-H interactions in LiDFSI/PEO exhibited slight elevation compared to LiTFSI/PEO. This disparity could be attributed to the higher polarization of $DFSIs^-$. Hydrogen atoms tend to accumulate positive charge, while fluorine ones tend towards negatively charge, possibly fostering heightened interactions with PEO compared to $TFSI^-$.

Upon dissecting the interactions of newly introduced hydrogen atoms in $DFSI^-$, an intriguing insight emerged. A minor peak appears when these hydrogen atoms interact with PEO oxygen. While the peak's magnitude did not exceed g(r) = 1, indicative of a definitive interaction, it exhibited a relative maximum at ~ 2.6 Å. This observation hints at a potential hydrogen bonding interaction between these molecules, albeit of modest strength. This small peak is of the same form as the F-H interaction, which enhances the idea of hydrogen bonding, and is an additional interaction that $DFSI^-$ possesses and $TFSI^-$ lacks.

To finalize the theoretical analysis, we computed the MSDs of the ionic species (see *Figure 3-23*). Both linear and logarithmic scales were used for a better understanding of the results. We observed a small reduction in the ionic mobility in the LiDFSI/PEO system when compared with the LiTFSI/PEO. This is indicative of the interactions that appear when hydrogen is introduced in $DFSI^-$, hindering its movement inside the simulated system. This reduction is also observed for Li^+ because the new interactions are created between $DFSI^-$ and PEO, thus hindering the mobility of the polymer matrix too and, as a consequence, Li^+'s. However, the difference is too small to extract clear conclusions and, as the logarithmic scale plot shows, none of the systems perfectly reaches the diffusive regime of slope equal to 1. This is why Li TN obtained (0.271 vs 0.246 in the LiTFSI/PEO and LiDFSI/PEO, respectively) are not excessively significative.

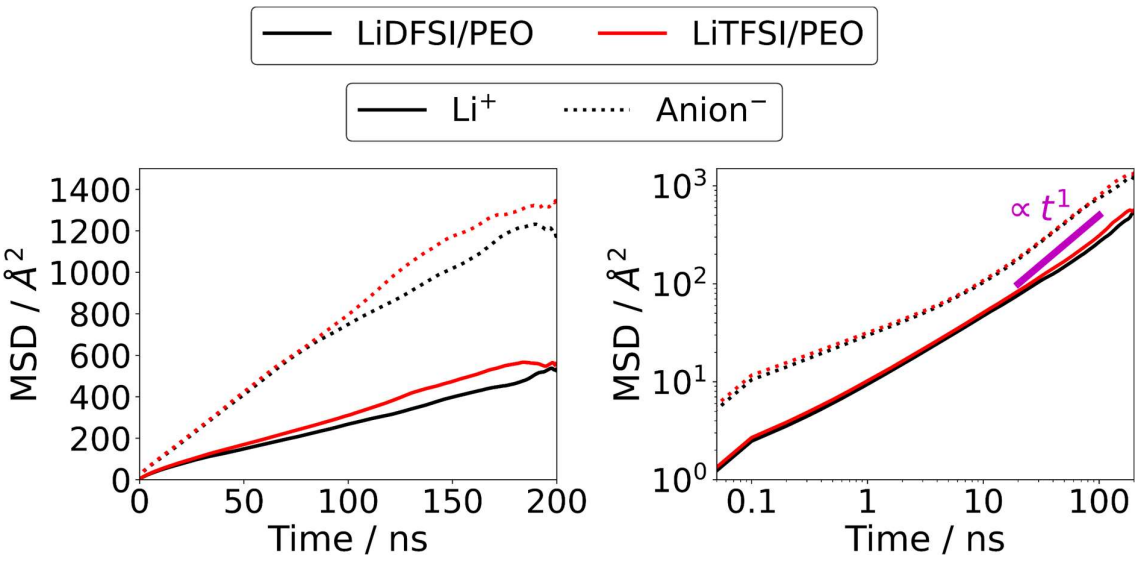

Figure 3-23: MSD of Li^+ (solid line) and anions (dotted lines) for LiDFSI/PEO, and LiTFSI/PEO systems. The left panel displays the MSD in a linear scale, while the right panel shows the analysis in a logarithmic scale, with a reference line of slope equal to 1 (indicative of Fickian regime).

However, an important observation warrants mention regarding these findings. A distinct pattern emerges in the anion's MSD beyond the first half of the simulation timeframe, spanning from 100 ns to 150 ns (excluding the data's final instances mentioned in *Section 2.2.5*). During this interval, a notable reduction in mobility becomes evident for $DFSI^-$, while $TFSI^-$ exhibits no corresponding change. Intriguingly, the behavior of Li^+ remains unaffected to any changes across the entire simulation period. Should this observed trend persist and extended further into longer time scales, eventually reaching the diffusive regime, a consequential augmentation in Li TN could materialize.

3.3.3. Experimental Validation

In this study we also had the opportunity to corroborate the theoretical results with the experiments performed in the laboratory by experimental groups that worked with the real systems. These analyses were not performed by the doctoral candidate, however their results are of great importance to validate the theoretical predictions made with the analysis of the MD simulations, so we have decided to include them in this Thesis. In the following, we present an overview of the main results and findings, which have also been published in collaboration with our experimental colleagues in a joint research paper *[175]*. As to the previous study, the theoretical analyses of this one, exposed until now, delve into more information of the included in the publication, due to the further development of analysis techniques by the doctorand during the development of the Thesis.

Firstly, we started with the analysis that are more easily comparable with the theory, which are the measurements of the ionic conductivity and the characterization of the system via X-ray diffraction patterns (*Figure 3-24*).

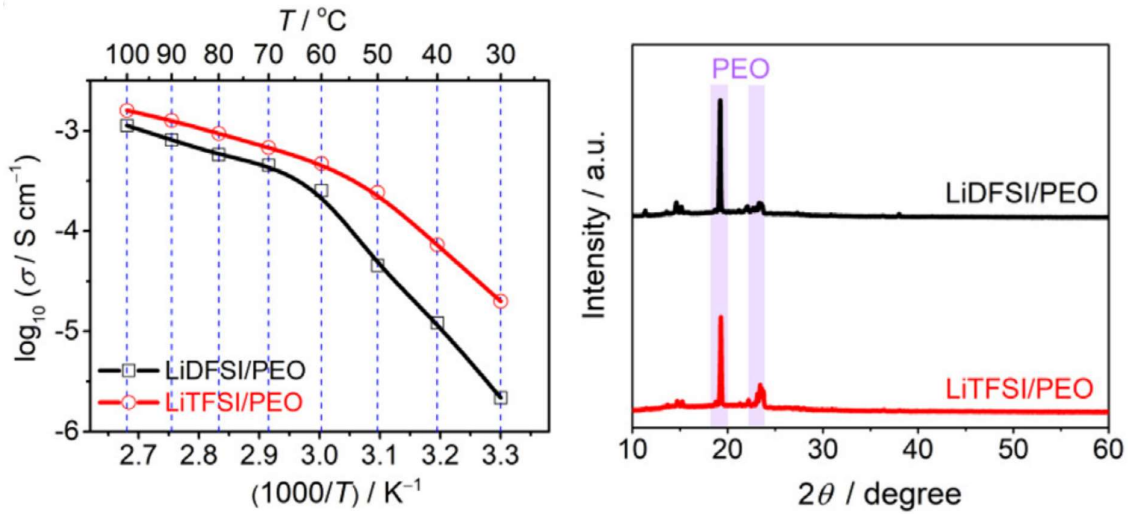

Figure 3-24: (Left) Arrhenius plots of ionic conductivity of the LiDFSI/PEO and LiTFSI/PEO electrolytes. (Right) XRD patterns of the electrolytes.

The total ionic conductivity of the LiDFSI/PEO and LiTFSI/PEO systems was measured at different temperatures, and, in the entire temperature range, the conductivity of the LiDFSI/PEO was smaller. The results are in great agreement with the MSD analysis (*Figure 3-23*) since both show a reduction of the mobility. However, experimentally we do see an increment in Li TN (0.39 vs 0.20, in LiDFSI/PEO and LiTFSI/PEO, respectively). This could be explained by the limitation of time scales of the MD simulations, which are not able to properly capture the diffusion of the ionic species at large time scales. But, as the experiments show, the mobility of the anion is further hindered in $DFSI^-$ thanks to the introduction of hydrogen into their structure, as expected. A much longer study of the diffusivity in simulations could capture the behaviour shown by $DFSI^-$ at long time intervals in comparison with $TFSI^-$, where a reduction in its mobility is observed (*Figure 3-23*), and could better reproduce the experimental results.

The X-ray diffraction (XRD) patterns show the characteristic displacement of the peaks of crystalline PEO at 19.3º and 23.7º, confirming that the PEO matrix is able to dissolve the Li-salts, producing a complete salt dissociation in both systems. Equivalent results were observed in the RDFs analysis (*Figure 3-19*) when the grade of salt dissociation was analyzed in the MD simulations.

Once we have shown that the structural and mobility characteristics predicted by the theoretical calculations were confirmed by the experiments performed over the real systems, we now move on to study if the hydrogenation of $TFSI^-$ fulfills its porpoise of increasing the stability of the system. The stability of the salts was evaluated via LSV of the salt dissolved in PC and PEO (*Figure 3-25*). The LiDFSI electrolyte shows lower anodic stability than the LiTFSI (5.4 V and 5.9 V *vs* Li^+/Li, respectively) due to the electron donating character of the hydrogen atoms. Nevertheless, a stability above 5 V *vs* Li^+/Li is sufficiently high for most electrode materials *[182]* and should not be a source of problems in the future analyses. When moving from liquid electrolytes to solid polymer electrolytes, dissolving the salts in PEO, both salts show stability enough for its use as SPEs in < 4V LMBs.

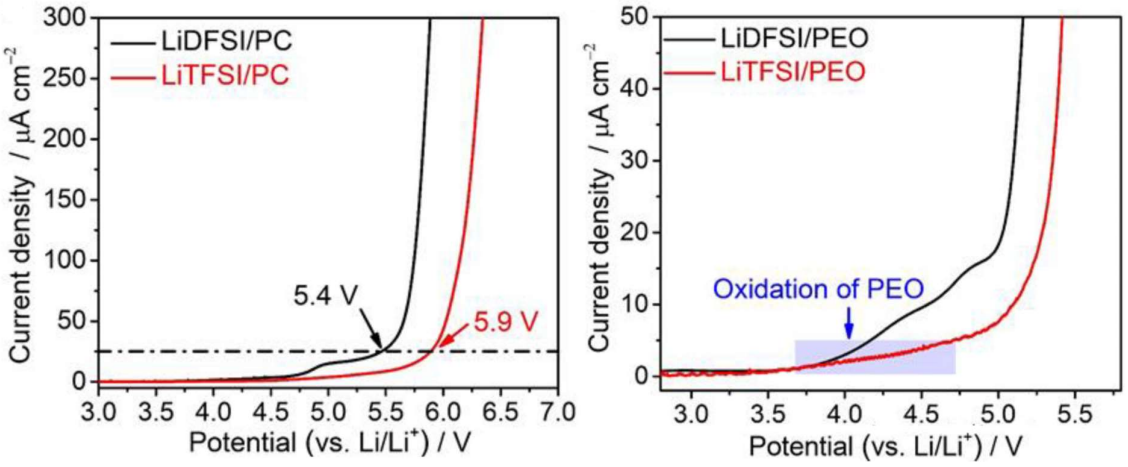

Figure 3-25: (Left) Linear sweep voltammetry profiles of the salts dissolved in PC. (Right) Linear sweep voltammetry profiles of the salts dissolved in PEO.

The interfacial stability with Li^0 electrode was characterized by galvanostatic cycling in a $Li^0||Li^0$ symmetric cell, with the Li-salts dissolved in PEO (*Figure 3-26*). LiTFSI/PEO suffered short-circuits problems after approximately 100 hours of cycling, as expected by previous works *[187]*, *[188]*. However, the cycling life of the LiDFSI/PEO system surpasses by far the life expectancy of the LiTFSI/PEO, reaching more than 3300 hours of stable cycling before showing problems with short-circuiting. This result points out the formation of a stable SEI, which additionally permits the diffusion of Li^+ through itself when the hydrogenated LiDFSI salt is employed.

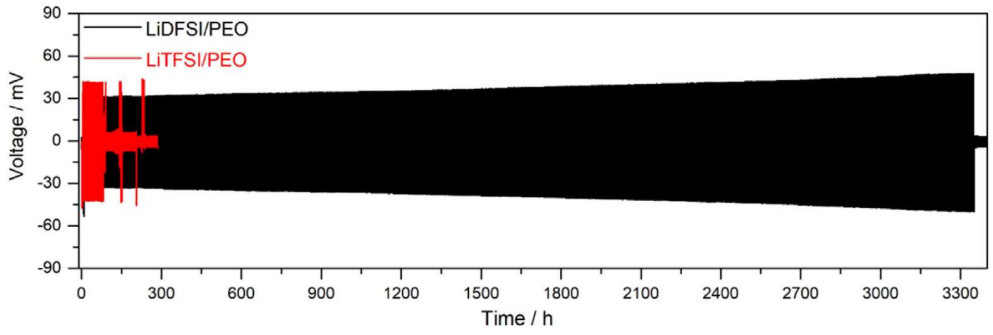

Figure 3-26: Galvanostatic cyclic of Li^0 anode in the PEO-based electrolytes.

To further characterize the SEI, we use a dissolution in DME (chemically analogue to PEO and with a similar ability to dissolve the salts). We analyzed its composition by X-ray photoelectron spectroscopy (XPS) (see *Figure 3-27*).

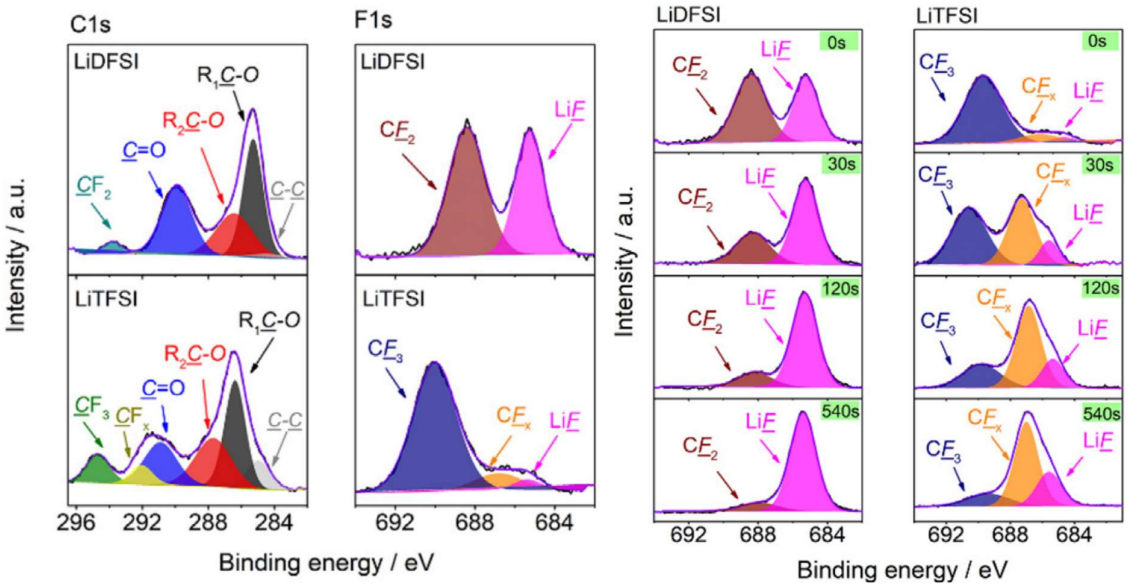

Figure 3-27: (Left) XPS spectra of C1s and F1s collected from the surface of Li^0 deposits. (Right) F1s spectra after various sputtering times.

In the left panel we show the C1s and F1s spectra of the deposition on the Li^0 surface, with the assignation of the peaks that conform the total spectra. The R_xC-O species of the C1s spectra are decompositions of the DME, while the C-F compounds are due to the reduction of the anions. The F1s spectra confirm the low observed presence of C-F compounds while showing a significant difference in the amount of LiF between the two systems, with a big contribution to the composition of the SEI in the LiDFSI. This is due to the easier decomposition of the -CF_2H group in $DFSI^-$ compared to the -CF_3 in $TFSI^-$.

In the right panel of *Figure 3-27* we can observe the F1s spectra after a prolongated sputtering. Here the LiF peak increases with time and becomes predominant in LiDFSI (with 84% after 120s). However, in LiTFSI, the increment in the LiF peak is much smaller (18% after 120s) and the CF_x peaks are the predominant components of the SEI. All these results confirm the facility to reduce $DFSI^-$ compared with $TFSI^-$.

To finalize the experimental analysis, we performed the cyclability tests with Li^0||$LiFePO_4$ cells to examine the applicability of the LiDFSI/PEO system on actual LMBs (*Figure 3-28*).

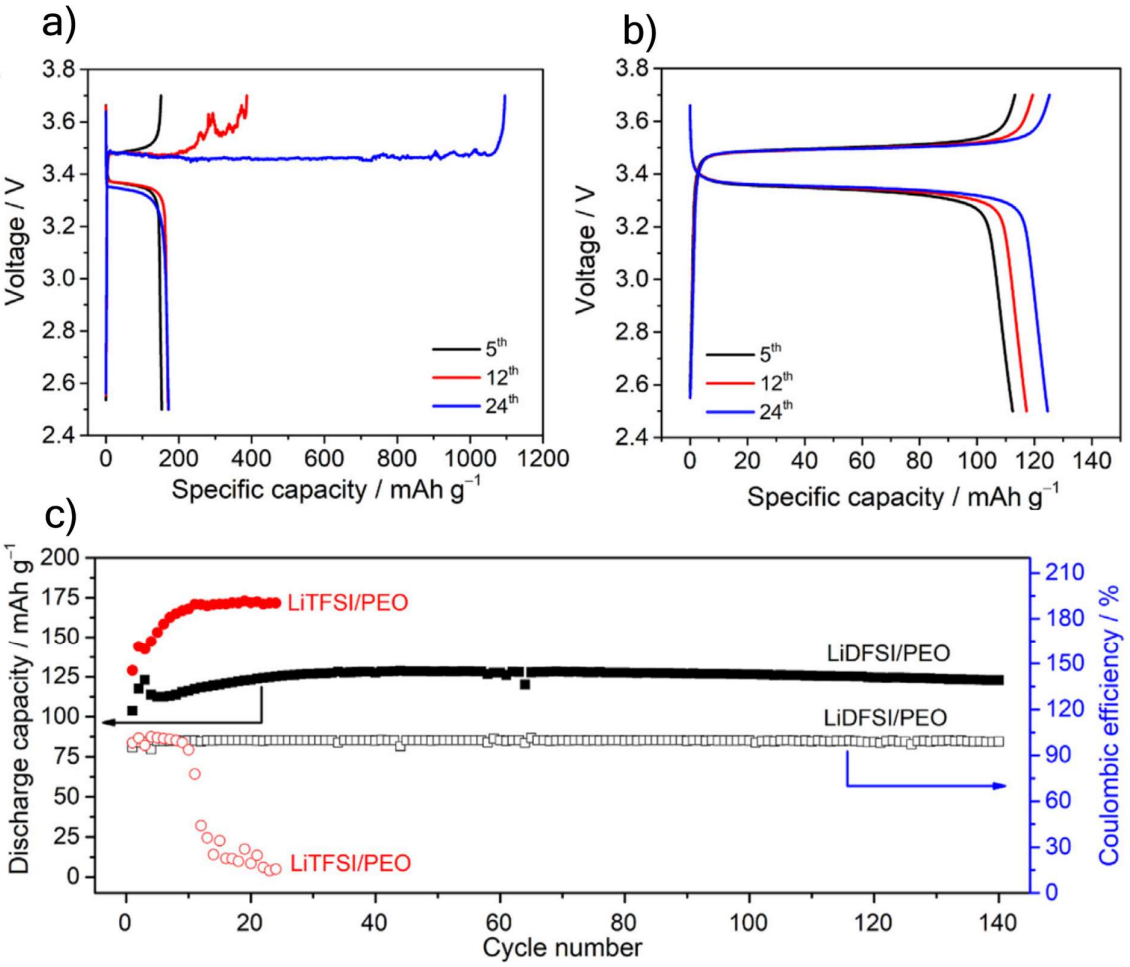

Figure 3-28: Discharge/charge profiles of LiTFSI/PEO (a), LiDFSI/PEO (b) and long-term cycling performance (c) of the Li^0||$LiFePO_4$ cells.

The LiDFSI/PEO cell shows higher stability in the charge/discharge profile while the LiTFSI/PEO shows prolonged charging process after the 12th cycle, attributed to the formation of dendrites on the Li^0 anode. In the long-term cycling analysis (with three formation cycles at C/5 rate and then at C/3), both show a low initial capacity (104 and 129 mAh/g for LiDFSI/PEO and LiTFSI/PEO, respectively). This could be ascribed to a poor contact between the electrolytes and the electrodes. After the initial cycles, LiTFSI cell shows a higher capacity but much lower cycle life than LiDFSI. Again, these results confirm the potential application of the LiDFSI/PEO electrolyte in Li^0||$LiFePo_4$ cells.

3.3.4. Conclusion

Our study, combining theoretical and experimental analysis, has stablished the success of the substitution of a fluorine atom with a hydrogen atom in both -CF_3 groups of $TFSI^-$ molecule, thereby forming $DFSI^-$. This alteration, motivated by the dual objective of hindering the mobility of $DFSI^-$ while fostering the creation of a more stable SEI, has proven to be a success. This transformation holds significance within the domain of environmentally friendly compound exploration, as the intact fluorinated groups of $TFSI^-$ are difficult to degrade in nature. By substituting them with semi-fluorinated -CF_2H groups, the resulting compound is rendered considerably more amenable to degradation via chemical processes.

The hydrogenation of $TFSI^-$ produces a discernible escalation in the interatomic interactions between $DFSI^-$ and their interaction with the PEO matrix. These augmented interactions, distinct from the LiTFSI/PEO system, hinder the anion mobility. While this phenomenon leads to a marginal reduction in the overall ionic conductivity of the system, the reduction is relatively modest. Remarkably, this reduction is counterbalanced by the concomitant increase observed in the Li TN, a critical factor contributing to the electrochemical performance of the system.

Importantly, the coordination structure of Li^+ remains essentially unaffected by the structural transformation, as both LiDFSI and LiTFSI salts exhibit complete dissociation when dissolved in a PEO matrix. Moreover, the heightened degradability shown by the -CF_2H groups of $DFSI^-$ bears additional benefits in the context of SEI formation. The presence of LiH and LiF facilitates the establishment of a more robust SEI, consequently extending the operational lifespan of the LiDFSI/PEO SPE. This longevity enhancement has far-reaching implications, effectively delaying the onset of short-circuits and reducing the growth of dendrites in the Li^0 electrode.

Chapter 4. Modification of the Polymer Chemistry

4.1. Introduction

PEO has been the polymer matrix most studied as base of the new solid polymer electrolyte (SPE) technology that arose to solve the problems that presented the liquid electrolytes when its applicability was tested in presence of a Li^0 metal anode *[71]*, *[72]*, *[73]*. It showed its benefits in conductivity terms since the early 70s and Prof. Armand was the first to propose it as a promising candidate for its use in rechargeable lithium batteries *[74]*, *[75]*. Well known and already seen in this Theis, is its high capacity of solvating lithium salts, provoking an almost perfect dissociation of the salt. However, this high solvability leaves the anion ($TFSI^-$ in many cases) in a free environment and facilitates its diffusion, implying a low Li TN of this system (~ 0.2). This behaviour also results in a gradient of anions and high polarization of the cells, involved in the low cycle life observed in the LiTFSI/PEO system *[8]*, *[190]*. PEO also suffers from crystallization at temperatures below 60 ºC, which hinders ionic conductivity.

These reasons indicate that some modifications must be made over the LiTFSI/PEO system, the basic structure of SPEs. In the previous Chapter we studied various approaches in the modification of $TFSI^-$ structure, with the idea of hindering its high mobility though the system. This hindering was looked for by the introduction of chemical groups that strengthen the electrostatic interactions, either between the proper anions or with the PEO. In this Chapter we move our focus to the other component: the PEO. Are there other polymer hosts that can overcome the problems shown by the PEO?

The great advantage of polymers is their high tuneability. Almost any imagined configuration can be achieved in the synthesis of new polymer matrices. Thus, we can configure the polymer structure based on the required characteristics. In this Chapter, we proceed with two different studies. Firstly, in *Section 4.2* we focus on trying to identify the ionic diffusion mechanism in a PCL matrix, compared to the PEO. Secondly, in *Section 4.3* we study the effect of increasing salt concentration on PEO and PCL polymers.

4.2. Diffusion Mechanism Characterization in PEO-PCL Blends

4.2.1. Theoretical Background

Polyethers have dominated the studies of SPEs for LMBs. Something that might be curious since in liquid electrolytes, the ether group -C-O-C- is commonly found in combination with carbonate -C(=O)- and ester -C(=O)-O- groups: propylene carbonate (PC), ethylene carbonate (EC), dimethyl carbonate (DMC), ethyl methyl carbonate (EMC), etc., are some of the most common solvents in LIBs. So, one may ask: Why do not apply this structure into a polymeric matrix? Actually, many carbonate polymers, with the poly (ε-caprolactone), named as PCL (see *Figure 4-1* for its structure), as the principal representant, have been studied in this field and the results are clear. In comparison with polyethers, polycarbonates show an increment of Li TN and a better anionic stability against high voltages *[191]*, *[192]*. This higher Li TN is thought to be due to a higher selectivity of the carbonate oxygen when coordinated with Li^+. However, the underlying precise diffusion mechanism is unknown *[193]*, *[194]*, *[195]*.

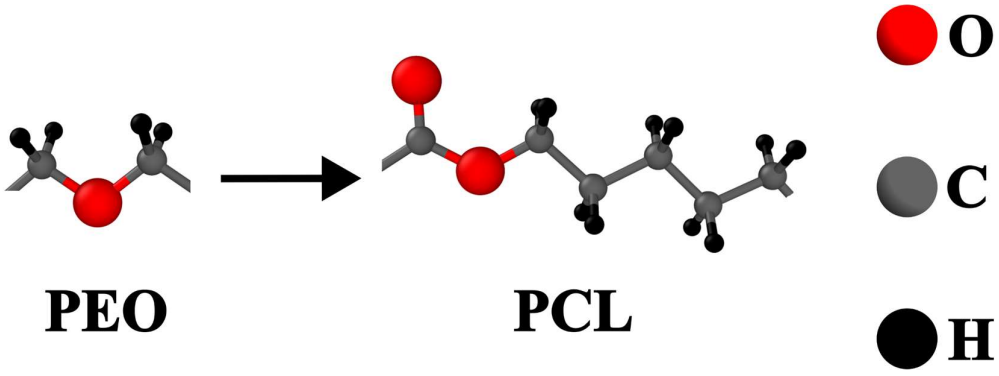

Figure 4-1: Chemical structure of the EO monomer in PEO (-CH_2-O-CH_2-) and the CL monomer in PCL (-C(=O)-O-$(CH_2)_5$-).

In this work we combine theoretical simulations with experimental results to shed light into the different ionic conduction mechanisms that carbonate polymers present, in comparison with the well-known ether polymers (PEO in particular). To do so, we use a blend matrix of PEO and PCL, in different molar ratios, with the LiTFSI salt dissolved in them (see *Figure 4-2*). Since we do not vary the salt, when referring to the different systems, we will make use of the following notation: PEO_xPCL_y (where *x* and *y* are the molar proportions of PEO and PCL in the blend, respectively).

Experimentally, we covered the entire range from a pure PEO system ($PEO_{100}PCL_0$) to a pure PCL system (PEO_0PCL_{100}), with three intermediate compositions ($PEO_{80}PCL_{20}$, $PEO_{50}PCL_{50}$, and $PEO_{20}PCL_{80}$). However, for the MD simulations we will only consider the pure PEO and PCL systems as well as the 50-50 mixture ($PEO_{50}PCL_{50}$).

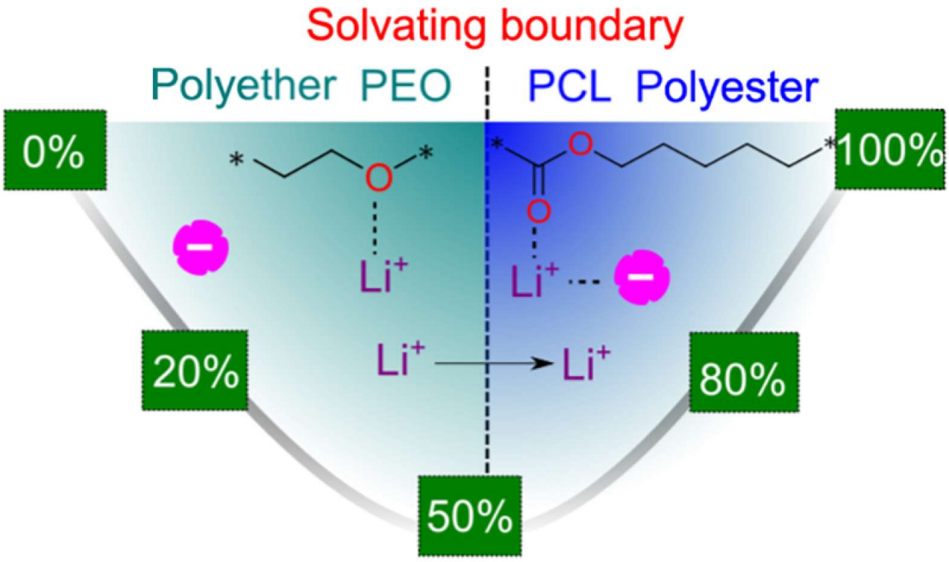

Figure 4-2: Schematic representation of the PEO-PCL blends studied, with the different molar ratios used. Adapted with permission from [200]. Copyright 2020 American Chemical Society.

Unlike the studies of the previous Chapter, whose importance relapse more in the novelty of the systems, here we are looking for a fundamental understanding of an already studied polymer blend *[196]*, *[197]*, *[198]*. LiTFSI possesses a higher thermal and chemical stability than other common Li salts studied with blends of PEO and PCL *[196]*. PCL is commercially available and thus, it has been used in other fields, such as biodegradable polymers *[199]*. This has helped to characterize its chemical properties *[195]*.

MD simulations were performed on the systems $PEO_{100}PCL_0$, PEO_0PCL_{100}, and $PEO_{50}PCL_{50}$ following the procedure detailed on *Section 2.2.6*. In all systems, the concentration [monomer]-Li^+ was kept constant at 20-1, independently of the ratio between PEO and PCL. 40 LiTFSI were inserted in each system with 40 PEO chains (20 monomers length), 40 PCL chains (also 20 monomers length), and 20 PEO and 20 PCL chains in the $PEO_{100}PCL_0$, PEO_0PCL_{100}, and $PEO_{50}PCL_{50}$ systems, respectively. The temperature was set at 343 K (70 ºC) and the simulations were performed during 200 ns. Only the structure of $TFSI^-$ was optimized at DFT level and its partial atomic charges computed with the ESP method (*Section 2.3.8*). All the parameters of the FF and the computed charges for $TFSI^-$ are available on *Appendix A.2*.

4.2.2. Theoretical Results

PCL possesses two different oxygen chemistries, an oxygen bonded via a double bond to a carbon (the carbonyl oxygen, denoted as O=), which stands out of the polymer chain, and the oxygen that forms part of the chain (the ether oxygen, denoted as -O-) (see *Figure 4-1*). To determine which of these oxygen types, or both, coordinate with Li^+, we firstly focused on the

PEO_0PCL_{100} system and compute the RDF while analyzing the oxygens separately, as illustrated in *Figure 4-3*.

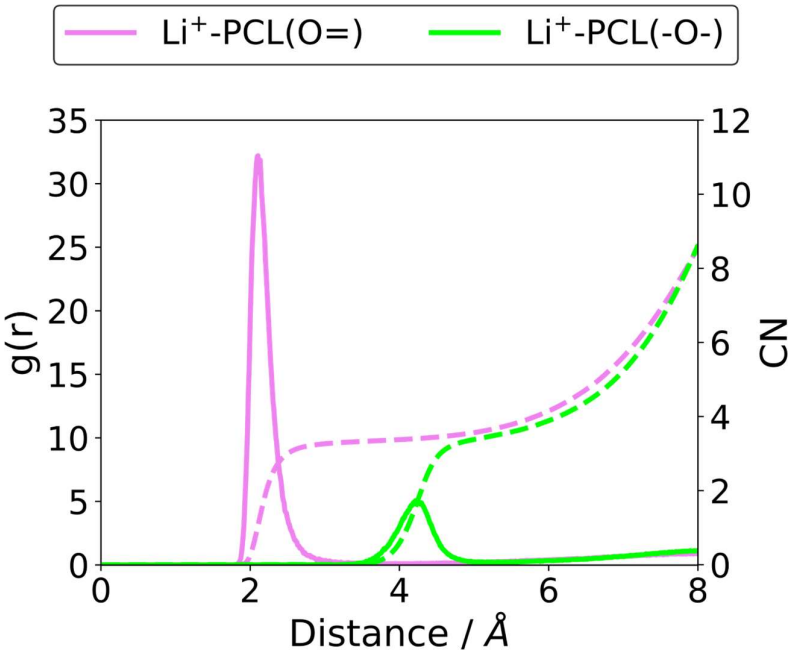

Figure 4-3: RDF (solid lines) and CN (dashed lines) analyses of Li^+ interaction with both types of oxygens in PCL (in the PEO_0PCL_{100} system) as defined in the main text.

The RDFs provide clear depiction of Li^+-PCL coordination, primarily occurring via carbonyl oxygen, with a CN of ~ 3.5. On the other hand, the ether oxygen presents a peak at a greater distance (> 4 Å), which means that no direct interaction exists between them. This peak corresponds to the interaction involving carbonyl oxygen, resulting in an increased distance between Li^+ and -O-. The coincidence in the CN for both oxygen types post the -O- peak reaffirms this conclusion. Notably, these results corroborate with previous studies *[191]*. Consequently, moving forward, our focus will solely be on carbonyl oxygens when referencing Li^+ coordination with PCL, simplifying the terminology by collectively using the term "oxygen" while omitting the ether oxygen.

Knowing already how the coordination with PCL is produced, we can analyze the differences in the coordination environment of Li^+ between the three molar ratios studied theoretically. We followed a similar approach to the previous studies. We first computed the RDFs between Li^+ and oxygens of $TFSI^-$ and the polymers, which, with the help of the CNs, gave us a first impression of the interaction of Li^+ (*Figure 4-4*). To analyze in more detail and shed light on the exact composition of the first solvation shell of Li^+, we examined its composition during the entire simulation and obtained the percentages of each different composition (*Figure 4-5*). Finally, to visually observe the different environments, representative examples of some single Li^+ were obtained with detailed information of their movement through the system (*Figure 4-7*

and *Figure 4-8*). More information about these last analyses techniques can be found on *Appendix A.1*.

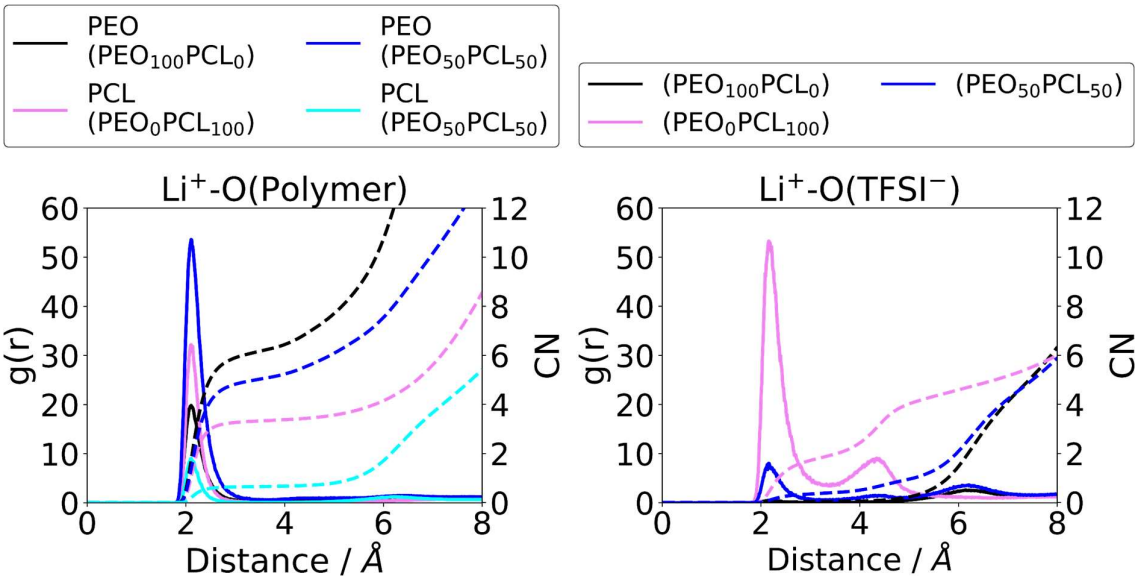

Figure 4-4: RDF (solid lines) and CN (dashed lines) analyses of the Li^+-O(Polymer) (left panel) and Li^+-O(TFSI$^-$) (right panel) interactions within the investigated $PEO_{100}PCL_0$, $PEO_{50}PCL_{50}$, and PEO_0PCL_{100} systems.

The analysis of the RDFs yielded an interesting finding. In the $PEO_{100}PCL_0$ system, we anticipated Li^+ coordination primarily with PEO, displaying a CN slightly exceeding 6 and no coordination with TFSI$^-$. However, in the PEO_0PCL_{100} system, a distinct coordination environment emerged. Here, Li^+ shows coordination with both PCL and TFSI$^-$ (with CNs approximately 3.5 and 2.5, respectively). The higher peak for Li^+-PCL compared to Li^+-PEO in the single polymer systems (as shown by the solid pink and black lines in the left panel of *Figure 4-4*), despite the CNs suggesting the opposite trend, can be elucidated through RDF normalization (refer to *Section 2.2.5*). The CL monomer in PCL is considerably larger than the EO monomer in PEO (*Figure 4-1*), while the number of chains and their length are identical (40 chains of 20 monomers). Consequently, this leads to a larger simulation box in PEO_0PCL_{100}, resulting in a reduction of the average density of PCL's oxygens. As the short-range density around a Li^+ is substantial, normalization amplifies the height of the coordination peak for Li^+-PCL compared to the Li^+-PEO interaction observed in the $PEO_{100}PCL_0$ system.

Moving now to the $PEO_{50}PCL_{50}$ system, we observe that Li^+ shows a much higher coordination with PEO than with PCL, while the interaction with TFSI$^-$ is rather low, but not completely null. So, although the system is a 50-50 mix in molar concentration of PEO and PCL, PEO possesses a much higher capacity to solvate Li^+. Again, to not confuse the reader, the greater height of the Li^+-PEO peak in the $PEO_{50}PCL_{50}$ system compared with the Li^+-PEO peak in the $PEO_{100}PCL_0$ system is explained by the normalization of the RDFs and the lower average density of the PEO.

In our initial analysis, we observed a distinct solvation mechanism for PCL compared to PEO. Notably, PCL does not dissolve the LiTFSI salt. Understanding the coordination of Li^+ in the PEO_0PCL_{100} and $PEO_{50}PCL_{50}$ systems requires a deeper examination. The exact composition of the first solvation shell of Li^+ (*Figure 4-5*) provides crucial insights.

As anticipated, the disparity between the $PEO_{100}PCL_0$ and PEO_0PCL_{100} systems (left panel) is evident. Even though the Li^+-O($TFSI^-$) RDF indicates strong coordination in the PEO_0PCL_{100} system, the simulation does not show the presence of pure salts. Interestingly, all coordination between Li^+ and $TFSI^-$ occurs concurrently with PCL, highlighting the intricate interplay. Li^+-PCL coordination is difficult to isolate while Li^+-PEO is dominant in its respective single polymer systems.

In the $PEO_{50}PCL_{50}$ system (right panel), we have more combinations of molecules that can form the first solvation shell of Li^+. In *Figure 4-5* we show the three more probable compositions, while all the other possibilities, with very low percentages each, are grouped under the *Other* label (including Li^+-PCL, Li^+-$TFSI^-$-PEO, and Li^+-$TFSI^-$-PEO-PCL). We proved the dominance of PEO over PCL with a 75 % of Li^+ coordinated only with the PEO. The second most probable composition is the Li^+-$TFSI^-$-PCL, which is the dominant composition in PEO_0PCL_{100}. This might indicate that PEO and PCL do not mix very well, forming separated regions. This way, the behavior of Li^+ mimics that observed in either the $PEO_{100}PCL_0$ or in a PEO_0PCL_{100} systems, depending on its location within these regions. The probability of finding a Li^+ coordinating with both PEO and PCL is minimal (~ 6.5 %). If the hypothesis of separated regions holds true, this occurrence might align with Li^+ positioned at the interface. Other possible combinations present exceedingly low percentages.

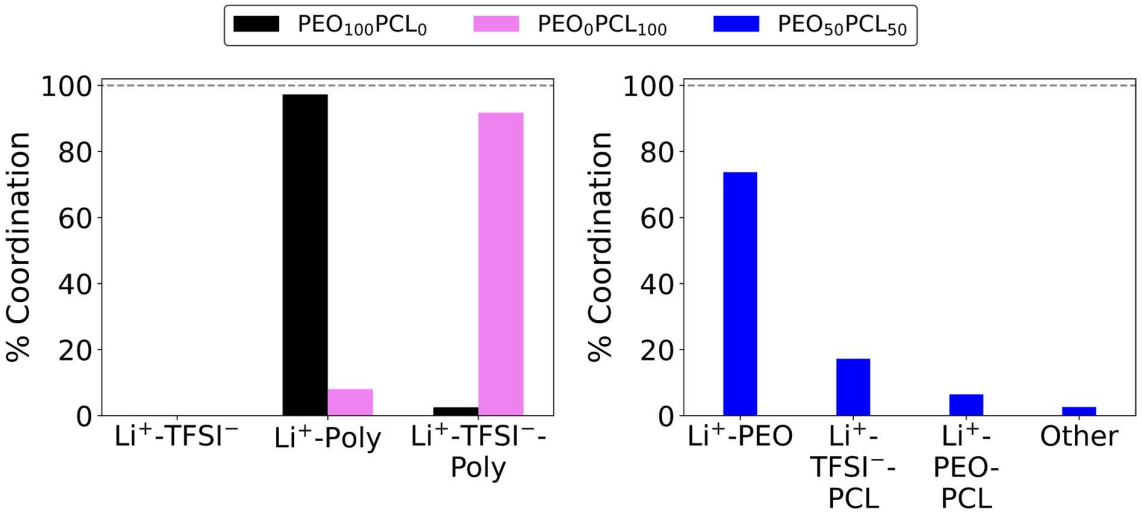

Figure 4-5: Percentage composition of the first solvation shell of Li^+ for the three investigated systems ($PEO_{100}PCL_0$ in black, PEO_0PCL_{100} in pink, and $PEO_{50}PCL_{50}$ in blue).

In *Figure 4-6*, a snapshot extracted from the MD simulation of the $PEO_{50}PCL_{50}$ system is presented, with PEO and PCL distinguished by color for clarity. The distribution of the two

polymers is noticeably non-uniform, showcasing distinct groupings. However, these groupings do not conform to perfect segregation into two distinct regions; rather, there is a significant and extensive interface region. Li^+ is also shown to illustrate that the majority of them reside within PEO regions, aligning with the data in the right panel of *Figure 4-5*.

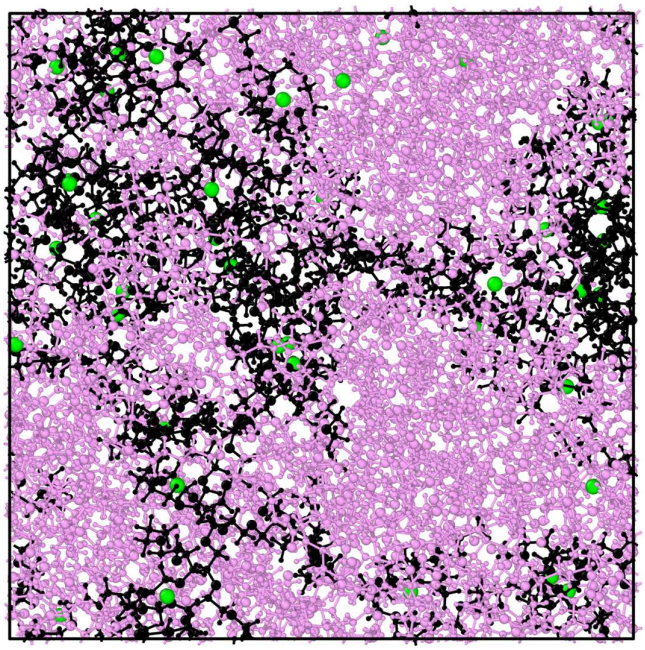

Figure 4-6: Snapshot of the MD simulation of the $PEO_{50}PCL_{50}$ with Li^+ in green, PEO in black and PCL in pink. $TFSI^-$, for better visualization, is not shown.

To easily visualize the difference in Li^+ diffusion mechanism between PEO and PCL we show a representative example of the exact coordination environment of one Li^+ for the $PEO_{100}PCL_0$ and PEO_0PCL_{100} systems in *Figure 4-7*. In the $PEO_{100}PCL_0$ system (left panel) we visualize the movement of a Li^+ through a PEO chain with isolated points of coordination with various $TFSIs^-$ that last only a few snapshots. On the contrary, the movement in the PEO_0PCL_{100} system (right panel) exhibits a completely different pattern, highlighting three key distinguishing features from PEO:

1) Li^+ does not move through the PCL chain. In the PEO_0PCL_{100} system, the oxygens of PCL are also differentiated, as PEO in the $PEO_{100}PCL_0$ system, however in PCL we do not see movement through the chain. The coordination points form straight lines.

2) The coordination with the $TFSIs^-$ is also long lasting. The points of coordination with the different $TFSIs^-$ (remember that here we do not show individually the oxygens of $TFSI^-$) also draw long lines that last many snapshots. This implies that the interaction between Li^+ and $TFSI^-$ is also strong, similar to the Li^+-PCL.

3) Li^+ can easily be coordinated with different PCL chains. While in the PEO, a Li^+ normally is surrounded by 6 monomers in a row of the same PEO chain, in PCL it coordinates with 3 or 4 monomers, normally not in a row, and commonly of different chains. This means that the interchain jumps are much more probable in PCL environment than in that of PEO.

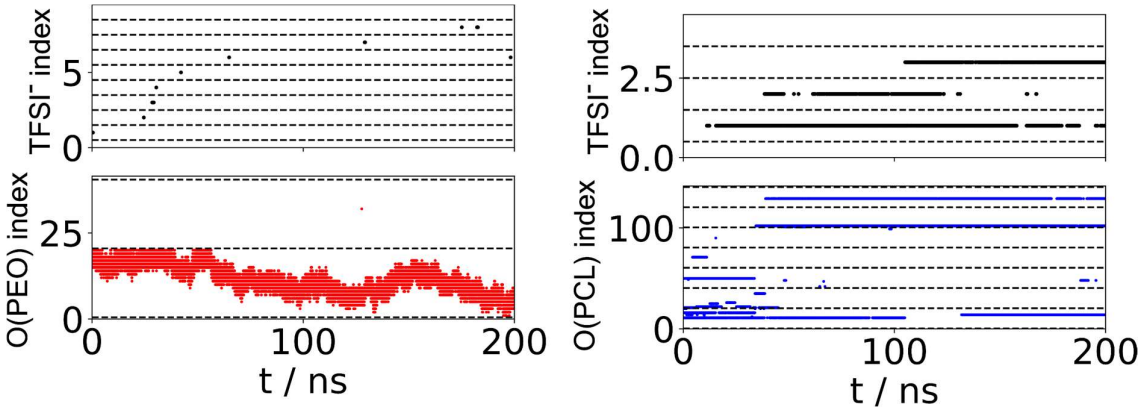

Figure 4-7: (Left) Representative example of Li^+ diffusion through the $PEO_{100}PCL_0$ system, and (right) through the PEO_0PCL_{100} system differentiating between the coordination with different $TFSIs^-$ in black points and with different oxygen atoms of different PEO chains (red points) and PCL chains (blue points).

These three distinguishing characteristics provide a comprehensive understanding of Li^+ diffusion mechanism with a PCL matrix. In PEO, diffusion is only driven by the polymer, affording Li^+ considerable freedom to move along the polymer chain. Conversely, in PCL, the role of $TFSI^-$ is pivotal in facilitating Li^+ diffusion, albeit with more constrained movement, indicating a more stable coordination environment.

To visually examine Li^+ movement within the $PEO_{50}PCL_{50}$ system, we selected three distinct environments as examples (*Figure 4-8*). In the a) panel, we observe a Li^+ situated in a Li^+-PEO environment. It remains coordinated to the same PEO chain throughout the entire simulation, with intermittent short-time interactions with $TFSI^-$ and PCL. In the b) panel we showcase an example of a Li^+-$TFSI^-$-PCL environment, where Li^+ does not interact with the PEO. Finally, the c) panel presents a case in which Li^+ transitions from PCL to PEO, during which $TFSIs^-$ that were coordinated with it in PCL environment are also shown to transition at the same time as PCL disappears from Li^+'s surroundings.

From these three examples we can derive insights into the behavior of Li^+ within the $PEO_{50}PCL_{50}$ system. Despite PEO being the dominant polymer, it is common for PCL to come into contact with Li^+ while travelling through the PEO chain. This interaction with PCL, although short-lived, is more probable than with $TFSI^-$, which aligns with the low percentage of Li^+-PEO-PCL coordination shown in *Figure 4-5*. Examining other Li^+ instances, finding prolonged interactions with both PEO and PCL concurrently is challenging. Thus, the low percentage of Li^+-PEO-PCL coordination can be attributed to cases where Li^+ is initially

coordinated with PEO and briefly encounters PCL in the coordination environment (as seen in the a) panel of *Figure 4-8*), rather than transitioning between polymers, which, as shown in c) panel, is occurs quickly.

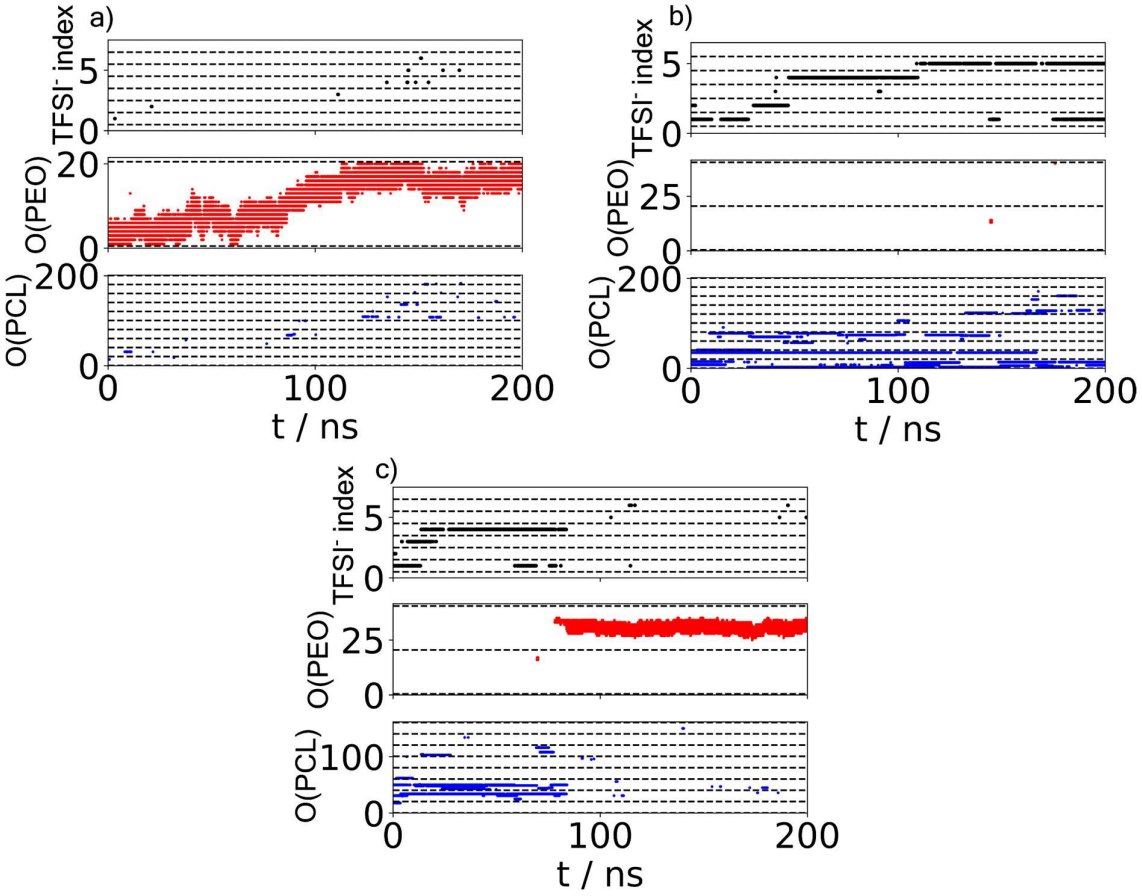

Figure 4-8: Three representative examples of Li^+ diffusion throughout the $PEO_{50}PCL_{50}$ system, differentiating between the coordination with distinct $TFSIs^-$ and oxygen atoms of different PEO and PCL chains.

To glean more information from this coordination analysis, we extracted data for all Li^+ in the systems and computed the residence time of interactions with various elements of the systems. These residence times can be seen as the measure of the horizontal lines formed by coordination points in *Figure 4-7* and *Figure 4-8*. The residence time is the time that a certain interaction lasts. We analyzed the residence time for Li^+-$TFSI^-$ and Li^+-Polymer interactions, differentiating between interactions with a single monomer and an entire chain in the latter case, to investigate intrachain and interchain movements, respectively. To ensure accuracy, we excluded single-snapshot coordination (lasting only one snapshot) and considered not lost if only a single point is missing, preventing random configurations due to thermal agitation from being considered as pure interactions. More information about the functioning of the Python code used to perform this analysis is found on *Appendix A.1*.

In this analysis, we plotted the probability distribution of a certain interaction against its duration in logarithmic scale (*Figure 4-9*), given the exponential decay characteristic. However, a pure exponential fitting ($y = Ae^x$) can not be performed because the tail of data at long times does not decay, but it remains constant due to the lack of enough data. So, a different approach must be taken to differentiate the systems. That is why we focus on two aspects in these plots.

Firstly, the velocity at which the probability reaches its minimum value, gauged by the slope of the fit until the first residence time where the probability equals the minimum. A more negative slope implies faster residence time decay. This minimum value corresponds to single-case residence times, and once this minimum is reached, the probability distribution remains nearly constant. Secondly, the residence times corresponding to the minimal probability value, denoted as the base width of the analysis. This interval provides insights into the interaction's capacity to be sustained over time. We think that this plot's shape is due to the limited statistics given by the relatively small number of interactions that we can simulate. We suppose that if sufficiently large systems could be simulated, the data would continue an exponential decay until the time length of the simulation.

These two values are partially correlated, where a greater slope corresponds to a lower start of the base interval. For example, in *Figure 4-9* (depicting the Li^+-$TFSI^-$ interaction in the $PEO_{100}PCL_0$ system), the slope is -2.25 ± 0.16, and the base interval is [1.6, 8.7] ns. We will present comparisons both visually and numerically, using plots when the visual difference is significant and using numerical values when the plots are similar.

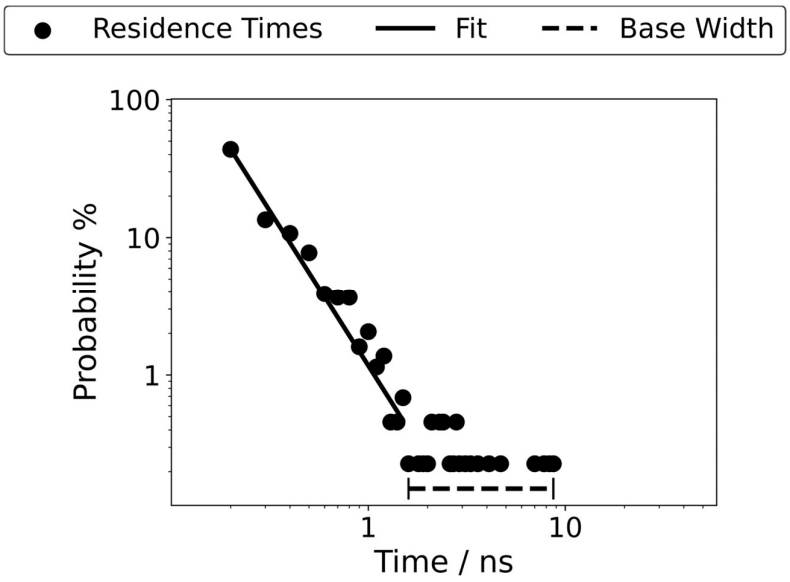

Figure 4-9: Example of the analysis performed on the residence time data, with the fit to the decay zone and the width of the base.

We start with the comparison of Li^+-$TFSI^-$ interactions across the three systems (*Table 4-1*). The slope is steeper in the $PEO_{100}PCL_0$ system compared to the PEO_0PCL_{100} system, indicating a more enduring interaction between ions in the latter. This is attributed to the possibility of

$TFSI^-$ being present in the coordination environment of Li^+ when solvated by PCL. As shown in *Figure 4-7*, this interaction can persist longer in PCL than in PEO. The base width indicates that some coordination lasts the entire simulation time (200 ns) in PCL, while in PEO, the maximum residence time is 8.7 ns. The different solvation mechanism of Li^+ in PCL results in a stronger interaction with $TFSI^-$ compared to PEO, where the polymer can completely dissolve the salt and break any possible interaction.

	$PEO_{100}PCL_0$	PEO_0PCL_{100}	$PEO_{50}PCL_{50}$
Slope of the Fit	-2.25 ± 0.16	-1.35 ± 0.09	-2.19 ± 0.14
Base Width	[1.6, 8.7]	[4.0, 200]	[1.8, 120.6]

Table 4-1: Slope of the fit to the decay part and interval of the base of the Li^+-$TFSI^-$ interaction.

In the $PEO_{50}PCL_{50}$ system, the behavior is mixed. Although the slope is similar to that of the $PEO_{100}PCL_0$ system (reflecting a comparable start of the base width interval), the maximum interval time is significantly higher. This can be attributed to the preferential solvation of Li^+ in the PEO regions (*Figure 4-6*), causing the short residence time part to be characterized by PEO. However, the small percentage of Li^+ solvated by PCL extends the maximum residence times, increasing the base width beyond PEO's capacity, though not reaching the values seen in PEO_0PCL_{100}.

Moving our attention to the interaction with the polymers, we have the interaction of Li^+ with individual monomers and with polymer chains as a whole (*Table 4-2*). The analysis of the interaction with the PEO chains is not shown in the table because the interaction follows a different behaviour and cannot be analyzed with the same tools. A comparison between the interaction with the PEO chain in the $PEO_{100}PCL_0$ system and with the PCL chain in the PEO_0PCL_{100} system is shown in *Figure 4-10*. Here the difference is clear. While the interaction with the PCL chain follows the expected behaviour, with the PEO chain it presents an initial region where the probability distribution does not exponentially decay, and a high final probability for times equal to the total simulation time stands out.

Let us firstly focus only on the $PEO_{100}PCL_0$ and PEO_0PCL_{100} systems to compare pure systems. The interaction with the PEO monomers has a higher slope than with PCL monomers, however the base interval is displaced to longer residence times, close to even reach the 200 ns. This is an effect of the different Li^+ movement on these polymers. In the PEO, Li^+ have more freedom of movement, thus, there are more interactions. This means that even when in PEO, the probability decays faster, it reaches the minimum value at a longer residence time.

In the PEO_0PCL_{100} system, the disparity between monomer and chain interactions is very small, featuring a comparable slope and a broader base. Again, we observe a higher occurrence of interactions with single monomers compared to complete chains, resulting in a smaller initial interval value for the chain. At these residence times, instances of monomer interactions are

more prevalent. However, the final interval value is greater for chains, given that the alternative is impossible. This suggests that within the PCL polymer, Li^+ displays a similar probability of exhibiting interchain and intrachain jumps.

			$PEO_{100}PCL_0$	PEO_0PCL_{100}	$PEO_{50}PCL_{50}$
PEO	Monomer	Slope of the Fit	-1.41 ± 0.03	-	-1.38 ± 0.03
		Base Width	[23.4, 194.9]	-	[15.7, 200]
PCL	Monomer	Slope of the Fit	-	-1.17 ± 0.03	-1.28 ± 0.05
		Base Width	-	[17.6, 123.1]	[7.1, 62.3]
	Chain	Slope of the Fit	-	-1.09 ± 0.04	-1.49 ± 0.06
		Base Width	-	[12.8, 199]	[4.2, 168.7]

Table 4-2: Slope of the fit to the decay part and interval of the base of the Li^+-Polymer interaction (both monomer and chain).

Conversely, in the $PEO_{100}PCL_0$ system, the interactions with the PEO chain show a substantial probability of a 200 ns interaction (*Figure 4-10*), indicating that a majority of Li^+ do not jump to a different chain throughout the entire simulation. On the other hand, the data for the PCL chain follows standard plot. We anticipate that the data for PEO and PCL monomers would exhibit a shape similar to that of the PCL chain.

These data indicate that the residence time of Li^+ with each monomer is similar in both PEO and PCL. But when Li^+ moves to another monomer, a notable distinction emerges. In PEO, it mainly shifts to a monomer within the same chain (intrachain jump, to an adjacent one at high probability), whereas in PCL, it can move within the same chain (intrachain jump) or to a different chain (interchain jump) without a clear preference.

Comparing how these data change when the two polymers are blended in the $PEO_{50}PCL_{50}$ system, intriguing patterns surface. The interaction with PEO monomers remains largely unaffected, displaying a similar slope and base interval. On the contrary, in PCL, the slope increases, and the interval shifts towards lower values. This shift is a consequence of Li^+ preferring solvation within PEO. Consequently, interactions with PCL decrease as Li^+ readily encounters available spaces to jump to within the PEO chain. A comparison of the interaction with the PEO chain between the $PEO_{100}PCL_0$ and $PEO_{50}PCL_{50}$ systems (*Figure 4-11*) unveils a reduction in the probability of short residence times and an increase in 200 ns interactions. This reflects the diminished available space within the PEO region in the blended system, resulting in a decreased probability of short-term interactions and a surge in longer-lasting interactions.

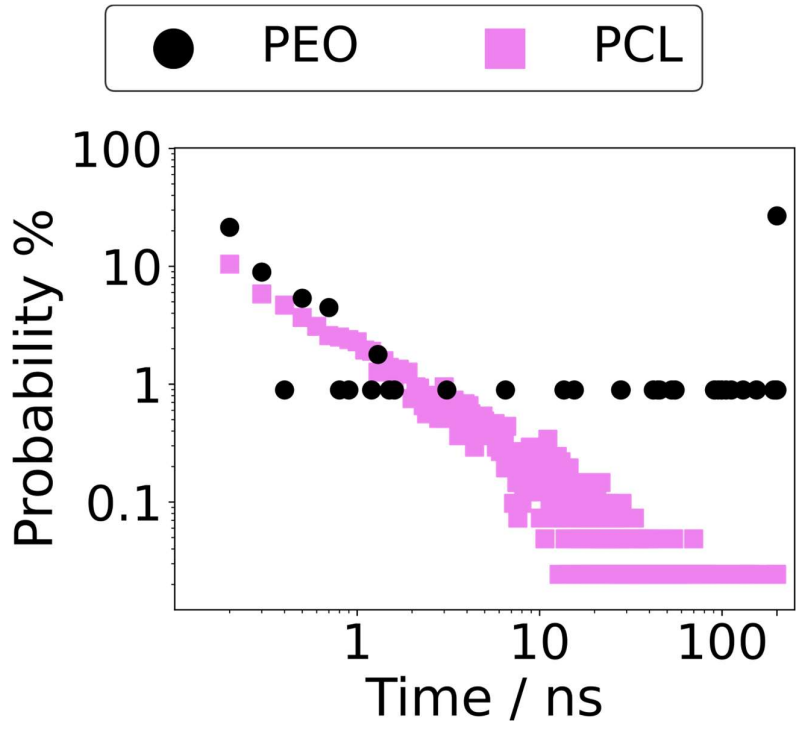

Figure 4-10: Probability distribution of the residence times of the Li^+-Polymer Chain interaction for the $PEO_{100}PCL_0$ (black dots) and PEO_0PCL_{100} (pink squares) systems.

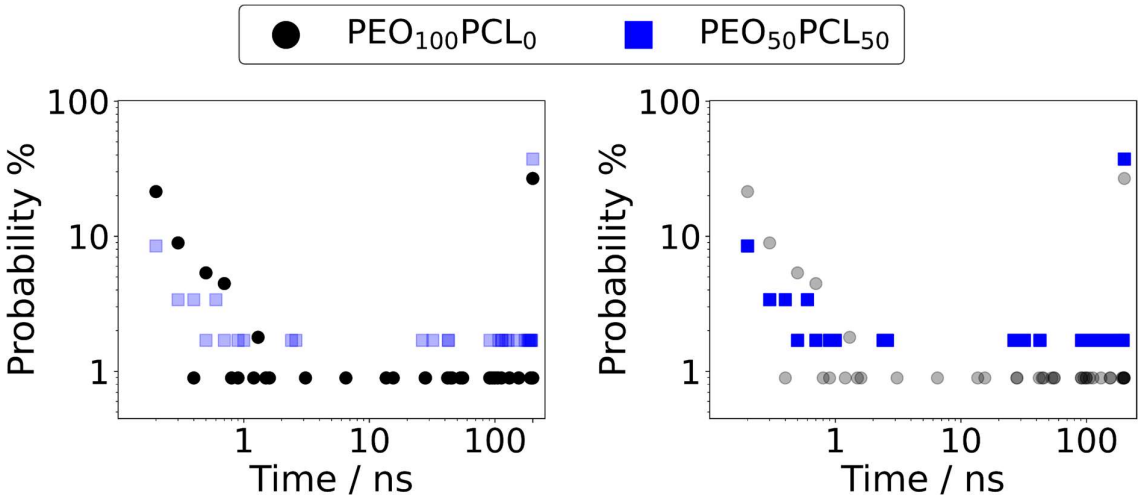

Figure 4-11: Probability distribution of the residence times of the Li^+-PEO chain interaction, remarked for the $PEO_{100}PCL_0$ (left panel), and $PEO_{50}PCL_{50}$ (right panel) systems.

To finalize our theoretical analysis, we computed the MSD of the ionic species in the three simulated systems (*Figure 4-12*). This analysis provides valuable information into how different Li^+ diffusion mechanisms influence ion diffusivity. Notably, we observe a high reduction in overall mobility upon the introduction of PCL into the blend. The MSD of $TFSI^-$

decreases as PCL content increases. However, for Li^+, we observe a substantial decrease from $PEO_{100}PCL_0$ to $PEO_{50}PCL_{50}$, but this reduction stabilizes, resulting in a similar mobility observed in the PEO_0PCL_{100} system. This observation can be explained by the dominance of PEO over PCL in the $PEO_{50}PCL_{50}$ blend. Given Li^+'s preference for coordinating with PEO, fewer available spaces for the movement are present. Hence, although Li^+ moves faster in PEO compared to PCL, the restricted spatial movement in PEO hinders its diffusivity. This can be seen, for example, in the right panel of *Figure 4-8*, where Li^+ movement through the PEO chain is notably limited. In a system containing only PCL, Li^+ movement is slow; however, the abundance of available spaces compensates for this, resulting in an average mobility similar to that in the $PEO_{50}PCL_{50}$ system. In the case of $TFSI^-$, the scenario differs. As $TFSI^-$ only coordinates with Li^+ in the presence of PCL, increased PCL content leads to higher interaction with Li^+ and consequently more hindrance to its movement. The pronounced interaction between Li^+ and $TFSI^-$ in the presence of PCL, where in the PEO_0PCL_{100} system $TFSI^-$ is nearly always bound to Li^+ (as seen in the left panel of *Figure 4-5*), results in the MSD of $TFSI^-$ being very similar to that of Li^+ in this system.

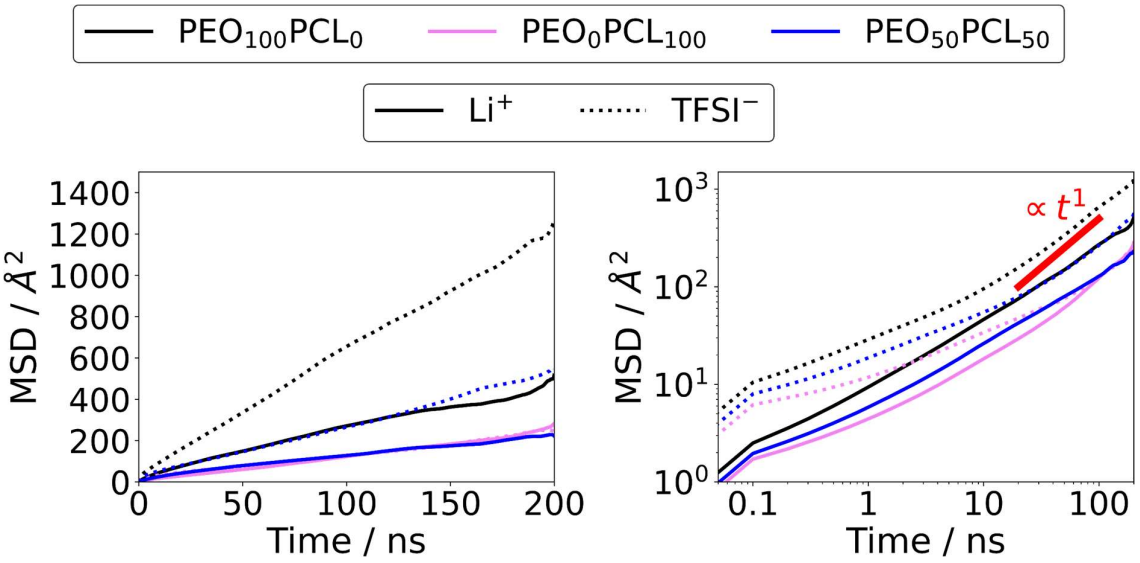

Figure 4-12: MSD of Li^+ (solid line) and $TFSI^-$ (dotted lines) for $PEO_{100}PCL_0$, PEO_0PCL_{100}, and $PEO_{50}PCL_{50}$ systems. The left panel displays the MSD in a linear scale, while the right panel shows the analysis in a logarithmic scale, with a reference line of slope equal to 1 (representing the Fickian regime) included.

These trends in the MSDs are corroborated by the calculated values of diffusion coefficients and Li TN (*Table 4-3*). Li^+ diffusion coefficient in the PEO_0PCL_{100} and $PEO_{50}PCL_{50}$ systems is nearly identical, while that of $TFSI^-$ diminishes with an increase in PCL ratio. Consequently, Li TN experiences an increment. The shift from $PEO_{100}PCL_0$ to $PEO_{50}PCL_{50}$ results in a modest increment (only 10%) in Li TN, given the reduction in mobility for both Li^+ and $TFSI^-$. However, further addition of PCL to the blend significantly restrains $TFSI^-$ mobility, while

Li^+ seems unaffected, producing an 80% increase in Li TN compared to the reference $PEO_{100}PCL_0$ system.

D ($x10^{-7}$ cm^2/s)	$PEO_{100}PCL_0$	PEO_0PCL_{100}	$PEO_{50}PCL_{50}$
D_{Li^+}	0.437	0.202	0.204
D_{TFSI^-}	1.096	0.190	0.443
Li TN	0.285	0.516	0.315

Table 4-3: Diffusion coefficients of the ionic species and Li TN for the investigated $PEO_{100}PCL_0$, PEO_0PCL_{100}, and $PEO_{50}PCL_{50}$ systems.

Representing the data in logarithmic scale (right panel of *Figure 4-12*) unveils additional insights into the short timescale mobility of ions. It is essential to note that the time axis in the MSD plots represents time intervals, not the simulation time (see *Section 2.2.5*). Interestingly, across all systems, $TFSI^-$ exhibits higher mobilities at short timescales than Li^+. Only in the PEO_0PCL_{100} system, when analyzing longer timescales, do the two curves tend to converge, resulting in similar diffusion coefficient values. However, this phenomenon is not observed in other systems. At these shot timescales (less than 10 ns), we are examining local movements rather than diffusivity effects. As Li^+ is a single atom, it cannot mirror the movements of $TFSI^-$ where the $-CF_3$ groups can move while the molecule is coordinated to Li^+. An important observation in logarithmic scales is that the curves deviate from the reference line with a slope of 1, indicating that the diffusive regime is not fully achieved in these simulations. Only the $TFSI^-$ curve in the $PEO_{100}PCL_0$ system approaches the unity slope at the longer times. This implies that while trends in the MSD curves are clear, the precise values of the diffusion coefficients should be analyzed with caution.

4.2.3. Experimental Validation

The conclusions drawn from the theoretical MD simulations regarding Li^+ diffusion mechanism's variations with the incorporation of PCL into a pure LiTFSI/PEO system were further validated through a series of experimental analyses. These experiments aimed to ascertain if real blends synthesized in the laboratory exhibited the same characteristics unveiled theoretically. It is important to note that other researchers conducted the experimental analyses, and although not directly performed by the author of this Thesis, their inclusion here is of paramount importance, as they critically validate the theoretical hypotheses presented. The integration of both theoretical and experimental analyses led to their combined publication as a unified piece of work *[200]*. However, it is worth nothing that the analyses presented in this Thesis offer a more in-depth understanding of the differences in Li^+ diffusion mechanisms

between PEO and PCL. These insights were gained through analyses conducted post-publication of the joint work, providing additional valuable information. All the following images have been reprinted or adapted with permission from *[200]*. Copyright 2020 American Chemical Society.

In these experimental analyses, two additional molar ratios ($PEO_{20}PCL_{80}$ and $PEO_{80}PCL_{20}$) were investigated apart from the three ratios studied theoretically. The objective was to gather data concerning Li^+ coordination environment in the presence of varying PCL concentrations. To achieve this, Raman and infrared (IR) spectroscopy analyses were performed, focusing on the S-N-S vibration of $TFSI^-$ and the C=O vibration of PCL, respectively *(Figure 4-13)*. In the left panel, the Raman spectra were centered on the S-N-S vibration of the $TFSI^-$. When $TFSI^-$ is isolated, this vibration occurs at 740 cm^{-1}. However, when it coordinates with Li^+, it shifts to a higher wavenumber, typically around 747 cm^{-1} *[201]*, *[202]*. The Raman spectra clearly illustrates the peak shift from the $PEO_{100}PCL_0$ system, where it indicates complete LiTFSI dissociation, to the PEO_0PCL_{100} system, where the interaction between Li^+ and $TFSI^-$ is maximized within the studied concentration range. In the intermediate ratios, the peak exhibits minimal shifts at low PCL concentrations, with a noticeable shift observed only at $PEO_{20}PCL_{80}$. This result aligns seamlessly with the data provided by the RDFs shown in *Figure 4-4*.

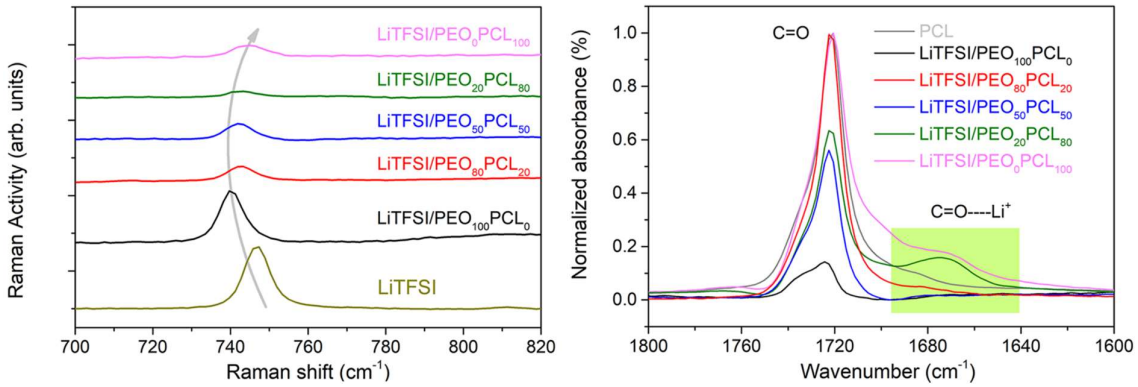

Figure 4-13: (Left) Raman spectra of the S-N-S vibration of LiTFSI for the different systems studied. (Right) IR spectra analysis of Li^+ interaction with the carbonyl oxygen of PCL.

Additionally, IR spectroscopy was employed, focusing on the C=O vibration of PCL (right panel of *Figure 4-13*). In its free state (neat PCL), this vibration is observed at 1720 cm^{-1} and a shift to smaller wavenumbers would be indicative of coordination with Li^+. The analysis revealed the appearance of a second peak only at higher PCL ratios ($PEO_{20}PCL_{80}$ and PEO_0PCL_{100}), confirming that below these concentrations, Li^+ does not coordinate with PCL but solely with PEO. This substantiates that PEO solvation mechanism has a stronger effect compared to PCL's. Once again, these results agree with the theoretical findings, particularly in the $PEO_{50}PCL_{50}$ system, where a low percentage of solvation in PCL was observed for Li^+.

The analyses conducted thus far affirm that only at higher PCL concentrations (above 80 % molar ratio) is Li^+ solvated within the PCL region of the blend. Moreover, only in this

environment does the LiTFSI salt remain undissociated, showcasing interaction between them. Shifting the focus to how these distinct solvation mechanisms affect ion mobility, we proceeded to measure the ionic conductivities (see *Figure 4-14*).

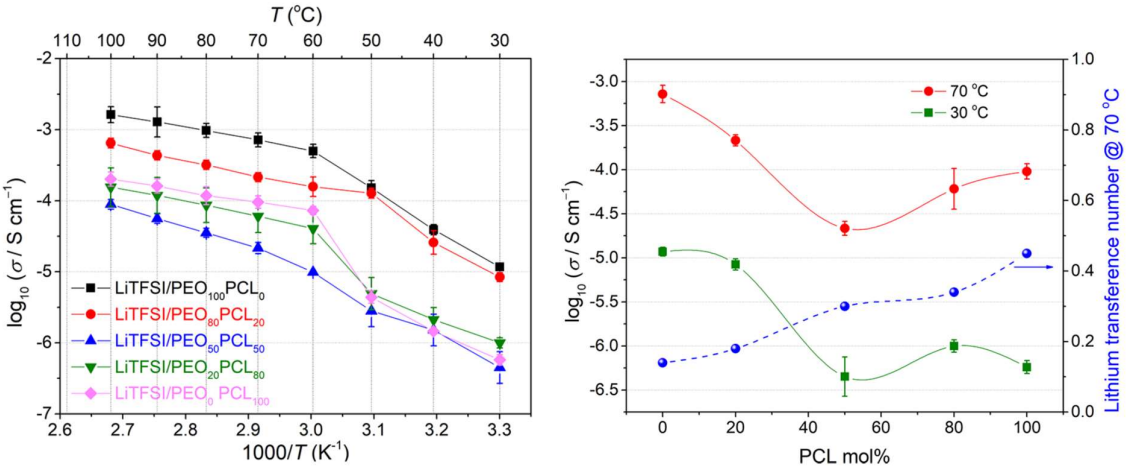

Figure 4-14: (Left) Arrhenius plots for different LiTFSI/PEO$_x$PCL$_y$ electrolytes. (Right) Ionic conductivity dependence on the content of PCL at 70 ºC and 30 ºC, with Li TN at 70 ºC.

Over the wide temperature range studied (100ºC - 30ºC), the $PEO_{100}PCL_0$ system shows the highest conductivity. All systems show a significant decline below 60 ºC due to the crystallization of both PEO and PCL. Comparing the pure 100% systems, the higher conductivity of $PEO_{100}PCL_0$ with respect to PEO_0PCL_{100} at all temperatures can be ascribed to the superior segmental mobility of the EO monomer. This observation aligns with the theoretical results (*Figure 4-12* and *Table 4-3*). When a small amount of PCL is added into the PEO system ($PEO_{80}PCL_{20}$), a notable reduction in conductivity is observed. However, when PEO is added to the PCL system ($PEO_{20}PCL_{80}$), similar conductivities to the PEO_0PCL_{100} system are obtained.

An intermediate performance might be expected for the $PEO_{50}PCL_{50}$ system; however, that was not the case. Instead, a minimum in ionic conductivity was observed throughout the temperature range for this system. This is illustrated more clearly in the right panel, where two temperatures (70ºC and 30ºC) are plotted against PCL content, alongside Li TN at 70ºC. Despite the observed minimum in ionic conductivity in the $PEO_{50}PCL_{50}$ system, Li TN does exhibit an increasing trend with an increase in PCL concentration. This trend aligns with the findings from MD simulations, where the maximum Li TN corresponded to the PEO_0PCL_{100} system.

4.2.4. Conclusion

On the basis of the combination of the presented theoretical and experimental results, we are in disposition of explaining the mechanism of solvation and diffusion of LiTFSI on a PCL

matrix, as well as understanding how this mechanism is affected in blend systems, where the molar ratio of PEO and PCL is varied from $PEO_{100}PCL_0$ to PEO_0PCL_{100}. A schematic representation of the mechanism proposed is provided in *Figure 4-15*.

In a neat PEO system, LiTFSI can undergo complete dissolution owing to the high chelation capability of ether monomers. Li^+ presents a semi-free movement within the PEO chain, moving to adjacent monomers. However, $TFSI^-$, lacking interaction with Li^+, showcases high diffusivity, while Li^+ continually drags the PEO chain with it. This provokes a high ionic conductivity, with a major contribution from $TFSI^-$, reflected in a low Li TN of approximately 0.2 in experimental measures and 0.28 in MD simulations. Conversely, in a neat PCL system, carboxyl oxygens do not possess the chelating effect required for complete LiTFSI salt dissociation. The solvation mechanism of Li^+ in this system involves both PCL and $TFSI^-$ in its coordination environment. Unlike PEO, Li^+ does not coordinate with consecutive CL monomers but anchors to 3 or 4 oxygens, which may not belong to the same chain. Li^+ can easily jump to other available positions, whether through interchain or intrachain jumps. This mechanism results in a reduced overall ionic conductivity compared to PEO. However, the reduction is more severe for $TFSI^-$, consequently increasing Li TN to approximately 0.5. This suggests a balanced contribution from Li^+ and $TFSI^-$ in the LiTFSI conductivity.

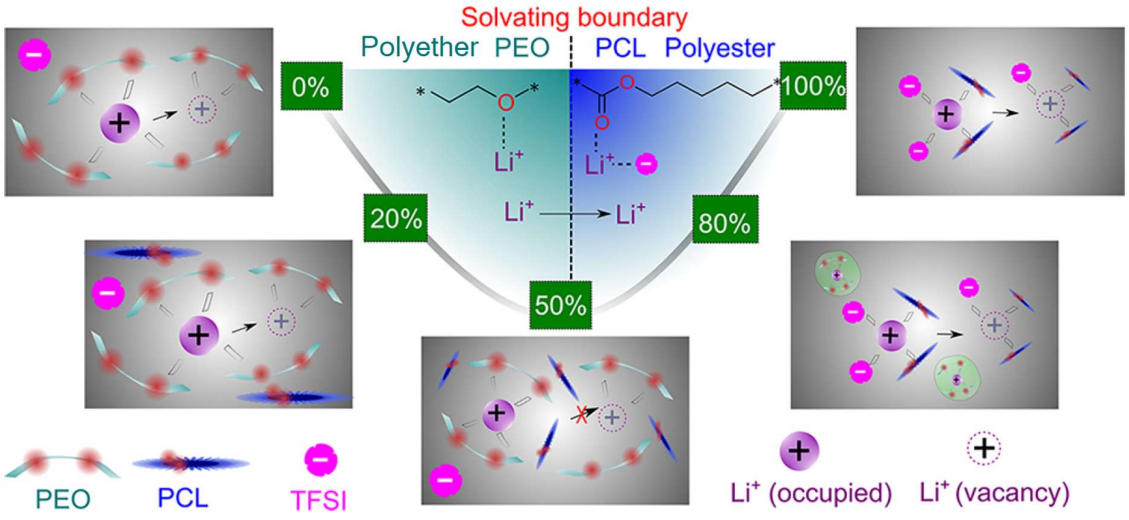

Figure 4-15: Schematic representation of the solvation and diffusion mechanism of the PEO-PCL blends and its modification based on the content of PCL. Adapted with permission from [200]. Copyright 2020 American Chemical Society.

When we move from a complete PEO system to a complete PCL system by varying the molar ratio between the two polymers, we observe that Li^+ preferentially coordinates with the PEO. This preference reduces available coordination spaces, saturating PEO as we replace it with PCL. The mobility of Li^+ decreases more rapidly than that of $TFSI^-$, resulting in a decrease in total ionic conductivity but an increase in Li TN. This trend persists until the molar content of PEO and PCL is approximately equal. In the $PEO_{50}PCL_{50}$ system, the saturation of PEO is nearing completion, and some Li^+ must jump into the PCL regions. In this situation, Li^+

mobility reaches its minimum, and $TFSI^-$ begins to experience hindered mobility due to the presence of Li^+ in the PCL regions, given that $TFSI^-$ coordinates with Li^+ in this environment. Consequently, this configuration yields a minimum in ionic conductivity, even as Li TN continues to rise. As we further increase the concentration of PCL and reduce PEO, more Li^+ are compelled to coordinate with PCL, incorporating $TFSI^-$ into their environment. This decreases their mobility and further elevates Li TN.

4.3. Increasing Salt Concentration: Polymer in Salt

4.3.1. Theoretical Background

SPEs can effectively mitigate the safety challenges associated with liquid electrolytes when in contact with Li^0 metal anodes in LMBs. The reduction of dendrite growth, owing to enhanced mechanical and chemical stability provided by polymers, is a well-known benefit *[66]*, *[68]*, resulting in significantly prolonged cycle-life for the battery devices. However, despite these advantages, the conductivities reached by conventional SPEs remain relatively low *[69]*, *[70]*.

This Thesis delves into various strategies aimed at enhancing the performance of LiTFSI/PEO-based SPEs in LMBs, which serve as the fundamental framework for most studies *[76]*, *[77]*, *[78]*. These strategies encompass alterations in the chemical structure of the lithium salt (detailed in *Sections 3.2* and *3.3*), seeking to establish novel interactions among molecules. Additionally, the investigation involves integrating the lithium salt with different polymer matrices, as discussed in *Section 4.2,* to explore alternative ionic diffusion mechanisms. The outcomes of these investigations have demonstrated that achieving enhanced electrochemical stability of the electrolyte and improved mobility characteristics is indeed feasible. However, a critical aspect of these systems that has yet to receive sufficient attention is ionic concentration. The conductivity of a system depends on both the velocity of the ionic species and its concentration. Even if the ions exhibit high mobility, a low concentration can lead to low overall conductivity, as there would be a scarcity of charge carriers moving through the electrolyte.

In this Thesis, all studies until now have been performed at low ionic concentrations (with a monomer-Li^+ ratio around r 20-1). Most research on similar SPEs typically spans concentrations between r 6-1 and r 32-1 *[78]*, *[79]*, *[203]*. These systems, where the polymer largely governs the behavior due to the low salt concentration, are termed “salt in polymer electrolytes”. Studies examining the influence of concentration on the diffusion properties of the system have been conducted *[168]*, *[204]*, *[205]*, revealing an increase in Li TN with minimal impact on ionic conductivity.

Following this tendency, we developed for this study the idea of pushing forward the ionic concentration of LiTFSI up to the regime of “polymer in salt” systems. Polymer in salt solid electrolytes (PISSEs) are a type of electrolyte in which the salt exceeds 50 wt. % *[206]*, *[207]*. These systems have been rarely studied due to the complexity of working with such concentrated systems. However, when done, they present high conductivities *[208]*, *[209]*. This arises from the formation of extensive amorphous salt regions due to the limited polymer content. Once understood the diffusion mechanism in PEO and PCL matrices (*Section 4.2*) at low concentrations, our aim is to investigate how increasing the LiTFSI concentration in pure PEO and PCL systems affects the mobility of Li^+ within the electrolyte. Starting with a relatively low concentration of r 6-1, we studied the extremes at r 1-2, r 1-4, and r 1-6 monomers per Li^+ (referred to as supersaturated systems henceforth as they share many characteristics). To prevent unwieldy and impractical system sizes, the number of polymer chains is systematically reduced as the salt concentration is increased, ensuring a roughly

constant total number of atoms and manageable system dimensions for the MD simulations (see *Table 4-4*).

	Number of LiTFSI	Number of polymer chains
r 6-1	120	30
r 1-2	576	12
r 1-4	768	8
r 1-6	864	6

Table 4-4: Number of LiTFSI species and polymer chains (PEO and PCL of 24 monomer length) at different salt concentrations.

MD simulations on the LiTFSI/PEO and LiTFSI/PCL at the four concentrations studied were performed using the detailed information on *Section 2.2.6*. However, some changes have been made to this procedure in this study. First, an extra optimization step is included. After the compression, instead of directly heating the systems up to the simulation temperature, we continue raising the temperature until reaching 600 K and include an NVT optimization step at this temperature. This is made to break possible metastable configurations. Then the systems are cooled down to the simulation temperature, which is kept at 343 K (70 ºC). Besides, the length of the simulation is increased to 400 ns (doubling the previous simulation times). This was made with the idea of reaching the Fickian regime more easily, since in previous studies was observed that this regime might be difficult to reach with only 200 ns of simulation. Like in the previous studies, the structure of $TFSI^-$ was optimized at DFT level to obtain the partial atomic charges with the ESP method *(Section 2.3.8*). The FF parameters of all the species can be found on *Appendix A.2*.

4.3.2. Theoretical Results

We started our theoretical analysis by computing the MSD to observe the effects of increasing salt concentration, transitioning from the salt in polymer regime to the polymer in salt regime (*Figure 4-16*). In the case of the LiTFSI/PEO system, as shown in a) and b) panels, we observe a significant disparity at concentration r 6-1 compared to the supersaturated systems. At r 6-1, the mobility of $TFSI^-$ is much higher than at other concentrations. Conversely, at supersaturated concentration, $TFSI^-$ diffusion is lower than that of Li^+. This difference is reflected in Li TN value, exceeding 0.5 (see *Table 4-5*). These values substantially surpass those observed at low concentrations (~ 0.2-0.3). Upon transitioning to the polymer in salt regime, the diffusivity of $TFSI^-$ is minimally affected by the increased concentration and remains nearly constant. On the

other hand, Li^+ exhibits an increase in mobility with concentration, peaking at r 1-4 and r 1-6, where it seems to stabilize. Plotting the MSD data on a logarithmic scale (b) panel), we clearly observe a distinction in Li^+ diffusion mechanisms between r 6-1 and the other concentrations. The former displays a slope lower than 1, while the latter closely aligns with the reference line, thus reaching the Fickian regime when analyzing movements at time steps exceeding approximately 100 ns.

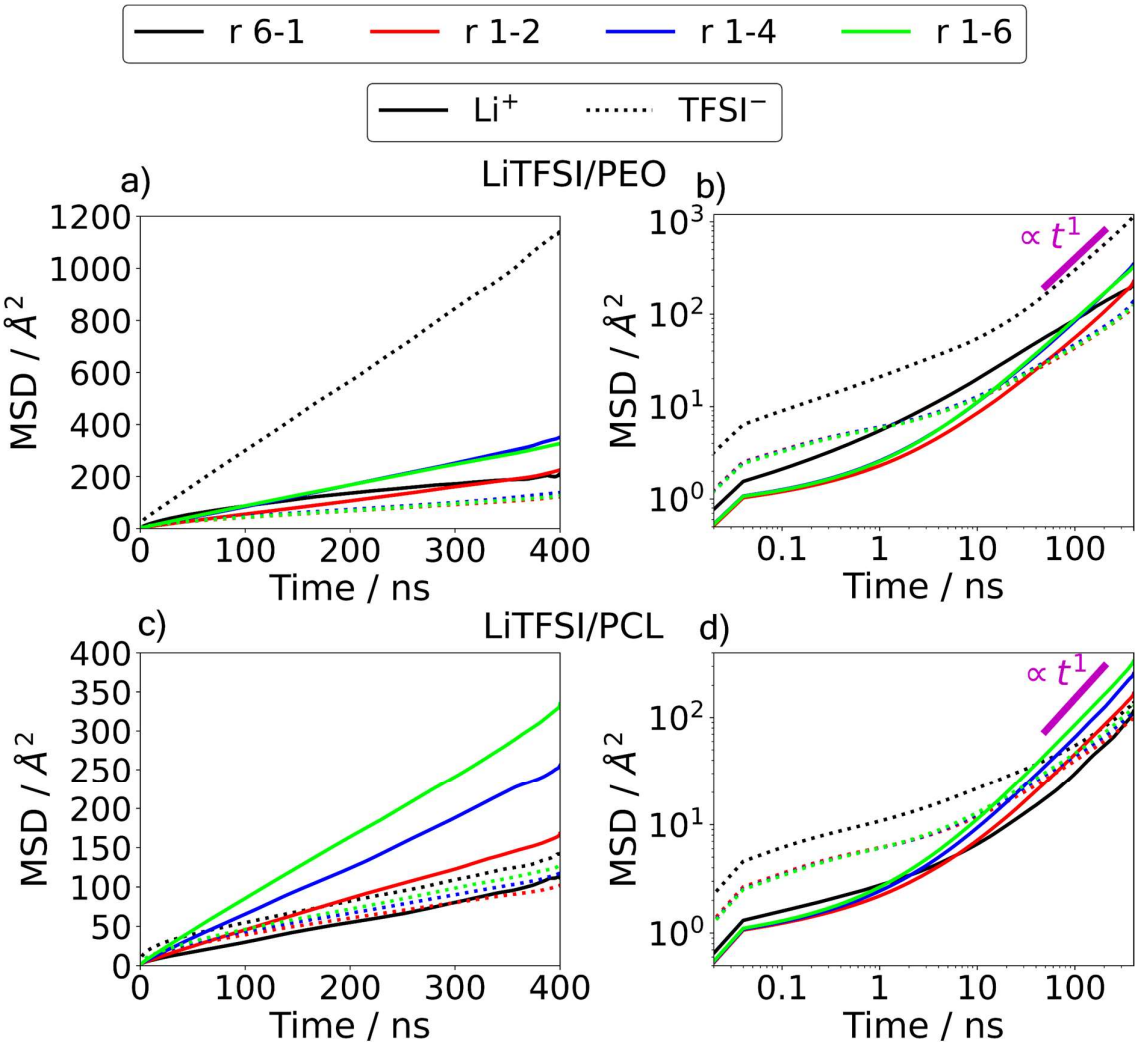

Figure 4-16: MSD of Li^+ (solid line) and $TFSI^-$ (dotted lines) for a) and b) LiTFSI/PEO and c) and d) LiTFSI/PCL systems for different concentrations. The a) and c) panels display the MSD in a linear scale, while the b) and d) panels show the analysis in a logarithmic scale, with a reference line of slope of 1 (representing the Fickian regime).

Moving now to the LiTFSI/PCL system (c) and d) panels), which possesses a different diffusion mechanism at low concentrations (*Section 4.2*), we observe a substantial increment of Li^+ diffusion with increasing concentration. However, for $TFSI^-$, the r 6-1 system presents higher anionic mobility. In the supersaturated systems, the diffusion of $TFSI^-$ increases with

concentration, but with lower mobility than at r 6-1. So, in the LiTFSI/PCL system, something must change when reaching the polymer in salt regime too. In logarithmic scale, $TFSI^-$ does not reach the diffusive regime at any concentration, but Li^+ reaches it more easily at higher concentrations.

Using this MSD data to compute the diffusion coefficients (*Table 4-5*), we clearly see the increment of diffusivity of Li^+ in both polymer matrices with increasing salt concentration, surpassing the values of $TFSI^-$ diffusion coefficients. This is attached to higher Li TNs, reaching values close to 0.75. Of note is the observation that at higher concentrations, the diffusion coefficients in both LiTFSI/PEO and LiTFSI/PCL systems tend to converge, suggesting that the diffusion mechanism of the ionic species becomes independent of the nature of the polymer matrix.

D ($x10^{-8}$ cm^2/s)	LiTFSI/PEO			LiTFSI/PCL		
	D_{Li+}	D_{TFSI-}	Li TN	D_{Li+}	D_{TFSI-}	Li TN
r 6-1	0.991	4.664	0.175	0.408	0.478	0.460
r 1-2	0.876	0.430	0.670	0.672	0.324	0.675
r 1-4	1.395	0.451	0.756	1.052	0.408	0.721
r 1-6	1.336	0.460	0.744	1.311	0.468	0.737

Table 4-5: Diffusion coefficients of the ionic species and Li TN for the investigated LTFSI/PEO and LiTFSI/PCL systems at different salt concentrations.

Based on these data, a significant transformation appears to occur within these systems as the salt concentration reaches the polymer in salt regime. Despite PEO and PCL having distinct solvation mechanisms at low concentrations, it is intriguing to see how these mechanisms change, resulting in remarkably similar ion diffusivity at higher concentrations. It is as if polymers no longer exert a significant influence on the diffusion process under these conditions.

To shed light into the supposition that the diffusion mechanism becomes independent of the polymer matrix when the regime of polymer in salt is reached, we examine now the coordination environments of Li^+ using RDF analysis (*Figure 4-17*). a) and c) panels depict Li^+-O(Polymer) interaction with PEO and PCL respectively (similarly to the previous study in *Section 4.2* for the case of PCL, only the carbonyl oxygen (O=) is taken into consideration for the analysis). A decrease of the height of the coordination peak is observed in the supersaturated systems, but the reduction of the CNs is much more exacerbated. Following the opposite trend, in b) and d) panels we track the Li^+-O($TFSI^-$) interaction. Here the interaction increases in the high concentration systems, with the corresponding increment in the Li TN.

This change in coordination is more pronounced in the LiTFSI/PEO system compared to the LiTFSI/PCL system. Specifically, at concentration r 6-1, Li^+ coordinates with 6 oxygen atoms from PEO and exhibits minimal coordination with $TFSI^-$ in the LiTFSI/PEO system. Conversely, in the LiTFSI/PCL system, Li^+ coordinates with approximately 3.5 oxygen atoms from PCL and 2.5 from $TFSI^-$. As the systems reach supersaturation, Li^+ environment becomes remarkably similar in both polymers, involving less than one oxygen atom from the polymer and around 5 from $TFSI^-$. The RDFs further validate that the polymer's contribution to Li^+ coordination diminishes, elucidating the convergence of MSD observed in both PEO and PCL systems.

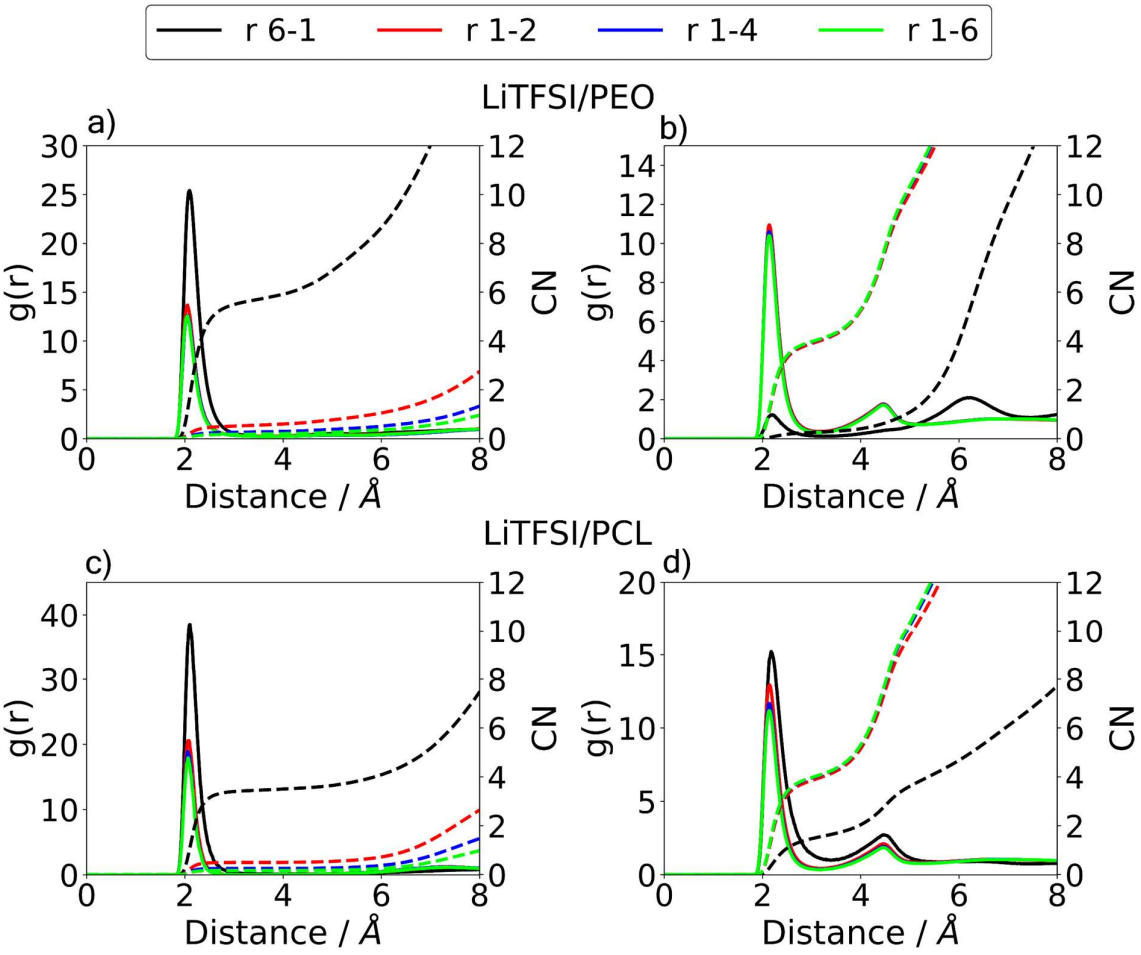

Figure 4-17: RDF (solid lines) and CN (dashed lines) analyses of the a) Li^+-O(PEO), b) Li^+-O($TFSI^-$) in LiTFSI/PEO, c) Li^+-O(PCL), and d) Li^+-O($TFSI^-$) in LiTFSI/PCL interactions at different concentrations.

The convergence in Li^+ behavior across different polymer matrices can be ascribed to the substantial number of salt molecules within the system, surpassing the polymer's capacity to dissolve them effectively. To confirm this supposition, we analyzed the saturation level of the polymers by looking at the percentage of monomers coordinated with a Li^+ (left panel of *Figure*

4-18). At concentration r 6-1, PEO is already at 90% saturation, while PCL is only at 60%. This discrepancy arises from the different solvation mechanism of these two polymers, previously discussed in *Section 4.2*. With an average of 6 monomers per Li^+, PEO effectively solvates most of Li^+ and could potentially reach 100% saturation. However, achieving complete occupation of all monomers would correspond to an idealized system, and in reality, some of the monomers remain unoccupied. In contrast, in PCL, Li^+ coordinates with an average of 3.5 oxygen atoms, resulting in a larger quantity of available oxygens.

At the supersaturated concentrations, nearly 100% of polymer oxygens coordinate with at least one Li^+ due to the significant number of Li^+ in relation to the number of monomers (*Table 4-4*). While achieving a perfect 100% saturation is unattainable, PEO consistently falls slightly below the level of saturation observed in PCL. This difference can be ascribed to the smaller spatial separation between oxygens in PEO, making it more challenging for crown structures to form consecutively along the entire chain. Conversely, in PCL, where coordination does not necessarily occur with consecutive monomers, it is easier for all monomers to coordinate with a Li^+.

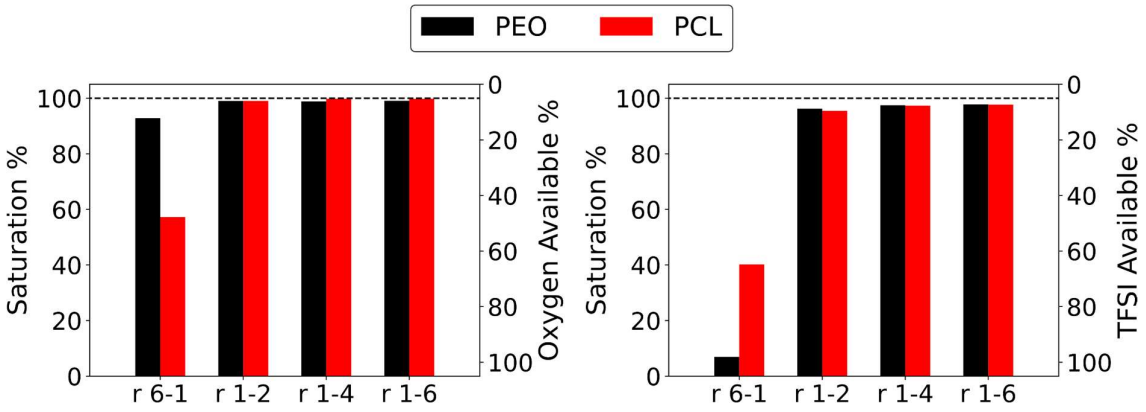

Figure 4-18: Percentage of monomer (left panel) and $TFSI^-$ (right panel) that are coordinated with Li^+ (i.e., percentage of saturation or, inversely, of availability) of the LiTFSI/PEO and LiTFSI/PCL systems at different concentrations.

We conducted a similar analysis with $TFSIs^-$, examining the percentage of molecules interacting with Li^+. In contrast to the polymers, at concentration r 6-1, the percentage of occupied $TFSIs^-$ is lower in PEO than in PCL. This discrepancy arises because $TFSI^-$ does not enter the coordination environment in PEO, whereas in PCL, it does so in conjunction with the polymer. As concentrations increase, the saturation level of $TFSI^-$ also rises significantly, resembling the trend observed in polymers, although not reaching as close to 100%. These analyses lead us to conclude that the converging behavior of the polymers is attributed to the fact that, in the polymer in salt regime, the polymers become completely saturated and the remaining Li^+ then form an amorphous Li-TFSI compound.

To delve deeper into the distinct nature of these supersaturated systems, we conducted a detailed analysis of the first coordination shell of Li^+ to discern whether interactions with the

polymers and $TFSI^-$ occur simultaneously or separately (*Figure 4-19*). The left panel displays results for the LiTFSI/PEO system, while the right panel depicts the LiTFSI/PCL system. At concentration r 6-1, the composition shows an intriguing contrast. In the LiTFSI/PEO system, dominant coordination occurs exclusively with the polymer, while in the LiTFSI/PCL system, coordination occurs concurrently with $TFSI^-$ and the polymer. Notably, at this low concentration, there is no distinct Li^+-$TFSI^-$ interaction observed in either system. This result is similar to the described in previous study (*Section 4.2*) performed at r 20-1, where the increment in salt concentration is mainly reflected in an increased Li^+-$TFSI^-$-PEO environment and no significant change is observed in LiTFSI/PCL system.

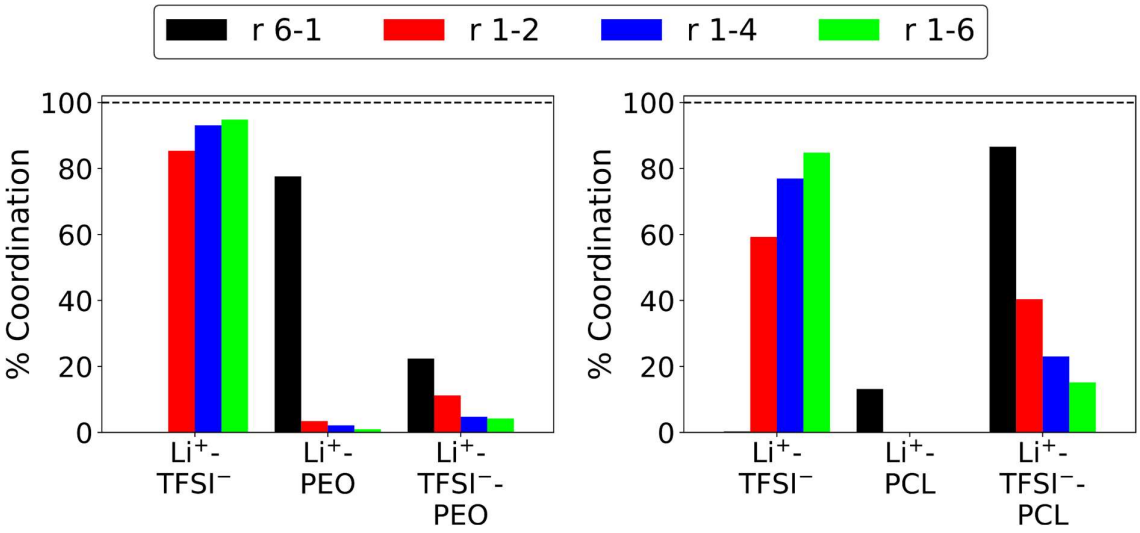

Figure 4-19: Percentage composition of the first solvation shell of Li^+ for the LiTFSI/PEO (left panel) and LiTFSI/PCL (right panel) at different concentrations.

As concentrations increase, aligning with the observed convergence tendency, the coordination environments become more similar. While the coordination environments in both PEO and PCL systems exhibit similarities, some notable differences emerge. First, PEO demonstrates the ability to completely solvate a small amount of Li^+ even at these concentrations, whereas no discernible Li^+-PCL interaction is observed. Second, the percentage of the Li^+-$TFSI^-$-Polymer environment is more significant in PCL than in PEO, with a smaller occurrence of the pure Li^+-$TFSI^-$ environment. This disparity arises from the minor Li^+-PEO interaction, which occupies part of the polymer. Consequently, when both the polymer and $TFSI^-$ are present, Li^+ coordinates with three or four monomers of PEO and only one or two of PCL. This dynamic allows for a higher number of Li^+ to be coordinated with PCL. However, the Li^+-$TFSI^-$ environment is the predominant in both polymers in the supersaturated regime, incrementing its importance with concentration, as expected. Here the polymer does not play any role in the diffusion of the ionic species as they move in a polymer-free environment. A snapshot of the LiTSI/PCL system at concentration r 1-2 can be seen in *Figure 4-20* where a significant amount of LiTFSI salt can be observed and much Li^+ is found in regions composed of only $TFSI^-$ and no PCL.

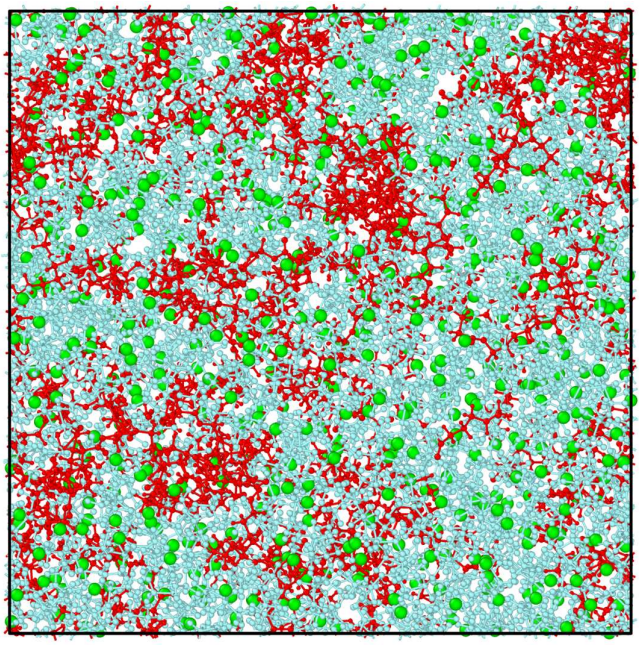

Figure 4-20: Snapshot of the LiTFSI/PCL system at r 1-2, with Li^+ in green, $TFSI^-$ in light blue, and PCL in red.

An intriguing aspect to analyze is the variation in Li^+ displacement as it transitions into polymer in salt configurations. To explore this, we tracked the movement of selected Li^+ by looking at their coordination points with other molecules in the system (*Figure 4-21*). Similar to previous studies in this Thesis, we distinguish between different monomers in the polymer panels, while in $TFSI^-$, differentiation is based on the molecules rather than individual oxygen atoms.

We show one example per polymer for the r 6-1 concentration (a) and d) panels for PEO and PCL, respectively), and two examples per polymer for the supersaturated concentrations. Among these two, one represents a Li^+ that interacts with the polymer (b) and e) panels for PEO and PCL, respectively), while the other does not interact with the polymer (c) and f) panels for PEO and PCL, respectively). Given the minor differences between concentrations r 1-2, r 1-4, and r 1-6, we have not differentiated between them in these plots. The purpose of these visualizations is to highlight significant differences in Li^+ diffusion mechanisms. As each plot represents a single Li^+ example, drawing conclusions from small differences between systems becomes challenging. An example from r 1-2 may be indistinguishable from another at r 1-6.

In the LiTFSI/PEO system, the influence of $TFSI^-$ at r 6-1 starts to be important (a) panel). At lower concentrations, the Li^+-$TFSI^-$ interaction is negligible. However, the high saturation of PEO significantly impacts Li^+ diffusion. With most monomers occupied, Li^+ movement along the chain is highly restricted, allowing $TFSI^-$ to enter the first coordination shell of Li^+ more easily. However, this interaction remains brief. In supersaturated concentrations, two different behaviors emerge depending on whether Li^+ interacts with PEO. When Li^+ interacts with PEO (b) panel), its movement is highly restricted within the PEO chain, nearly immobilizing it in its initial position. $TFSI^-$ is usually present in the environment too, but the duration of its interaction is longer compared to r 6-1. On the other hand, when no interaction occurs with

PEO (c) panel), Li^+ moves within the Li^+-$TFSI^-$ conglomerate, engaging in longer-lasting interactions with $TFSI^-$ molecules.

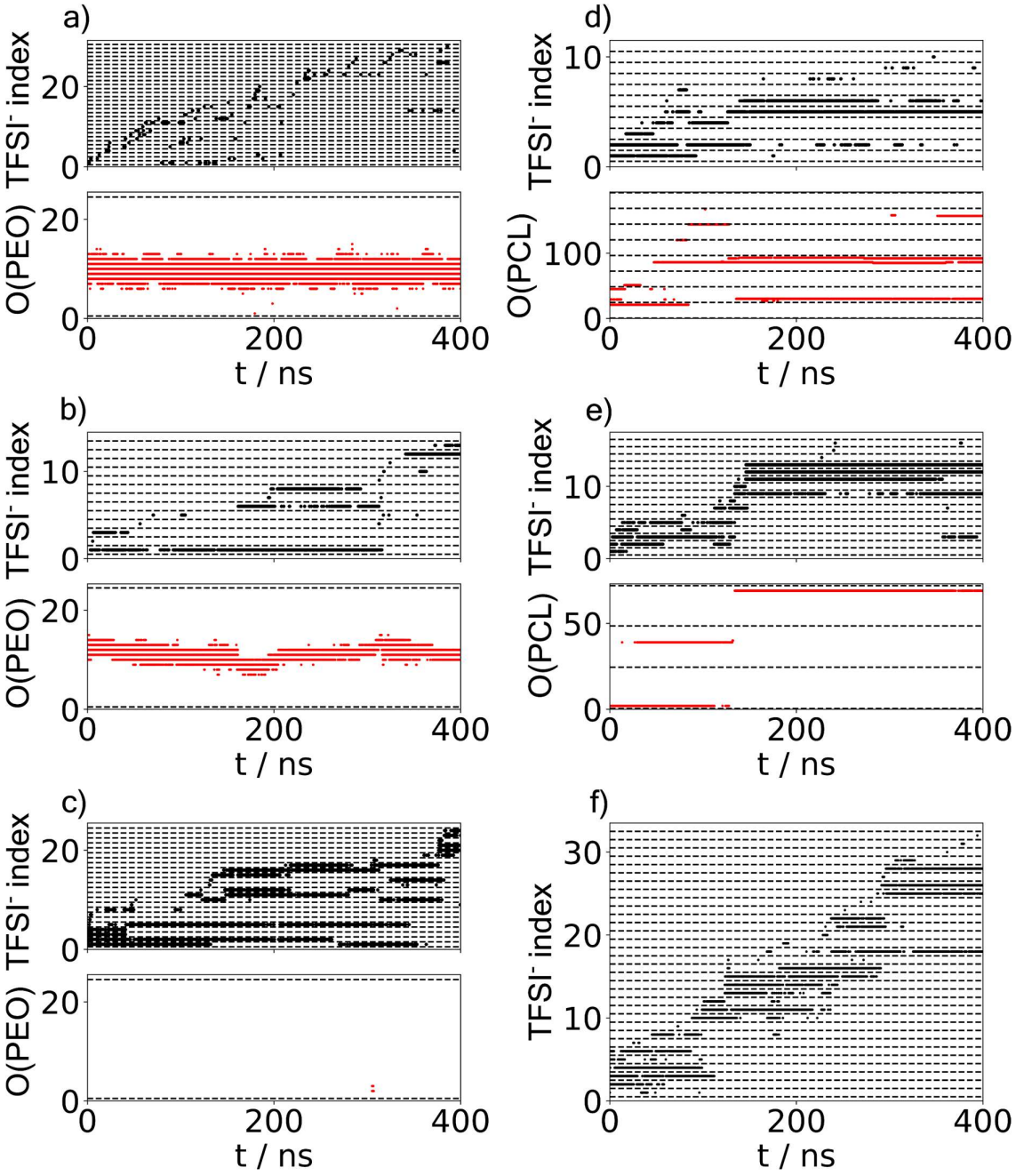

Figure 4-21: Representative example of Li^+ diffusion through the a) (r 6-1), b) and c) supersaturated LiTFSI/PEO and d) (r 6-1), e) and f) supersaturated LiTFSI/PCL systems, differentiating between the coordination with different $TFSIs^-$ and oxygen atoms of the polymer chains.

In the LiTFSI/PCL system, Li^+ diffusion mechanism at r 6-1 resembles what was previously described at r 20-1 in *Section 4.2*, albeit with a higher presence of $TFSI^-$ in the coordination

environment of Li^+ (d) panel). Intrachain movement form one monomer to an adjacent monomer does not exist; instead, the primary diffusion mechanism of Li^+ involves jumping to other available positions, usually with $TFSI^-$ molecules also in coordination. Like in the LiTFSI/PEO system, when the superconcentrated regime is reached in the LiTFSI/PCL system, the behavioral division is marked by the presence or absence of the polymer in the vicinity of Li^+. When the polymer is present (e) panel), $TFSI^-$ dominates over PCL, in contrast to the LiTFSI/PEO system. This distinction explains the higher percentage of Li^+-$TFSI^-$-PCL observed in *Figure 4-19* compared to Li^+-$TFSI^-$-PEO, as the stronger solvation power of PEO with Li^+ limits its coordination. Conversely, when PCL is absent (f) panel), the diffusion mechanism is similar to that of PEO (as expected), involving movement through the Li^+-$TFSI^-$ phase with some long-lasting interactions.

The convergence of results observed in MSD and RDF analyses (*Figure 4-16* and *Figure 4-17*, respectively) stems from over 80% of Li^+ not in contact with the polymer at r 1-6 concentration. This percentage of Li^+ interacts solely with $TFSI^-$ and moves independently of the polymer. Thus, the choice of polymer matrix to dissolve the salt does not significantly affect the solvation process; the salt will solvate until complete saturation, leaving a significant amount of salt to interact only with itself.

Continuing our analysis, we have seen that in the supersaturated systems, the amount of LiTFSI exceeds that of the polymer, and a substantial portion of the system consists of an amorphous phase of Li^+-$TFSI^-$. This led us to inquire about the ordering of these ions and whether they form small or large clusters. The clustering methodology followed was similar with the approach detailed in *[210]*. This algorithm is implemented in a Python code which can be found on *Appendix A.1*.

1) Initially, we select one Li^+ as a reference and identify all $TFSI^-$ coordinated with it. To accomplish this, we use a cutoff defined by the first minimum of the Li^+-O($TFSI^-$) RDF (as shown in the right panel of *Figure 4-17*), set at 3.25 Å.

2) Using each of $TFSI^-$ identified in the previous step as a reference, we conduct a reverse search to identify all Li^+ coordinated with them, using the same cutoff.

3) This procedure is iterated, using Li^+ as reference to look for new $TFSI^-$ and $TFSI^-$ as references to look for new Li^+ until all ions of the cluster have served as reference, and no new ions are added.

4) We repeat the above steps with a different Li^+ that is not already part of a found cluster until all Li^+ are either part of a cluster or have served as a reference.

Once the clusters have been identified, we can classify them and analyze the difference between the LiTFSI/PEO and LiTFSI/PCL systems at different concentrations. Depending on their size, the clusters have been divided into 6 categories: Isolated, Ion-Pair, Small-Cluster, Medium-Cluster, Large-Cluster, and Super-Cluster. Isolated clusters (referred to as *Iso* in the figures) are those formed only by 1 ion (they are no real clusters, but isolated ions). Ion-Pair clusters

(*Pairs*) are formed by 2 ions. Due to the method followed to define a cluster, Ion-Pairs will always be formed by 1 Li^+ and 1 $TFSI^-$. Small (*S*), Medium (*M*), and Large-Clusters (*L*) are differentiated by their size, less than 8 ions for *S*, between 9 and 16 ions for *M* and more than 16 ions for *L*. Finally, the Super-Cluster size (*Super*) is defined as a cluster formed by most of the ions of the system. This category is reserved for supersaturated systems, in which a differentiation between a cluster formed by for example 20 ions and another formed by 1000 ions was necessary.

Another classification can be easily made by the net charge of the clusters: positive, negative, and neutral. Positive clusters are those composed of more Li^+ than $TFSI^-$. Negative clusters possess more $TFSI^-$ than Li^+. And neutral clusters have the same number of Li^+ and $TFSI^-$. By definition Isolated clusters can only be positive or negative and Ion-Pair cluster, neutral. It is important to mention that given this cluster identification procedure, no clusters formed only by $TFSIs^-$ can be identified, as the first reference point is always a Li^+. All the $TFSIs^-$ that do not form part of any cluster once all Li^+ have served as reference will automatically form part of Isolated negative clusters (i.e., isolated $TFSI^-$). This is due to the fact that, as depicted in *Sections 3.2* and *3.3*, no clear interaction appears between $TFSIs^-$ and no cluster structure should be formed without Li^+ as bridge between different $TFSIs^-$. Another clarification is that in this analysis, the polymer has not been considered at any point, so a Li^+ that forms part of a cluster, can also be coordinated with the polymer. According to this, since no isolated Li^+ can be found in the systems, when we refer to Isolated positive clusters (i.e., isolated Li^+), these correspond to Li^+ that are completely solvated by the polymer.

After having defined the methodology for clusters identification and classification, we can now proceed with the analysis. *Figure 4-22* presents the distribution of clusters within the LiTFSI/PEO system at four concentrations. The probabilities illustrated in this figure have been appropriately weighed according to cluster sizes. Essentially, these probabilities represent the likelihood of finding an ion within a specific cluster, considering both its size and net charge (refer to *Eq. 4.1*).

$$Prob_n^q = \frac{n}{fN} \sum_{i=0}^{f} C_{n_i}{}^q \; x\; 100 \qquad 4.1$$

Where $Prob_n^q$ is the probability that an ion belongs to a cluster of size n and net charge q (where q denotes whether the net charge is positive, negative, or zero), $C_{n_i}{}^q$ is the number of clusters of size n and net charge q at the snapshot i, f is the number of snapshots analyzed in the simulation, and N is the total number of ions in the system.

This weighting is crucial to provide an accurate representation to the reader and to enhance comprehension of the system's characteristics, particularly within the context of supersaturated systems. Without this weighting, a raw probability analysis could potentially mislead the interpretation.

For instance, in a hypothetical scenario where 10 Li^+ are completely solvated by PEO, and 1000 Li^+ are part of a single supercluster, a simple probability analysis might suggest a 91 % occurrence of isolated positive clusters and a 9 % occurrence of supercluster. However, this interpretation would be misleading, as it would inaccurately imply that isolated positive clusters dominate the system, when, in reality, they do not. Applying *Eq 4.1* to this simple example (supposing a 10-snapshot simulation, all of them of equal cluster structure), it would lead to a $Prob^{-}_{1000}$ = 99% and $Prob^{+}_{1}$= 1 %. The net charge of the 1000-ion supercluster would be negative if we suppose all $TFSIs^-$ form part of it.

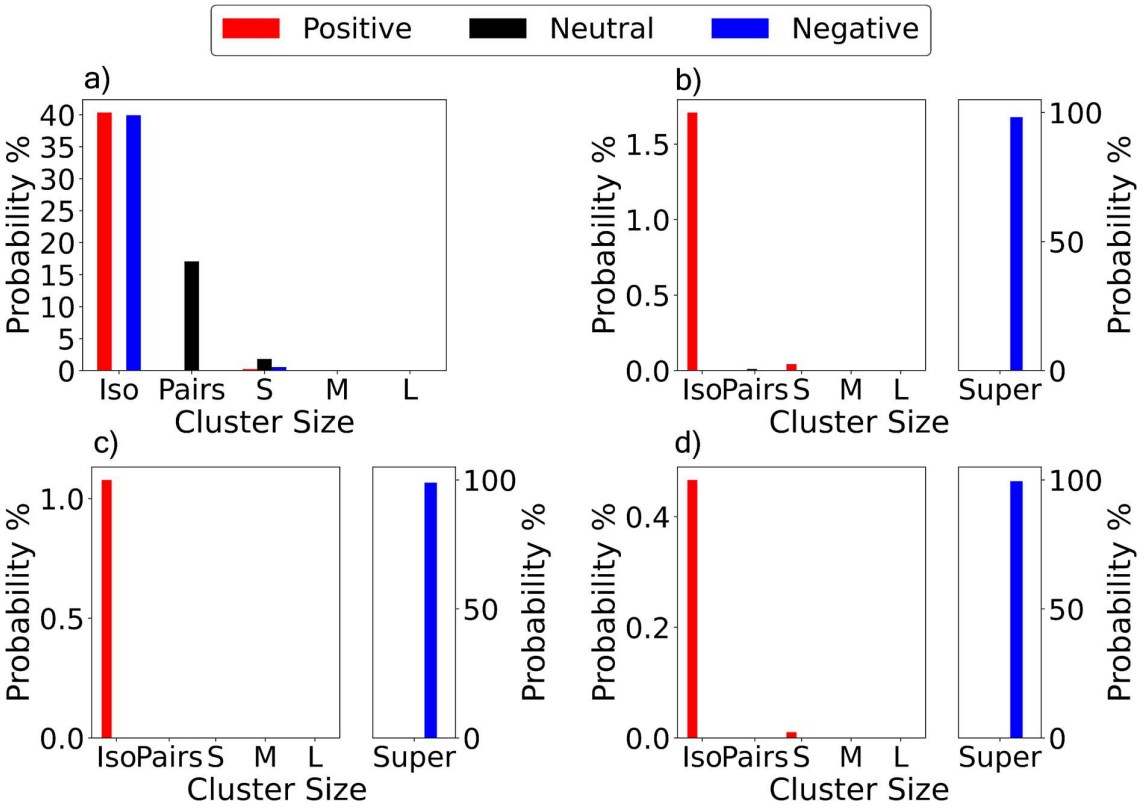

Figure 4-22: Analysis of the Li^+-$TFSI^-$ clusters formed in the LiTFSI/PEO system at a) r 6-1, b) r 1-2, c) r 1-4, and d) r 1-6 concentration, divided by size and net charge.

At r 6-1, PEO still dominates the behavior of the system, resulting in the predominance of isolated ions. Here we can see how the approximately 20% of Li^+-$TFSI^-$-PEO interaction shown in *Figure 4-19* takes the form of Ion-Pairs, with Li^+ and $TFSI^-$ interacting primarily among themselves and with PEO, excluding another ion. Additionally, the presence of Small Clusters, (preferably neutral in charge), is noted. However, there are no medium or large clusters formed at this stage.

In the remaining supersaturated concentrations, the cluster analysis yields distinct outcomes, albeit with striking similarities among them. These systems exhibit the formation of a single Super-Cluster, consistently negatively charged. Additionally, a diminishing presence of Isolated positive clusters is observed as the concentration increases, aligning with the Li^+-PEO

environment depicted in *Figure 4-19*. This indicates the powerful solvation capability of PEO, which can effectively solvate certain Li^+ even at exceedingly high concentrations. A residual probability is also noted for ion pairs and small clusters.

Further insights into the composition of the superclusters can be gleaned by analyzing the exact number of Li^+ and $TFSI^-$ constituents that form them (*Figure 4-23*). To facilitate the visualization, a line denoting neutral, equally composed clusters has been added into the plots. Besides, logarithmic scale is used to show the probability distribution since it drastically drops for the less abundant clusters.

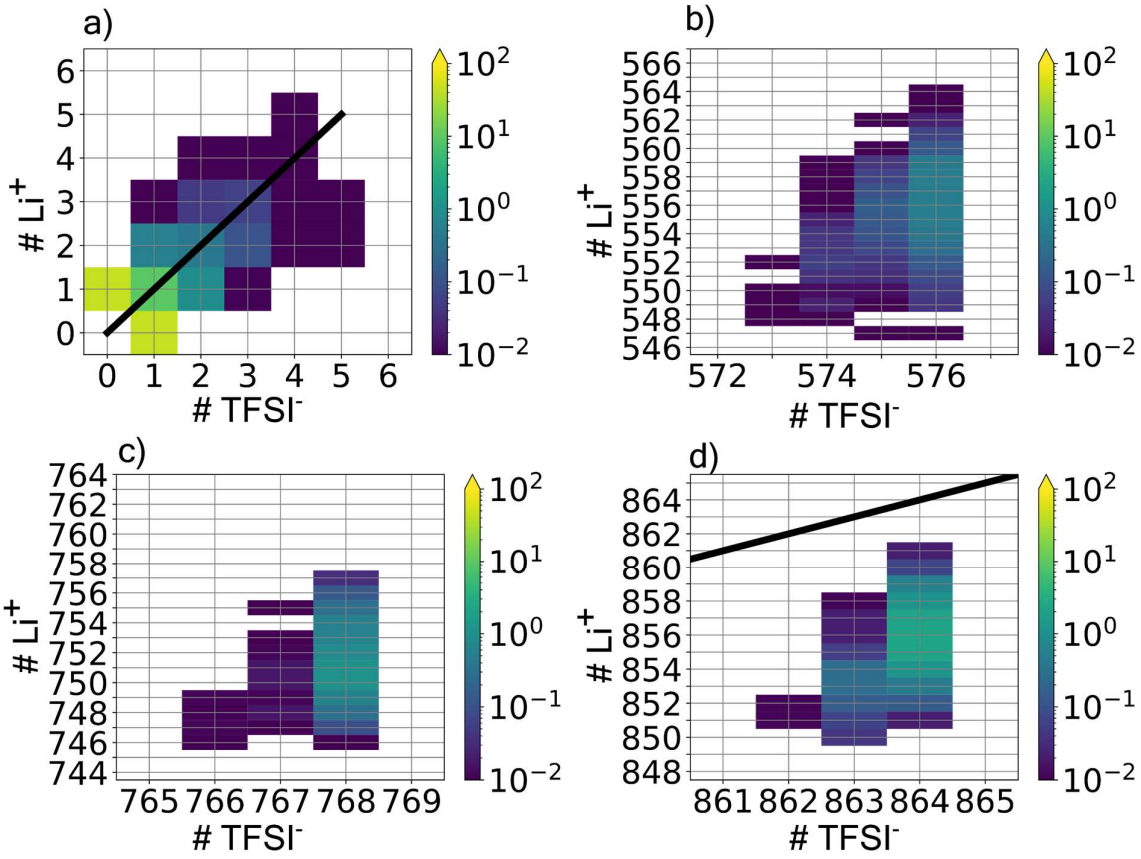

Figure 4-23: Maps with the probability distribution of the clusters in the LiTFSI/PEO system at a) r 6-1, b) r 1-2, c) r 1-4, and d) r 1-6 concentration with the exact number of Li^+ and $TFSI^-$ that compose the cluster and the line of equal composition marked.

In a) panel at r 6-1, the cluster map distribution is very symmetrical with respect to the neutral line. However, as we move to other concentrations –b) panel for r 1-2, c) for r 1-4, and d) for r 1-6)– the map shrinks, concentrating at certain compositions, especially favoring superclusters formed by all $TFSI^-$ in the system (see *Table 4-4* for the number of ions), and edging closer to neutrality.

Now analyzing the LiTFSI/PCL system, we observed a markedly distinct behavior. In *Figure 4-24*, the cluster analysis for these systems reveals a significant deviation in comparison to the LiTFSI/PEO system.

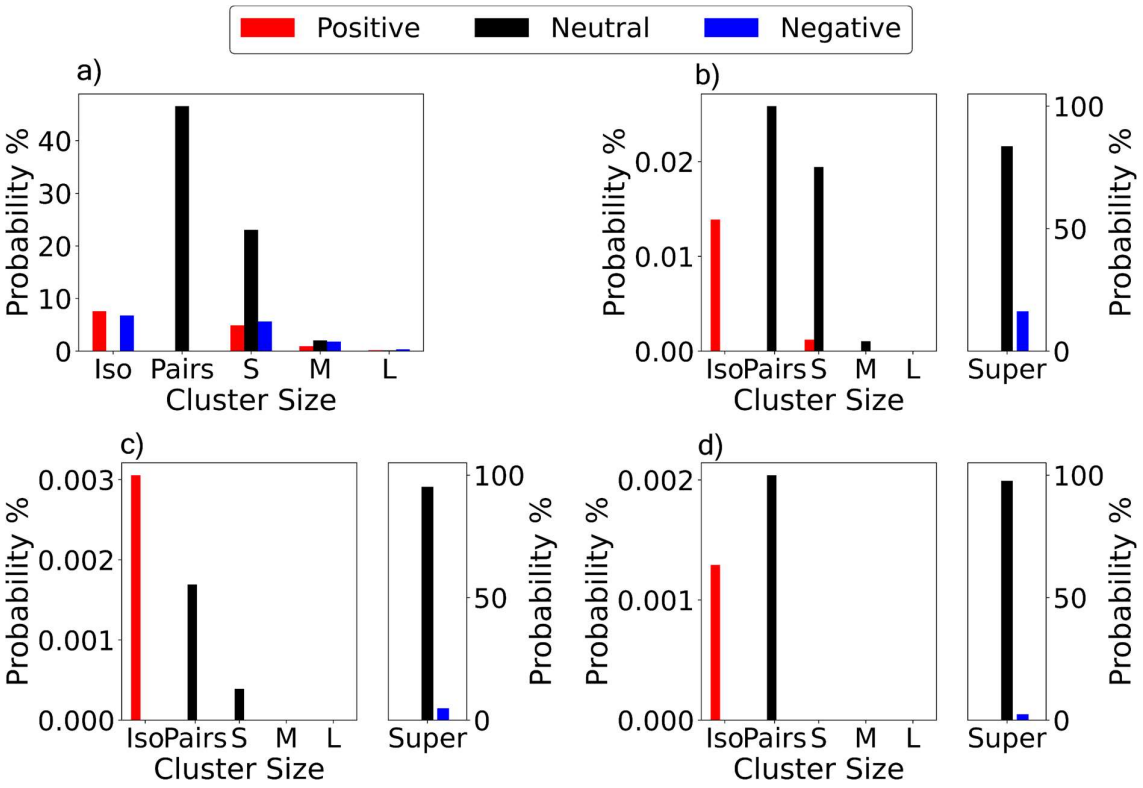

Figure 4-24: Analysis of the Li^+-$TFSI^-$ clusters formed in the LiTFSI/PCL system at a) r 6-1, b) r 1-2, c) r 1-4, and d) r 1-6 concentration, divided by size and net charge.

In the r 6-1 concentration (a) panel), the presence of isolated ions is drastically reduced. Ion pairs predominate at this concentration, accompanied by a notable abundance of small clusters (mainly of neutral charge), and a presence of clusters reaching medium and large sizes. As concentration increases, a substantial shift occurs. Most ions aggregate to form a neutral supercluster, with a minor presence of negative superclusters that diminishes as the concentration rises. Interestingly, in these supersaturated systems, the importance of non-supercluster formations becomes negligible. It remains evident that PCL's solvation ability with Li^+ is notably inferior to that of PEO. This is highlighted by the fact that even Li^+ coordinated with PCL becomes part of a supercluster.

The distribution maps (*Figure 4-25*) illustrate the contrast with PEO.

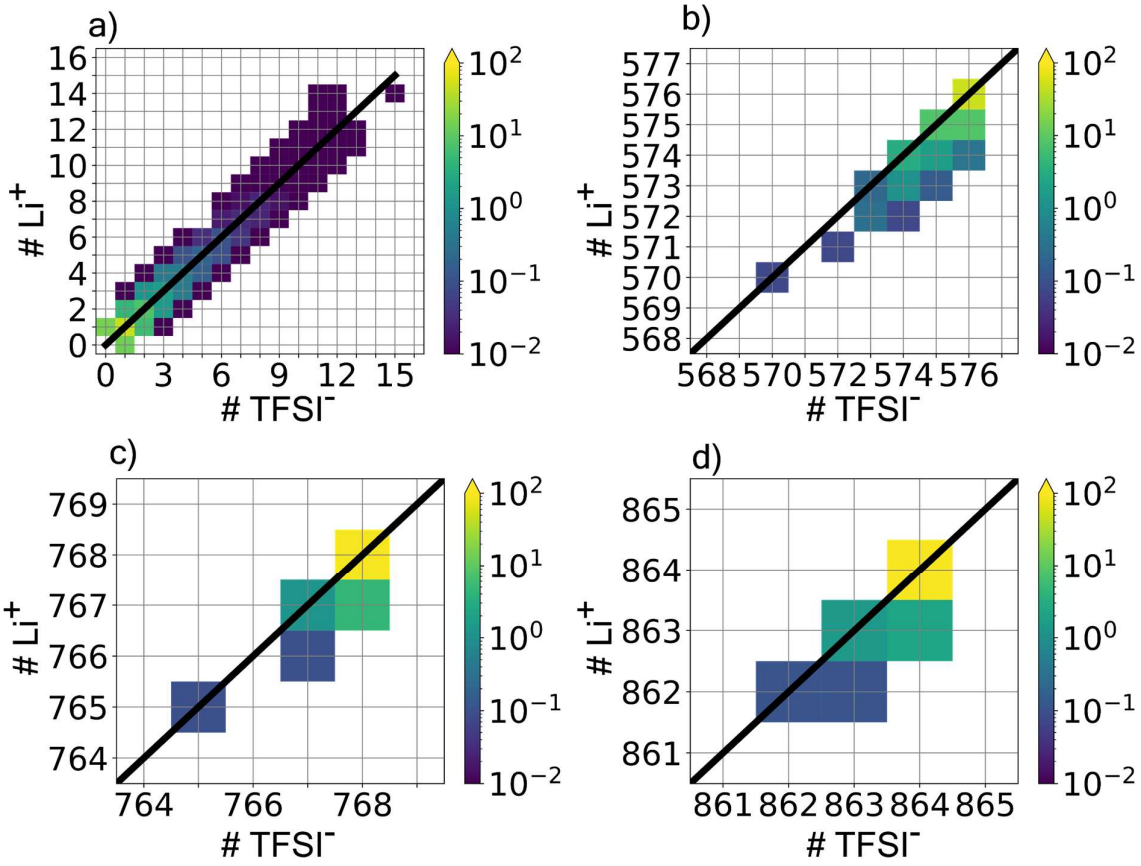

Figure 4-25: Maps with the probability distribution of the clusters in the LiTFSI/PCL system at a) r 6-1, b) r 1-2, c) r 1-4, and d) r 1-6 concentration with the exact number of Li^+ and $TFSI^-$ that compose the cluster and the line of equal composition marked.

At r 6-1, the map retains its characteristic symmetry concerning the neutral line but extends to encompass larger clusters. Unlike PEO, where clusters typically consist of no more than 5 ions of a particular type, PCL clusters can comprise up to 15 ions of each ion type. In the supersaturated systems, in contrast to PEO, the map displays a narrower spread, predominantly showcasing the supercluster formed by all Li^+ and $TFSI^-$ in the system. Additionally, the maps exhibit a slight tendency toward negative net charge, albeit only with one Li^+ less than $TFSI^-$.

4.3.3. Conclusion

This study elucidates the effects of increasing salt concentration in both the LiTFSI/PEO and LiTSI/PCL systems, eventually attaining the polymer in salt regime. In this regime, salt concentration reached levels where it overwhelms the polymers' capacity to solvate it. Upon reaching a Li^+ to monomer ratio of 6, the system behavior becomes invariant to the nature of the polymer. A small amount of Li^+ coordinates with the polymer until nearly all monomers are occupied, while the majority of ions conglomerate to form a singular supercluster. Within this supercluster, Li^+ can move in a $TFSI^-$ environment without direct interaction with the

polymer. Consequently, the diffusion mechanism of Li^+ becomes indifferent to the polymer matrix used for dissolving the salt.

This phenomenon leads to a notable augmentation in Li^+ diffusivity with increasing concentration, surpassing the mobility of $TFSI^-$. Consequently, Li TN values of up to 0.75 are achieved, signifying a considerably higher mobility of Li^+ compared to $TFSI^-$ within the Li^+-$TFSI^-$ phase of these systems. This pronounced Li^+ mobility can be attributed to the low dissociation energy of the LiTFSI salt, which enables swift jumps between different $TFSI^-$ molecules. Conversely, stronger ion-ion interactions would hinder Li^+ mobility by fostering enduring interactions.

However, the effect of the polymer is not entirely negligible. It affects the small amount of Li^+ it can solvate, highlighting distinctions in the supercluster composition between PEO and PCL systems. PEO, owing to its high solvation capabilities, is able to completely solvate some Li^+, resulting in a negatively charged supercluster. In contrast, PCL's limited solvation capacity leads to coordination of Li^+ with $TFSI^-$ within the supercluster, resulting in a primarily neutral supercluster composed of all system ions, particularly at exceedingly high salt concentrations.

General Summary and Conclusion

In this Thesis we have studied the possible application of different polymeric systems as electrolyte for LMBs. The pursuit of such technology emerges as indispensable for the necessity of more powerful energy storage devices, especially of the kind of small portable rechargeable batteries. The continuously growing market of electric vehicles would incredibly benefit from longer driving ranges and faster charges, and this could be the ultimate step to erase the actual dominance of fuel vehicles. However, it is evident that the current technology of LIBs falls short in meeting these challenges. Research and studies on LMBs have consistently pointed to them as the most promising alternative.

In our research, we used two distinct theoretical simulation techniques to delve into the atomistic level interactions that govern the behaviour of various systems, ultimately discerning which of these systems hold the greatest promise for future designs. These two techniques are classical MD simulations and *Ab Initio* DFT calculations.

The DFT calculations, although primarily utilized for pinpointing charge distribution on the anions constituting the lithium salt, play a crucial role in our studies. This is because ascribing specific, fixed charges to each atom is fundamental in defining the electrostatic interactions between atoms in MD simulations.

Classical MD simulations hove formed the cornerstone of this Thesis. While they may appear deceptively simple, relying on straightforward classical mechanics to define interatomic interactions, their predictive power has been more than substantiated. Their remarkable ability to replicate and forecast results observed in experimental macroscopic systems, employing simple approximations, underscores the indispensable role of MD simulations in this field of study.

In our analyses, we harnessed both conventional MD simulations techniques, including MSDs and RDFs, and novel analysis methods tailored to the unique characteristics of the systems under study. These specific analysis tools were developed in the Python programming language (*Appendix A.1*). Notably, the theoretical results extracted from our simulations were corroborated by experimental data gathered from real systems synthesized in laboratory settings.

This Thesis comprises four distinct studies, each delving into a unique facet of SPEs as the foundation for LMBs. The first two studies retained PEO as the polymer matrix in which the salt is dissolved, while altering the chemical structure of the $TFSI^-$. This was done with two distinct objectives: first, to hinder the anionic mobility, thereby enhancing the low Li TN value of the reference LiTFSI/PEO system (*Section 3.2*), and second, to introduce hydrogen into the anion to induce the formation of a more stable SEI and employ more environmentally friendly compounds (*Section 3.3*).

In the subsequent two studies, we shifted our focus to the polymer itself. Here we kept LiTFSI as the unalterable salt and varied the chemistry of the polymer, aiming for two specific objectives. The first was to elucidate the diffusion mechanism of Li^+ in PCL and in blends of

PEO and PCL (*Section 4.2*). The second focused on investigating the effect of increasing the salt content to the point where the polymer matrix becomes insignificant to the general behaviour of the system (*Section 4.3*).

- **First study**. We designed a new strategy to hinder the mobility of $TFSI^-$, which is a significant challenge within the LiTFSI/PEO system. The absence of intermolecular interactions among $TFSI^-$, both with one another and with PEO, allows them to move essentially freely without encountering any hinderances. Consequently, this results in too low Li TN values, typically around 0.2-0.3, indicating that most of the ionic conductivity originates from the anions rather than Li^+. Our approach involved introducing an aromatic ring in the extreme of the $TFSI^-$ (creating $BTFSI^-$ and $TPBTFSI^-$) to induce interactions between anions via $\pi - \pi$ stacking through electrostatic interactions and steric effects. The obtained reduction in anionic mobility was remarkable, incrementing Li TN values to approximately 0.35 in theoretical studies (limited by the atomic fix charges) and up to 0.75 in experimental measurements. Most importantly, this adjustment had only a minor impact on the overall ionic conductivity while enhancing the stability of the system. The theoretical analyses confirmed that an interaction between the aromatic rings did exist in certain geometrical configurations. Experimental investigations into the performance of these electrolytes revealed a substantial increase in cycle life, indicating the formation of a more stable SEI that curtailed dendrite growth. Notably, the LiBTFSI/PEO system outperformed our expectations, demonstrating more effective interaction between aromatic rings compared to the LiTPBTFSI/PEO system, thanks to the clean rings, and longer cyclability.

- **Second study**. We followed previous works which indicated that the substitution of one fluorine atom by hydrogen in the $-CF_3$ groups of $TFSI^-$, forming $DFTFSI^-$, entailed the formation of a much more stable SEI, which allowed for an increase in the cyclability of the cells. We made the same substitution in both $-CF_3$ groups, forming $DFSI^-$. The absence of these groups, changed to the more easily degradable $-CF_2H$ groups, converted $DFSI^-$ into an environment friendly molecule. We studied theoretically the effect of this change in the LiDFSI/PEO electrolyte and found that no large effect was observed. Specifically, the increment in the dissociation energy of the LiDFSI salt was not an impediment for a complete salt dissociation in PEO. Besides, the new hydrogen atoms interacted with the PEO, slightly hindering the general mobility of the anions, and reducing the conductivity. However, this reduction was by far overcome by the increment in stability provided by the new SEI formed by the decomposition products of $DFSI^-$, which allow for much longer cycle life compared to the standard LiTFSI/PEO system.

- **Third study**. We wanted to identify the diffusion mechanism of Li^+ in other polymer chemistry. Its movement throught PEO was already known and well characterized, with a segmental motion throught the PEO chain, coordinated with 6 consecutive oxygens, and some unusual, but not impossible, interchain jumps. In this movement, the intervention of $TFSI^-$ is residual. However, its diffusion mechanism inside a PCL matrix was not very clear. Thanks to the MD simulations we identified it. The carbonyl oxygen

of PCL, opposite to the ether oxygen of PEO, is not able to completely dissociate the LiTFSI salt. Besides, the larger monomer size and stronger electrostatic interaction with Li^+ prevents the movement of Li^+ inside the PCL chain. Overall, Li^+ coordinates with 3-4 oxygens of PCL, not necessarily from the same chain, and 1-2 $TFSI^-$ molecules. It can equally jump to other available space via intrachain or interchain pathways. Similarly, we identified the effect of mixing PEO and PCL in the same electrolyte in different ratios. The preferential solvation of Li^+ in PEO over PCL was observed as minor Li^+-PCL interaction appears unless the amount of PCL was much greater than PEO and the latter is already saturated. This way Li^+ has no other option than to coordinate with the PCL. The mobility of $TFSI^-$ is reduced as Li^+ coordinates with the PCL, since in this case it exists a Li^+-$TFSI^-$ interaction too. This produces an increment of Li TN attached to the increment content of PCL. However, the conductivity does not follow the same trend, but it experiences a minimum in the system composed of equal amount of PEO and PCL, produced by a mixing of effects (saturation of PEO which does not allow the movement of Li^+ and starting of Li^+-$TFSI^-$ interaction, which hinders the anion mobility).

- **Fourth study**. Here we examined the effect of increasing the concentration of LiTFSI in both pure PEO and PCL matrices, without blending them, until reaching the polymer in salt regime, where the salt represents more than 50 wt. %. We expanded the monomer-Li^+ ratio from a ratio of r 20-1 to a maximum of r 1-6, effectively multiplying the salt content by 120-fold. This significant increment led to Li TN values approaching 1 (~ 0.75), compared to the lower concentration systems, with only a minor reduction in Li^+ mobility. As macroscopic-scale conductivity relies on both ionic mobility and concentration, a substantial increment in ionic conductivity is anticipated in these polymer-in-salt systems. Another noteworthy discovery was the emergence of independence in ionic movement from the polymer in these higher concentrations. This phenomenon was attributed to the copious amount of salt dissolved in the systems, where even a small fraction of it completely saturates the polymer, while the remaining salt migrates within a large, unified cluster composed solely of Li^+ and $TFSI^-$. In this environment, the polymer ceases to play a significant role. The formation of such extensive supercluster, as opposed to smaller clusters, facilitates more efficient Li^+ diffusion. This improved diffusion is enabled by the relatively low dissociation energy of the LiTFSI salt, allowing Li^+ to move with minimal coordination to the $TFSI^-$, approaching nearly unhindered movement.

In conclusion, this Thesis underscores the effectiveness of MD simulations as an important tool for prediction and analysis within the realm of utilizing polymeric systems as electrolytes for LMBs. The standard LiTFSI/PEO system encounters a multitude of challenges when subjected to practical applications, necessitating the exploration of new alternatives. However, armed with the knowledge of these issues, we possess the capability to deliberately design innovative substitutes that address these challenges. Specifically, through the deliberate chemical modification of both the lithium salt and the polymer matrix, we can finely tune the behavior of these resulting systems according to our whim. In this Thesis, MD simulations have been instrumental in identifying the key atomic-level interactions governing these systems and

imparting upon them the attributes necessary for enhanced performance and safety. The insights garnered in this Thesis not only advance our understanding of existing systems, but also contribute to the future design of novel molecules, offering the potential for further improving the performance achieved by the systems investigated here.

Appendix

A.1. Python Codes Explanation

Throught the development of this Thesis, a series of Python codes have been coded to perform certain analysis over the MD simulation trajectories. These analyses are very specific to the systems and characteristics we wanted to study and could not be performed with the internal algorithmics of GROMACS, or with external tools such as TRAVIS (*[109]*, *[110]*). In this section, we elucidate the operational principles and underlying concepts of these custom scripts. Some of these codes are only tools for plotting data or making simple analyses. However, it is worthwhile to provide a concise overview of their functions as well.

These codes are accessible to the public, allowing any user to review, adapt, and apply them to their own MD simulations. It is important to remark that these codes have been developed by a Python enthusiast who aimed for maximum universality in their utility. However, it is worth highlighting that, due to their amateur origin, users may encounter errors when utilizing them.

As some of these codes are too extensive to be include in this Thesis, they are instead available at the GitHub repository (https://github.com/mcs-cice/Thesis-Sergio-Rodriguez-Python-Codes).

- **Analysis_RDF_MSD.py**

  This is a simple code which collects some useful functions to analyze the output files of the RDF and MSD analyses made with TRAVIS software. It includes functions to read the files, to compute the average value and error of a set of data, and to compute the CN corresponding to the first minimum of the RDF. The most important function is the one used to compute the diffusion coefficient from an MSD. The procedure is explained with examples in *Section 2.2.5*. As a summary, it takes the MSD data in logarithmic scale and plots a tangent line of slope equal to 1 in each of the points. Defining an upper and lower limit, we select the region of data which follows the reference line during the larger time. These data are fitted according to *Eq. 2.38* to obtain the diffusion coefficient.

- **Process_Trajectory_PDB_to_TXT.py**

  This code reads a trajectory file, output from GROMACS, in .pdb format and extracts the crucial information in a .txt format file. This output .txt trajectory is used as input for all the following analysis codes. This is done to reduce the weight of the trajectory file and better manage them. Also, to have a standard format for the trajectory files independently of their origin, and to be easily processed with the following codes. The average reduction of weight is of ~ 58 %, thus it weighs less than half after this processing. The code writes the time of the snapshot and its box side length (supposed cubic) at the start of each snapshot. Then, for each atom it writes its number and

identification name, the number and identification name of the molecule it belongs to and the 3 spatial coordinates. The only change the code introduces is that, in case some atom identification names are identical (e.g., the case where all the carbon atoms are named as C independently of the molecule they belong to), it adds letter by letter the identification name of the molecule they belong to until all the atoms have a unique identification name.

From here, the following codes share the same structure to analyze the required characteristic. They take as input file the trajectory file processed by the *Process_Trajectory_PDB_&_TXT.py* code and the first steps of the analyses are common.

1) First, an identification of the system we are dealing with is made, with the identification names of the molecules and atoms, number and times of the snapshots, indexes of the molecules, etc. This creates a series of libraries of data for latter easily identify the atoms and molecules.

2) Then the code asks for a series of useful information. It starts asking for the reference and observable atoms/molecules to identify the interactions to study. It also asks for the interval time to perform the analysis. Finally, for the cutoff to define a distance limit for the interaction length. Although this information questionary might slightly vary from code to code. It is important to remark that when an atom is chosen as reference or observable, only these types of atoms are considered, while if a molecule is chosen, all the atoms of the molecule can interact.

3) After that, we go through all the snapshots inside the interval time chosen, extracting the information from the reference and observable atoms/molecules position. Since the MD simulations apply PBC to the simulation box, we also must apply them. To not duplicate the interactions, PBC are only applied, as a general rule, to the observable atoms/molecules. In function of the cutoff chosen for the interactions, the atoms that are closer than the cutoff (plus a small distance to avoid approximation errors), are replicated in the corresponding positions. This creates what is commonly named in the codes as "hypercube": the simulation box of a certain snapshot including the observable atoms/molecules and the necessary replicas applying PBC.

4) Finally, we measure the distances between each reference and observable atom/molecule (including the imaginary atoms replicated by PBC) and the information of those observables that are closer than the cutoff is saved for future analysis.

Let us see what different analyses have been made with this information.

- **Coordination_&_Venn_Diagram.py**

  This code is used to analyze the coordination environment of Li^+. With the information of the observable atoms/molecules, we classify it by different environments. The exact

composition of the first coordination shell of Li^+ is categorized by the number of cases of each different environment, differentiating between the number of molecules of each type. At the end of the file, the sum of each different environment is shown in total number of cases and in percentage. In case we only pick 2 or 3 different observables, the code also plots the composition percentage in a Venn diagram (see example on *Figure A-1*). Besides, if only 2 observables are chosen, it also plots a probability map of the number of different molecules of each type (see example of *Figure A-2*).

However, for clearer visualization and comparison of the data, we decided to plot the results in bar plots in this Thesis (*Figure 3-6*, *Figure 3-20*, *Figure 4-5*, and *Figure 4-19*).

The results are written in a *Coord.txt* file to be able to pick the information of different systems and plot them together. As can be seen in the following example, in the *Coord.txt* files appear more information than what is shown in the plots.

This is an example of *Coord.txt* file and the plots of the analysis corresponding to the PEO_0PCL_{100} system of *Section 4.2* study, with *OY* as the identification name of TFSI⁻´s oxygens and *O2* of PCL´s:

COORDINATION RESULTS:

Isolated LI Atoms: 0

Coordination with 1 type of molecule:

LI coordinating only with OY:

1 different molecule: 0

2 different molecule: 11

3 different molecule: 103

LI coordinating only with O2:

1 different molecule: 4

2 different molecule: 385

3 different molecule: 2195

4 different molecule: 2359

5 different molecule: 1497

6 different molecule: 30

Coordination with 2 types of molecules:

LI coordinating with OY and O2:

		Diff. O2				
		1	2	3	4	5
	1	791.0	11532.0	33280.0	13416.0	139.0
Diff. OY	2	1326.0	9209.0	2914.0	162.0	0.0
	3	425.0	262.0	0.0	0.0	0.0

Isolated LI: 0 (0.00 %)

LI coordinated with OY: 114 (0.14 %)

LI coordinated with O2: 6470 (8.08 %)

LI coordinated with OY and O2: 73456 (91.77 %)

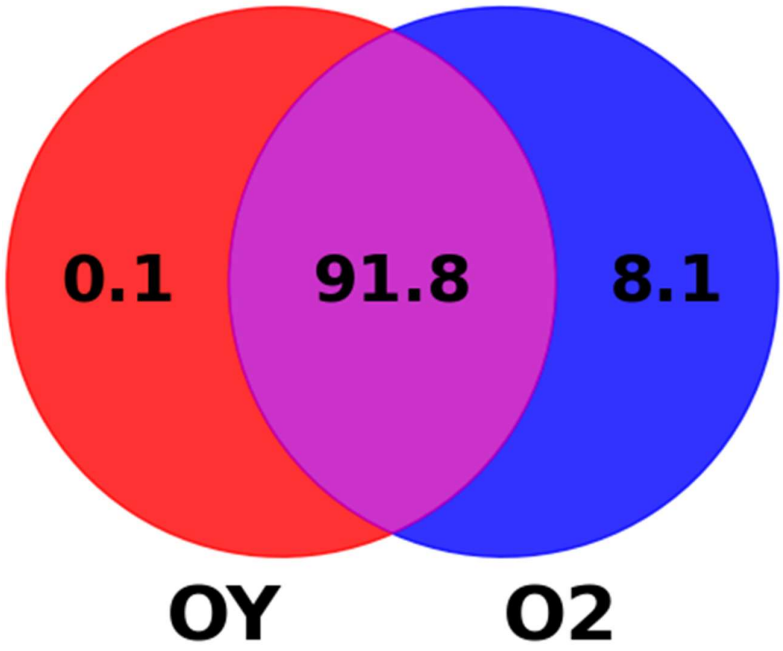

Figure A-1: Venn diagram of the percentage composition of Li^+ first coordination shell in the PEO_0PCL_{100} system of Section 4.2.

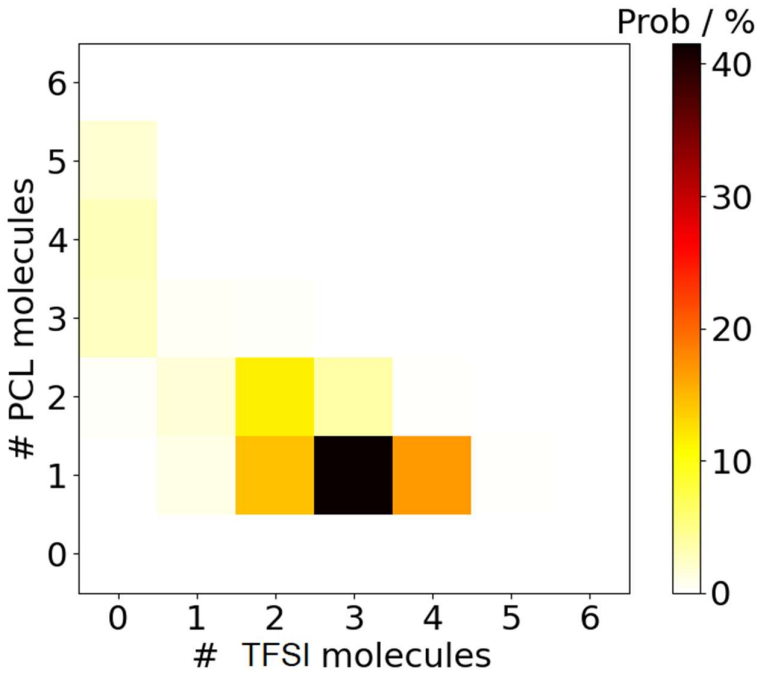

Figure A-2: Probability map of the number of PCL and $TFSI^-$ molecules that form Li^+ first coordination shell in the PEO_0PCL_{100} system of Section 4.2.

- **Saturation_Level.py**

  This code is used to analyze the saturation level of the molecules with respect to a certain observable molecule. Here the selection of reference and observable atoms/molecules is a bit different, since we only select the molecule of which we want to measure the saturation of the others (in our case is Li^+). From the other molecules, we can select if the coordination is produced with only some atoms or with the entire molecule. It serves to differentiate between polymers, where the saturation is measured by monomers, and anions, where it is measured by entire molecules. Then, it averages the level of saturation of each molecule type with respect to Li^+ in each snapshot and prints the results on the terminal. Then it is just a matter of collecting data from different systems and plotting them together to compare them. This analysis can be found in *Figure 4-18*, where the different saturation levels are plotted in bars.

- **Lithium_Diffusion_Mechanism.py**

  This code is used to analyze the movement of Li^+ through the system by considering the exact points of coordination with the rest of the molecules of the system. The code asks to differentiate which observable molecules should be treated as polymer structures. In case a system is treated as polymer structure, differentiation between atoms is made. If no polymer structure is selected, the molecule will be treated as a single entity and no

internal structure is differentiated. It also allows us to choose the number of reference atoms the user wants to analyze at the same time to have a clearer view of the general behaviour.

Then, the coordination points are shown differentiated by molecule type and, inside each, by temporal order. The molecule that coordinates in the first snapshot is referred to as molecule number 1, the first different molecule that enters the coordination environment will be done as molecule 2, and so on. This is made to observe if during the whole simulation the same molecules enter and leave the coordination environment or if they are always new ones. Also, this molecule numeration is made to show in the plots only the molecules that actually coordinate with the reference atom and omit empty molecules. In case a polymer structure is selected, internal structure is shown to visually observe the displacement of Li^+ or the different jumps it makes.

This analysis can be found in *Figure 3-7*, *Figure 3-21*, *Figure 4-7*, *Figure 4-8*, and *Figure 4-21*.

- **Residence_Time.py**

  This code serves to analyze the residence times of the interactions inside the system, specifically for the interactions of Li^+ with the other molecules. This code is similar to *Lithium_Diffusion_Mechanism.py*, but once we have the coordination points, instead of plotting them, we measure the length of the interactions. As explained in the main text (*Section 4.2.2*), to avoid random changes in the coordination environment due to thermal agitations, single-snapshots changes are omitted. Both for considering interactions that only last one snapshot (omitting them), and for interruptions in the interactions that are absent only one snapshot (continuing the interaction).

  We take each of the points of coordination. If that point was already present in previous snapshot, we omit it (as it has already been analyzed). If not, we look from this time till the coordination is lost.

  Then, we create a distribution of how many interactions exist in terms of their time length. In the analyses performed with this code in this Thesis, all the distributions present a similar shape, except for the interactions with PEO chains, with a high probability of short-length, and a fast exponential decay to interactions lengths that are only present a couple of times in the simulation (see an example in *Figure A-3*). Then, depending on the interaction, it can disappear from a certain time length or to have cases until the total of the simulation time. These data are also written into a *Res_Times.txt* file.

  This is an example of *Res_Times.txt* file, corresponding to the $PEO_{100}PCL_0$ system of *Section 4.2* study, with the residence times of the Li^+-$TFSI^-$ and Li^+-PEO chain interactions. For simplicity, the time lengths that does not have interactions are not saved.

Time TFSI / ns 0.2 0.3 0.4 0.5 0.6 0.7 0.8 0.9 1.0 1.1 1.2 1.3
1.4 1.5 1.6 1.8 1.9 2.0 2.1 2.3 2.4 2.6 2.7 2.8
2.9 3.1 3.3 3.6 4.1 4.7 7.0 7.8 8.3 8.7

Cases TFSI 191.0 59.0 47.0 34.0 17.0 16.0 16.0 7.0 9.0 5.0 6.0
2.0 2.0 3.0 1.0 1.0 1.0 1.0 2.0 2.0 2.0 1.0 1.0
2.0 1.0 1.0 1.0 1.0 1.0 1.0 1.0 1.0 1.0 1.0

Time PEO / ns 0.2 0.3 0.4 0.5 0.7 0.8 0.9 1.2 1.3 1.5 1.6 3.1
6.5 13.6 15.5 27.8 28.0 42.0 44.4 45.5 53.0 55.1
55.3 90.9 91.0 95.2 99.3 99.5 105.2 112.4 130.4
154.2 154.7 192.1 195.1 197.9 198.1 198.4 198.9
199.9 200.0

Cases PEO 24.0 10.0 1.0 6.0 5.0 1.0 1.0 1.0 2.0 1.0 1.0 1.0
1.0 1.0 1.0 1.0 1.0 1.0 1.0 1.0 1.0 1.0 1.0 1.0
1.0 1.0 1.0 1.0 1.0 1.0 1.0 1.0 1.0 1.0 1.0 1.0
1.0 1.0 1.0 1.0 30.0

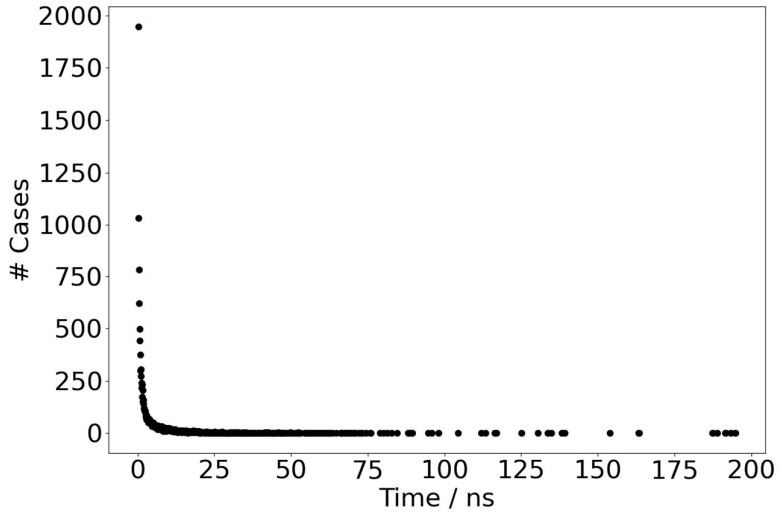

Figure A-3: Example of the number of cases of the Li^+-PEO monomer interaction in the $PEO_{100}PCL_0$ system of the study of Section 4.2 in function of the interaction time length.

Another code (*Plot_Res_Times.py*) is used to read, analyze, and plot different Res_Times.txt files.

- **Plot_Res_Times.py**

  This code reads multiple *Res_Times.txt* files coming from the analysis performed with the *Cluster_Analysis.py* code, differentiating between all the interactions in each file. Then, it asks for which of them we want to make the analysis, plotting the data in logarithmic scale and obtaining the values to compare the systems: slope of the exponential decay region and the width of the minimal probability value region (as explained in the main text in *Section 4.2.2*)

  This analysis can be found in *Table 4-1* and *Table 4-2*. Then it also plots the comparative between the different systems observed on *Figure 4-10* and *Figure 4-11*.

- **Cluster_Analysis.py**

  This code is used to analyze the clusters formed by the ionic species of the systems. The code, as explained in the main text (*Section 4.3.2*), follows the approximation suggested by Molinari et al. *[210]*, where an iterative search of positive and negative neighbors is made.

  The code writes the information into a *Clusters.txt* file. For each snapshot, it writes the molecule numbers corresponding to the anions, to the cations and the time of the snapshot. Then, in each line, a different cluster can be found. In the case of isolated anions, they do not appear in the list, but knowing the number of anion molecules, and the number of them that form part of the different clusters, we can easily extract the number of isolated anions.

  Here we can find an example of the first snapshot of the *Clusters.txt* file for the PEO_0PCL_{100} system of the study of *Section 4.2*:

  Anion: 1 - 40

  Cation: 81 - 120

  t = 0 ps

  81

  82 28

  83 39

  84 31

  85

  86

  87 32 40 118 30 94 12

88 29 34 103 27 35 96 112 26 1 100

89 36 38

90 10 11

91 15

92

93

95 3 4

97 18

98

99 17

101 7

102 13

104 5 9 25 117 107 19

105 37

106

108 6

109 22

110

111

113

114 20 21 120 2

115 33

116

119 8

Since this analysis can be very time consuming, especially in the supersaturated systems of *Section 4.3*, the posterior classification and further analysis is made with another code (*Plot_Clusters.py*).

- **Plot_Clusters.py**

  This code reads one of the *Clusters.txt* files created by the *Clusters_Analysis.py* code. It analyzes the clusters of all the snapshots classifying them by size and net charge (as explained in the main text in *Section 4.3.2*).

  It possesses an option to check at each point of the classification that no cluster or ion has been lost. Then, it plots the results in two separate ways. First, by size and net charge in probability bars (*Figure 4-22* and *Figure 4-24*) and second in a probability map where the exact number or each ions is shown (*Figure 4-23* and *Figure 4-25*).

A.2. Force Field Parameters

- **TFSI**

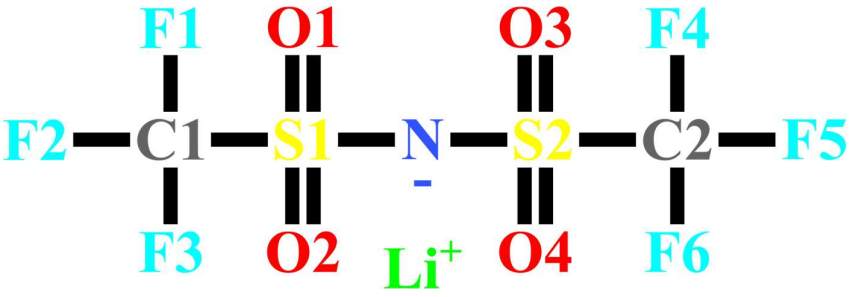

Figure A-4: Schematic representation and atom identification of Li-TFSI.

Atom	Charge / e	Atom	Charge / e
C1	0.032	S2	0.548
F1	-0.051	O3	-0.293
F2	-0.045	O4	-0.317
F3	-0.050	C2	-0.037
S1	0.505	F4	-0.017
O1	-0.294	F5	-0.036
O2	-0.303	F6	-0.043
N	-0.299	Li	0.7000

Table A-1: Partial atomic charges of Li-TFSI, with a scale factor of 0.7 applied.

Atom	σ / Å	ε / kJ mol^{-1}
C	3.50	0.276
F	2.95	0.222
S	3.55	1.046
O	2.96	0.711
N	3.25	0.711
Li	2.13	0.076

Table A-2: Lennard-Jones parameters of Li-TFSI.

Bond	Radius / Å	K_b / kJ mol^{-1} Å^{-2}	Angle	θ / degree	K_θ / kJ mol^{-1} rad^{-2}
C-F	1.332	3071.056	F-C-F	109.1	644.336
C-S	1.770	2845.120	F-C-S	109.5	418.400
S-O	1.440	5857.600	C-S-O	108.9	619.232
S-N	1.670	3631.712	C-S-N	103.0	836.800
			N-S-O	107.0	1004.160
			O-S-O	119.0	870.232
			S-N-S	125.6	671.000

Torsion	C_0 / kJ mol^{-1}	C_1 / kJ mol^{-1}	C_2 / kJ mol^{-1}	C_3 / kJ mol^{-1}	C_4 / kJ mol^{-1}	C_5 / kJ mol^{-1}
F-C-S-O	0.7255	2.1765	0.0000	-2.9020	0.0000	0.0000
F-C-S-N	0.6610	1.9830	0.000	-2.6440	0.0000	0.0000
C-S-N-S	45.4636	-36.3221	-18.7348	5.755	4.335883	0.0000
S-N-S-O	-0.0075	-0.0225	0.0000	0.0300	0.0000	0.0000

Table A-3: Force field parameters for the bond, angle, and dihedral interactions (in Rickaert-Bellemans form) of Li-TFSI.

- **DFSI**

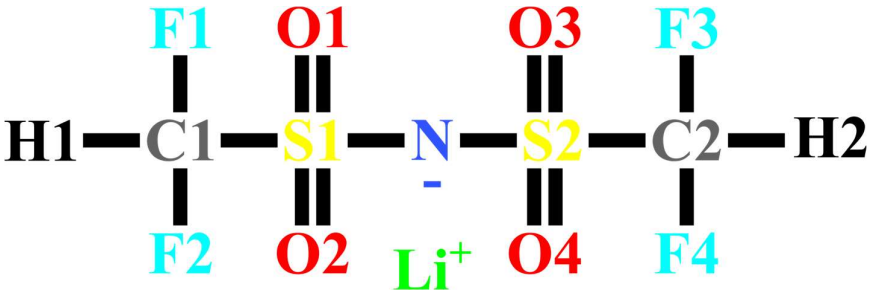

Figure A-5: Schematic representation and atom identification of Li-DFSI.

Atom	Charge / e	Atom	Charge / e
C1	-0.235	S2	0.485
F1	-0.048	O3	-0.332
F2	-0.068	O4	-0.298
H1	0.158	C2	-0.127
S1	0.394	F4	-0.028
O1	-0.289	F5	-0.040
O2	-0.279	F6	0.208
N	-0.201	Li	0.7000

Table A-4: Partial atomic charges of Li-DFSI, with a scale factor of 0.7 applied.

Atom	σ / Å	ε / kJ mol^{-1}
C	3.50	0.276
F	2.95	0.222
S	3.55	1.046
H	2.50	0.126
O	2.96	0.711
N	3.25	0.711
Li	2.13	0.076

Table A-5: Lennard-Jones parameters of Li-DFSI.

Bond	Radius / Å	K_b / kJ mol^{-1} Å^{-2}	Angle	θ / degree	K_θ / kJ mol^{-1} rad^{-2}
C-F	1.332	3071.056	F-C-F	109.1	644.336
C-H	1.090	2845.120	F-C-S	109.5	418.400
C-S	1.770	2845.120	C-S-O	108.9	619.232
S-O	1.440	5857.600	C-S-N	103.0	836.800
S-N	1.670	3631.712	N-S-O	107.0	1004.160
			O-S-O	119.0	870.232
			S-N-S	125.6	671.000
			F-C-H	107.0	334.720
			H-C-S	109.5	292.880

Torsion	C_0 / kJ mol^{-1}	C_1 / kJ mol^{-1}	C_2 / kJ mol^{-1}	C_3 / kJ mol^{-1}	C_4 / kJ mol^{-1}	C_5 / kJ mol^{-1}
F-C-S-O	0.7255	2.1765	0.0000	-2.9020	0.0000	0.0000
F-C-S-N	0.6610	1.9830	0.000	-2.6440	0.0000	0.0000
C-S-N-S	45.4636	-36.3221	-18.7348	5.755	4.335883	0.0000
S-N-S-O	-0.0075	-0.0225	0.0000	0.0300	0.0000	0.0000
H-C-S-O	0.0000	0.0000	0.0000	0.0000	0.0000	0.0000
H-C-S-N	0.0000	0.0000	0.0000	0.0000	0.0000	0.0000

Table A-6: Force field parameters for the bond, angle, and dihedral interactions (in Rickaert-Bellemans form) of Li-DFSI.

- **BTFSI**

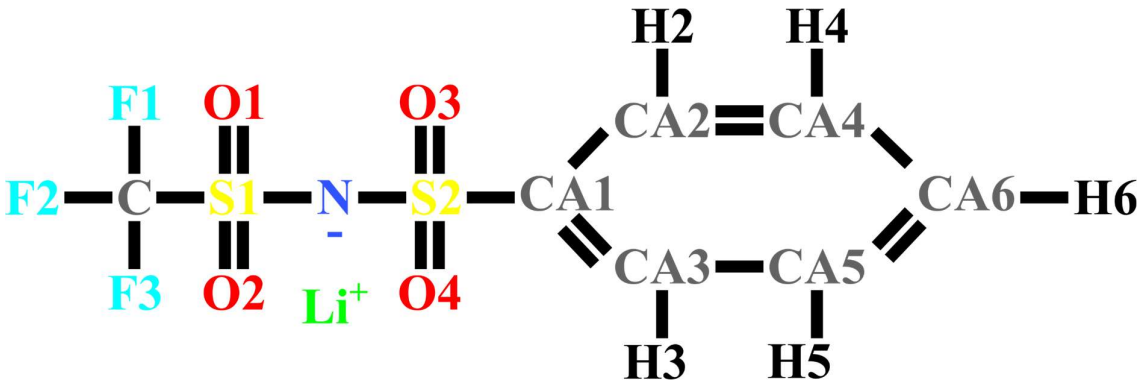

Figure A-6: Schematic representation and atom identification of Li-BTFSI.

Atom	Charge / e	Atom	Charge / e
C	0.101	CA2	-0.129
F1	-0.086	CA3	-0.016
F2	-0.062	CA4	-0.048
F3	-0.080	CA5	-0.115
S1	0.597	CA6	-0.110
O1	-0.331	H2	0.122
O2	-0.350	H3	0.082
N	-0.361	H4	0.068
S2	0.669	H5	0.083
O3	-0.374	H6	0.081
O4	-0.365	LI	0.7
CA1	-0.076		

Table A-7: Partial atomic charges of Li-BTFSI, with a scale factor of 0.7 applied.

Atom	σ / Å	ε / kJ mol^{-1}
C	3.50	0.276
F	2.95	0.222
S	3.55	1.046
O	2.96	0.711
N	3.25	0.711
CA	3.55	0.293
H	2.42	0.126
Li	2.13	0.076

Table A-8: Lennard-Jones parameters of Li-BTFSI.

Bond	Radius / Å	K_b / kJ mol^{-1} Å^{-2}	Angle	θ / degree	K_θ / kJ mol^{-1} rad^{-2}
F-C	1.332	3071.056	F-C-F	109.1	644.336
C-S	1.770	2845.120	S-C-F	109.5	418.400
S-O	1.440	5857.600	C-S-O	108.9	619.232
S-N	1.670	3631.712	O-S-O	119.0	870.272
S-CA	1.770	2845.120	O-S-N	107.0	1004.160
CA-CA	1.400	3924.592	C-S-N	103.0	836.800
CA-H	1.080	3071.056	S-N-S	125.6	671.000
			N-S-CA	103.0	836.800
			O-S-CA	107.2	619.232
			S-CA-CA	119.4	711.280
			CA-CA-CA	120.0	527.184
			CA-CA-H	120.0	292.880

Table A-9: Force field parameters for the bond and angle interactions of Li-BTFSI.

Torsion	C_0 / kJ mol^{-1}	C_1 / kJ mol^{-1}	C_2 / kJ mol^{-1}	C_3 / kJ mol^{-1}	C_4 / kJ mol^{-1}	C_5 / kJ mol^{-1}
F-C-S-O	0.7255	2.1765	0.0000	-2.9020	0.0000	0.0000
F-C-S-N	0.6610	1.9830	0.000	-2.6440	0.0000	0.0000
S-N-S-O	-0.0075	-0.0225	0.0000	0.0300	0.0000	0.0000
C-S-N-S	45.4636	-36.3221	-18.7348	5.755	4.33588	0.0000
S-N-S-CA	45.4636	-36.3221	-18.7348	5.755	4.33588	0.0000
N-S-CA-CA	0.0063	-4.1986	3.2133	0.9791	0.0000	0.0000
O-S-CA-CA	0.0000	0.0000	0.0000	0.0000	0.0000	0.0000
S-CA-CA-CA	30.3340	0.0000	-30.3340	0.0000	0.0000	0.0000
S-CA-CA-H	30.3340	0.0000	-30.3340	0.0000	0.0000	0.0000
CA-CA-CA-CA	30.3340	0.0000	-30.3340	0.0000	0.0000	0.0000
CA-CA-CA-H	30.3340	0.0000	-30.3340	0.0000	0.0000	0.0000
H-CA-CA-H	30.3340	0.0000	-30.3340	0.0000	0.0000	0.0000

Table A-10: Force field parameters for the dihedral interactions (in Rickaert-Bellemans form) of Li-BTFSI.

- **TPBTFSI**

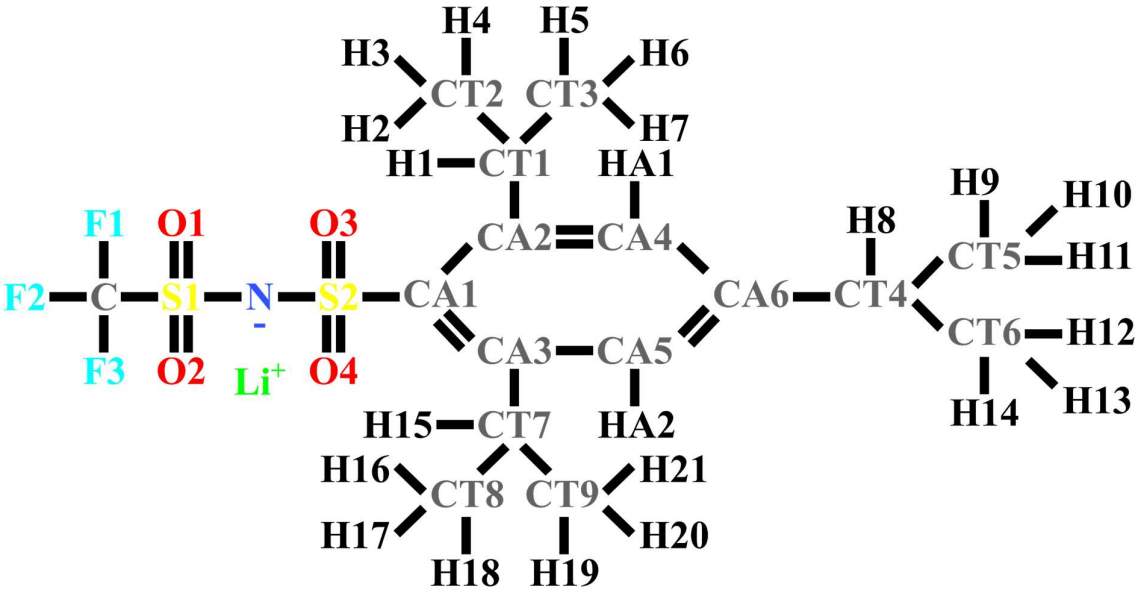

Figure A-7: Schematic representation and atom identification of Li-TPBTFSI.

Atom	Charge / e	Atom	Charge / e	Atom	Charge / e	Atom	Charge / e
C	0.159	CA3	-0.349	H7	-0.003	CT7	0.477
F1	-0.101	CA4	-0.496	HA1	0.230	H15	-0.024
F2	-0.058	CA5	0.179	CT4	0.266	CT8	-0.377
F3	-0.092	CA6	-0.224	H8	-0.003	H16	0.066
S1	0.652	CT1	-0.369	CT5	-0.332	H17	0.120
O1	-0.399	H1	0.236	H9	0.070	H18	0.054
O2	-0.345	CT2	-0.180	H10	0.086	CT9	-0.224
N	-0.464	H2	0.066	H11	0.069	H19	0.037
S2	0.862	H3	0.026	CT6	-0.112	H20	0.023
O3	-0.419	H4	0.011	H12	0.022	H21	0.037
O4	-0.405	CT3	-0.107	H13	0.016	LI	0.700
CA1	-0.506	H5	0.050	H14	0.016		
CA2	1.020	H6	-0.005	HA2	0.044		

Table A-11: Partial atomic charges of Li-TPBTFSI, with a scale factor of 0.7 applied.

Atom	σ / Å	ε / kJ mol^{-1}	Atom	σ / Å	ε / kJ mol^{-1}
C	3.50	0.276	CA	3.55	0.293
F	2.95	0.222	HA	2.42	0.126
S	3.55	1.046	CT	3.50	0.276
O	2.96	0.711	H	2.50	0.26
N	3.25	0.711	Li	2.13	0.076

Table A-12: Lennard-Jones parameters of Li-TPBTFSI.

Bond	Radius / Å	K_b / kJ mol^{-1} Å^{-2}	Angle	θ / degree	K_θ / kJ mol^{-1} rad^{-2}
F-C	1.332	3071.056	F-C-F	109.1	644.336
C-S	1.770	2845.120	S-C-F	109.5	418.400
S-O	1.440	5857.600	C-S-O	108.9	619.232
S-N	1.670	3631.712	O-S-O	119.0	870.272
S-CA	1.770	2845.120	O-S-N	107.0	1004.160
CA-CA	1.400	3924.592	C-S-N	103.0	836.800
CA-HA	1.080	3071.056	S-N-S	125.6	671.000
CA-CT	1.510	2652.656	N-S-CA	103.0	836.800
CT-CT	1.529	2242.624	O-S-CA	107.2	619.232
CT-H	1.090	2845.120	S-CA-CA	119.4	711.280
			CA-CA-CA	120.0	527.184
			CA-CA-HA	120.0	292.880
			CA-CA-CT	120.0	527.184
			CA-CT-CT	114.0	527.184
			CA-CT-H	109.5	292.880
			CT-CT-H	110.7	313.800
			CT-CT-CT	112.7	488.273
			H-CT-H	107.8	276.144

Torsion	C_0 / kJ mol^{-1}	C_1 / kJ mol^{-1}	C_2 / kJ mol^{-1}	C_3 / kJ mol^{-1}	C_4 / kJ mol^{-1}	C_5 / kJ mol^{-1}
F-C-S-O	0.7255	2.1765	0.0000	-2.9020	0.0000	0.0000
F-C-S-N	0.6610	1.9830	0.000	-2.6440	0.0000	0.0000
S-N-S-O	-0.0075	-0.0225	0.0000	0.0300	0.0000	0.0000
C-S-N-S	45.4636	-36.3221	-18.7348	5.755	4.33588	0.0000
S-N-S-CA	45.4636	-36.3221	-18.7348	5.755	4.33588	0.0000
N-S-CA-CA	0.0063	-4.1986	3.2133	0.9791	0.0000	0.0000
O-S-CA-CA	0.0000	0.0000	0.0000	0.0000	0.0000	0.0000
S-CA-CA-CA	30.3340	0.0000	-30.3340	0.0000	0.0000	0.0000
S-CA-CA-H	30.3340	0.0000	-30.3340	0.0000	0.0000	0.0000
CA-CA-CA-CA	30.3340	0.0000	-30.3340	0.0000	0.0000	0.0000
CA-CA-CA-HA	30.3340	0.0000	-30.3340	0.0000	0.0000	0.0000
CA-CA-CT-H	0.0000	0.0000	0.0000	0.0000	0.0000	0.0000
CA-CA-CT-CT	0.0000	0.0000	0.0000	0.0000	0.0000	0.0000
CA-CA-CA-CT	30.3340	0.0000	-30.3340	0.0000	0.0000	0.0000
HA-CA-CA-CT	30.3340	0.0000	-30.3340	0.0000	0.0000	0.0000
CA-CT-CT-H	0.9665	2.8995	0.0000	-3.8660	0.0000	0.0000
H-CT-CT-H	0.6276	1.8828	0.0000	-2.5104	0.0000	0.0000
H-CT-CT-CT	0.6276	1.8828	0.0000	-2.5104	0.0000	0.0000

Table A-13: Force field parameters for bond, angle, and dihedral interaction (in Rickaert-Bellemans form) of Li-TPBTFSI.

- **PEO**

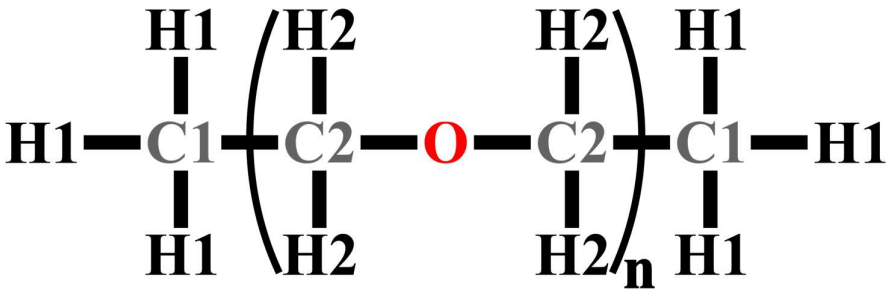

Figure A-8: Schematic representation and atom identification of PEO.

Atom	Charge / e	σ / Å	ε / kJ mol^{-1}
C1	-0.180	3.50	0.276
H1	0.060	2.50	0.126
C2	0.140	3.50	0.276
H2	0.030	2.50	0.126
O	-0.400	2.90	0.596

Table A-14: Partial atomic charges and Lennard-Jones parameters of PEO.

Bond	Radius / Å	K_b / kJ mol^{-1} Å^{-2}	Angle	θ / degree	K_θ / kJ mol^{-1} rad^{-2}
C-C	1.529	2242.624	C-C-H	110.7	313.800
C-H	1.090	2845.120	H-C-H	107.8	276.144
C-O	1.410	2677.760	C-C-O	109.5	418.400
			O-C-H	109.5	292.880
			C-O-C	109.5	502.080

Torsion	C_0 / kJ mol^{-1}	C_1 / kJ mol^{-1}	C_2 / kJ mol^{-1}	C_3 / kJ mol^{-1}	C_4 / kJ mol^{-1}	C_5 / kJ mol^{-1}
H-C-C-H	0.6270	1.8828	0.0000	-2.5104	0.0000	0.0000
O-C-C-H	0.9791	2.9370	0.0000	-3.9162	0.0000	0.0000
C-O-C-C	1.7154	2.8451	1.0460	-5.6066	0.0000	0.0000
C-O-C-H	1.5899	4.7698	0.0000	-6.3597	0.0000	0.0000
O-C-C-O	-1.1506	1.1506	0.0000	0.0000	0.0000	0.0000

Table A-15: Force field parameters for the bond, angle, and dihedral interactions (in Rickaert-Bellemans form) of PEO.

- **PCL**

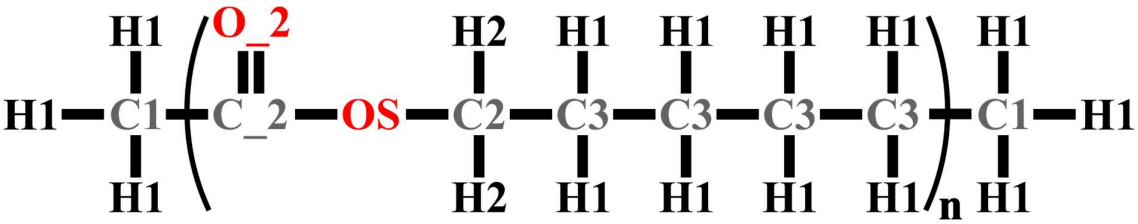

Figure A-9: Schematic representation and atom identification of PCL.

Atom	Charge / e	σ / Å	ε / kJ mol^{-1}
C1	-0.180	3.50	0.276
C2	0.190	3.50	0.276
C3	-0.120	3.50	0.276
C_2	0.510	3.75	0.439
H1	0.060	2.50	0.126
H2	0.030	2.42	0.063
OS	-0.330	3.00	0.711
O_2	-0.430	2.96	0.879

Table A-16: Partial atomic charges and Lennard-Jones parameters of PCL.

Bond	Radius / Å	K_b / kJ mol^{-1} Å^{-2}	Angle	θ / degree	K_θ / kJ mol^{-1} rad^{-2}
C_2-C	1.522	2652.656	H-C-C_2	109.5	295.880
H-C	1.090	2845.120	H-C-H	107.8	276.144
O_2-C_2	1.229	4769.760	O_2-C_2-C	120.4	669.440
OS-C_2	1.327	1790.752	OS-C_2-C	111.4	677.808
OS-C	1.410	2677.760	O_2-C_2-OS	123.4	694.544
C-C	1.529	2242.624	C_2-OS-C	116.9	694.544
			OS-C-C	109.5	418.400
			OS-C-H	109.5	292.800
			H-C-C	110.7	313.800
			C-C-C	112.7	488.273
			C_2-C-C	111.1	527.184

Table A-17: Force field parameters for the bond and angle interactions of PCL.

Torsion	C_0 / kJ mol^{-1}	C_1 / kJ mol^{-1}	C_2 / kJ mol^{-1}	C_3 / kJ mol^{-1}	C_4 / kJ mol^{-1}	C_5 / kJ mol^{-1}
O_2-C_2-C-H	0.0000	0.0000	0.0000	0.000	0.0000	0.0000
OS-C_2-C-H	0.2762	0.8284	0.0000	-1.1046	0.0000	0.0000
C-OS-C_2-C	31.2064	-9.7675	-21.4388	0.0000	0.0000	0.0000
O_2-C_2-OS-C	21.4388	0.0000	-21.4388	0.0000	0.0000	0.0000
C_2-OS-C-C	-2.1966	5.2007	0.5272	-3.5313	0.0000	0.0000
H-C-OS-C_2	0.4142	1.2427	0.0000	-1.6569	0.0000	0.0000
OS-C-C-C	2.8744	0.5816	2.0920	-5.5480	0.0000	0.0000
OS-C-C-H	0.9791	2.9372	0.0000	-3.9162	0.0000	0.0000
H-C-C-C	0.6276	1.8828	0.0000	-2.5104	0.0000	0.0000
H-C-C-H	0.6276	18828	0.0000	-2.5104	0.0000	0.0000
C-C-C-C	2.9288	-1.4644	0.2092	-1.6736	0.0000	0.0000
C_2-C-C-C	-4.2342	7.2216	1.9079	-4.8953	0.0000	0.0000
H-C-C-C_2	-0.1590	-0.4770	0.0000	0.6360	0.0000	0.0000
O_2-C_2-C-C	3.1066	-3.7761	-5.1380	5.8274	0.0000	0.0000
OS-C_2-C-C	-1.1569	-3.4706	0.0000	4.6275	0.0000	0.0000

Table A-18: Force field parameters for the dihedral interaction of PCL.

Bibliography

[1] International Energy Outlook - U.S. Energy Information Administration (EIA). (n.d.). https://www.eia.gov/outlooks/ieo/

[2] Schmuch, R., Wagner, R., Hörpel, G., Placke, T., & Winter, M. (2018). Performance and cost of materials for lithium-based rechargeable automotive batteries. Nature Energy, 3(4), 267-278.

[3] Feng, X., Ouyang, M., Liu, X., Lu, L., Xia, Y., & He, X. (2018). Thermal runaway mechanism of lithium ion battery for electric vehicles: A review. Energy Storage Materials, 10, 246-267.

[4] EUROBAT. (2023, April 14). Home - EUROBAT. *https://www.eurobat.org/*

[5] Boaretto, N., Garbayo, I., Valiyaveettil-SobhanRaj, S., Quintela, A., Li, C., Casas-Cabanas, M., & Aguesse, F. (2021). Lithium solid-state batteries: State-of-the-art and challenges for materials, interfaces and processing. *Journal of Power Sources*, *502*, 229919.

[6] Blue Solutions. (n.d.). Blue Solutions | Bolloré. *https://www.blue-solutions.com/en*

[7] Judez, X., Eshetu, G. G., Li, C., Rodriguez-Martinez, L. M., Zhang, H., & Armand, M. (2018). Opportunities for rechargeable solid-state batteries based on Li-intercalation cathodes. *Joule*, *2*(11), 2208-2224.

[8] Zhang, H., Li, C., Piszcz, M., Coya, E., Rojo, T., Rodriguez-Martinez, L. M., ... & Zhou, Z. (2017). Single lithium-ion conducting solid polymer electrolytes: advances and perspectives. *Chemical Society Reviews*, *46*(3), 797-815.

[9] Zhang, H., Han, H., Cheng, X., Zheng, L., Cheng, P., Feng, W., ... & Zhou, Z. (2015). Lithium salt with a super-delocalized perfluorinated sulfonimide anion as conducting salt for lithium-ion cells: Physicochemical and electrochemical properties. *Journal of Power Sources*, *296*, 142-149.

[10] Eshetu, G. G., Judez, X., Li, C., Martinez-Ibañez, M., Gracia, I., Bondarchuk, O., ... & Armand, M. (2018). Ultrahigh performance all solid-state lithium sulfur batteries: salt anion's chemistry-induced anomalous synergistic effect. *Journal of the American chemical society*, *140*(31), 9921-9933.

[11] Martinez-Ibañez, M., Boaretto, N., Santiago, A., Meabe, L., Wang, X., Zugazua, O., ... & Zhang, H. (2023). Highly-concentrated bis (fluorosulfonyl) imide-based ternary gel polymer electrolytes for high-voltage lithium metal batteries. *Journal of Power Sources*, *557*, 232554.

[12] Aneke, M., & Wang, M. (2016). Energy storage technologies and real life applications–A state of the art review. *Applied Energy*, *179*, 350-377.

[13] Neumann, J., Petranikova, M., Meeus, M., Gamarra, J. D., Younesi, R., Winter, M., & Nowak, S. (2022). Recycling of Lithium-Ion Batteries—Current State of the Art, Circular Economy, and Next Generation Recycling. Advanced energy materials, 12(17), 2102917.

[14] Fichtner, M., Edström, K., Ayerbe, E., Berecibar, M., Bhowmik, A., Castelli, I. E., ... & Weil, M. (2022). Rechargeable batteries of the future—the state of the art from a BATTERY 2030+ perspective. Advanced Energy Materials, 12(17), 2102904.

[15] Zubi, G., Dufo-López, R., Carvalho, M., & Pasaoglu, G. (2018). The lithium-ion battery: State of the art and future perspectives. *Renewable and Sustainable Energy Reviews*, *89*, 292-308.

[16] Harper, G., Sommerville, R., Kendrick, E., Driscoll, L., Slater, P., Stolkin, R., ... & Anderson, P. (2019). Recycling lithium-ion batteries from electric vehicles. nature, 575(7781), 75-86.

[17] Hannan, M. A., Hoque, M. M., Hussain, A., Yusof, Y., & Ker, P. J. (2018). State-of-the-art and energy management system of lithium-ion batteries in electric vehicle applications: Issues and recommendations. *Ieee Access*, *6*, 19362-19378.

[18] Xu, C., Dai, Q., Gaines, L., Hu, M., Tukker, A., & Steubing, B. (2020). Future material demand for automotive lithium-based batteries. *Communications Materials*, *1*(1), 99.

[19] Zhu, P., Gastol, D., Marshall, J., Sommerville, R., Goodship, V., & Kendrick, E. (2021). A review of current collectors for lithium-ion batteries. Journal of Power Sources, 485, 229321.

[20] Antolini, E. (2004). LiCoO2: formation, structure, lithium and oxygen nonstoichiometry, electrochemical behaviour and transport properties. Solid state ionics, 170(3-4), 159-171.

[21] Liu, C., Neale, Z. G., & Cao, G. (2016). Understanding electrochemical potentials of cathode materials in rechargeable batteries. *Materials Today*, *19*(2), 109-123.

[22] Fergus, J. W. (2010). Recent developments in cathode materials for lithium ion batteries. *Journal of power sources*, *195*(4), 939-954.

[23] Xu, B., Qian, D., Wang, Z., & Meng, Y. S. (2012). Recent progress in cathode materials research for advanced lithium ion batteries. *Materials Science and Engineering: R: Reports*, *73*(5-6), 51-65.

[24] Lu, Z., MacNeil, D. D., & Dahn, J. R. (2001). Layered cathode materials Li [Ni x Li (1/3− 2x/3) Mn (2/3− x/3)] O 2 for lithium-ion batteries. *Electrochemical and Solid-State Letters*, *4*(11), A191.

[25] Liu, Q., Su, X., Lei, D., Qin, Y., Wen, J., Guo, F., ... & Li, Y. (2018). Approaching the capacity limit of lithium cobalt oxide in lithium ion batteries via lanthanum and aluminium doping. *Nature Energy*, *3*(11), 936-943.

[26] Simon, B., Flandrois, S., Guerin, K., Fevrier-Bouvier, A., Teulat, I., & Biensan, P. (1999). On the choice of graphite for lithium ion batteries. *Journal of power sources*, *81*, 312-316.

[27] Moradi, B., & Botte, G. G. (2016). Recycling of graphite anodes for the next generation of lithium ion batteries. *Journal of Applied Electrochemistry*, *46*(2), 123-148.

[28] Belharouak, I., Koenig Jr, G. M., & Amine, K. (2011). Electrochemistry and safety of Li4Ti5O12 and graphite anodes paired with LiMn2O4 for hybrid electric vehicle Li-ion battery applications. *Journal of Power Sources*, *196*(23), 10344-10350.

[29] Stephen. (2017). Mitsubishi Chooses Super-Efficient Toshiba SCiB Battery For EVs. *Japanese Car Auctions - Integrity Exports*. *https://integrityexports.com/blog/mitsubishi-chooses-toshiba-scib-battery-for-evs/*

[30] Honda begins European demonstration program of EV-neo electric scooter. (n.d.). Green Car Congress. *https://www.greencarcongress.com/2011/06/evneo20110615.html*

[31] SCiB™ Rechargeable battery | Toshiba. (n.d.). *https://www.global.toshiba/ww/products-solutions/battery/scib.html*

[32] De las Casas, C., & Li, W. (2012). A review of application of carbon nanotubes for lithium ion battery anode material. *Journal of Power Sources*, *208*, 74-85.

[33] Fang, R., Chen, K., Yin, L., Sun, Z., Li, F., & Cheng, H. M. (2019). The regulating role of carbon nanotubes and graphene in lithium-ion and lithium–sulfur batteries. *Advanced Materials*, *31*(9), 1800863.

[34] Sehrawat, P., Julien, C., & Islam, S. S. (2016). Carbon nanotubes in Li-ion batteries: A review. *Materials Science and Engineering: B*, *213*, 12-40.

[35] Zhu, S., Sheng, J., Chen, Y., Ni, J., & Li, Y. (2021). Carbon nanotubes for flexible batteries: recent progress and future perspective. *National Science Review*, *8*(5), nwaa261.

[36] Li, Q., Chen, J., Fan, L., Kong, X., & Lu, Y. (2016). Progress in electrolytes for rechargeable Li-based batteries and beyond. *Green Energy & Environment*, *1*(1), 18-42.

[37] Campion, C. L., Li, W., & Lucht, B. L. (2005). Thermal decomposition of LiPF6-based electrolytes for lithium-ion batteries. *Journal of The Electrochemical Society*, *152*(12), A2327.

[38] Botte, G. G., White, R. E., & Zhang, Z. (2001). Thermal stability of LiPF6–EC: EMC electrolyte for lithium ion batteries. *Journal of Power Sources*, *97*, 570-575.

[39] Sharova, V., Moretti, A., Diemant, T., Varzi, A., Behm, R. J., & Passerini, S. (2018). Comparative study of imide-based Li salts as electrolyte additives for Li-ion batteries. *Journal of Power Sources*, *375*, 43-52.

[40] Zhang, H., Arcelus, O., & Carrasco, J. (2018). Role of asymmetry in the physiochemical and electrochemical behaviors of perfluorinated sulfonimide anions for lithium batteries: A DFT study. *Electrochimica Acta*, *280*, 290-299.

[41] Osada, I., de Vries, H., Scrosati, B., & Passerini, S. (2016). Ionic-liquid-based polymer electrolytes for battery applications. *Angewandte Chemie International Edition*, *55*(2), 500-513.

[42] Ishikawa, M., Sugimoto, T., Kikuta, M., Ishiko, E., & Kono, M. (2006). Pure ionic liquid electrolytes compatible with a graphitized carbon negative electrode in rechargeable lithium-ion batteries. *Journal of power sources*, *162*(1), 658-662.

[43] Sugimoto, T., Atsumi, Y., Kikuta, M., Ishiko, E., Kono, M., & Ishikawa, M. (2009). Ionic liquid electrolyte systems based on bis (fluorosulfonyl) imide for lithium-ion batteries. *Journal of Power Sources*, *189*(1), 802-805.

[44] Bedrov, D., Piquemal, J. P., Borodin, O., MacKerell Jr, A. D., Roux, B., & Schröder, C. (2019). Molecular dynamics simulations of ionic liquids and electrolytes using polarizable force fields. *Chemical reviews*, *119*(13), 7940-7995.

[45] Stephan, A. M. (2006). Review on gel polymer electrolytes for lithium batteries. *European polymer journal*, *42*(1), 21-42.

[46] Cheng, X., Pan, J., Zhao, Y., Liao, M., & Peng, H. (2018). Gel polymer electrolytes for electrochemical energy storage. *Advanced Energy Materials*, *8*(7), 1702184.

[47] Long, L., Wang, S., Xiao, M., & Meng, Y. (2016). Polymer electrolytes for lithium polymer batteries. *Journal of Materials Chemistry A*, *4*(26), 10038-10069.

[48] Xue, Z., He, D., & Xie, X. (2015). Poly (ethylene oxide)-based electrolytes for lithium-ion batteries. *Journal of Materials Chemistry A*, *3*(38), 19218-19253.

[49] Zheng, F., Kotobuki, M., Song, S., Lai, M. O., & Lu, L. (2018). Review on solid electrolytes for all-solid-state lithium-ion batteries. *Journal of Power Sources*, *389*, 198-213.

[50] Fergus, J. W. (2010). Ceramic and polymeric solid electrolytes for lithium-ion batteries. *Journal of Power Sources*, *195*(15), 4554-4569.

[51] Agubra, V. A., & Fergus, J. W. (2014). The formation and stability of the solid electrolyte interface on the graphite anode. *Journal of Power Sources*, *268*, 153-162.

[52] Verma, P., Maire, P., & Novák, P. (2010). A review of the features and analyses of the solid electrolyte interphase in Li-ion batteries. *Electrochimica Acta*, *55*(22), 6332-6341.

[53] Wang, A., Kadam, S., Li, H., Shi, S., & Qi, Y. (2018). Review on modeling of the anode solid electrolyte interphase (SEI) for lithium-ion batteries. *npj Computational Materials*, *4*(1), 1-26.

[54] Zhang, S. S. (2006). A review on electrolyte additives for lithium-ion batteries. *Journal of Power Sources*, *162*(2), 1379-1394.

[55] Bruce, P. G., Freunberger, S. A., Hardwick, L. J., & Tarascon, J. M. (2012). Li–O2 and Li–S batteries with high energy storage. *Nature materials*, *11*(1), 19-29.

[56] Kim, H., Jeong, G., Kim, Y. U., Kim, J. H., Park, C. M., & Sohn, H. J. (2013). Metallic anodes for next generation secondary batteries. *Chemical Society Reviews*, *42*(23), 9011-9034.

[57] Liu, B., Zhang, J. G., & Xu, W. (2018). Advancing lithium metal batteries. *Joule*, *2*(5), 833-845.

[58] Whittingham, M. S. (1976). Electrical energy storage and intercalation chemistry. *Science*, *192*(4244), 1126-1127.

[59] Whittingham, M. S. Chalcogenide battery. US Patent 4009052.

[60] Cheng, X. B., Zhang, R., Zhao, C. Z., & Zhang, Q. (2017). Toward safe lithium metal anode in rechargeable batteries: a review. *Chemical reviews*, *117*(15), 10403-10473.

[61] Wang, D., Zhang, W., Zheng, W., Cui, X., Rojo, T., & Zhang, Q. (2017). Towards high-safe lithium metal anodes: suppressing lithium dendrites via tuning surface energy. *Advanced Science*, *4*(1), 1600168.

[62] Xu, W., Wang, J., Ding, F., Chen, X., Nasybulin, E., Zhang, Y., & Zhang, J. G. (2014). Lithium metal anodes for rechargeable batteries. *Energy & Environmental Science*, *7*(2), 513-537.

[63] Lin, D., Liu, Y., & Cui, Y. (2017). Reviving the lithium metal anode for high-energy batteries. *Nature nanotechnology*, *12*(3), 194-206.

[64] Hobold, G. M., Lopez, J., Guo, R., Minafra, N., Banerjee, A., Shirley Meng, Y., ... & Gallant, B. M. (2021). Moving beyond 99.9% Coulombic efficiency for lithium anodes in liquid electrolytes. *Nature Energy*, *6*(10), 951-960.

[65] Cheng, X. B., Zhang, R., Zhao, C. Z., Wei, F., Zhang, J. G., & Zhang, Q. (2016). A review of solid electrolyte interphases on lithium metal anode. *Advanced science*, *3*(3), 1500213.

[66] Kim, K. J., Balaish, M., Wadaguchi, M., Kong, L., & Rupp, J. L. (2021). Solid-state Li–metal batteries: challenges and horizons of oxide and sulfide solid electrolytes and their interfaces. *Advanced Energy Materials*, *11*(1), 2002689.

[67] Cheng, X. B., Zhao, C. Z., Yao, Y. X., Liu, H., & Zhang, Q. (2019). Recent advances in energy chemistry between solid-state electrolyte and safe lithium-metal anodes. *Chem*, *5*(1), 74-96.

[68] Dudney, N. J., West, W. C., & Nanda, J. (Eds.). (2015). *Handbook of solid state batteries* (Vol. 6). World Scientific.

[69] Zhang, H., Li, C., Piszcz, M., Coya, E., Rojo, T., Rodriguez-Martinez, L. M., ... & Zhou, Z. (2017). Single lithium-ion conducting solid polymer electrolytes: advances and perspectives. *Chemical Society Reviews*, *46*(3), 797-815.

[70] Zhang, H., Chen, Y., Li, C., & Armand, M. (2021). Electrolyte and anode-electrolyte interphase in solid-state lithium metal polymer batteries: A perspective. *SusMat*, *1*(1), 24-37.

[71] Shin, J. H., Henderson, W. A., & Passerini, S. (2005). PEO-based polymer electrolytes with ionic liquids and their use in lithium metal-polymer electrolyte batteries. *Journal of the Electrochemical Society*, *152*(5), A978.

[72] Wang, C., Yang, Y., Liu, X., Zhong, H., Xu, H., Xu, Z., ... & Ding, F. (2017). Suppression of lithium dendrite formation by using LAGP-PEO (LiTFSI) composite solid electrolyte and lithium metal anode modified by PEO (LiTFSI) in all-solid-state lithium batteries. *ACS applied materials & interfaces*, *9*(15), 13694-13702.

[73] Yin, J., Xu, X., Jiang, S., Wu, H., Wei, L., Li, Y., ... & Gao, Y. (2022). High ionic conductivity PEO-based electrolyte with 3D framework for Dendrite-free solid-state lithium metal batteries at ambient temperature. *Chemical Engineering Journal*, *431*, 133352.

[74] M. B. Armand, J. M. Chabagno and M. J. Duclot, The 2nd International conference on solid electrolyte. Ext. Abs., St. Andrews, Scotland, 1978.

[75] M. B. Armand, J. M. Chabagno and M. J. Duclot, Fast Ion Transport in Solids, ed. P. Vashista, J. N. Mundy and G. K. Shenoy, North-Holland, Amsterdam, 1979, p. 131.

[76] Armand, M. B. (1986). Polymer electrolytes. *Annual review of materials science*, *16*(1), 245-261.

[77] Hovington, P., Lagacé, M., Guerfi, A., Bouchard, P., Mauger, A., Julien, C. M., ... & Zaghib, K. (2015). New lithium metal polymer solid state battery for an ultrahigh energy: nano C-LiFePO4 versus nano Li1. 2V3O8. *Nano letters*, *15*(4), 2671-2678.

[78] Diddens, D., Heuer, A., & Borodin, O. (2010). Understanding the lithium transport within a rouse-based model for a PEO/LiTFSI polymer electrolyte. *Macromolecules*, *43*(4), 2028-2036.

[79] Rey, I., Lassegues, J. C., Grondin, J., & Servant, L. (1998). Infrared and Raman study of the PEO-LiTFSI polymer electrolyte. *Electrochimica Acta*, *43*(10-11), 1505-1510.

[80] Verlet, L. (1967). Computer" experiments" on classical fluids. I. Thermodynamical properties of Lennard-Jones molecules. *Physical review*, *159*(1), 98.

[81] Hockney, R. W., & Eastwood, J. W. (2021). Computer simulation using particles. crc Press.

[82] Ryckaert, J. P., & Bellemans, A. (1978). Molecular dynamics of liquid alkanes. *Faraday Discussions of the Chemical Society*, *66*, 95-106.

[83] Campañá, C., Mussard, B., & Woo, T. K. (2009). Electrostatic potential derived atomic charges for periodic systems using a modified error functional. *Journal of Chemical Theory and Computation*, *5*(10), 2866-2878.

[84] Chen, D. L., Stern, A. C., Space, B., & Johnson, J. K. (2010). Atomic charges derived from electrostatic potentials for molecular and periodic systems. *The Journal of Physical Chemistry A*, *114*(37), 10225-10233.

[85] Bayly, C. I., Cieplak, P., Cornell, W., & Kollman, P. A. (1993). A well-behaved electrostatic potential based method using charge restraints for deriving atomic charges: the RESP model. *The Journal of Physical Chemistry*, *97*(40), 10269-10280.

[86] Hirshfeld, F. L. (1977). Bonded-atom fragments for describing molecular charge densities. *Theoretica chimica acta*, *44*(2), 129-138.

[87] Glendening, E. D., Landis, C. R., & Weinhold, F. (2012). Natural bond orbital methods. *Wiley interdisciplinary reviews: computational molecular science*, *2*(1), 1-42.

[88] Jones, J. E. (1924). On the determination of molecular fields.—I. From the variation of the viscosity of a gas with temperature. *Proceedings of the Royal Society of London. Series A, Containing Papers of a Mathematical and Physical Character*, *106*(738), 441-462.

[89] Jones, J. E. (1924). On the determination of molecular fields.—II. From the equation of state of a gas. *Proceedings of the Royal Society of London. Series A, Containing Papers of a Mathematical and Physical Character*, *106*(738), 463-477.

[90] Lennard-Jones, J. E. (1931). Cohesion. *Proceedings of the Physical Society (1926-1948)*, *43*(5), 461.

[91] Franco, A. A., Rucci, A., Brandell, D., Frayret, C., Gaberscek, M., Jankowski, P., & Johansson, P. (2019). Boosting rechargeable batteries R&D by multiscale modeling: myth or reality?. *Chemical reviews*, *119*(7), 4569-4627.

[92] Van der Ven, A., Deng, Z., Banerjee, S., & Ong, S. P. (2020). Rechargeable alkali-ion battery materials: theory and computation. *Chemical reviews*, *120*(14), 6977-7019.

[93] Bedrov, D., Piquemal, J. P., Borodin, O., MacKerell Jr, A. D., Roux, B., & Schröder, C. (2019). Molecular dynamics simulations of ionic liquids and electrolytes using polarizable force fields. *Chemical reviews*, *119*(13), 7940-7995.

[94] Dommert, F., Wendler, K., Berger, R., Delle Site, L., & Holm, C. (2012). Force fields for studying the structure and dynamics of ionic liquids: a critical review of recent developments. *ChemPhysChem*, *13*(7), 1625-1637.

[95] Senftle, T. P., Hong, S., Islam, M. M., Kylasa, S. B., Zheng, Y., Shin, Y. K., ... & Van Duin, A. C. (2016). The ReaxFF reactive force-field: development, applications and future directions. *npj Computational Materials*, *2*(1), 1-14.

[96] Tschöp, W., Kremer, K., Hahn, O., Batoulis, J., & Bürger, T. (1998). Simulation of polymer melts. II. From coarse-grained models back to atomistic description. Acta Polymerica, 49(2-3), 75-79.

[97] Akkermans, R. L., & Briels, W. J. (2001). A structure-based coarse-grained model for polymer melts. The Journal of Chemical Physics, 114(2), 1020-1031.

[98] Joshi, S. Y., & Deshmukh, S. A. (2021). A review of advancements in coarse-grained molecular dynamics simulations. Molecular Simulation, 47(10-11), 786-803.

[99] Shen, K. H., Fan, M., & Hall, L. M. (2021). Molecular dynamics simulations of ion-containing polymers using generic coarse-grained models. Macromolecules, 54(5), 2031-2052.

[100] Ewald, P. P. (1921). Die Berechnung optischer und elektrostatischer Gitterpotentiale. *Annalen der physik*, *369*(3), 253-287.

[101] Darden, T., York, D., & Pedersen, L. (1993). Particle mesh Ewald: An N· log (N) method for Ewald sums in large systems. *The Journal of chemical physics*, *98*(12), 10089-10092.

[102] Berendsen, H. J., Postma, J. V., Van Gunsteren, W. F., DiNola, A. R. H. J., & Haak, J. R. (1984). Molecular dynamics with coupling to an external bath. *The Journal of chemical physics*, *81*(8), 3684-3690.

[103] Bussi, G., Donadio, D., & Parrinello, M. (2007). Canonical sampling through velocity rescaling. *The Journal of chemical physics*, *126*(1), 014101.

[104] Nosé, S. (1984). A molecular dynamics method for simulations in the canonical ensemble. *Molecular physics*, *52*(2), 255-268.

[105] Hoover, W. G. (1985). Canonical dynamics: Equilibrium phase-space distributions. *Physical review A*, *31*(3), 1695.

[106] Andersen, H. C. (1980). Molecular dynamics simulations at constant pressure and/or temperature. *The Journal of chemical physics*, *72*(4), 2384-2393.

[107] Parrinello, M., & Rahman, A. (1981). Polymorphic transitions in single crystals: A new molecular dynamics method. *Journal of Applied physics*, *52*(12), 7182-7190.

[108] Nosé, S., & Klein, M. L. (1983). Constant pressure molecular dynamics for molecular systems. *Molecular Physics*, *50*(5), 1055-1076.

[109] Brehm, M., & Kirchner, B. (2011). TRAVIS-a free analyzer and visualizer for Monte Carlo and molecular dynamics trajectories.

[110] Brehm, M., Thomas, M., Gehrke, S., & Kirchner, B. (2020). TRAVIS—A free analyzer for trajectories from molecular simulation. *The Journal of chemical physics*, *152*(16).

[111] Jorgensen, W. L., Maxwell, D. S., & Tirado-Rives, J. (1996). Development and testing of the OPLS all-atom force field on conformational energetics and properties of organic liquids. *Journal of the American Chemical Society*, *118*(45), 11225-11236.

[112] Kaminski, G. A., Friesner, R. A., Tirado-Rives, J., & Jorgensen, W. L. (2001). Evaluation and reparametrization of the OPLS-AA force field for proteins via comparison with accurate quantum chemical calculations on peptides. *The Journal of Physical Chemistry B*, *105*(28), 6474-6487.

[113] Essmann, U., Perera, L., Berkowitz, M. L., Darden, T., Lee, H., & Pedersen, L. G. (1995). A smooth particle mesh Ewald method. *The Journal of chemical physics*, *103*(19), 8577-8593.

[114] Berendsen, H. J., van der Spoel, D., & van Drunen, R. (1995). GROMACS: A message-passing parallel molecular dynamics implementation. *Computer physics communications*, *91*(1-3), 43-56.

[115] Lindahl, E., Hess, B., & Van Der Spoel, D. (2001). GROMACS 3.0: a package for molecular simulation and trajectory analysis. *Molecular modeling annual*, *7*(8), 306-317.

[116] Van Der Spoel, D., Lindahl, E., Hess, B., Groenhof, G., Mark, A. E., & Berendsen, H. J. (2005). GROMACS: fast, flexible, and free. *Journal of computational chemistry*, *26*(16), 1701-1718.

[117] Pronk, S., Páll, S., Schulz, R., Larsson, P., Bjelkmar, P., Apostolov, R., ... & Lindahl, E. (2013). GROMACS 4.5: a high-throughput and highly parallel open source molecular simulation toolkit. *Bioinformatics*, *29*(7), 845-854.

[118] Plimpton, S. (1995). Fast parallel algorithms for short-range molecular dynamics. *Journal of computational physics*, *117*(1), 1-19.

[119] Thompson, A. P., Aktulga, H. M., Berger, R., Bolintineanu, D. S., Brown, W. M., Crozier, P. S., ... & Plimpton, S. J. (2022). LAMMPS-a flexible simulation tool for particle-based materials modeling at the atomic, meso, And continuum scales. *Computer Physics Communications*, *271*, 108171.

[120] D.A. Case, H.M. Aktulga, K. Belfon, I.Y. Ben-Shalom, J.T. Berryman, S.R. Brozell, D.S. Cerutti, T.E. Cheatham, III, G.A. Cisneros, V.W.D. Cruzeiro, T.A. Darden, N. Forouzesh, G. Giambaşu, T. Giese, M.K. Gilson, H. Gohlke, A.W. Goetz, J. Harris, S. Izadi, S.A. Izmailov, K. Kasavajhala, M.C. Kaymak, E. King, A. Kovalenko, T. Kurtzman, T.S. Lee, P. Li, C. Lin, J. Liu, T. Luchko, R. Luo, M. Machado, V. Man, M. Manathunga, K.M. Merz, Y. Miao, O. Mikhailovskii, G. Monard, H. Nguyen, K.A. O'Hearn, A. Onufriev, F. Pan, S. Pantano, R. Qi, A. Rahnamoun, D.R. Roe, A. Roitberg, C. Sagui, S. Schott-Verdugo, A. Shajan, J. Shen, C.L. Simmerling, N.R. Skrynnikov, J. Smith, J. Swails, R.C. Walker, J. Wang, J. Wang, H. Wei, X. Wu, Y. Wu, Y. Xiong, Y. Xue, D.M. York, S. Zhao, Q. Zhu, and P.A. Kollman (2023), Amber 2023, University of California, San Francisco.

[121] Case, D. A., Cheatham III, T. E., Darden, T., Gohlke, H., Luo, R., Merz Jr, K. M., ... & Woods, R. J. (2005). The Amber biomolecular simulation programs. *Journal of computational chemistry*, *26*(16), 1668-1688.

[122] Brooks, B. R., Bruccoleri, R. E., Olafson, B. D., States, D. J., Swaminathan, S. A., & Karplus, M. (1983). CHARMM: a program for macromolecular energy, minimization, and dynamics calculations. *Journal of computational chemistry*, *4*(2), 187-217.

[123] Jo, S., Kim, T., Iyer, V. G., & Im, W. (2008). CHARMM-GUI: a web-based graphical user interface for CHARMM. *Journal of computational chemistry*, *29*(11), 1859-1865.

[124] Phillips, J. C., Braun, R., Wang, W., Gumbart, J., Tajkhorshid, E., Villa, E., ... & Schulten, K. (2005). Scalable molecular dynamics with NAMD. *Journal of computational chemistry*, *26*(16), 1781-1802.

[125] Abraham, M. J., Murtola, T., Schulz, R., Páll, S., Smith, J. C., Hess, B., & Lindahl, E. (2015). GROMACS: High performance molecular simulations through multi-level parallelism from laptops to supercomputers. *SoftwareX*, *1*, 19-25.

[126] Blum, V., Gehrke, R., Hanke, F., Havu, P., Havu, V., Ren, X., ... & Scheffler, M. (2009). Ab initio molecular simulations with numeric atom-centered orbitals. *Computer Physics Communications*, *180*(11), 2175-2196.

[127] Max Born; J. Robert Oppenheimer (1927). "Zur Quantentheorie der Molekeln" [On the Quantum Theory of Molecules]. Annalen der Physik (in German). 389 (20): 457–484

[128] Slater, J. C. (1928). The self consistent field and the structure of atoms. *Physical Review*, *32*(3), 339.

[129] Hartree, D. R. (1928, January). The wave mechanics of an atom with a non-Coulomb central field. Part I. Theory and methods. In *Mathematical Proceedings of the Cambridge Philosophical Society* (Vol. 24, No. 1, pp. 89-110). Cambridge university press.

[130] Hartree, D. R. (1928, January). The wave mechanics of an atom with a non-coulomb central field. Part II. Some results and discussion. In *Mathematical Proceedings of the Cambridge Philosophical Society* (Vol. 24, No. 1, pp. 111-132). Cambridge University Press.

[131] Fock, V. (1930). Näherungsmethode zur Lösung des quantenmechanischen Mehrkörperproblems. Zeitschrift für Physik, 61(1), 126-148.

[132] Hohenberg, P., & Kohn, W. (1964). Inhomogeneous electron gas. *Physical review*, *136*(3B), B864.

[133] Kohn, W., & Sham, L. J. (1965). Self-consistent equations including exchange and correlation effects. *Physical review*, *140*(4A), A1133.

[134] Dirac, P. A. (1930, July). Note on exchange phenomena in the Thomas atom. In *Mathematical proceedings of the Cambridge philosophical society* (Vol. 26, No. 3, pp. 376-385). Cambridge University Press.

[135] Vosko, S. H., Wilk, L., & Nusair, M. (1980). Accurate spin-dependent electron liquid correlation energies for local spin density calculations: a critical analysis. *Canadian Journal of physics*, *58*(8), 1200-1211.

[136] Perdew, J. P., & Wang, Y. (1992). Accurate and simple analytic representation of the electron-gas correlation energy. *Physical review B*, *45*(23), 13244.

[137] Lee, C., Yang, W., & Parr, R. G. (1988). Development of the Colle-Salvetti correlation-energy formula into a functional of the electron density. *Physical review B*, *37*(2), 785.

[138] Becke, A. D. (1988). Density-functional exchange-energy approximation with correct asymptotic behavior. *Physical review A*, *38*(6), 3098.

[139] Perdew, J. P., Chevary, J. A., Vosko, S. H., Jackson, K. A., Pederson, M. R., Singh, D. J., & Fiolhais, C. (1992). Atoms, molecules, solids, and surfaces: Applications of the generalized gradient approximation for exchange and correlation. *Physical review B*, *46*(11), 6671.

[140] Perdew, J. P., Burke, K., & Ernzerhof, M. (1996). Generalized gradient approximation made simple. *Physical review letters*, *77*(18), 3865.

[141] Kim, K., & Jordan, K. D. (1994). Comparison of density functional and MP2 calculations on the water monomer and dimer. *The Journal of Physical Chemistry*, *98*(40), 10089-10094.

[142] Stephens, P. J., Devlin, F. J., Chabalowski, C. F., & Frisch, M. J. (1994). Ab initio calculation of vibrational absorption and circular dichroism spectra using density functional force fields. *The Journal of physical chemistry*, *98*(45), 11623-11627.

[143] Adamo, C., & Barone, V. (1999). Toward reliable density functional methods without adjustable parameters: The PBE0 model. *The Journal of chemical physics*, *110*(13), 6158-6170.

[144] Heyd, J., Scuseria, G. E., & Ernzerhof, M. (2003). Hybrid functionals based on a screened Coulomb potential. *The Journal of chemical physics*, *118*(18), 8207-8215.

[145] Gudla, H., Zhang, C., & Brandell, D. (2020). Effects of solvent polarity on Li-ion diffusion in polymer electrolytes: An all-atom molecular dynamics study with charge scaling. *The Journal of Physical Chemistry B*, *124*(37), 8124-8131.

[146] Kresse, G., & Hafner, J. (1993). Ab initio molecular dynamics for liquid metals. *Physical review B*, *47*(1), 558.

[147] Kresse, G., & Furthmüller, J. (1996). Efficiency of ab-initio total energy calculations for metals and semiconductors using a plane-wave basis set. *Computational materials science*, *6*(1), 15-50.

[148] Kresse, G., & Furthmüller, J. (1996). Efficient iterative schemes for ab initio total-energy calculations using a plane-wave basis set. *Physical review B*, *54*(16), 11169.

[149] Gaussian 16, Revision C.01, Frisch, M. J.; Trucks, G. W.; Schlegel, H. B.; Scuseria, G. E.; Robb, M. A.; Cheeseman, J. R.; Scalmani, G.; Barone, V.; Petersson, G. A.; Nakatsuji, H.; Li, X.; Caricato, M.; Marenich, A. V.; Bloino, J.; Janesko, B. G.; Gomperts, R.; Mennucci, B.; Hratchian, H. P.; Ortiz, J. V.; Izmaylov, A. F.; Sonnenberg, J. L.; Williams-Young, D.; Ding, F.; Lipparini, F.; Egidi, F.; Goings, J.; Peng, B.; Petrone, A.; Henderson, T.; Ranasinghe, D.; Zakrzewski, V. G.; Gao, J.; Rega, N.; Zheng, G.; Liang, W.; Hada, M.; Ehara, M.; Toyota, K.; Fukuda, R.; Hasegawa, J.; Ishida, M.; Nakajima, T.; Honda, Y.; Kitao, O.; Nakai, H.; Vreven, T.; Throssell, K.; Montgomery, J. A., Jr.; Peralta, J. E.; Ogliaro, F.; Bearpark, M. J.; Heyd, J. J.; Brothers, E. N.; Kudin, K. N.; Staroverov, V. N.; Keith, T. A.; Kobayashi, R.; Normand, J.; Raghavachari, K.; Rendell, A. P.; Burant, J. C.; Iyengar, S. S.; Tomasi, J.; Cossi, M.; Millam, J. M.; Klene, M.; Adamo, C.; Cammi, R.; Ochterski, J. W.; Martin, R. L.; Morokuma, K.; Farkas, O.; Foresman, J. B.; Fox, D. J. Gaussian, Inc., Wallingford CT, 2016.

[150] P. Giannozzi, S. Baroni, N. Bonini, M. Calandra, R. Car, C. Cavazzoni, D. Ceresoli, G. L. Chiarotti, M. Cococcioni, I. Dabo, A. Dal Corso, S. Fabris, G. Fratesi, S. de Gironcoli, R. Gebauer, U. Gerstmann, C. Gougoussis, A. Kokalj, M. Lazzeri, L. Martin-Samos, N. Marzari, F. Mauri, R. Mazzarello, S. Paolini, A. Pasquarello, L. Paulatto, C. Sbraccia, S. Scandolo, G. Sclauzero, A. P. Seitsonen, A. Smogunov, P. Umari, R. M. Wentzcovitch, J.Phys.: Condens.Matter 21, 395502 (2009)

[151] P. Giannozzi, O. Andreussi, T. Brumme, O. Bunau, M. Buongiorno Nardelli, M. Calandra, R. Car, C. Cavazzoni, D. Ceresoli, M. Cococcioni, N. Colonna, I. Carnimeo, A. Dal Corso, S. de Gironcoli, P. Delugas, R. A. DiStasio Jr, A. Ferretti, A. Floris, G. Fratesi, G. Fugallo, R. Gebauer, U. Gerstmann, F. Giustino, T. Gorni, J Jia, M. Kawamura, H.-Y. Ko, A. Kokalj, E. Küçükbenli, M .Lazzeri, M. Marsili, N. Marzari, F. Mauri, N. L. Nguyen, H.-V. Nguyen, A. Otero-de-la-Roza, L. Paulatto, S. Poncé, D. Rocca, R. Sabatini, B. Santra, M.

Schlipf, A. P. Seitsonen, A. Smogunov, I. Timrov, T. Thonhauser, P. Umari, N. Vast, X. Wu, S. Baroni, J.Phys.: Condens.Matter 29, 465901 (2017)

[152] Jeong, K., Park, S., & Lee, S. Y. (2019). Revisiting polymeric single lithium-ion conductors as an organic route for all-solid-state lithium ion and metal batteries. *Journal of materials chemistry A*, *7*(5), 1917-1935.

[153] Zhou, Q., Ma, J., Dong, S., Li, X., & Cui, G. (2019). Intermolecular chemistry in solid polymer electrolytes for high-energy-density lithium batteries. *Advanced Materials*, *31*(50), 1902029.

[154] Jin, Z., Xie, K., Hong, X., Hu, Z., & Liu, X. (2012). Application of lithiated Nafion ionomer film as functional separator for lithium sulfur cells. *Journal of Power Sources*, *218*, 163-167.

[155] Tu, Z., Choudhury, S., Zachman, M. J., Wei, S., Zhang, K., Kourkoutis, L. F., & Archer, L. A. (2017). Designing artificial solid-electrolyte interphases for single-ion and high-efficiency transport in batteries. Joule, 1(2), 394-406.

[156] Meziane, R., Bonnet, J. P., Courty, M., Djellab, K., & Armand, M. (2011). Single-ion polymer electrolytes based on a delocalized polyanion for lithium batteries. *Electrochimica Acta*, *57*, 14-19.

[157] Bouchet, R., Maria, S., Meziane, R., Aboulaich, A., Lienafa, L., Bonnet, J. P., ... & Armand, M. (2013). Single-ion BAB triblock copolymers as highly efficient electrolytes for lithium-metal batteries. *Nature materials*, *12*(5), 452-457.

[158] Lago, N., Garcia-Calvo, O., Lopez del Amo, J. M., Rojo, T., & Armand, M. (2015). All-solid-state lithium-ion batteries with grafted ceramic nanoparticles dispersed in solid polymer electrolytes. *ChemSusChem*, *8*(18), 3039-3043.

[159] Kurono, R., Mehta, M. A., Inoue, T., & Fujinami, T. (2001). Preparation and characterization of lithium ion conducting borosiloxane polymer electrolytes. *Electrochimica acta*, *47*(3), 483-487.

[160] Yang, Y., Inoue, T., Fujinami, T., & Mehta, M. A. (2001). Blended lithium ion conducting polymer electrolytes based on boroxine polymers. *Solid State Ionics*, *140*(3-4), 353-359.

[161] Blazejczyk, A., Wieczorek, W., Kovarsky, R., Golodnitsky, D., Peled, E., Scanlon, L. G., ... & Scrosati, B. (2004). Novel solid polymer electrolytes with single lithium-ion transport. *Journal of the Electrochemical Society*, *151*(10), A1762.

[162] Blazejczyk, A., Szczupak, M., Wieczorek, W., Cmoch, P., Appetecchi, G. B., Scrosati, B., ... & Peled, E. (2005). Anion-binding calixarene receptors: Synthesis, microstructure, and effect on properties of polyether electrolytes. *Chemistry of materials*, *17*(6), 1535-1547.

[163] Gorecki, W., Roux, C., Clémancey, M., Armand, M., & Belorizky, E. (2002). NMR and conductivity study of polymer electrolytes in the imide family: P (EO)/Li [N (SO2CnF2n+ 1)(SO2CmF2m+ 1)]. *ChemPhysChem*, *3*(7), 620-625.

[164] Zhang, H., Chen, F., Lakuntza, O., Oteo, U., Qiao, L., Martinez-Ibañez, M., ... & Armand, M. (2019). Suppressed mobility of negative charges in polymer electrolytes with an ether-functionalized anion. *Angewandte Chemie*, *131*(35), 12198-12203.

[165] Zhang, H., Oteo, U., Judez, X., Eshetu, G. G., Martinez-Ibanez, M., Carrasco, J., ... & Armand, M. (2019). Designer anion enabling solid-state lithium-sulfur batteries. *Joule*, *3*(7), 1689-1702.

[166] Borodin, O., & Smith, G. D. (2006). Mechanism of ion transport in amorphous poly (ethylene oxide)/LiTFSI from molecular dynamics simulations. *Macromolecules*, *39*(4), 1620-1629.

[167] Ebadi, M., Costa, L. T., Araujo, C. M., & Brandell, D. (2017). Modelling the polymer electrolyte/Li-metal interface by molecular dynamics simulations. *Electrochimica acta*, *234*, 43-51.

[168] Brooks, D. J., Merinov, B. V., Goddard III, W. A., Kozinsky, B., & Mailoa, J. (2018). Atomistic description of ionic diffusion in PEO–LiTFSI: Effect of temperature, molecular weight, and ionic concentration. *Macromolecules*, *51*(21), 8987-8995.

[169] Thakuria, R., Nath, N. K., & Saha, B. K. (2019). The nature and applications of π–π interactions: a perspective. *Crystal Growth & Design*, *19*(2), 523-528.

[170] Zhuang, W. R., Wang, Y., Cui, P. F., Xing, L., Lee, J., Kim, D., ... & Oh, Y. K. (2019). Applications of π-π stacking interactions in the design of drug-delivery systems. *Journal of controlled release*, *294*, 311-326.

[171] Huang, Q., Wei, T., Zhang, M., Dong, L. Z., Zhang, A. M., Li, S. L., ... & Lan, Y. Q. (2017). A highly stable polyoxometalate-based metal–organic framework with π–π stacking for enhancing lithium ion battery performance. *Journal of Materials Chemistry A*, *5*(18), 8477-8483.

[172] Kolek, M., Otteny, F., Schmidt, P., Mück-Lichtenfeld, C., Einholz, C., Becking, J., ... & Esser, B. (2017). Ultra-high cycling stability of poly (vinylphenothiazine) as a battery cathode material resulting from π–π interactions. *Energy & environmental science*, *10*(11), 2334-2341.

[173] Park, S. J., Zhao, H., Ai, G., Wang, C., Song, X., Yuca, N., ... & Liu, G. (2015). Side-chain conducting and phase-separated polymeric binders for high-performance silicon anodes in lithium-ion batteries. *Journal of the American Chemical Society*, *137*(7), 2565-2571.

[174] Qiao, L., Rodriguez Pena, S., Martínez-Ibañez, M., Santiago, A., Aldalur, I., Lobato, E., ... & Zhang, H. (2022). Anion π–π stacking for improved lithium transport in polymer electrolytes. *Journal of the American Chemical Society*, *144*(22), 9806-9816.

[175] Qiao, L., Oteo, U., Zhang, Y., Peña, S. R., Martínez-Ibañez, M., Santiago, A., ... & Armand, M. (2020). Trifluoromethyl-free anion for highly stable lithium metal polymer batteries. *Energy Storage Materials*, *32*, 225-233.

[176] Zhang, H., Oteo, U., Zhu, H., Judez, X., Martinez-Ibañez, M., Aldalur, I., ... & Armand, M. (2019). Enhanced lithium-ion conductivity of polymer electrolytes by selective introduction of hydrogen into the anion. *Angewandte Chemie*, *131*(23), 7911-7916.

[177] Tong, B., Wang, P., Ma, Q., Wan, H., Zhang, H., Huang, X., ... & Zhou, Z. (2020). Lithium fluorinated sulfonimide-based solid polymer electrolytes for Li|| LiFePO4 cell: The impact of anionic structure. *Solid State Ionics*, *358*, 115519.

[178] Harrison, W. J., Mateer, D. L., & Tiddy, G. J. (1996). Liquid-crystalline J-aggregates formed by aqueous ionic cyanine dyes. *The journal of physical chemistry*, *100*(6), 2310-2321.

[179] Balakrishnan, K., Datar, A., Oitker, R., Chen, H., Zuo, J., & Zang, L. (2005). Nanobelt self-assembly from an organic n-type semiconductor: propoxyethyl-PTCDI. *Journal of the American Chemical Society*, *127*(30), 10496-10497.

[180] Che, Y., Datar, A., Balakrishnan, K., & Zang, L. (2007). Ultralong nanobelts self-assembled from an asymmetric perylene tetracarboxylic diimide. *Journal of the American Chemical Society*, *129*(23), 7234-7235.

[181] Wei, W., Liu, D., Wei, Z., & Zhu, Y. (2017). Short-range π–π stacking assembly on P25 TiO2 nanoparticles for enhanced visible-light photocatalysis. *ACS Catalysis*, *7*(1), 652-663.

[182] Xu, K. (2014). Electrolytes and interphases in Li-ion batteries and beyond. *Chemical reviews*, *114*(23), 11503-11618.

[183] Oteo, U., Martinez-Ibañez, M., Aldalur, I., Sanchez-Diez, E., Carrasco, J., Armand, M., & Zhang, H. (2019). Improvement of the cationic transport in polymer electrolytes with (difluoromethanesulfonyl)(trifluoromethanesulfonyl) imide salts. *ChemElectroChem*, *6*(4), 1019-1022.

[184] Wells, A. S., & Coombe, V. T. (2006). On the freshwater ecotoxicity and biodegradation properties of some common ionic liquids. *Organic Process Research & Development*, *10*(4), 794-798.

[185] Neumann, J., Cho, C. W., Steudte, S., Köser, J., Uerdingen, M., Thöming, J., & Stolte, S. (2012). Biodegradability of fluoroorganic and cyano-based ionic liquid anions under aerobic and anaerobic conditions. *Green chemistry*, *14*(2), 410-418.

[186] Banks, R. E., Smart, B. E., & Tatlow, J. C. (Eds.). (1994). *Organofluorine Chemistry: Principles and Commercial Applications*. Springer Science & Business Media.

[187] Yang, X., Sun, Q., Zhao, C., Gao, X., Adair, K., Zhao, Y., ... & Sun, X. (2019). Self-healing electrostatic shield enabling uniform lithium deposition in all-solid-state lithium batteries. Energy Storage Materials, 22, 194-199.

[188] Yang, X., Gao, X., Zhao, C., Sun, Q., Zhao, Y., Adair, K., ... & Sun, X. (2020). Suppressed dendrite formation realized by selective Li deposition in all-solid-state lithium batteries. *Energy Storage Materials*, *27*, 198-204.

[189] Ein-Eli, Y., & Koch, V. R. (1997). Chemical oxidation: a route to enhanced capacity in Li-ion graphite anodes. *Journal of the Electrochemical Society*, *144*(9), 2968.

[190] Linert, W., Camard, A., Armand, M., & Michot, C. (2002). Anions of low Lewis basicity for ionic solid state electrolytes. *Coordination chemistry reviews*, *226*(1-2), 137-141.

[191] Mindemark, J., Lacey, M. J., Bowden, T., & Brandell, D. (2018). Beyond PEO—Alternative host materials for Li+-conducting solid polymer electrolytes. *Progress in Polymer Science*, *81*, 114-143.

[192] Xu, H., Xie, J., Liu, Z., Wang, J., & Deng, Y. (2020). Carbonyl-coordinating polymers for high-voltage solid-state lithium batteries: Solid polymer electrolytes. *MRS Energy & Sustainability*, *7*.

[193] Tominaga, Y., Shimomura, T., & Nakamura, M. (2010). Alternating copolymers of carbon dioxide with glycidyl ethers for novel ion-conductive polymer electrolytes. *Polymer*, *51*(19), 4295-4298.

[194] Mindemark, J., Sun, B., Törmä, E., & Brandell, D. (2015). High-performance solid polymer electrolytes for lithium batteries operational at ambient temperature. *Journal of Power Sources*, *298*, 166-170.

[195] Bergfelt, A., Lacey, M. J., Hedman, J., Sångeland, C., Brandell, D., & Bowden, T. (2018). ε-Caprolactone-based solid polymer electrolytes for lithium-ion batteries: synthesis, electrochemical characterization and mechanical stabilization by block copolymerization. *RSC advances*, *8*(30), 16716-16725.

[196] Chiu, C. Y., Chen, H. W., Kuo, S. W., Huang, C. F., & Chang, F. C. (2004). Investigating the effect of miscibility on the ionic conductivity of LiClO4/PEO/PCL ternary blends. *Macromolecules*, *37*(22), 8424-8430.

[197] Li, J., Zhang, Y., Jiacuo, Y., Shang, Y., Huo, H., & Jiang, S. (2012). Miscibility and rheologically determined phase diagram of poly (ethylene oxide)/poly (ε-caprolactone) blends. *Polymer bulletin*, *68*, 1405-1423.

[198] Huo, H., Yang, Y., & Zhao, X. (2014). Effects of lithium perchlorate on the nucleation and crystallization of poly (ethylene oxide) and poly (ε-caprolactone) in the poly (ethylene oxide)–poly (ε-caprolactone)–lithium perchlorate ternary blend. *CrystEngComm*, *16*(7), 1351-1358.

[199] Woodruff, M. A., & Hutmacher, D. W. (2010). The return of a forgotten polymer—Polycaprolactone in the 21st century. *Progress in polymer science*, *35*(10), 1217-1256.

[200] Meabe, L., Peña, S. R., Martinez-Ibañez, M., Zhang, Y., Lobato, E., Manzano, H., ... & Zhang, H. (2020). Insight into the ionic transport of solid polymer electrolytes in polyether and polyester blends. *The Journal of Physical Chemistry C*, *124*(33), 17981-17991.

[201] Navarro-Suárez, A. M., & Johansson, P. (2019). A Silatrane: Molecule-Based Crystal Composite Solid-State Electrolyte for All-Solid-State Lithium Batteries. *Batteries & Supercaps*, *2*(11), 956-962.

[202] Martinez-Ibañez, M., Sanchez-Diez, E., Qiao, L., Zhang, Y., Judez, X., Santiago, A., ... & Zhang, H. (2020). Unprecedented improvement of single Li-Ion conductive solid polymer electrolyte through salt additive. *Advanced Functional Materials*, *30*(16), 2000455.

[203] Gorecki, W., Jeannin, M., Belorizky, E., Roux, C., & Armand, M. (1995). Physical properties of solid polymer electrolyte PEO (LiTFSI) complexes. *Journal of Physics: Condensed Matter*, *7*(34), 6823.

[204] Timachova, Ksenia, Hiroshi Watanabe, and Nitash P. Balsara. "Effect of molecular weight and salt concentration on ion transport and the transference number in polymer electrolytes." *Macromolecules* 48.21 (2015): 7882-7888.

[205] Pożyczka, K., et al. "Ionic conductivity and lithium transference number of poly (ethylene oxide): LiTFSI system." *Electrochimica Acta* 227 (2017): 127-135.

[206] Angell, C. A., Liu, C., & Sanchez, E. (1993). Rubbery solid electrolytes with dominant cationic transport and high ambient conductivity. *Nature*, *362*(6416), 137-139.

[207] Liu, W., Yi, C., Li, L., Liu, S., Gui, Q., Ba, D., ... & Liu, J. (2021). Designing polymer-in-salt electrolyte and fully infiltrated 3D electrode for integrated solid-state lithium batteries. *Angewandte Chemie*, *133*(23), 13041-13050.

[208] Wang, Z., Gao, W., Huang, X., Mo, Y., & Chen, L. (2001). Ion transport in polyacrylonitrile-based electrolytes with high LiTFSI contents. *Electrochemical and Solid-State Letters*, *4*(9), A148.

[209] Yi, C., Liu, W., Li, L., Dong, H., & Liu, J. (2019). Polymer-in-salt solid electrolytes for lithium-ion batteries. *Functional Materials Letters*, *12*(06), 1930006.

[210] Molinari, N., Mailoa, J. P., & Kozinsky, B. (2018). Effect of salt concentration on ion clustering and transport in polymer solid electrolytes: a molecular dynamics study of peo–litfsi. *Chemistry of Materials*, *30*(18), 6298-6306.